ACOUSTIC TRANSDUCTION – MATERIALS AND DEVICES

Period 1 January 2000 to 31 December 2000

Annual Report

VOLUME III

OFFICE OF NAVAL RESEARCH
Contract No: N00014-96-1-1173

APPROVED FOR PUBLIC RELEASE –
DISTRIBUTION UNLIMITED

Reproduction in whole or in part is permitted for any
purpose of the United States Government

Kenji Uchino

PENNSTATE

1855

THE MATERIALS RESEARCH LABORATORY
UNIVERSITY PARK, PA

20010817 102

REPORT DOCUMENTATION PAGE

Public reporting burden for this collection of information is estimated to average 1 hour per response, including the time for reviewing instructions, searching existing data sources, gathering and maintaining the data needed, and completing and reviewing the collection of information. Send comments regarding this burden estimate or any other aspect of this collection of information, including suggestions for reducing this burden, to Washington Headquarters Services, Directorate for Information Operations and Reports, 1215 Jefferson Davis Highway, Suite 1204, Arlington, VA 22202-4302, and to the Office of Management and Budget, Paperwork Reduction Project (0704-0188), Washington, DC 20503.

1. AGENCY USE ONLY (Leave blank)	2. REPORT DATE	3. REPORT TYPE AND DATES COVERED
	7/12/2001	ANNUAL REPORT 01/01/2000--12/31/2000

4. TITLE AND SUBTITLE
ACOUSTIC TRANSDUCTION -- MATERIALS AND DEVICES

5. FUNDING NUMBERS
ONR CONTRACT NO.
N00014-96-1-11173

6. AUTHOR(S)
Materials Research Laboratory
The Pennsylvania State University
University Park, Pa 16802

7. PERFORMING ORGANIZATION NAME(S) AND ADDRESS(ES)

8. PERFORMING ORGANIZATION REPORT NUMBER

9. SPONSORING / MONITORING AGENCY NAME(S) AND ADDRESS(ES)
Office of Naval Research   Office of Naval Research
ONR 321SS   Regional Office Chicago
Ballston Centre Tower One   536 S. Clark Str. RM 208
800 N. Quincy Street   Chicago IL 60605-1588
Arlington, VA 2217-5660

10. SPONSORING / MONITORING AGENCY REPORT NUMBER

11. SUPPLEMENTARY NOTES

12a. DISTRIBUTION / AVAILABILITY STATEMENT

12b. DISTRIBUTION CODE

13. ABSTRACT (Maximum 200 words)

SEE FOLLOWING PAGE

14. SUBJECT TERMS

15. NUMBER OF PAGES

16. PRICE CODE

17. SECURITY CLASSIFICATION OF REPORT	18. SECURITY CLASSIFICATION OF THIS PAGE	19. SECURITY CLASSIFICATION OF ABSTRACT	20. LIMITATION OF ABSTRACT
UNCLASSIFIED	UNCLASSIFIED	UNCLASSIFIED	

NSN 7540-01-280-5500

GENERAL INSTRUCTIONS FOR COMPLETING SF 298

The Report Documentation Page (RDP) is used in announcing and cataloging reports. It is important that this information be consistent with the rest of the report, particularly the cover and title page. Instructions for filling in each block of the form follow. It is important to *stay within the lines* to meet *optical scanning requirements*.

Block 1. Agency Use Only *(Leave blank)*.

Block 2. Report Date. Full publication date including day, month, and year, if available (e.g. 1 Jan 88). Must cite at least the year.

Block 3. Type of Report and Dates Covered. State whether report is interim, final, etc. If applicable, enter inclusive report dates (e.g. 10 Jun 87 - 30 Jun 88).

Block 4. Title and Subtitle. A title is taken from the part of the report that provides the most meaningful and complete information. When a report is prepared in more than one volume, repeat the primary title, add volume number, and include subtitle for the specific volume. On classified documents enter the title classification in parentheses.

Block 5. Funding Numbers. To include contract and grant numbers; may include program element number(s), project number(s), task number(s), and work unit number(s). Use the following labels:

C	- Contract	PR	- Project
G	- Grant	TA	- Task
PE	- Program Element	WU	- Work Unit Accession No.

Block 6. Author(s). Name(s) of person(s) responsible for writing the report, performing the research, or credited with the content of the report. If editor or compiler, this should follow the name(s).

Block 7. Performing Organization Name(s) and Address(es). Self-explanatory.

Block 8. Performing Organization Report Number. Enter the unique alphanumeric report number(s) assigned by the organization performing the report.

Block 9. Sponsoring/Monitoring Agency Name(s) and Address(es). Self-explanatory.

Block 10. Sponsoring/Monitoring Agency Report Number. *(If known)*

Block 11. Supplementary Notes. Enter information not included elsewhere such as: Prepared in cooperation with...; Trans. of...; To be published in.... When a report is revised, include a statement whether the new report supersedes or supplements the older report.

Block 12a. Distribution/Availability Statement. Denotes public availability or limitations. Cite any availability to the public. Enter additional limitations or special markings in all capitals (e.g. NOFORN, REL, ITAR).

DOD	-	See DoDD 5230.24, "Distribution Statements on Technical Documents."
DOE	-	See authorities.
NASA	-	See Handbook NHB 2200.2.
NTIS	-	Leave blank.

Block 12b. Distribution Code.

DOD	-	Leave blank.
DOE	-	Enter DOE distribution categories from the Standard Distribution for Unclassified Scientific and Technical Reports.
NASA	-	Leave blank.
NTIS	-	Leave blank.

Block 13. Abstract. Include a brief *(Maximum 200 words)* factual summary of the most significant information contained in the report.

Block 14. Subject Terms. Keywords or phrases identifying major subjects in the report.

Block 15. Number of Pages. Enter the total number of pages.

Block 16. Price Code. Enter appropriate price code *(NTIS only)*.

Blocks 17. - 19. Security Classifications. Self-explanatory. Enter U.S. Security Classification in accordance with U.S. Security Regulations (i.e., UNCLASSIFIED). If form contains classified information, stamp classification on the top and bottom of the page.

Block 20. Limitation of Abstract. This block must be completed to assign a limitation to the abstract. Enter either UL (unlimited) or SAR (same as report). An entry in this block is necessary if the abstract is to be limited. If blank, the abstract is assumed to be unlimited.

ABSTRACT

This report describes research performed over the period 1st January 2000 to 31st December 2000 on a MURI under Office of Naval Research contract N00014-96-1-1173 on the topic "Acoustic Transduction Materials and Devices". This program brings together researchers from the Materials Research Laboratory (MRL), the Applied Research Laboratory (ARL) and the Center for Acoustics and Vibrations (CAV) at the Pennsylvania State University. As has become customary over many years, research on the program is detailed in the technical appendices of published work, and only a brief narrative description connecting these studies is given in the text.

The program combines a far reaching exploration of the basic phenomena contributing to piezoelectric and electrostrictive response with the highly applied thrusts necessary to produce the "pay-off" in new applications relevant to Navy needs. Polarization vector tilting in the ferroelectric phase of perovskite structure crystals at compositions close to a morphotropic phase boundary (MPB) was first underscored on this program some four years ago, and is now widely accepted as one mode for exploiting the large intrinsic spontaneous strain in the ferroelectric to produce exceedingly strong anhysteritic piezoelectric response and very large electric field controlled elastic strain. New evidence for the importance of both spontaneous (monoclinic) and electric field induced tilting on the properties of both single and polycrystal MPB systems is presented in this report.

The puzzling phenomena associated with relaxor ferroelectric response have long been a topic of study in MRL, where the micro-polar region model and the application of Vogel/Fulcher to the dielectric slowing down were first applied. The current "pay-off" is in the greatly enhanced relaxor ferroelectric electrostrictive response from high electron energy irradiated polyvinylidene difluoride: triflouroethylene (PVDF: TrFE) co-polymer discussed in this report. This development opens a new field of high strain, high energy density actuators with tremendous practical applicability. Now the possibility of engineering this response by chemical manipulation in the terpolymer systems without irradiation further enhances the exciting possibilities.

In composite structures, the early promise of the flextensional cymbal type actuators is now being fully realized and programs exploring large area cymbal transducer arrays are progressing very well, both at MRL/ARL and at NRL. The connection with CAV at Penn State is particularly important in keeping the MURI faculty aware of problems endemic to water as our host medium and the effects of turbulence in flow and the need for many types of acoustic noise control.

New designs of piezoelectric transformers and motors are demanding materials with lower loss levels under continuous high driving, and important progress is reported in separating and understanding the components of this loss and in designing new doping schemes for ceramics which enhance power capability almost tenfold. New piezoelectric micro-motor designs look particularly attractive and appear to offer significant advantages over electromagnetics for very small-scale applications. Thick and thin film studies for MEMS are progressing well and offering new insights into fatigue and switching behavior in the ferroelectrics.

ACOUSTIC TRANSDUCTION – MATERIALS AND DEVICES

Period 1 January 2000 to 31 December 2000

Annual Report

VOLUME III

OFFICE OF NAVAL RESEARCH
Contract No: N00014-96-1-1173

APPROVED FOR PUBLIC RELEASE –
DISTRIBUTION UNLIMITED

Kenji Uchino

APPENDICES

VOLUME I

GENERAL SUMMARY PAPERS

1. Uchino, K., Encyclopedia of Vibration, Partial Charge "Electrostrictive Materials", Academic Press, London (2000). [in press]
2. Uchino, K., and Y. Ito, Encyclopedia Smart Materials, J. Harvey, Edit., Partial Charge "Smart Ceramics: Transducers, Sensors and Actuators", John Wiley & Sons, New York (2000). [in press]
3. Wennu Ma, L.E. Cross, "Observation of the flexoelectric effect in relaxor PB ($Mg_{1/3}NB_{2/3}$) O_3 ceramics", Applied Physics Letters. Volume #8 number 19 pp. 2920
4. R. Hatt and W. Cao, "Landau-Ginzburg Model for Antiferroelectric Phase Transition Based on Microscopic Symmetry", Phys. Rev. B, vol. **62**, pp. 818-823 (2000).

2.0 MATERIALS STUDIES

2.1 Polycrystal Perovskite Ceramics

5. A.S. Bhalla, R. Guo, R. Roy, "The Perovskite Structure - A Review of Its Role in Ceramic Science and Technology, "*Mat. Res. Innovat.,* **4(1)**, 3-26, (2000)
6. E.F. Alberta, R. Guo, L.E. Cross, A.S. Bhalla, "Structure-Property Diagrams of Ferroic Solid Solutions. Part I: Perovskite Ferroelectrics with Morphotropic Phase Boundaries," *Ferroelectrics Review*, 3, 1, (2001)
7. B. Noheda, J.A. Gonzalo, L.E. Cross, R. Guo, S-E. Park, D.E. Cox, G. Shirane, "Tetragonal-to-Monoclinic Phase Transition in a Ferroelectric Perovskite: the Structure of $PbZr_{0.52}Ti_{0.48}O_3$, "*Phys. Rev. B,* **61(13)**, 8687-8689, (2000)
8. B. Noheda, D.E. Cox, G. Shirane, R. Guo, B. Jones, L.E. Cross, "Stability of the monoclinic phase in the ferroelectric perovskite $PbZr_{(1-x)}Ti_xO_3$, "*Los Alamos Natl. Lab., Prepr. Arch., Condens. Matter,* **1-8,** arXiv:cond-mat/0006152, (2000)
9. R. Guo, L.E. Cross, S-E. Park, B. Noheda, D.E. Cox, G. Shirane, "Origin of the high piezoelectric response in $PbZr_{1-x}Ti_xO_3$," *Phys. Rev. Letters,* **84(23)**, 5423-5426, (2000)
10 W. Jiang and W. Cao, "Nonlinear Elastic Properties of Lead Zirconate Titanate Ceramics", J. Appl. Phys. vol. **88**: 6684-6689 (2000).
11. Chen, Y. H., D. Viehland and K. Uchino, "Substituent Effects in $0.65Pb(Mg_{1/3}Nb_{2/3})O_3$-$0.35PbTiO_3$ Piezoelectric Ceramics" J. Electroceramics, **6**, 13-20 (2001). (First Author Supervised by Candidate).
12. W.H. Jiang and W. Cao, " Intrinsic and Coupling-induced Elastic Nonlinearity of Lanthanum-doped Lead Magnesium Niobate-Lead Titanate Electrostrictive Ceramic", Appl. Phys. Lett., vol. **77**, pp. 1387-1389 (2000).

1

VOLUME II

2.0 MATERIALS STUDIES

2.2 Single Crystal Systems

13. L.E. Cross, J. Fousek, " Engineering Multidomain Ferroic Samples", Ferroelectrics, 2001, Vol. 252, pp. 171-180.

14. Wada, Satoshi, Takaaki Tsurmi, Miour Osada, Masato Kakihana, Seung Eek Park, L.Eric Cross and Thomas R. Shrout. "Change of Macroscopic and Microscopic Symmetries in Relaxor PZN Single Crystal Under Bias Filed." Transactions of the Material Research Society of Japan, **25** (1). 281-284 (2000).

15. Wada, Satoshi, Takaaki Tsurmi, Miour Osada, Masato Kakihana, Seung Eek Park, L.Eric Cross and Thomas R. Shrout. "Dipolar Behavior in PZN Relaxor Single crystals under Bias Fields." Transactions of the Materials Research Society of Japan **25** (1), 281-284 (2000).

16. Belegundu, U., X. Du and K. Uchino, "Switching Current in $Pb(Zn_{1/3}Nb_{2/3})O_3-PbTiO_3$ Single Crystals," Symp. LL Proc., Mater. Res. Soc. Fall Mtg. '99, (LL.1.9, Boston, Nov. 29-Dec.3. 1999), Vol.**604**, 39-44 (2000).

17. Yu Lu, D.-Y. Jeong, Z. Y. Cheng, Q. M. Zhang, H. Luo, Z. Yin, and D. Viehland. Phase Transitional Behavior and Piezoelectric Properties of the orthorhombic Phase of PMN-PT Single Crystals. Appl. Phys. Lett. **78**, 3109 (2001).

18. Yu Lu, Z.-Y. Cheng, E. Park, S. F. Liu and Q. M. Zhang. Linear Electro-optic Effect of $0.88Pb(Zn_{1/3} Nb_{2/3})-0.12PbTiO_3$ Single Crystal. Jpn. J. Appl. Phys. **39**, 141-145 (2000).

19. Y. Barad, Yu Lu, Z. Y. Cheng, S. E. Park, and Q. M. Zhang. Composition, Temperature, and Crystal Orientation Dependence of Linear Electro-optic Properties of PZN-PT Single Crystals. Appl. Phys. Lett. **77**, 1247-1249 (2000).

20. Y. Lu, Z.-Y. Cheng, Y. Barad, and Q. M. Zhang. Photoelastic Effects in the Tetragonal PZN-PT Single Crystals near the Morphotropic Phase Boundary. J. Appl. Phys. **89**, 5075 (2001).

2.3 High Strain Polymers

21. Vivek Bharti, H. S. Xu, G. Shanthi, Q. M. Zhang, and Kuming Liang. Polarization and Structural Properties of High Energy Electron Irradiated P(VDF-TrFE) Copolymer Films. J. Appl. Phys. **87**, 452-461 (2000).

22. Haisheng Xu, G. Shanthi, V. Bharti, Q. M. Zhang, and T. Ramatowski. Structural, Conformational, and Polarization Changes of P(VDF-TrFE) Copolymer Induced by High Energy Electron Irradiation. Macromolecules, **33**, 4125-4131(2000).

23. Q. M. Zhang, Z. Y. Cheng, and Vivek Bharti. Relaxor Ferroelectric Behavior in High Energy Electron Irradiated P(VDF-TrFE) copolymers. Appl. Phys. **A70**, 307-312 (2000).

24. Vivek Bharti and Q. M. Zhang. Dielectric Study of Relaxor Ferroelectric P(VDF-TrEF) Copolymer System. Phys. Rev. B. **63**, 184103 (2001).

25. Z.Y. Cheng, Vivek Bharti, T.B. Xu, Hansheng Xu, T. Mai, and Q. M. Zhang. Electrostrictive P(VDF-TrFE) Copolymers. Sensors and Actuators A-Phys. **90**, 138-147 (2001)

26. Z. Y. Cheng, V. Bharti, T. Mai, T. B. Xu, Q. M. Zhang, K. Hamilton, T. Ramotowski, K. A. Wright, and R. Ting. Effect of High Energy Electron Irradiation on the Electromechanical Properties of Poly(vinylidene fluoride-trifluorethylene) 50/50 and 65/35 Copolymers. IEEE Trans. UFFC <u>47</u>, 1296 (2000).

27. Vivek Bharti, Z.-Y. Cheng, T, Mai, Q. M. Zhang, T. Ramotowski, K. A. Wright. High Electromechanical Coupling Factor and Electrostrictive Strain over a Broad Frequency Range in Electrostrictive Poly(vinylidene fluoride-trifluoroethylene) Copolymer. Japn. J. Appl. Phys. <u>40</u>, 672 (2001).

28. Vivek Bharti, G. Shanthi, H. Xu, Q. M. Zhang, and K. Liang. Evolution of Transitional Behavior and Structure of Electron Irradiated P(VDF-TrFE) Copolymer Films. Mater. Lett. <u>47</u>, 107-111 (2001).

29. F. Xia, H. Xu, F. Fang, B. Razivi, Z. Y. Cheng, Yu Lu, Baoming Xu, and Q. M. Zhang. Thickness Dependence Behavior of Ferroelectric Switching in P(VDF-TrFE) Spin Cast Films. Appl. Phys. Lett. <u>78</u>, 1122 (2001).

30. Q. M. Zhang, H. S. Xu, Fei Fang, Z.-Y. Cheng, Xia Feng, and H. You. Observation of Critical Thickness of Crystallization in Spin Cast Ferroelectric Thin Films. J. Appl. Phys. <u>89</u>, 2613 (2001).

31. Shizhuo Yin, Q. M. Zhang, K.-W. Chung, R. Yang, Z. Y. Cheng, and Yu Lu. Investigation of the Electro-optic Properties of Electron-irradiated P(VDF-TrFE) Copolymer. Opt. Eng. <u>39</u>, 670-672 (2000).

32. Hai-Sheng Xu, Z.-Y. Cheng, Vivek Bharti, Shexi Wang, and Q. M. Zhang. All-Polymer Electromechanical Systems Consisting of Electrostrictive Poly(vinylidene fluoride-trifluoroethylene) and Conductive Polyaniline. J. Appl. Poly. Sci. <u>75</u>, 945-951 (2000).

33. H. Xu, Z.Y. Cheng, D. Olson, T. Mai, Q. M. Zhang, and G. Kavarnos. Ferroelectric and Electromechanical Properties of P(VDF-TrFE-CTFE) Terpolymer. Appl. Phys. Lett. <u>78</u>, 2360 (2001).

3.0   TRANSDUCER STUDIES

3.1   Composite Structures

34. Uchino, K., "Piezoelectro Composites," Chap.5.24, Comprehensive Composite Materials, Elsevier Science, Oxford, UK (2000).

35. Tressler, J. and K. Uchino, "Piezoelectric Composite Sensors," Chap.5.22, Comprehensive Composite Materials, Elsevier Science, Oxford, UK (2000).

VOLUME III

36. Meyer, R.J. Jr., A. Dogan, C. Yoon, S. Pilgrim and R.E. Newnham, "Displacement Amplification of Electroactive Materials Using the Cymbal Flextensional Transducer," Sensors & Actuators A, vol.87, pp. 157-162 (2001).

37. Dogan, A., K. Uchino and R. E. Newnham, "Flextensional Composite Transducers: Designing, Fabrication and Application," Proc. NATO- Advanced Research Workshop: Piezoelectric Materials: Advance in Science, Technology and Applications, (Predeal, Romania, May 24-27, 1999, Kluwer Academic Publ., p.357-374 (2000).

3

38.   Zhang, J., A.C. Hladky-Hennion, W.J. Hughes, and R.E. Newnham, "Modeling and Underwater Characterization of Cymbal Transducers and Arrays," IEEE Transactions on Ultrasonics, Ferroelectrics, and Frequency Control, vol. 48 (2), pp. 560-568 (2001).

39.   Zhang, J., W. J. Hughes, R. J. Meyer Jr., K. Uchino and R. E. Newnham, "Cymbal Array: A Broad Band Sound Projector," Ultrasonics 37, 523-529 (2000).

40.   Zhang, J., A.C. Hladky-Hennion, W.J. Hughes, and R.E. Newnham, " A Miniature Class V flextensional cymbal transducer with directional beam   pattern: The Double-Driver," Ultrasonics, vol. 39, pp. 91-95 (2001).

41.   Meyer, R.J. Jr. and R.E. Newnham, "Flextensional transducers with Shape Memory Caps for Tunable Devices," Journal of Intelligent Materials Systems and Structures, vol. 11, pp. 199-205 (2001).

42.   Meyer, R.J. Jr., S. Alkoy, J. Cochran, T. Ritter, and R.E. Newnham, "Pre-focused Lead Titanate > 25 MHz Single Element Transducers from Hollow Spheres," IEEE Transactions on Ultrasonics, Ferroelectrics, and Frequency Control, vol. 48 (2), pp. 488-493 (2001).

43.   Y. Bai, Z.Y. Cheng, V. Bharti, H. S. Xu, and Q. M. Zhang. High Dielectric Constant Ceramic Powder Polymer Composites. Appl. Phys. Lett. 76, 3804-3806 (2000).

44.   M.R. Shen and W. Cao, "Acoustic Bandgap Formation in a Periodic Structure with Multilayer Unit Cells", J. Phys. D: Applied Physics, vol. **33**, pp. 1150-1154 (2000).

45.   T.B. Xu, Z-Y. Cheng, Q. M. Zhang, R. Baughman, C. Cui, A. Zakhidov, and J. Su. Fabrication and Characterization of 3-Dimensional Periodic Ferroelectric Polymer-Silica Opal Composites and Inverse Opal. J. Appl. Phys. 88(1), 405-409 (2000).

3.2   Piezoelectric Transformers

46.   Uchino, K., B. Koc, P. Laoratanakul and A. Vazquez Carazo, "Piezoelectric Transformers –New Perspective--," Proc. 3rd Asian Mtg. Ferroelectrics, D1d.1, Hong Kong, Dec. 12-15 (2000).

47.   Koc, B., and K. Uchino, "Disk Type Piezoelectric Transformer with Crescent Shape Input Electrodes," Proc. NATO- Advanced Research Workshop: Piezoelectric Materials: Advance in Science, Technology and Applications, (Predeal, Romania, May 24-27, 1999, Kluwer Academic Publ., p.375-382 (2000).

3.3   High Power Level Materials

48.   Uchino, K. and S. Hirose, "Loss Mechanisms in Piezoelectrics: How to Measure Different Losses Separately," IEEE UFFC Transactions, **48**, 307-321 (2001).

49.   Uchino, K., and J. Zheng, Y. H. Chen, X. Du and S. Hirose, "Loss Mechanisms in Piezoelectrics and Resonance/ Antiresonance," Proc. 101st Annual Mtg. of Amer. Ceram. Soc., Symp. Electronic Ceramic Materials and Devices, (Indianapolis, April 25 – 28, 1999), p.79-100 (2000).

50.   Uchino, K., J. Zheng, Y. H. Chen, X. Du, S. Hirose and S. Takahashi, "Loss Mechanisms in Piezoelectrics –Extrinsic and Intrinsic Losses--," Mater. Res. Soc. Fall Mtg. '99, (LL.1.6, Boston, Nov. 29-Dec.3, 1999), Vol. **604**, 25-31 (2000).

51. Chen, Y. H., S. Hirose, D. Viehland and K. Uchino, "Doping Effects in $Pb(Mg_{1/3}Nb_{2/3})O_3$-$PbTiO_3$ Ceramics for High Power Transduction Applications," Mater. Res. Soc. Fall Mtg. '99, (LL.5.8, Boston, Nov. 29-Dec.3, 1999), Vol. **604**, 215-220 (2000).

52. Chen, Y. H., S. Hirose, D. Viehland, S. Takahashi and K. Uchino, " Mn-Modified $Pb(Mg_{1/3}Nb_{2/3})O_3$-$PbTiO_3$ Ceramics: Improved Mechanical Quality Factors for High-Power Transducer Applications," Jpn. J. Appl. Phys. 39, 4843-4852 (2000).

53. Gao, Y. Y. H. Chen, J. Ryu, K. Uchino and D. Viehland, " Eu and Yb Substituent Effects on the Properties of $Pb(Zr_{0.52}Ti_{0.48})O_3$-$Pb(Mn_{1/3}Sb_{2/3})O_3$ Ceramics: Development of a New High-Power Piezoelectric with Enhanced Vibrational Velocity," Jpn. J. Appl. Phys., 40, 79-85 (2001).

VOLUME IV

3.4 Fluid Structure Interactions

54. Lauchle, G. C., W. A. Kargus IV. Scaling of Turbulent Wall Pressure Fluctuations Downstream of a Rearward Facing Step. *J. Acoust. Soc. Am.* **107**: L1-L6 (2000).

55. Capone, D. E., G. C. Lauchle. Modeling the Unsteady Lift and Drag on a Finite-Length Cylinder in Cross Flow. *J. Fluids and Struct.* **14**: 799-817 (2000).

56. Gavin, J. R., G. C. Lauchle. Modeling the Space-Time Correlations in the Wake Region of a Turbulent Boundary Layer. *Proc. of the ASME Noise Control and Acoustics Division 2000*, NCA-Vol. 27, pp 227-241 (2000).

57. Gavin, J. R., G. C. Lauchle, M. L. Jonson. Prediction of Turbulence Ingestion Forces for Rotors with Arbitrary Rake and Skew. *Proc. of the ASME Noise Control and Acoustics Division 2000.* NCA-Vol. 27, pp 217-226 (2000).

58. Lauchle, G. C, D. K. McLaughlin. Review of: *Acoustics of Fluid Structure Interactions* by M. S. Howe in *Noise Control Eng. J.* **48**: 70-71 (2000).

4.0 ACTUATOR STUDIES

4.1 Materials and Designs

59. Koc, B. and K. Uchino, "Piezoelectric Ultrasonic Motors," Chap.6.34, Comprehensive Composite Materials, Elsevier Science, Oxford, UK (2000).

60. Uchino, K., "Recent Trend of Piezoelectric Actuator Developments –Material, Design and Drive Technique Related Issues--," Proc. Actuator 2000 (7th Int'l Conf. New Actuators, June 19-21, 2000), p.34-39 (2000).

61. Yao, K., K. Uchino, Y. Xu, S. Dong, and L. C. Lim, "Compact Piezoelectric Stacked Actuators for High Power Applications," IEEE Trans. UFFC, 47, 819-825 (2000).

62. Liu, Rubin,L.e. Cross, Gareth Knowles, Bruce Bower, and Brookd Childers. " A Stackable Bonding-Free Flextensional Piezoelectirc Actuator" Journal of Electroceramics **4** (1), 201-206 92000)

63. A. E. Glazounov, Q. M. Zhang, C. Kim. Torsional Actuator Based on Mechanically Amplified Shear Piezoelectric Response. Sensors and Actuators A79, 22-30 (2000).

4.2   Photostriction

64.   Poosanaas, P., K. Tonooka and K. Uchino, "Photostrictive Actuators," J. Mechatronics
            10, 467-487 (2000).
65.   Uchino, K., P. Poosanaas and K. Tonooka, "Photostrictive Actuators–New Perspective-,"
            Proc. 3rd Asian Mtg. Ferroelectrics, C3p.105, Hong Kong, Dec. 12-15 (2000).
66.   Uchino, K., P. Poosanaas and K. Tonooka, "Photostrictive Actuators–New Perspective-,"
            Proc. 5th Euroconf. Appl. Polar Dielectrics, O-43, Jurmala, Latvia, Aug. 27-30
            (2000).
67.   Poosanaas, P., K. Tonooka, I. R. Abothu, S. Komarneni, and K. Uchino, "Influence of
            Composition and Dopant on Photostriction in Lanthanum-Modified Lead
            Zirconate Titanate Ceramics," J. Intelligent Mater. Systems and Structures **10**,
            439-445 (2000). (
68.   Poosanaas, P., Dogan, A., Prasadarao, A. V., Komarneni, S. and Uchino, K., "Effect of
            Ceramic Processing Methods on Photostrictive Ceramics", J. Advanced
            Performance Mater. **6**, 57-69 (1999).

VOLUME V

4.3   High Force Actuators

69.   A. E. Glazounov, Q. M. Zhang, and C. Kim. Torsional Actuator and Stepper Motor Based on
            Piezoelectric d_{15} Shear Response. J. Intel. Mater. Syst. & Struct. 11(6), 456-468 (2000).
70.   Galante, T., J. Frank, J. Bernard, W. Chen, G.A. Lesieutre, and G.H. Koopmann, "A
            High-Force, High-Displacement Piezoelectric Inchworm Actuator," Journal of
            Intelligent Materials Systems and Structures, Vol. 10, No. 12, December, 2000,
            pp. 962-972.

4.4   Piezoelectric Motors

71.   Koc, B. and K. Uchino, "Piezoelectric Ultrasonic Motors," Chap.6.34, Comprehensive
            Composite Materials, Elsevier Science, Oxford, UK (2000).
72.   Uchino, K., and B. Koc, "Compact Piezoelectric Ultrasonic Motors," Proc. NATO-
            Advanced Research Workshop: Piezoelectric Materials: Advance in Science,
            Technology and Applications, (Predeal, Romania, May 24-27, 1999, Kluwer
            Academic Publ., p.309-320 (2000).
73.   Koc, B., J. F. Tressler and K. Uchino, "A Miniature Piezoelectric Rotary Motor Using
            Two Orthogonal Bending Modes of a Hollow Cylinder," Proc. Actuator 2000 (7th
            Int'l Conf. New Actuators, June 19-21, 2000), p.242-245 (2000).
74.   Koc, B., J. F. Tressler and K. Uchino, "A Miniature Piezoelectric Rotary Motor Using
            Two Orthogonal Bending Modes of a Hollow Cylinder," Proc. Actuator 2000 (7th
            Int'l Conf. New Actuators, June 19-21, 2000), p.242-245 (2000).
75.   Bouchilloux, P., B. Koc and K. Uchino, "New Concept for Resonant Longitudinal-Shear
            Ultrasonic Motor," Symp. LL Proc., Mater. Res. Soc. Fall Mtg. '99, (LL.2.10,
            Boston, Nov. 29-Dec.3, 1999), Vol.**604**, 71-78 (2000).

76. Koc. B., P. Bouchilloux, and K. Uchino, "Piezoelectric Micromotor Using A Metal-Ceramic Composite Structure," IEEE Trans. Ultrasonic, Ferroelectrics, and Frequency Control **47** (4), 836-843 (2000).

4.5   Acoustic Absorbers

77. Davis, C.L. and G.A. Lesieutre, "An Actively Tuned Solid State Vibration Absorber Using Capacitive Shunting of Piezoelectric Stiffness," Journal of Sound and Vibration, Vol. 232(3), 4 May 2000, pp. 601-617.
78. Patricia L. Driesch, Hisao Iwata, Gary H. Koopmann, and Jeff Dosch. Nov. 2000. Development and evaluation of a surface acoustic intensity probe. Review of Scientific Instruments, 71 (11), pp. 1-6.
79. W. Huang. G. H. Koopmann, S. J. Sharp, and W. Chen. April 2000. Enhanced Low Frequency Transmission Loss of Lightweight Trim Panels. Journal of Intelligent Material Systems and Structures, Volume 11, No 4.
80. E.W. Constans, A.D. Belegundu, and G.H. Koopmann. 2000. Optimally Designed Shell Enclosures with Tuned Absorbers for Minimizing Sound Power. Optimization and Engineering, 1, 67-86, (an International Journal, Kluwer Publishers)

VOLUME VI

5.0   MODELING AND CHARACTERIZATION

5.1   Design and Simulation

81. K. Uchino, "Designing With Piezoelctric Devices" Internation Center for Actuators and Transducers, Materials Research Institute, The Pennsylvanis State University, University Park, PA (2000)
82. W.K. Qi, and W. Cao, "Finite Element Study on 1-D Array Transducer Design", IEEE Transaction, Ultra. Ferro. and Frequency Control, vol. **47**, pp. 949-955 (2000).
83. T.A. Ritter, K. K. Shung, W. Cao and T. R. Shrout, "Electromechanical Properties of Thin Strip Piezoelectric Vibrators at High Frequency", J. Applied Phys, vol. **88**, pp. 394-397 (2000).
84. T.A. Ritter, K. K. Shung, W. Cao and T. R. Shrout, "Electromechanical Properties of Thin Strip Piezoelectric Vibrators at High Frequency", J. Applied Phys, vol. **88**, pp. 394-397 (2000).

5.2   Thick and Thin Films

85. Kalpat, S., X. Du, I. R. Abothu, A. Akiba, H. Goto and K. Uchino, "Effect of Crystal Orientation on Dielectric Properties of Lead Zirconate Titanate Thin Films Prepared by Reactive RF-Sputtering," Jpn. J. Appl. Phys., **40**, 158-162 (2001).
86. Kalpat, S., X. Du, I. R. Abothu, A. Akiba, H. Goto, S. Trolier-McKinstry and K. Uchino, "Dielectric Properties of Highly Oriented Lead Zirconate Titanate Thin Films Prepared by Reactive RF-Sputtering," Symp. LL Proc., Mater. Res. Soc. Fall Mtg. '99, (LL.1.3, Boston, Nov. 29-Dec.3, 1999), Vol. **604**, 3-8 (2000).
87. S. Trolier-McKinstry, "Piezoelectric Films for MEMS Applications," J. Ceram. Soc. Jpn. 109 (5) S76-S79 (2001).

88. Jeong Hwan Park, Fei Xu, and Susan Trolier-McKinstry, "Dielectric and Piezoelectric Properties of Sol-Gel Derived Lead Magnesium Niobium Titanate Films with Different Textures," J. Appl. Phys. 89(1) 568 - 574 (2001).

89. Q. F. Zhou, E. Hong, R. Wolf, and S. Trolier-McKinstry, "Dielectric and Piezoelectric Properties of PZT 52/48 Thick Films with (100) and Random Crystallographic Orientation," Ferroelectric Thin Films, Vol 655 (2000).

90. L.-P. Wang, R. Wolf, Q. F. Zhou, S. Trolier-McKinstry and R. J. Davis, "Wet-etch patterning of lead zirconate titanate (PZT) thick films for microelectromechanical systems (MEMS) application," Mat. Res. Soc. Symp. Vol.657 (MEMS)

5.3   *Domain Studies*

91. Uchino, K., and H. Aburatani, "Field Induced Acoustic Emission in Ferroelectric Ceramics," Proc. 101st Annual Mtg. of Amer. Ceram. Soc., Symp. Electronic Ceramic Materials and Devices, SE-56, (Indianapolis, April 25 – 28, 1999), (2000).

92. J. Fousek [ab], L.E. Cross [b], "Engineering Multidomain Ferroic Samples, Dept of Physics and International Center for Piezoelectric Research, University of Technology, Liberec, 46117 Czech Republic and [b] Materials Research Laboratory, The Pennsylvania State University, University Park, PA 16802, USA. (June 2000)

93. J.H. Yin, and W. Cao, "Domain Configurations in Domain-Engineered $0.955Pb(Zn_{1/3}Nb_{2/3})O_3-0.045PbTiO_3$ Single Crystals", J. Appl. Phys, vol. **87**, pp. 7438-7441 (2000).

94. Rajeev Ahluwalia, "Computer Simulations of Domain Pattern Formation in Ferroelectrics", AIP Conference Proceedings Series, © 2001 American Institute of Physics, Proceedings of the 2001 Workshop on Fundamental Physics of Ferroelectrics Williamsburg, Va, 2001

95. R. Ahluwalia and W. Cao, "Influence of Dipolar Defects on Switching Behavior in Ferroelectrics", Phys. Rev. B, vol. **63**, pp. 012103 (2000)

96. Uchino, K., and H. Aburatani, "Field Induced Acoustic Emission in Ferroelectric Ceramics," Proc. 101st Annual Mtg. of Amer. Ceram. Soc., Symp. Electronic Ceramic Materials and Devices, SE-56, (Indianapolis, April 25 – 28, 1999), (2000).

TRANSDUCER STUDIES

Composite Structures

Continued

APPENDIX 36

Displacement amplification of electroactive materials using the cymbal flextensional transducer

R.J. Meyer Jr.[a,*], A. Dogan[b], C. Yoon[c], S.M. Pilgrim[c], R.E. Newnham[a]

[a]*Materials Research Laboratory, The Pennsylvania State University, University Park, PA 16802, USA*
[b]*Anadolu University, Faculty of Engineering, Ceramic Engineering Department, Eskisehir, Turkey*
[c]*New York State College of Ceramics at Alfred University, Alfred NY, USA*

Abstract

High performance electroactive materials were studied as the driver element for the "cymbal" flextensional transducer. The compositions included were commercially available Navy Type I and PKI552 lead zirconate titanate (PZT) piezoceramic, relaxor lead magnesium niobate-lead titanate (PMN-PT) ceramic, lead zinc niobate-lead titanate (PZN-PT) single crystal, and lead lanthanum stannate zirconate titanate (PLSnZT) ceramic with antiferroelectric to ferroelectric transitions. Displacement amplifications from $14\times$ to $50\times$ were found for various cymbal configurations. The influence of material properties, cymbal design, and drive signal on the displacement amplification factor is discussed. © 2001 Elsevier Science B.V. All rights reserved.

1. Introduction

The "cymbal" metal-ceramic flextensional transducer has been developed for many actuator and ultrasonic applications [1,2]. This device was derived from the commercially successful "moonie" structure [3,4] that consists of a poled piezoelectric disk bonded to metal end caps. The metal caps have specially designed geometries to accommodate an air cavity between the metal and ceramic. The cymbal modification was a result of eliminating strain gradients near the center of the moonie caps. This new design, categorized as a class V flextensional device, further improved the displacement characteristics [5]. In addition, the transducer was simpler and more cost effective to manufacture.

Increased sensitivity and amplified motions are obtained through conversion of radial stresses into large axial motions. When driven electrically with the field parallel to the poling direction, the piezoelectric disk expands axially in proportion to the material's piezoelectric d_{33} coefficient. In addition, the lateral dimensions contract as a function of the piezoelectric d_{31} coefficient. The lateral contraction is amplified and transferred to the axial direction through the flexing end caps. This results in an addition of d_{31} and d_{33}

effects. A large displacement in the dome region of 40 μm @ 1 MV/m (compared to 1 μm @ 1 MV/m for uncapped lead zirconate titanate (PZT)) with reasonable generative force (approximately 20 N) was obtained for the cymbal. Moonies and cymbals are suitable for many actuator applications and help to bridge the gap between the high-force, low-displacement multilayer structures and the high-displacement, low-force bender type actuators. Compact and inexpensive moonie and cymbal hydrophones have also found many applications including towed undersea arrays, fish finding, underwater imaging, and geophysical research.

Ease of fabrication and the ability to tailor performance to the desired application are attractive features of the cymbal design. Resonance frequency, force, displacement and response times of this structure are controlled through the choice of the cap and driver materials, together with the geometry and overall dimensions, thereby accommodating this design to numerous applications. The versatility of the design is well known and has been the topic of many publications [6,7,8]. As ultrasound and actuator applications expand, so do the demands placed on device performance.

During the past decade, new materials have been developed to improve the performance of transducers and actuators. Single crystal perovskites with very large coupling coefficients and highly anisotropic piezoelectric properties are being grown for a variety of applications [9]. Electrostrictive relaxor ferroelectrics [10], and antiferroelectric-to-

---

* Corresponding author. Tel.: +1-814-863-0180.
E-mail address: rmeyer@psu.edu (R.J. Meyer Jr.).

ferroelectric phase switching materials [11] are also being developed for high power devices with large displacements.

This paper compares the amplification effects of the cymbal design using several commercial PZT compositions with the newer electrostrictive lead magnesium niobate-lead titanate (PMN-PT) ceramics, lead zinc niobate-lead titanate (PZN-PT) single crystals, and lead lanthanum stannate zirconate titanate (PLSnZT) with antiferroelectric to ferroelectric transitions. Actuator displacements of capped and uncapped disks were measured as a function of electric field.

2. Experimental procedure

2.1. Disk materials

A commercially available lead magnesium niobate (PMN)-based relaxor composition of $0.96(0.91Pb(Mg_{1/3}Nb_{2/3})O_3$–$0.09PbTiO_3)$–$0.04BaTiO_3$ (B400090, supplied by Lockhead Martin was used as a base material. The base composition was modified by sol–gel route reactions to add 2 mol% ZnO and 2 mol% TiO_2 using titanium isopropoxide $(Ti(OCH(CH_3)_2)_4)$ and zinc acetate dihydrate $(Zn(CH_3CO_2)_2 \cdot H_2O)$ [12]. Samples were pelletized, sintered and machined to 12.7 mm diameters with thickness of 1 mm. Fired-on silver was used as an electrode material [13].

An antiferroelectric-to-ferroelectric (AFE-FE) phase switching ceramic with a composition of $(Pb_{0.98}La_{0.02}(Zr_{0.66}Sn_{0.24}Ti_{0.10})_{0.995}O_3)$ (PLSnZT) was obtained from previous material studies at the Materials Research Lab, Pennsylvania State University [11]. Disks were machined and polished to 12.7 mm diameter and 1 mm in thickness. Sputtered gold electrodes were used for electrical contact.

Single crystal disk samples of PZN-PT $(0.955Pb(Zn_{1/3}Nb_{2/3})O_3$–$0.045PbTiO_3)$ (PZN–4.5%PT) were cut perpendicular to the $\langle 0\,0\,1 \rangle$ crystallographic direction and polished to 12.7 mm in diameter and 1 mm thickness. Samples were gold sputtered and poled through the thickness. Crystal samples were provided by TRS Ceramics, State College PA.

Along with the newer samples just described, lead zirconate titanate ceramics PKI552 (PiezoKinetics Inc., Bellefonte, PA) and Navy Type I (PKI 402; PiezoKinetics Inc.) were measured for comparison [14]. All disks were 12.7 mm in diameter and 1 mm thick.

2.2. Cymbal production

12.7 mm diameter caps were cut from titanium or brass sheets using a hardened steel punch. Caps were polished to remove any burrs on the edge of the blank. The cymbal shape, illustrated in Fig. 1 was formed from the blank using machined dies under 350 MPa of pressure. Each cap was fabricated with a 320 μm cavity depth, 3.2 mm top and a flange width of 1.85 mm.

The surface of the flange and driver material were roughened with sandpaper to enhance bonding. Bonding layers
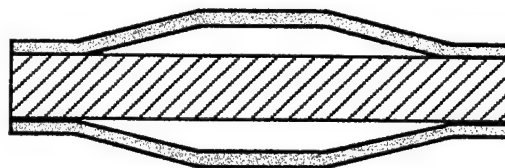
Fig. 1. Schematic structure of cymbal Class V flextensional transducers. The "driver" (hatched area) and the punched metal caps (solid area) have typical dimensions of 12.7 mm in diameter and about 2 mm total thickness.

were applied using a screen-printing technique. The epoxy used to bond the caps to the ceramic was manufactured by Emerson and Cuming. A ratio of three parts 45 LV epoxy resin to one part 15 LV resin hardener was used. After bonding, the ceramic and caps were clamped and the epoxy was allowed to cure in air at 60°C for a minimum of 4 h.

2.3. Cymbal characterization

Displacement was measured using a linear variable differential transducer (LVDT) and a computer controlling a 10 kV power supply (Trek, model 610B). The LVDT fixture was designed to minimize the force imposed on the device. LVDT output was monitored using a lock-in amplifier (Stanford Research Systems, model SR830). The sample fixture was immersed in insulating oil (Galden HT-200) to prevent arcing. A unipolar or sinusoidal electrical signal was used to drive the elements and the cymbal transducers up to 1 MV/m at 0.1 Hz. Phase switching materials were evaluated up to 4 MV/m. To assay the PMN and piezooelectric actuators under bias field, an increasing bias was applied in 0.1 MV/m increments in conjunction with a 0.5 MV/m, 0.1 Hz ac sinusoidal driving signal. To avoid sample breakdown, a maximum bias field of 1.0 MV/m was applied. The peak-to-peak displacement was recorded to compare samples.

3. Experimental results

3.1. Ceramic drivers

Displacements for uncapped samples of PMN, Navy Type I, and PKI552 bulk ceramics are plotted in Fig. 2. From this plot it can be seen that at high field, PMN ceramics gave a larger displacement than the traditional PZTs. It is also evident that PMN exhibited less hysteresis than PKI552 material but PMN has nonlinear displacement properties, characteristic of the relaxor composition [15]. The PKI552 composition showed large hysteresis associated with ferroelectric domain motion. The area within the loop represents dielectric loss that can result in significant heat generation during operation. The low loss Navy Type I ceramic provides linear actuation and little hysteresis but at lower strain.
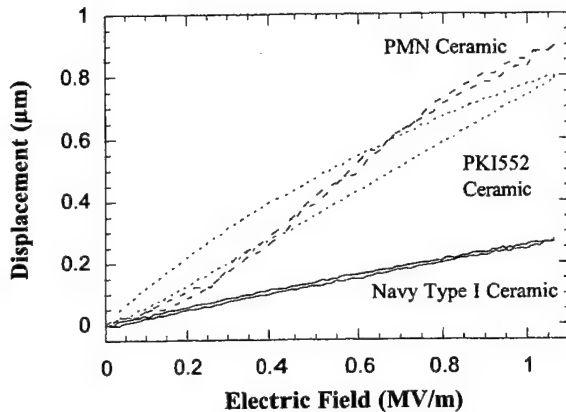
Fig. 2. Field dependent axial displacement for uncapped 1 mm thick ceramic samples of Navy Type I, PKI552 and PMN ceramics. Measurements were done at 0.1 Hz.
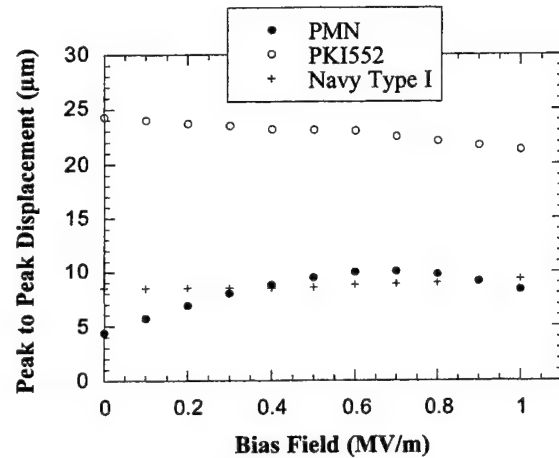

Fig. 4. Plot of the peak-to-peak axial displacement as a function of dc bias field for cymbal actuators driven under a 500 V ac sinusoidal signal.

Since each of these ceramics is 1 mm in thickness, the maximum strain observed at 1 kV was roughly 0.08% for the PMN sample.

Adding cymbal caps to these same ceramics and improved the axial displacement characteristics dramatically. The caps were made from 250 μm thick titanium and had cavity depths of 320 μm. The results are plotted in Fig. 3. The cymbal made from PKI552 material had the highest axial displacement at 1 MV/m and showed more than 25× amplification over the uncapped ceramic alone. For Navy Type I and PMN cymbals, amplification factors of 26× and 14× were measured, respectively. The displacement characteristics of the capped ceramics resembled those of the uncapped ceramic with the largest hysteresis for PKI552. Even though the PMN ceramic disk had a higher displacement at 1 MV/m than PKI552, the cymbal structure's axial displacement is a combination of the effective d_{33} and the amplification effect from the d_{31} of the material. For the piezoceramic, the d_{33} and d_{31} are roughly 550 and −270 pm/V,

respectively [16]. For electrostrictive PMN, the effective piezoelectric coefficients based on peak values are about 700 and −200 pm/V [11]. Device response with the PMN-based materials may improve with an optimized cap.

Relaxor ferroelectrics are normally driven under bias fields to utilize the higher effective d_{33} coefficients which are represented by the region of the displacement versus field plot where the slope is the highest. In the next set of experiments, a dc bias field was applied. Starting with a bias field of 0.1 MV/m and increasing in 0.1 MV/m steps, the maximum displacement of the transducer was measured as a function of a 0.5 MV/m sinusoidal electric field. The peak-to-peak displacement is plotted in Fig. 4 as a function of bias field for the same cymbals described earlier. As can been seen in the plot, the PMN sample had a peak value near 0.6 MV/m where the total displacement was greatest. The piezoceramics showed relatively little change in peak-to-peak displacement for Navy Type I PZT. The PKI552 composition decreased by 10% from 0 to 1.0 MV/m bias. In this experiment, the 0.5 MV/m ac driving signal resulted in negative fields on the ceramic. Since there is no remnant polarization in the relaxor, a negative field results in a positive displacement whereas the piezoceramics decrease in dimension. This results in an inherently larger peak-to-peak displacement for the piezoceramics when the device is used in the bipolar mode as long as the negative field does not depolarize the material. In the unipolar, dc-biased mode, the lower hysteresis of electrostrictors may be advantageous. It appears, however, that the piezoelectric materials are best suited to this cymbal design.

The large displacement generated from the antiferroelectric-to-ferroelectric field induced phase change was also examined. The PLSnZT bulk disk and cymbal displacement characteristics are plotted in Fig. 5. The bulk disk showed very little strain up to electric fields of 2.4 MV/m. At higher fields, the induced phase change provided an abrupt increase in axial displacement. The maximum strain produced from this sample was 0.18% at 3 MV/m. A large hysteresis was
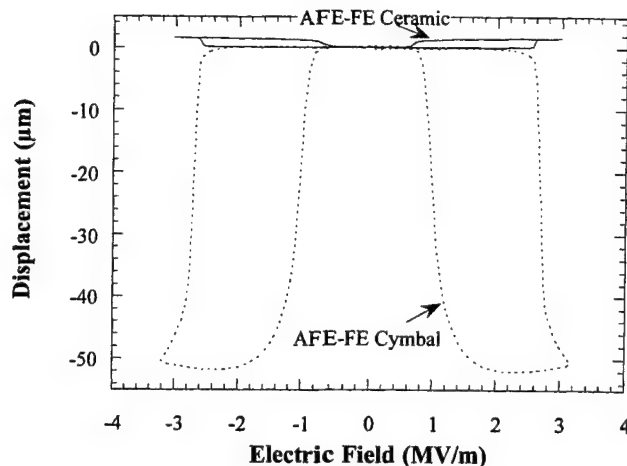

Fig. 3. Axial displacement for cymbal actuators plotted as a function of a low frequency unipolar field. Cymbals were made with titanium caps with a cavity of 320 μm and PMN, Navy Type I and PKI552 ceramic drivers.

Fig. 5. Displacement plotted as a function of electric field for antiferro-electric-to-ferroelectric phase switching PLSnZT ceramic and cymbal. Brass caps, 200 μm in thickness and 320 μm cavity depth were used to build the cymbal.
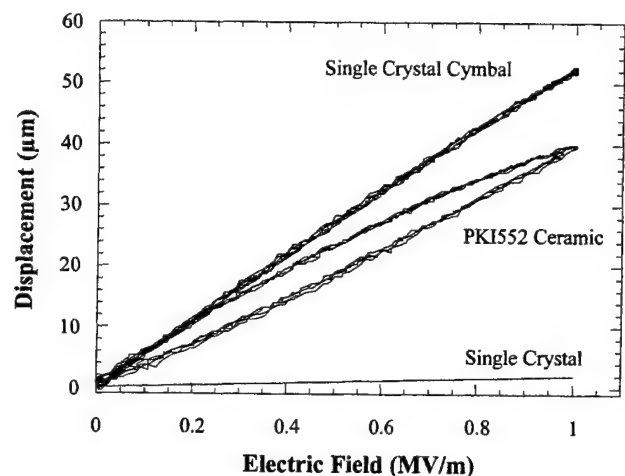

Fig. 6. Displacements plotted as a function of applied electric field for capped and uncapped $\langle 0\,0\,1 \rangle$ oriented single crystal. Plotted for comparison is a PKI552 cymbal with identical 150 μm thick brass caps.

also observed. Since the material reverts to the antiferro-electric phase, no remnant polarization resulted. Thus, negative fields also produced positive displacements.

An interesting characteristic of this material is that it undergoes a volumetric expansion that can be as large as 0.49% [17]. Thus, the effective d_{33} and d_{31} coefficients have the same sign and work against one another in the cymbal structure. With the large amplification of the lateral motion, a total negative displacement of 52 μm was obtained for an AFE-FE cymbal as shown in Fig. 5. Less stiff, 200 μm thick brass caps with a 320 μm cavity depth were used because the displacement and switching characteristics of this material is a strong function of pre-stress [18]. With these caps, nearly 30× amplification of the AFE-FE ceramic displacement was obtained.

3.2. Single crystal drivers

In the case of single crystals, the crystallographic orientation is important in optimizing the piezoelectric properties. PZN–4.5%PT crystals were chosen to demonstrate performance as a cymbal driver material. For this experiment 150 μm thick brass caps were used with a $\langle 0\,0\,1 \rangle$ oriented crystal disk and compared with a PKI552 ceramic with similar caps. Axial displacements of the uncapped crystal and the two cymbals are plotted in Fig. 6. Based on these results, the cymbal caps provided a 27× amplification of the crystal motion. The displacement was linear and nearly anhysteresic. For the PKI552 piezoceramic, the thinner lower modulus brass cap gave an amplification factor of 50× at 1 MV/m. This is twice the value obtained with the stiffer Ti caps (Fig. 2). The effects of cap modulus and thickness have been studied previously and are consistent with these results [6,7]. Regarding the single crystals, the values reported for d_{33} and d_{31} for the $\langle 0\,0\,1 \rangle$ orientation are approximately 2250 pm/V and −1000 pm/V, respectively

[19]. These coefficients are nearly 3× that of PKI552 ceramic [16]. Thus, a similar or larger amplification factor was expected.

To further investigate cymbal performance, 200 μm thick brass caps were mounted on the PKI552 ceramic and the PZN–4.5%PT crystal. These ceramic and crystal cymbals gave axial displacement amplification factors of 50× and 19×, respectively. The decreased amplification factor with the thicker brass caps is attributed to clamping of the single crystal. Comparing the elastic constants of the crystal and PKI552 ceramics, it can be seen that the single crystal's compliance ($s_{11}^{E} \approx 72 \times 10^{-12} m^2/N$; $s_{33}^{E} \approx 120 \times 10^{-12} m^2/N$) [20] is more than four times greater than the ceramic ($s_{11}^{E} \approx 16 \times 10^{-12} m^2/N$; $s_{33}^{E} \approx 20 \times 10^{-12} m^2/N$) [16]. It is apparent that the large piezoelectric activity of the single crystals comes at the expense of a more compliant structure. Consequently, this reduces its ability to drive the metal caps.

Another reason for decreased amplification in the crystal may result from the cymbal structure itself. The elastic constant and piezoelectric force coefficient varies as a function of direction in the plane of the disk. The effect of this anisotropy on the flexing cap is unclear. To investigate, two square plates 12.7 mm on a side, one having edges along $\langle 1\,1\,0 \rangle$ and one along $\langle 1\,0\,0 \rangle$ directions were made. Rectangular cymbal caps, 150 μm thick with cavity depths of 320 μm were bonded to each plate which was 1 mm thick. The displacement for these plates was 71 and 64 μm, respectively, and it is plotted in Fig. 7. This is an amplification factor of 35 for the $\langle 1\,0\,0 \rangle$-edged plate. This was the expected result, since the compliance in the $\langle 1\,0\,0 \rangle$ direction is less than the $\langle 1\,1\,0 \rangle$ [20]. Based on these experiments, it is concluded that both cymbal cap design and crystallographic engineering must be carefully employed to optimize the use of single crystal cymbals.
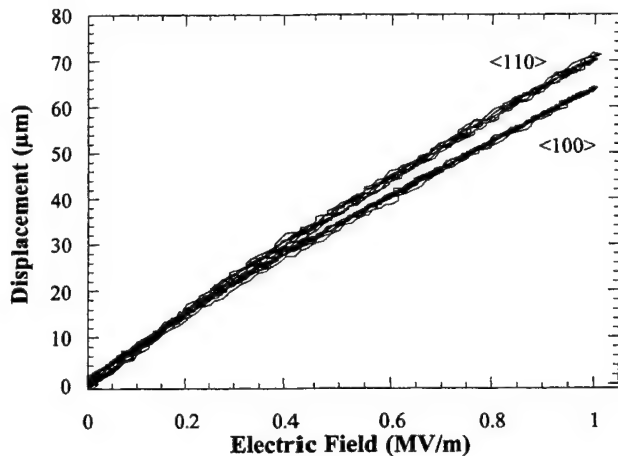
Fig. 7. Displacement plotted as a function of electric field for two PZN–4.5%PT single crystal $\langle 0\,0\,1\rangle$ plates, one having edges along $\langle 1\,1\,0\rangle$ and one with edges along $\langle 1\,0\,0\rangle$. The crystal thicknesses were 1 mm and the rectangular brass caps were 150 μm thick with a 320 μm cavity depth.

4. Summary

Several materials were used as drivers for the cymbal Class V actuators. The displacement characteristics of the cymbal were found to be dependent upon the materials effective piezoelectric coefficients and the elastic properties. For the cymbal configuration comparing PMN, Navy Type I and PKI552, amplification factors of 14, 26, and 25× were found. AFE-FE phase switching ceramic had a 30× amplification with its cap geometry. Single crystal PZN-PT had an amplification factor of 27× compared to 50× for PKI552 cymbal with identical cap geometry. The linear and anhystertic nature of the single crystal cymbals will provide many advantages in actuator design. For each application, the driver and cap configurations must be carefully chosen to meet the requirements for displacement, force, and speed. Further discussion of force and speed will appear in later publications.

Acknowledgements

References

[1] A. Dogan, Q. Xu, K. Onitsuka, S. Yoshikawa, K. Uchino, R.E. Newnham, High displacement ceramic-metal composite actuator, Ferroelectrics 156 (1994) 1–6.

[2] A. Dogan, R. Newnham, Metal-Electroactive Ceramic Composite Actuator, US Patent 5,729,077 (1998).

[3] Y. Sugawara, K. Onitsuka, S. Yoshikawa, Q. Xu, R.E. Newnham, K. Uchino, Metal ceramic composite actuators, J. Am. Ceram. Soc. 75 (1992) 996.

[4] R.E. Newnham, Q.C. Xu, S. Yoshikawa, Transformed Stress Direction Acoustic Transducer, US Patent 4,999,819 (1991).

[5] L.H. Royster, The flextensional concept: a new approach to the design of underwater acoustic transducers, Appl. Acoustics 3 (1970) 117–126.

[6] A. Dogan, Flextensional Moonie and Cymbal Actuator, Ph.D. Thesis, The Pennsylvania State University, University Park, PA, 1994.

[7] J.F. Tressler, Capped Ceramic Underwater Sound Projector: The Cymbal, Ph.D. Thesis, The Pennsylvania State University, University Park, PA, 1997.

[8] J.F. Fernandez, A. Dogan, J.T. Fielding, K. Uchino, R.E. Newnham, Tailoring the performance of ceramic-metal piezocomposite actuators, cymbals, Sens. Actuators A 65 (1998) 228–237.

[9] S.E. Park, T.R. Shrout, Ultrahigh strain and piezoelectric behavior in relaxor based ferroelectric single crystals, J. Appl. Phys. 82 (4) (1997) 1804–1811.

[10] S.M. Pilgrim, M. Massuda, J.D. Prodey, Electromechanical properties of some Pb(Mg1/3Nb2/3)O3–PbTiO3–(Ba, Sr)TiO3 ceramics: Part 2, J. Am. Ceram. Soc. 78 (6) (1995) 1501–1506.

[11] M.J. Pan, K.A. Markowski, S.E. Park, S.Yoshikawa, L.E. Cross, Antiferroelectric-to-ferroelectric phase switching PLSnZT ceramics-I: structure, compositional modification, and electrical properties, in: Proceedings of the 10th International Symposium on the Application of Ferroelectrics, Vol. 1, 1996, pp. 267–270

[12] Y.S. Cho, S.M. Pilgrim, H. Giesche, K. Bridger, Dielectric and electromechanical properties of chemically modified PMN-PT-BT ceramics, accepted J. Am. Ceram. Soc. (1999).

[13] C.H. Yoon, S.M. Pilgrim, K. Bridger, Tailoring of electromechanical properties of Pb(Mg2/3Nb2/3)O3–PbTiO3–BaTiO3-based relaxors, in: Proceedings of the Dielectric Symposium, 102nd Annual Meeting of the American Ceramic Society, St. Louis, MO, April 2000.

[14] Piezoelectric Ceramic for Sonar Transducers, DOD-STD 1376A(SH) 1988.

[15] S.M. Pilgrim, A.E. Bailey, M. Massuda, J.D. Prodey, A.E. Sutherland, Effective electromechanical properties of some Pb(Mg1/3Nb2/3)O3–PbTiO3–(Ba,Sr)TiO3 ceramics, in: Proceedings of the ISAF 1992, Greenville, SC, August 1992.

[16] PiezoKinetics, Company Catalog, 2000.

[17] C.T. Blue, J.C. Hicks, S.E. Park, S. Yoshikawa, L.E. Cross, In situ X-ray diffraction study of the antiferroelectric-ferroelectric phase transition in PLSnZT, Appl. Phys. Lett. 68 (21) (1996) 2942–2944.

[18] M.J. Pan, S.E. Park, K.A. Markowski, S. Yoshikawa, L.E. Cross, Antiferroelectric-to-ferroelectric phase switching PLSnZT ceramics-II: effect of pre-stress conditions on the strain behavior, in: Proceedings of the 10th International Symposium on the Application of Ferroelectrics, Vol. 2, 1996, pp. 259-262.

[19] S.F. Liu, S.E. Park, T.R. Shrout, L.E. Cross, Electric field dependence of piezoelectric properties for rhombohedral $0.955Pb(Zn_{1/3}Nb_{2/3})O_3$–$0.045PbTiO_3$ single crystals, J. Appl. Phys. 85 (5) (1999) 2810–2814.

[20] J. Yin, B. Jiang, W. Cao, Elastic, piezoelectric and dielectric properties of $0.955Pb(Zn_{1/3}Nb_{2/3})O_3$–$0.045PbTiO_3$ single crystal with designed multidomains, IEEE Trans. Ultrasound Ferroelectrics Frequency Control 47 (1) (2000) 285–291.

Biographies

Richard J. Meyer Jr. was born in Pittsburgh, PA, 7 May 1971. He studied ceramic science and engineering and graduated with a BSc degree in 1993 as the student Marshal for the Materials Science and Engineering department. He received his Masters degree in 1995 in Materials at the Materials Research Laboratory under the direction of Thomas Shrout and Shoko Yoshikawa. He completed his PhD in October 1998 with the

development of high frequency 1–3 composite transducers. After graduation he studied 1 year as a post-doctoral scholar under the supervision of Dr. R. E. Newnham, then was promoted to his current position as Research Associate at the Materials Research Laboratory, Penn State University. His research interests include ceramic processing, development of undersea and medical ultrasonic devices and composites materials for actuators and transducers.

Robert E. Newnham was born in Amsterdam, NY, on 28 March 1929. He received the BSc degree in Mathematics in 1950 from Hartwick College, Oneonta, NY, the MSc degree in Physics from the Colorado State University, Fort Collins, CO, a PhD in Physics and Mineralogy from the Pennsylvania State University, and second doctorate in Crystallography from the Cambridge University, UK, in 1960. He is ALCOA Professor Emeritus of Solid State Science at the Pennsylvania State University, University Park, PA. Previously, he was a staff member of the Laboratory for Insulation Research at the Massachusetts Institute of Technology, Cambridge, MA. His research interests are in structure-property relations, electroceramics, and composite materials for electronic applications.

Aydin Dogan was born in Ankara, Turkey, on 22 February 1966. He received the BSc degree in materials science and metallurgical engineering in 1988 and the MSc degree in 1990, both from Middle East Technical University in Ankara-Turkey. He received the PhD degree in materials program (Solid State Science) at the Pennsylvania State University, University Park, PA. He worked as design engineer and consulter for automobile sensor in NGK insulators-Japan. He is currently working as Asst. Prof. Dr. in Ceramic Engineering Department at Anadolu University, Eskisehir-Turkey. His research interests include electronic ceramics, ferroelectrics, sensors, actuators, smart materials and systems.

Chang H. Yoon is a post-doctoral research fellow at New York State College of Ceramics at Alfred University. He received his PhD degree in ceramic science from The New York State College of Ceramics at Alfred University in 1998. His research has included sol–gel processing for enhancing electrostrictive properties of transducers and nonlinear electromechanical coupling in electrostrictive materials.

Steven M. Pilgrim was born in Chambersburg, Pennsylvania, in 1962. He received an Honor BSc in polymer science with highest distinction and a PhD in Solid State Science with highest distinction from The Pennsylvania State University in 1983 and 1987, respectively. He is currently Associate Professor of Materials Science and Engineering at The New York State College of Ceramics at Alfred University and an adjunct graduate professor at The University of Maryland, College Park. At Alfred University, he is co-director of the Laboratory for Electronic Ceramics. Dr. Pilgrim's primary research interests are electrostrictors and piezoelectrics for electromechanical actuators, smart materials, and nonstructural composites. He serves as an associate editor of the IEEE Transactions on Ultrasonics, Ferroelectrics, and Frequency Control and is a member of the American Chemical Society, the American Ceramics Society, the Materials research Society, and Tau Beta Phi.

APPENDIX 37

FLEXTENSIONAL COMPOSITE TRANSDUCERS: DESIGNING, FABRICATION AND APPLICATION

Aydin Dogan, Kenji Uchino*, Robert E. Newnham *
Anadolu University, Ceramic Engineering Department
26470 Eskisehir TURKEY; * The Pennsylvania State University,
Materials Research Laboratory, University Park- PA 16802

Abstract

The design, fabrication and application of flextensional composite transducers are summarized in this study. The moonie and cymbal type flextensional transducer consist of a ceramic driving element sandwiched between two truncated conical metal or plastic endcaps. These transducers can be used as both sensors and actuators. Piezoelectric, electrostrictive and antiferroelectric-ferroelectric switching types of ceramic can be used as the driving element in either single layer or multilayer form. In the cymbal and moonie transducer designs, the flexibility and durability of metals and the driving power of the ceramic element are combined.

Poled ferroelectric ceramics (Curie groups ∞m) possess three independent piezoelectric coefficients: d_{31}, d_{33}, and d_{15}. Each of the piezoelectric coefficients can be used as the driving element of a composite cymbal or moonie transducer. Cymbal transducers can also be fabricated from ring shaped ceramics sandwiched between truncated metal endcaps. Polarization and electric field directions of the samples can be altered systematically to make use of the three different piezoelectric coefficients as driving elements. The cymbal is a versatile performer. Desired actuation and sensing performance can be tailored by engineering the flexibility of the endcaps or changing the cavity dimensions beneath the endcaps. Possible design changes can be also investigated with FEM by using computational tools. Cymbal and moonie transducers can be used as hydrophones, acceleration sensors, positioners, and in many other applications.

1. Introduction

Accentric materials show piezoelectricity, which is defined as the ability of developing an electrical charge proportional to a mechanical stress. The piezoelectric response may be either direct or converse. For the direct piezoelectric response, the electrical displacement is proportional to the stress applied to the material. In the converse effect, material strain is proportional to the field applied across the material. This quality of piezoelectric materials has led to their use in transducers, which convert electrical energy to mechanical energy, and vice versa. These electromechanical transducers have

357

found applications where they are used in either active, e.g. ultrasonic probes, or passive modes, e.g. hydrophones.

A number of monolithic materials exhibit piezoelectric behavior. Ceramics, polymers and as well as their composites belong to this materials group. Conflicting goals in optimizing physical and electromechanical properties of transducers have led the researchers to look at the composite materials.

Superior properties have been obtained with piezocomposites consisting of an active piezoelectric ceramic in an inactive polymer. The microstructural arrangement of component phases in the composite, sometimes referred to as connectivity, is a critical parameter for the electromechanical performance of the composite. For a composite containing two phases, there are sixteen different connectivity patterns. Over the past two decades, researchers have investigated several methods to process piezocomposites and improve their properties. The 0-3, 3-1, and 2-2 connectivities have been worked on extensively. There are several excellent review papers on connectivity patterns and the processing techniques used to form piezocomposites [1], [2]. Various composite have different applications. Competition is still going on to determine the composite with the best electromechanical performance.

Second generation piezocomposites include the moonie and cymbal with 2-(0)-(2) connectivity. Ceramic-metal composites generally have a simple design with metal faceplates, shells or caps that couple the ceramic to the surrounding medium. The metal component transfers the incident stress to the ceramic or the displacement to the medium. Flextensional transducers are good examples of ceramic-metal composites. In flextensional transducers, the flexural vibration of the metal shell causes an extensional vibration of the piezoelectric ceramic. The moonie and cymbal transducers possessing 2-(0)-2 connectivity are miniaturized versions of flextensionals. This paper describes the moonie and cymbal type composite transducers.

2. Principle

The moonie and cymbal transducers consist of an electro-active ceramic driving element sandwiched between two metal endcaps with shallow cavities on their inner surface. Designs of the moonie and cymbal transducers are illustrated graphically in Figure 1 and Figure 2. In the case of the moonie, the cavities are in the shape of a half moon, whereas the cymbal has a truncated cone-shaped cavity. The presence of these cavities allows the metal caps to serve as mechanical transformers for converting and amplifying a portion of the incident axial-direction stress into tangential and radial stresses of opposite sign. Thus, the d_{33} and d_{31} contributions of the PZT now add together (rather then subtracting) in the effective d value of a device, such as a hydrophone or accelerometer. Regarding the converse effect, the radial motion of the ceramic driving element is transferred and amplified by the metal endcaps in axial direction. Hence, moonie and cymbal can be used as both sensors and actuators.
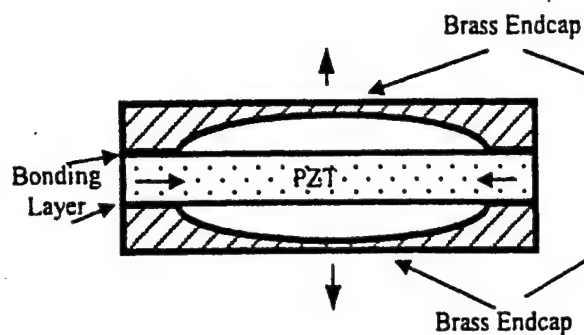
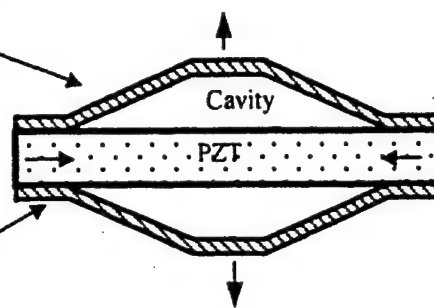Figure 1. Schematic of Moonie Transducer.

Figure 2. Schematic Cymbal Transducer.

2.1 FIRST APPROXIMATION FOR THE CHARGE CALCULATION ON THE CYMBAL AND MOONIE TRANSDUCER

Let us assume that we have a flextensional transducer which has cone shaped endcaps The charge created under an applied stress on the cymbal transducer at uniaxial direction perpendicular to the metal endcaps can be estimated as follows.

The force is applied to the cone on the summit and transferred to the piezoelectric ceramic. The essential parameters for the calculation are marked on Figure 3.
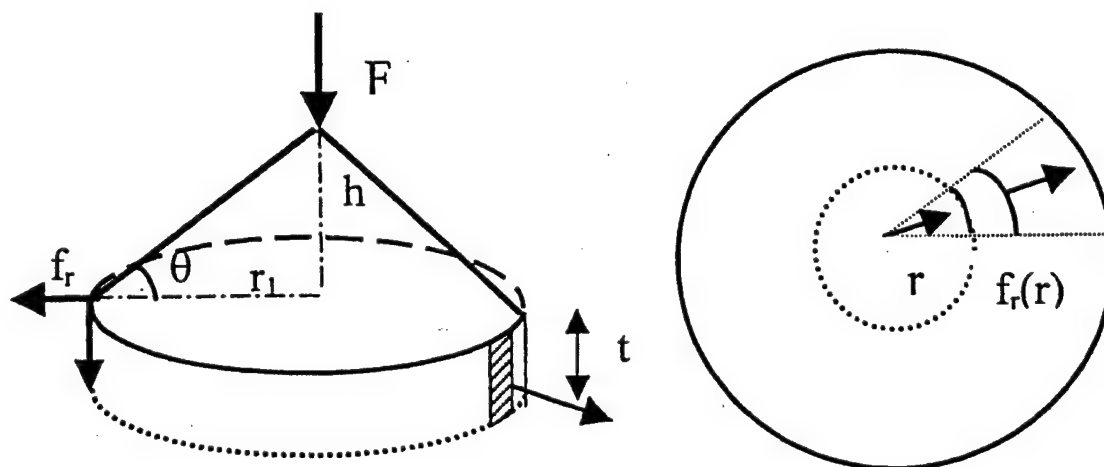
Figure 3. Front and top view of flextensional tranduser cone shaped endcap
Where: h, cavity depth; r_1, cavity radius; t, thickness of ceramic, θ angle between cone and piezoelectric ceramic.

$$\frac{h}{r_1} = \tan\theta \tag{1}$$

The total force on the entire circumference is

$$2\pi r_1 f_r = \frac{F}{2\tan\theta} \tag{2}$$

and the force per unit area at $r = r_1$ is

$$\frac{f_r}{t} = \frac{F}{4\pi r_1 t \tan\theta} \tag{3}$$

where t is the thickness of the ceramic disk.
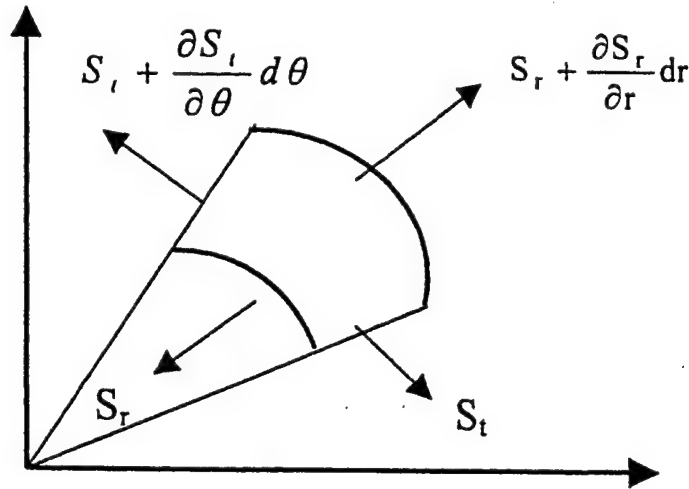
Figure 4. Stress distrubition on a finite segment of ceramic element.

When a force balance is written and solved for plane stress case, the following equation is obtained.

$$S_r = S_t = \frac{F}{4\pi r_1 t \tan\theta} \tag{4}$$

The charge generation is calculated from,

$$\int_{0}^{r_1} \underbrace{d_{31}\underbrace{(S_r + S_t)}_{P(r)}\underbrace{2\pi r dr}} = d_{31}\frac{r_1}{2t}\frac{F}{\tan\theta} \qquad (5)$$

when two endcaps are used:

$$Q = d_{31}\frac{r_1}{t}\frac{F}{\tan\theta} \qquad (6)$$

$$C = \in \frac{\pi r_1^{\,2}}{t} \qquad (7)$$

$$V = \frac{Q}{C} = d_{31}\frac{1}{\in \pi r_1}\frac{F}{\tan\theta} \qquad (8)$$

where is the Q charge; C, Capacitance; V, voltage, and $\in$ the dielectric permittivity.

For example: For a flextensional transducer with conical endcap, which has 9.0 mm cavity diameter and 0.2 mm cavity depth and consisting of 1.0-mm thick PZT-5A ceramic disc with 153 pC/N d_{31} coefficient, the calculated effective charge is around 17,500 pC/N

The effective piezoelectric coefficients of moonie and cymbal transducers, with a 12.7-mm outer diameter and 9.0-mm cavity diameter and 0.2-mm cavity depth consisting of PZT-5A ceramic, are shown in Figure 5. In moonie and cymbal structure d_{31} and d_{33} coefficients work together (in general in piezoceramics they work always against each other due to poisson effect). This is part of the reason of high effective charge coefficient. The moonie shows highly position dependent behavior for the effective piezoelectric coefficient. The cavity beneath the endcap of the moonie actuator plays a crucial role on the characteristics of the moonie [3]. The effective piezoelectric coefficient increases with increasing cavity diameter and cavity depth. The effective piezoelectric coefficient of the moonie transducer decreases rapidly with increasing the endcap thickness. The piezoelectric charge coefficient of moonie transducers also show position dependent behavior similar to that of the displacement.

Placing a groove 9.0-mm in diameter, 0.2-mm in depth, and 1.0-mm in width in the
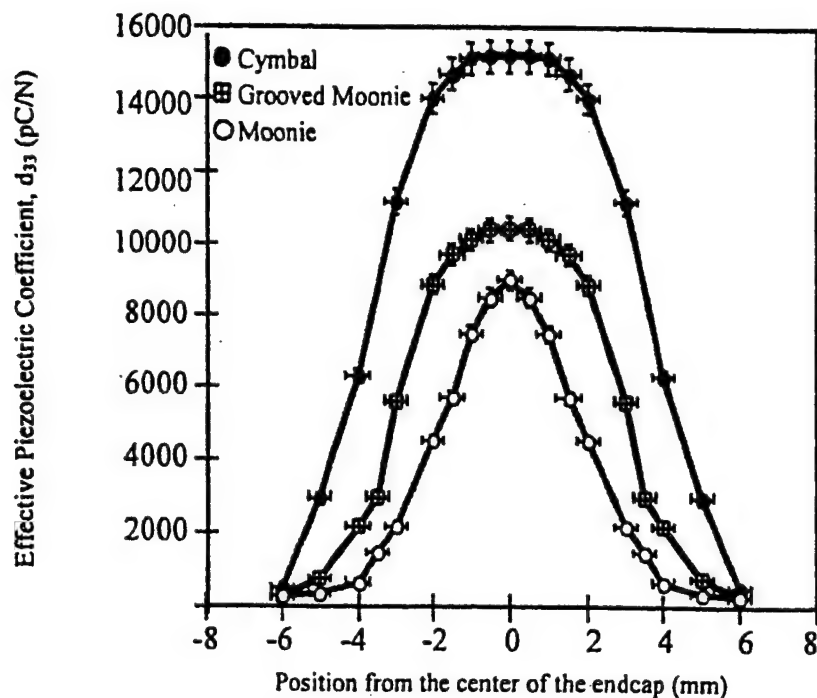
Figure 5. Effective piezoelectric charge coefficient of same size various design of flextensional transducers.

brass endcaps increased the effective piezoelectric coefficient almost 20%. The piezoelectric charge coefficient is simply the ratio of the applied stress and the induced charge. Thus, we can say that the groove on the endcaps increases the stress transformation ratio and therefore the generated charge. The moonies with grooved endcaps also showed less position-dependent behavior. For the 2-mm diameter section at the center of the samples, the effective piezoelectric coefficient is about 11,000 pC/N.

With the cymbal endcaps, the piezoelectric coefficients increased almost 60%. For a cymbal 12.7-mm in diameter and 1.7-mm in total thickness, an effective piezoelectric coefficient of more than 15,000 pC/N was measured over the 4-mm diameter center section of the cymbal transducer. We have concluded that the thick metal region near the edge of the moonie metal endcaps is a passive region, which does not assist stress transfer, and acts to decrease the total efficiency. Cymbal endcaps transfer the stress more efficiently and improve the energy transfer markedly. The calculated result for conical endcap and the measured result for cymbal with truncated conical endcaps are in very good agreement.

3. Fabrication Method

When fabricating the composite moonie and cymbal transducers, piezoelectric, electrostrictive, or antiferro- to- ferroelectric ceramics can be used as the driving element in either single layer or multilayer form. Shallow cavities beneath the endcaps of the moonie transducers are machined into the inner surface of each of the end caps. Brass, phosphor bronze, other flexible metals and their alloys, and even acrylic can be

used as endcap materials.

For cymbals the truncated conical endcaps are punched using a specially designed punch to fabricate the transducers rapidly at minimal cost. Shaping and cutting operations are carried out simultaneously during processing. The final product requires only surface treatment for good bonding. Moreover, endcaps can be easily fabricated from metal sheets by punching. With this fabrication routes it is possible to fabricate identical endcaps with minimal labor.

The metal moonie and cymbal endcaps are bonded to the electro-active ceramic disks around the circumference using soldering alloy or epoxies such as Eccobond epoxy resin from Emerson & Cuming, taking special care not to fill the cavity. The thickness of the epoxy bonding layer must be very thin, approximately 20 µm. Using silver epoxy as a gluing agent, composite actuators may also be stacked together at the center of the endcaps to achieve still higher displacements. Moonie and cymbal transducers can be easily fabricated 3-50 mm in diameter and 1-3 mm in total thickness. Currently most of the studies are done on the 12.7-mm diameter 1.5-mm thick samples.

4. Design Optimization With the Support of Finite Element Analysis

Finite element programs ATILA, MARK, and ANSYS were used for the design and development stages of the moonie and cymbal transducers. The cymbal actuator is a second-generation moonie-type composite developed using FEA analysis in collaboration with experiment. Finite Element Analysis has identified high stress concentration in the metal endcaps just above the edge of the ceramic metal bonding layer near the edge of cavity [4].

The stress concentration on the brass endcap just above the bonding layer reduces the effective force transfer from the PZT to the cap. It is possible to eliminate part of the stress concentration by removing a portion of the endcap just above the bonding region where the maximum stress concentration is observed. An enhancement in properties has been observed by introducing a ring shaped groove on the exterior surface of the endcaps [5]. By moving the groove toward the edge of the actuator, the displacement increases. The highest displacement was achieved when the groove was above the edge of bonding layer. It is found that the deeper and wider the groove, the higher the displacement [6].

In reality, placing a ring shaped groove on the endcap does not eliminate the stress but further concentrates it into a very narrow region. Stress concentrations at the groove edges are a potential source of fatigue and may eventually produce failure under long-term usage. Moreover, additional labor is required to machine the groove into the endcaps.

The cymbal transducer with truncated endcaps has been designed to remove much of the stress concentration and to produce higher and more reproducible displacements.

Although this new design looks similar to the earlier moonie design, it has a different displacement mechanism. Displacement is primarily a flexural motion of the endcap for the original moonie design, but for the new design, the displacement is created by the combination of flexural and rotational motions. Figure 6 shows the displacement values of the different endcap designs with a fixed cavity depth (0.20-mm) and diameter (9.0 mm). A linear Voltage Differential Transformer (LVDT) was used for displacement analysis of the transducers. A variable electric field up to 1kV/mm with triangular waveform at 0.1 Hz is applied to the sample. A moonie actuator with 0.30-mm thick brass endcaps provides a 22-μm displacement. Using the ring-shaped groove design, the displacement was increased to 32 μm with a groove 9.0 mm in diameter, 0.2 mm in depth, and 1.0 mm in width machined into the brass endcaps of the same actuator. A cymbal actuator with uniformly thick punched endcaps exhibits around 40-μm displacements, about twice the moonie displacement, and about 50 times larger than uncapped PZT.
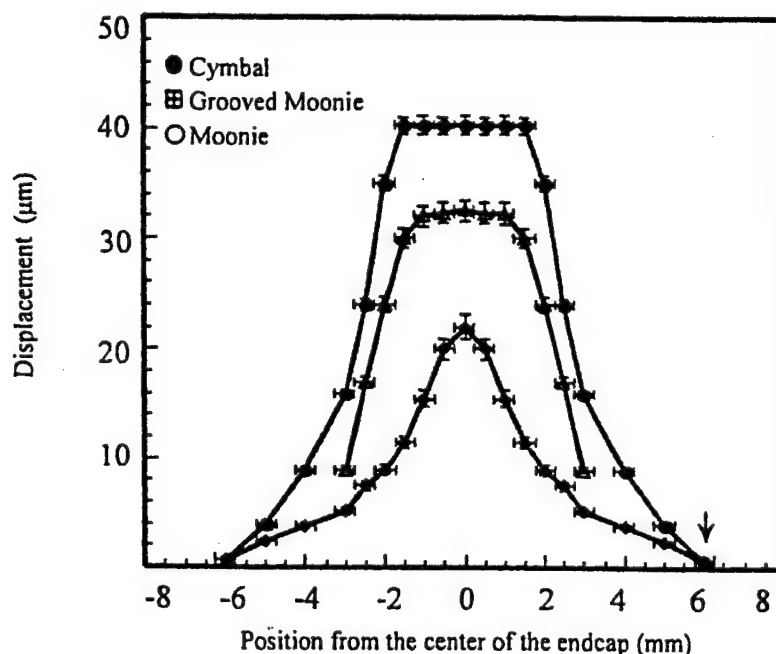
Figure 6. Displacement characteristics of moonie and cymbal flextensional transducers.

4.1 EFFECT OF SIZE AND SHAPE

The dimensions of the cavity beneath the endcaps play a crucial role in the cymbal performance. Engineering the flexibility of the endcaps or changing cavity dimensions can tailor the desired actuation. The displacement, which is the result of converse piezoelectric effect, has a quadratic relationship with the cavity diameter. Figure 7 shows the calculated and experimental results of displacement cavity relation of cymbal transducer with constant endcap thickness (0.25mm) and PZT thickness (1.0 mm). Figure 8 shows the optimal cavity depth, which is around 0.25 mm for a cymbal transducer with constant cavity diameter (9.0 mm) and PZT thickness (1.0 mm).
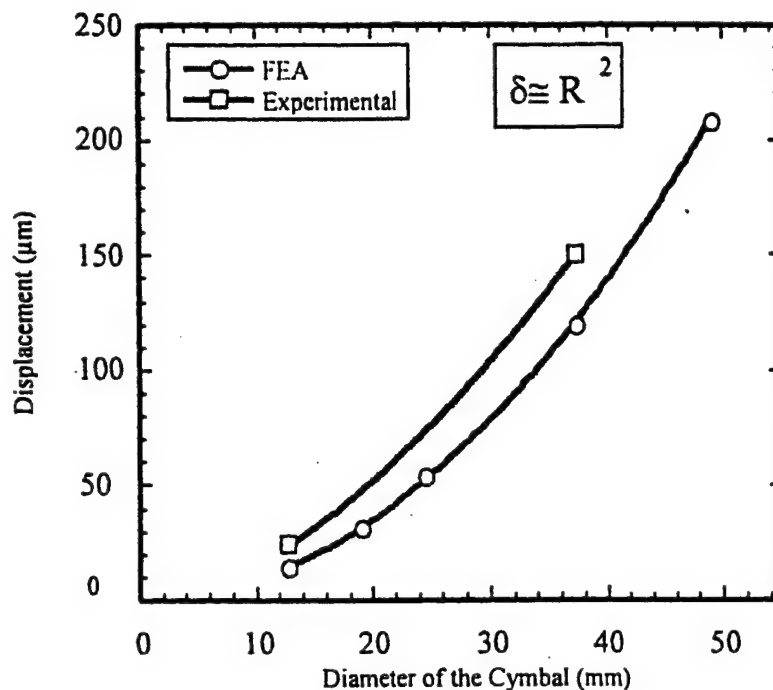
Figure 7. Displacement cavity relation of cymbal transducer with constant endcap thickness (0.25mm) and PZT thickness (1.0 mm).

4.2 EFFECT OF ENDCAP MATERIAL

The flexibility and modulus of elasticity of the endcap material are important parameters defining the important actuator properties: displacement, response speed and generative force, of moonie and cymbal actuators and transducers. Figure 9 shows the effects of the Young's modulus of the metal endcaps and the hardness of the PZT ceramics on the displacement of composite cymbal actuators. Increasing the Young's modulus of the metal endcaps reduces the displacement of the cymbal actuator. This reduction is almost linear and the displacement of the highest Young's modulus metal endcaps is approximately 55% lower than that achieved using the most compliant metal endcaps. Similar behavior is observed for all PZT ceramic types. The linear decrease of the displacement with the increase if the Young's modulus of the metal confirms the spring-like nature of the endcaps.

Figure 10 shows the net displacement of the cymbal actuators made with different metal endcaps. The net displacement is the displacement produced by the actuator when it is electrically driven. If the actuator is loaded, a free deflection is produced and at each load, the application of an electric field produced a net displacement. The free deflection of the composite is related to the spring characteristics of the composite. Metals with low modulus of elasticity show higher displacement and higher free deflection. On the contrary, the maximum load, defined as the load for which 90% or the initial net displacement is maintained, increased with the modulus of the elasticity of the metal endcaps.
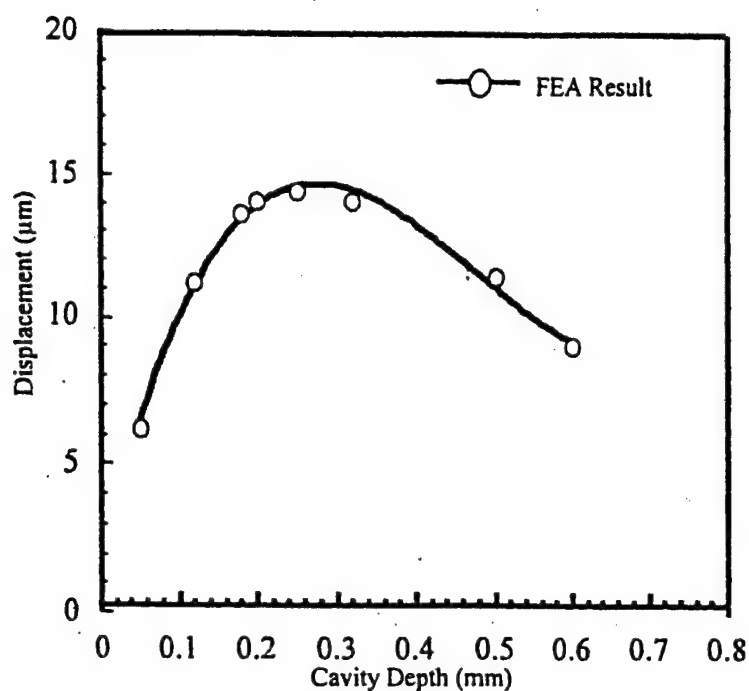
Figure 8. The optimal cavity depth for a cymbal transducer with constant cavity diameter (9.0 mm) and PZT thickness (1.0 mm).
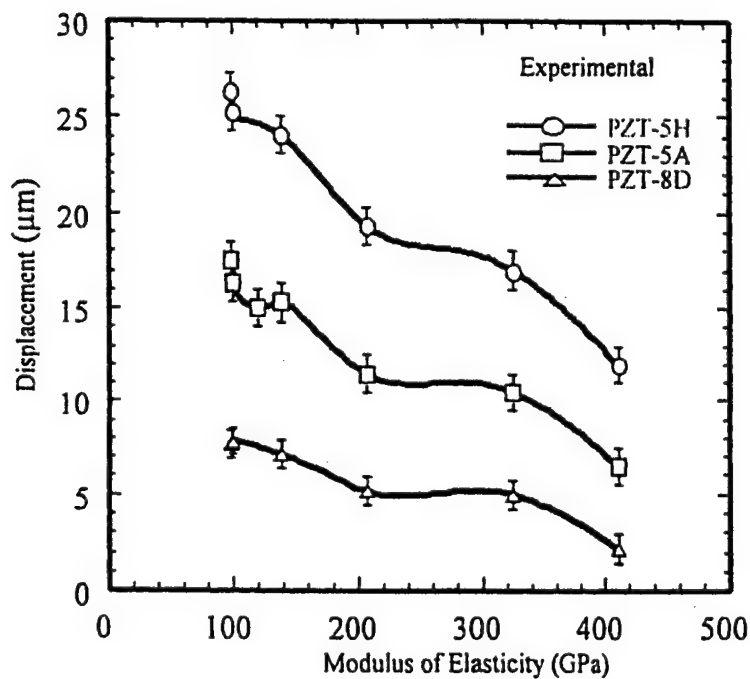
Figure 9. Effect of endcap modulus of elasticity on the displacement performance.
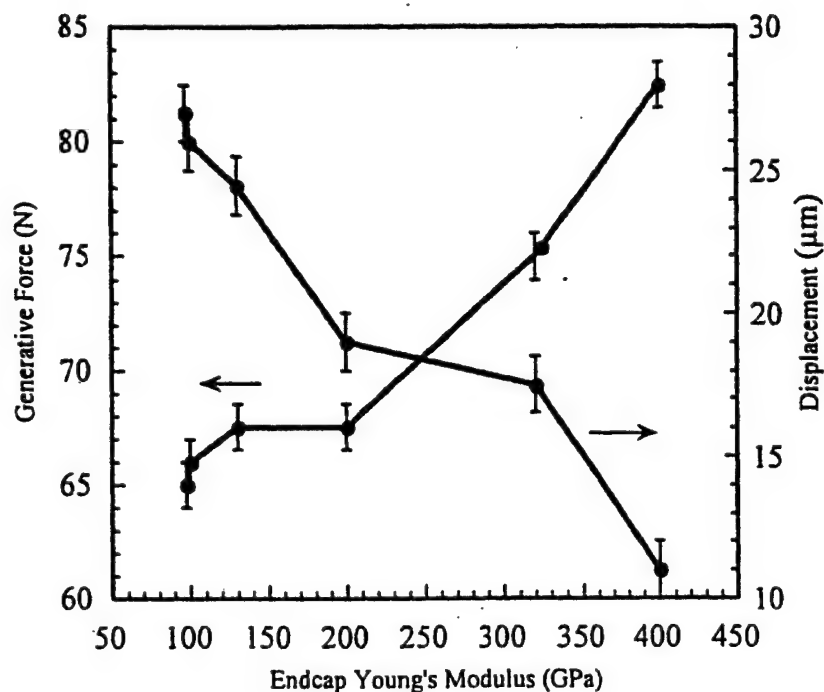
Figure 10. Trade- off between generative force and displacement for the cymbal.

4.3 EFFECT OF ELECTRO-ACTIVE CERAMIC DRIVING ELEMENT

PZT ceramics, PMNPT relaxor ferroelectrics and PNZST type antiferro-ferroelectric ceramic elements can be used in single layer or in multilayer form. Typical displacement hysteresis graphs of 12.7-mm diameter 1-mm thick samples made of all three kinds of electro-active ceramics materials are shown in the Figure 11. Displacement hysteresis for the cymbal transducers, 12.7 mm diameter 1.0 mm PZT thickness, and 9.0 mm cavity diameter 0.2 mm cavity depth, fabricated with all three kind of electro-active ceramic element are shown in Figure 12. Cymbal actuators with soft PZT ceramics exhibit linear displacement with a rather large hysteresis, which is the indication of losses. The cymbal actuator with the PMN-PT type of ceramic driving element shows larger displacement with lower losses. However, it exhibits a nonlinear displacement consistent with the relaxor characteristics of the PMN-PT ceramics. Linear displacement characteristics can be achieved by using charge driving electrical circuitry. PNZST is an antiferroelectric-ferroelectric type phase transition material. Unique property of this material is the volumetric expansion under applied electric field. With cymbal endcap design, this volumetric expansion is converted to a negative axial displacement.

4.4 VARIOUS DRIVING MODES TO ACTIVATE THE CYMBAL TRANSDUCER

Poled ferroelectric ceramics (Curie groups ∞m) possess three independent piezoelectric coefficients: d_{31}, d_{33}, and d_{15}. By careful designing, each of the piezoelectric coefficients can be activated as the driving mode of a composite cymbal or moonie transducer.
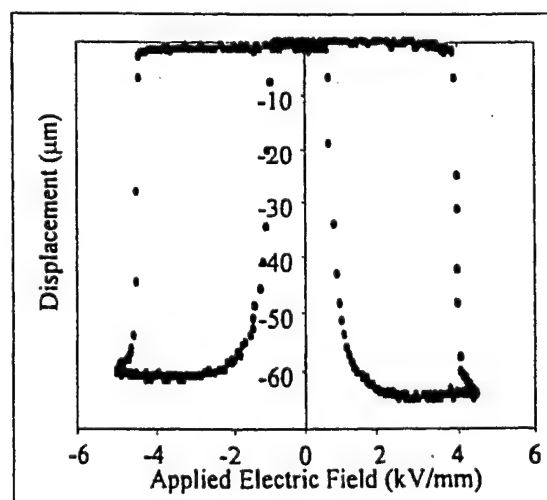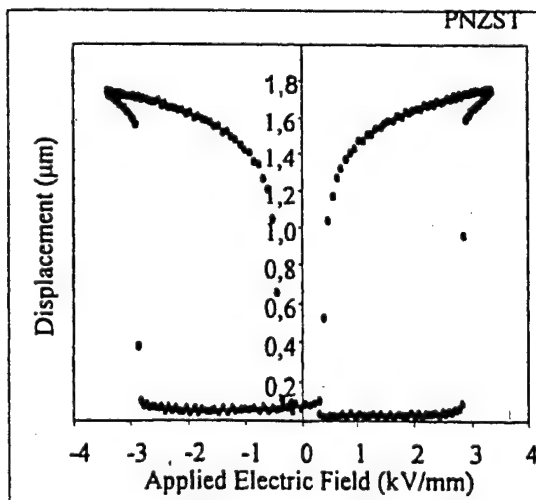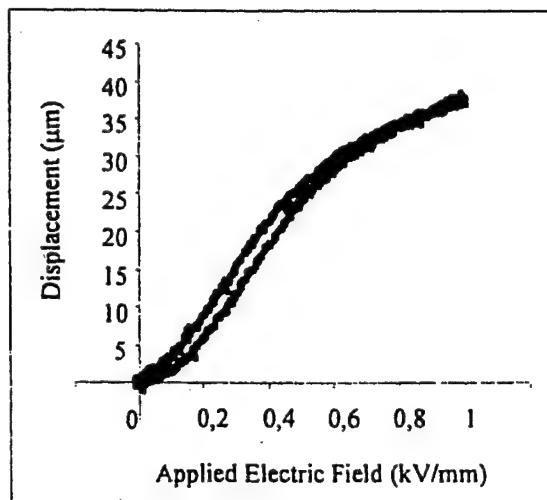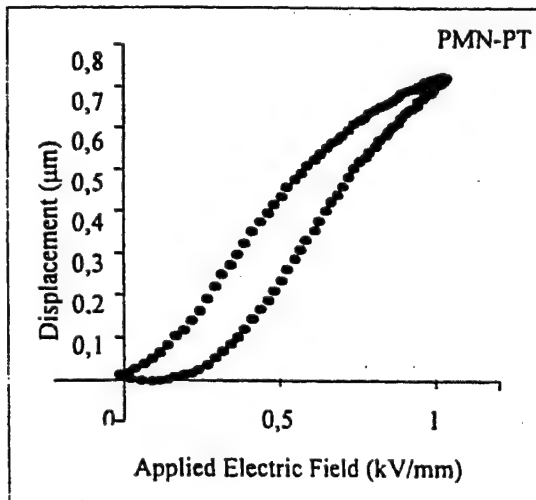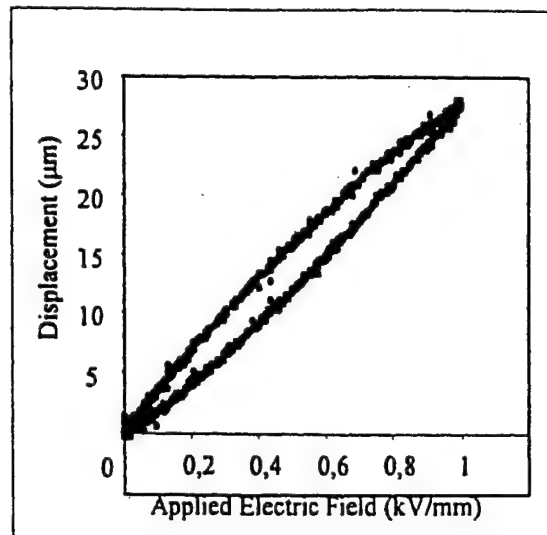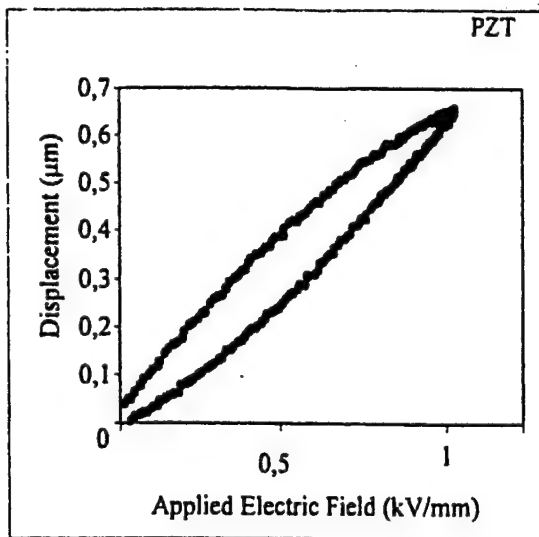
Figure 11. Hysteresis of various electro-active ceramics.

Figure 12. Hysteresis of cymbals with various electro-active ceramics.

Cymbal transducers can be fabricated from ring shaped ceramics sandwiched between truncated metal endcaps. Polarization and electric field directions of the samples can be altered systematically to make use of the three different piezoelectric coefficients as driving power. Figure 13 shows four combinations between electric field and internal polarization of the ceramic driving element. In case one, the radial mode d_{31} of the piezoelectric ceramic element is used to activate the endcaps. In case two, the longitudinal coefficient d_{33} is used to activate the metal endcaps. The shear mode d_{15} of the piezoceramic possesses the highest value piezoelectric coefficient value. Cases 3 and 4 are designed to activate the ceramic in a shear mode. Figure 14 shows the displacement versus inner ring diameter of the piezoelectric driving element relation of the cymbal transducer. From the graph, it may be seen that the d_{31} mode, which exhibits the highest displacement, is still the best mode to drive the cymbal transducer. Although d_{15} is the highest piezoelectric coefficient, it is not effective for driving cymbal transducer in the present design. It has to be kept in mind that the shear mode is a rather soft mode. A rigid solid disc has to be placed between the rings. In general increasing the size of the inner diameter decreases the displacement value, because of decreasing volume of the ceramic body and volumetric efficiency of transducer. From the manufacturing point of view, case 1 is the best, because it is easy to fabricate and easy to apply electric field without developing a short circuit. The other three cases are more difficult to fabricate and requires rather careful electric wiring.
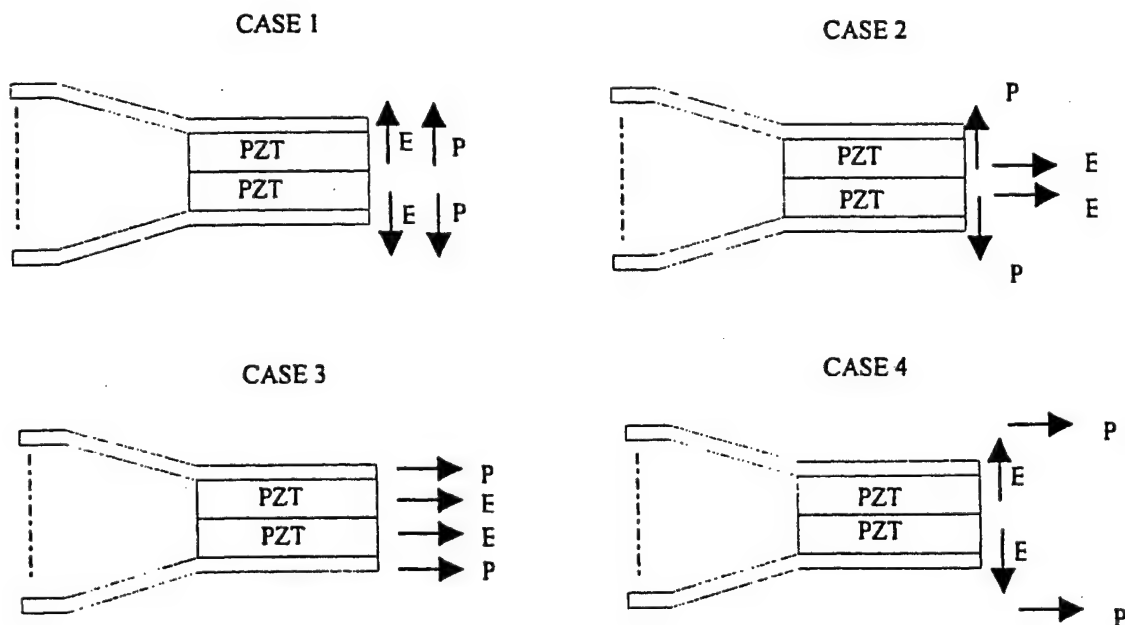

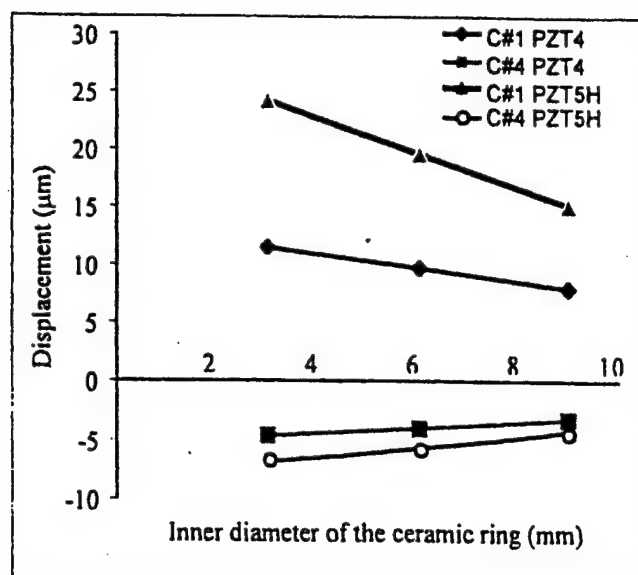Figure 13 Various driving modes of the cymbal transducer with a ceramic ring.

Figure 14. FEA results for displacement ceramic inner diameter relation.

5. Application of the moonie and cymbal transducers

Moonie and cymbal transducers have great potential for both sensor and actuator applications [7], [8]. They can also be utilized as the switching element in valve designs. There is a volume change inside the moonie and cymbal transducers during cycling. This volume change can be utilized in minipump applications.

5.1 ACTUATORS

Flextensional moonie and cymbal actuators with their moderate generative force and displacement values fill the gap between multilayer and bimorph actuators. Each solid-state actuator design has attractive features that can be exploited for certain applications. The advantages of the moonie and cymbal actuators are the easy tailoring of the desired actuator properties by altering the cavity size and endcap dimensions. Easy fabrication is another advantage. Several features of the various solid-state actuator designs are listed in Table I. It is rather difficult to compare the different actuators because of differences in geometry and various operating conditions for specific applications. To make a fair comparison, similar dimensions for each actuator were selected, and the measurement conditions are those specified in Table I. The rainbow actuator also partially covers the gap between multilayer and bimorph actuators [9]. For that type of actuator, a reduction step during processing of the ceramic element at high temperature results in a semiconducting layer and stress-bias. Although it shows flexural motion, the rainbow can be categorized as a monomorph or a unimorph type of actuator. The effective coupling factor of rainbow is theoretically smaller than the moonie and cymbal. High applied electric field, position-dependent displacement and cost are the main disadvantages of the rainbow actuator in comparison with the cymbal. In the moonie and cymbal design, multilayer piezoelectric ceramics can be used as the driving element

to reduce the applied voltage. The moonie and cymbal actuator can be used as a micropositioner for applications requiring small size with relatively quick response. OMRON Corporation has already succeeded in using the multilayer moonie actuator for an optical scanner [10]. Other applications for the cymbal and moonie include sensing and vibration suppression elements in the automotive and aerospace industry, switching element in valve design, micropositioners requiring small size with relatively quick response for precise positioning device in CD-ROM and magneto-optic memory storage driver, mini-pumps, relays, and switches, printer hammers, and linear and rotary ultrasonic motors

Table I. Comparison of the Solid State Ceramic Actuator Designs.

Features	Multilayer	Bimorph	Rainbow	Cymbal	Moonie
Dimensions	5x5x12. (LxWxT) mm^3	12.7x10x0.6 (LxWxT) mm^3	F 12.7 mm T= 0.5 mm	F 12.7 mm T= 1.7 mm	F 12.7 mm T= 1.7 mm
Drive Voltage (V)	100	100	450	100	100
Displacement (μm)	10	35	20	40	20
Contact surface (mm^2)	25	1	1	3	1
Generative Force (N)	900	0.5-1	1-3	15-60	3
Position dependent of displacement	None	Maximum at the tip	Maximum at the center	Maximum at the center but more diffuse	Maximum at the center
Stability under loading	Very high	very low	low	high	low
Fastest Response Time (μsec)	1- 5	100	100	5-50	5-50
Fabrication method	Tape casting and cofiring at 1200 °C	Bonding ceramic element with metal shim	Reducing ceramic element at 950 °C	Bonding ceramic element with metal endcaps	Bonding ceramic element with metal endcaps
Fabrication Cost	high	low	medium	low	medium

5.2 HYDROPHONE APPLICATION

Because of their very high piezoelectric charge coefficients, moonie and cymbal transducers can be used as hydrophones, accelerometers and air acoustic transducers. The advantages of the cymbal-type hydrophone are very large d_h (hydrostatic charge) and g_h (hydrostatic voltage) coefficients along with lightweight and inexpensive fabrication. Cymbal also has excellent potential for use as a shallow water projector.

Cymbal has a Q less than 10 when water loaded. The moderate TVR exhibited by a single element device can be greatly enhanced by incorporating them into a close packed array [11], [12]. Hydrophone figures of merit $(d_h.g_h)$ of some of the widely used composites and single element transducers are compared in the plot in Figure 15. Due to the size dependence of some transducers, the figure of merit is calculated for a 1-cm^2 transducer for a valid comparison. Cymbal exhibits the highest figure of merit among all composites. Figure 16 shows the pressure dependence of the effective d_h and g_h coefficient of identical transducers with different cap materials and 0.25 mm cavity depth. These data clearly show that caps made of stiffer metals are capable of withstanding higher pressures without degradation in performance. Stiffer caps are not as efficient in transferring stress to the piezoceramic, which is why the effective d_h coefficient drops for cymbals with stiffer.
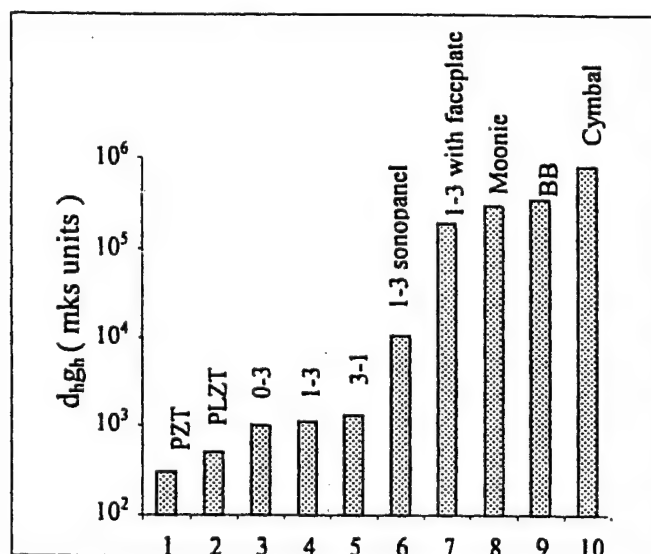
Figure 15. Hydrophone figures of merit $(d_h.g_h)$ of some of the widely used composites and single element transducers.

5.3. ULTRASONIC MOTOR APPLICATION

An ultrasonic motor was derived from moonie and cymbal design [13]. The motor is named the windmill because of the appearance of the slitted endcaps. Detailed information concerning this motor can be obtained from the article of K. Uchino and B. Koc "Compact piezoelectric ultrasonic motors" in this proceeding.
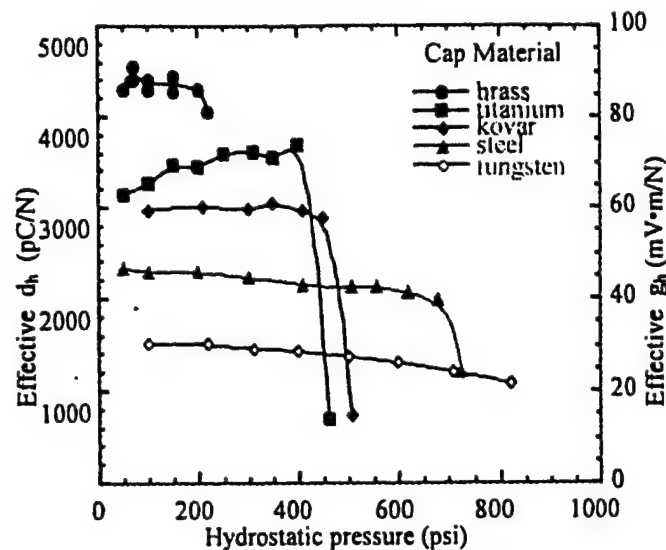
Figure 16. The pressure dependence of the effective d_h and g_h coefficients for same size cymbal transducers with different cap materials.

5.4 ACCELEROMETER APPLICATION

Cymbal transducer has been investigated for accelerometer applications [14]. A high effective piezoelectric charge coefficient (d_{33}) of the cymbal transducer was observed around 15000 pC/N, which is much higher than that of piezoelectric ceramic, around 550 pC/N. With this feature, the cymbal transducer is a good candidate for highly sensitive accelerometer applications. Figure 17 shows the Log sensitivity frequency relation of cymbal accelerometers with various endcaps in comparison with PZT itself. Cymbal accelerometers have more than two orders of magnitude higher sensitivity than PZT ceramics at low frequencies.
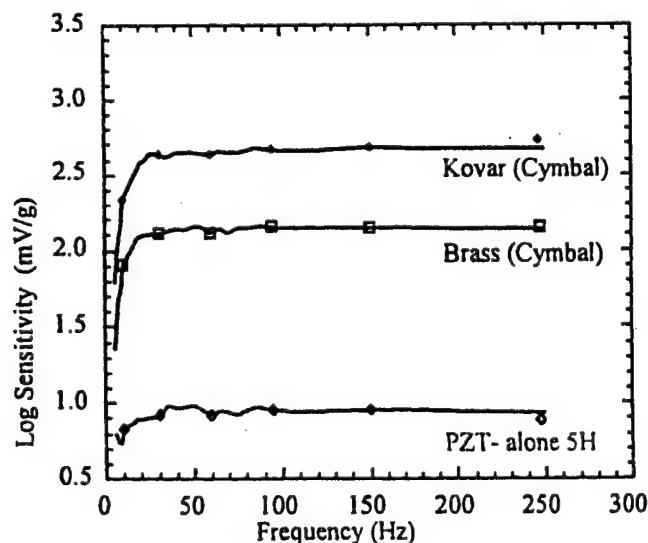
Figure 17. Acceleration sensitivity of cymbal in comparison with PZT itself.

374

REFERENCES

1. Newnham R.E., Skinner D.P. Cross L.E., "Connectivity and Piezoelectric-Pyroelectric Composites," *Mater Res Bull* 1978, 13, 525

2. Gururaja, T.R., A. Safari, R.E. Newnham and L.E. Cross, "Piezoelectric Ceramic-Polymer Composites for Transducer Applications," *Electronic Ceramics*, Edited by L.M. Levinson. Marcell Dekker. Inc., New York, 92 (1987)

3. A. Dogan, S. Yoshikawa, K. Uchino, R.E. Newnham, "The Effect of Geometry on the Characteristics of the Moonie Transducer and Reliability Issue", *IEEE Ultrasonic Symposium Proceedings*, Vol. II. pp. 935-939, 1994

4. Q. C. Xu, S. Yoshikawa, J. R. Belsick and R. E. Newnham, "Piezoelectric composites with high sensitivity and capacitance for use at high pressure," *IEEE Trans. on UFFC* Vol. 38, pp. 634-639, 1991.

5. Y. Sugawara, "Development of metal-ceramic composite piezoelectric actuators and their applications," M.S. Thesis, Sophia University, Tokyo Japan, 1991.

6. K. Onitsuka, A. Dogan, Q.C. Xu, S. Yoshikawa, R.E. Newnham," Design Optimization for Metal-Ceramic Composite Ceramic Composite Actuator, "*Ferroelectrics* Vol. 156, pp. 37-42, 1994.

7. J. F. Tressler, "Smart ceramic-metal composites for active vibration control," *M.S. Thesis*, Ceramic Science, The Pennsylvania State University, 1993.

8. K. Onitsuka, A. Dogan, J.F. Tressler, Q.C. Xu, S. Yoshikawa, R.E. Newnham, " Metal-Ceramic Composite Transducer, The Moonie", *J. Int. Mat. Sys. & Struct.*, Vol. 6, pp. 447-455, 1995.

9. H. Goto, K. Imanaka, "Super compact dual axis optical scanning unit applying a torsional spring resonator driven by a piezoelectric actuator," *Proc. of SPIE*, Vol. 1544, pp. 272-281, 1991

10. G. Haertling, "Rainbow ceramics, a new type of ultra high displacement actuator," *Bull. of Am. Ceramic Soc.*, Vol. 73, No 1, pp. 93-96, January 1994

11. J.F. Tressler, A. Dogan, J.F. Fernandez, J.T. Fielding, K. Uchino, R. E. Newnham "Capped Ceramic Hydrophone" *IEEE-UFFC Ultrasonic Symposium Proceeding*, Seattle 1995.

12. J.F. Tressler, R. E. Newnham, W.J. Hughes "Capped Ceramic underwater sound projector: The 'cymbal' transducer " *J.Acoust. Soc. Am. 105 (2), pp 591-600 Febuary 1999*

13. B. Koc, A. Dogan, Y. Xu, R.E.Newnham,and K. Uchino " An Ultrasonic Motor Using a Metal-Ceramic Composite Actuator Generating Torsional Displacement," *Jpn. J. Appl. Phys. Vol.* 37 (1998) pp 5659-5662

14. B. Koc, A. Dogan J.F. Fernandez, R.E. Newnham, and K. Uchino "Accelerometer application of the moonie and cymbal transducers" *Jpn. J. Appl. Phys. Vol.* 35 (1996) pp 4547-4549.

APPENDIX 38

Modeling and Underwater Characterization of Cymbal Transducers and Arrays

Jindong Zhang, Anne-Christine Hladky-Hennion, W. Jack Hughes, *Member, IEEE*, and Robert E. Newnham, *Member, IEEE*

Abstract—The cymbal is a miniaturized class V flextensional transducer that was developed for potential use as a shallow water sound projector and receiver. Single elements are characterized by high Q, low efficiency, and medium power output capability. Its low cost and thin profile allow the transducer to be assembled into large flexible arrays. Efforts were made to model both single element and transducer arrays by coupling finite element analysis (ATILA) and the integral equation formulation (EQI). The pressure and velocity distributions on the surface elements were calculated by ATILA and later used with EQI to calculate the far field properties of the transducer element and arrays. It eliminates the mesh of the fluid domain and makes the 3-D model of a transducer possible. Three-dimensional models of a cymbal transducer and a 3 × 3 cymbal array were developed in the modeling. Very good agreement was obtained between modeling and measurement for single element transducers. By coupling finite element analysis with the integral equation method using boundary elements, acoustic interaction effects were taken into account. Reasonable agreement was obtained between calculation and measurement for a 3 × 3 array.

I. Introduction

THE CYMBAL transducers are miniaturized class V flextensional transducers. They consist of a piezoelectric disk (poled in the thickness direction) sandwiched between two "cymbal-shaped" metal end caps. The metal caps serve as a mechanical transformer that transform the high impedance, small extensional motion of the ceramic into low impedance, large flexural motion of the shell. The cymbal originally was designed as an actuator, which provides a sizable displacement as well as moderate generative force, bridging the gap between the two most common actuators, bimorph and the multilayer [1]. It was later proposed [2] as an underwater transducer for use as a sound projector and hydrophone. Because the cymbal transducer is small compared to the wavelength in water around resonance, it has modest radiation efficiency as a sound projector and a relatively high Q. It is necessary to assemble them into arrays to achieve the desired source level and directivity. In

J. Zhang and R. E. Newnham are with the Materials Research Laboratory, The Pennsylvania State University, University Park, PA (e-mail: jxz132@psu.edu).

A. C. Hladky-Hennion is with the IEMN-Departement I.S.E.N., 59046 Lille, France.

W. J. Hughes is with the Applied Research Laboratory, The Pennsylvania State University, University Park, PA.

assembling arrays, it always is desirable to have the transducer elements close packed in the array to save space. When element-to-element spacing is much smaller than the acoustic wavelength, acoustic interactions occur that lead to different acoustic loading on each transducer element, depending on its position in the array [3]. This then results in significant variations in the volume velocity of each array element. These interactions reduce the acoustic output power of the array and, in some extreme cases, a transducer element may have a negative radiation resistance and absorb acoustic power. However, the acoustic interaction leads to increased radiation resistance, therefore improving the radiation efficiency [4]. The acoustic loading effect is advantageous in the case of cymbal array because it improves the radiation efficiency.

The objective of this paper is to characterize the cymbal as an underwater transducer and attempt to model both single element and array by coupling finite-element analysis and the integral equation method.

II. Finite Element Modeling of an Underwater Transducer

The finite-element method has been used extensively in modeling complex transducer structures for more than 20 years. Many FEA software packages are commercially available, including ANSYS [5], PZFLEX [6], and ATILA [7]. The ATILA is specially designed for underwater transducers, which take into account the coupling between the transducer mechanical structure and the surrounding medium. In modeling underwater transducers, two approaches usually are used.

In the first method, a finite fluid domain is modeled in addition to the mesh of the solid structure, which is adapted from the ATILA code. Kinematic and dynamic continuity conditions are imposed at the interface for displacement and pressure fields. To absorb various components of the radiated field, damper elements are applied on the external surface Γ of the surrounding fluid domain [8]. The use of damper elements provides detailed information about the acoustic near field properties.

This method necessitates the modeling of the fluid domain, which in some cases leads to large meshes and is not well suited to 3-D modeling. A second method is to model only the solid structure using the finite element method, then couple it to an integral equation formulation to account for the acoustic radiation problems. In this way the

size of the mesh and the computation time can be significantly reduced [9]. By coupling the finite element and integral equation (EQI) methods, transducer arrays can be modeled.

The EQI is based on the Helmholtz-Kirchhoff Integral Equation, which is expressed as [10]:

$$\int_{\Gamma} \left[p(r') \frac{\partial G(r,r')}{\partial n'} - \frac{\partial p(r')}{\partial n'} G(r,r') \right] dr' = \begin{cases} \alpha(r)p(r)/4\pi & r\epsilon\Gamma \\ p(r) & r\epsilon\Omega_f \end{cases} \quad (1)$$

where, $G(r,r') = \frac{1}{4\pi} \frac{e^{ik|r-r'|}}{|r-r'|}$ is the Green function. Γ is the external surface of the solid structure, Ω_f is the infinite fluid domain surrounding the solid structure, r is a point outside Γ, r' is a point on Γ, and $\alpha(r)$ is the solid angle at the point r.

The discretization of the integral equation on Γ consists of dividing the external surface of the structure into elements interconnected by nodes. On each element the pressure field and its normal derivative are connected to the nodal values by an interpolation function. Discretization leads to N equations with N unknowns, where N is the number of nodes in the grid. The matrix form of the system is:

$$[A]\{p\} = [B] \left\{ \frac{\partial p}{\partial n} \right\}. \quad (2)$$

Matrices [B] and [A] come from the integration of the Green function, and their normal derivatives are computed by the interpolation functions. The vectors {p} and {$\partial p/\partial n$} contain the nodal pressures of the system and their normal derivatives. The displacement vector normal to the surface is given by:

$$\frac{\partial p(r)}{\partial n} = \rho\omega^2 u_n(r). \quad (3)$$

The solution of the linear systems provides the pressures at the nodes of the surface, from which the pressure at any point in the fluid Ω_f can be calculated.

In our approach, the solid structure is first meshed with special surface elements. Through harmonic analysis, the displacement and pressure field of the solid structure and the surface elements can be computed as a function of frequency using the finite element code ATILA. Then by enforcing kinematic and dynamic continuity conditions at the interface, the far field and near field pressures in the fluid domain are calculated with EQI.

III. EXPERIMENTAL PROCEDURE

A. Fabrication of the Cymbal Transducer and Array

The detailed fabrication procedure of cymbal transducer and arrays was described in a previously published paper [11]. The piezoelectric ceramic disks (PKI402, Piezokinetics Inc., Bellefonte, PA) have a thickness of 1 mm and a diameter of 12.7 mm, and they were poled in the thickness direction. Titanium sheets of 0.25 mm thickness were used as the cap material. The shaped caps had a diameter of 12.7 mm. The cavity diameter was 9.0 mm at the bottom and 3.2 mm at the top. The cavity depth was 0.32 mm. Two different epoxy systems were used in this study. One is a high bonding strength insulating epoxy (Emerson and Cuming, Billerica, MA). A ratio of three parts 45 LV epoxy resin to one part 15 LV hardener was used. The other one is an E-solder conductive epoxy (Von-Roll ISOLA, New Haven, CT). In both cases, the thickness of the glue layer was approximately 40 μm. In the 3×3 array, the element center-to-center spacing was kept at 15 mm.

B. Characterization of the Cymbal and Arrays

Underwater calibration tests of single cymbals were performed at the Applied Research Laboratory, Penn State. The tank measured 5.5 m in depth, 5.3 m in width and 7.9 m in length. A pure tone sinusoidal pulse signal of 2-ms duration was applied to the test transducer, and its acoustic output was monitored with a standard F33 hydrophone. The test transducer and the standard were positioned at a depth of 2.74 m and separated by a distance of 3.16 m. The mechanical Q, transmitting voltage response (TVR), free-field voltage sensitivity (FFVS), and directivity pattern were evaluated.

In the underwater test, the cymbal transducer and array must be insulated from the conductive water in the tank. In addition, the array has to be rotated to observe the directivity pattern. A potting technique was devised for the transducer to maintain a mechanically free condition [11]. For single elements, a coaxial cable was first attached to the flange of the metal cap using silver epoxy. The cymbal and part of the cable then were potted in polyurethane with a thickness of about 0.5 mm. The polyurethane layer insulated the cymbal from the conductive water in the water tank. The 3×3 array was fixed at the end of a long plastic tube to allow rotation. The electrical lead wires passed through the plastic tube and were connected to the measurement system at the other end of the tube. The diameter of the tube is small compared to the wavelength in water so it does not interfere with the acoustic field generated by the array. The potted cymbal transducer and array are shown in Fig. 1.
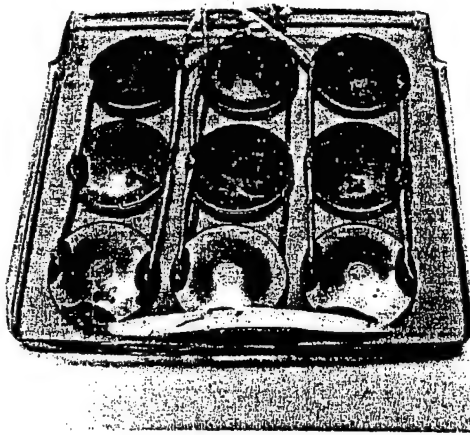
IV. RESULTS AND DISCUSSION

A. Single Element

Due to symmetry, only a quarter of the transducer structure was modeled. There are symmetry planes across XOY and XOZ. The mesh of the entire structure is too complicated to see any details; therefore, only the mesh of the surface element of the cymbal transducer is shown
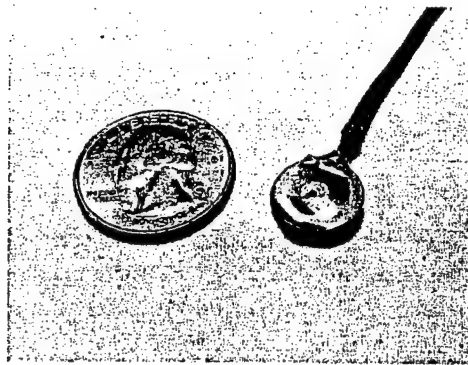
(a) single element

(b) 3x3 array

Fig. 1. Photographs of a cymbal transducer and a 3 × 3 array potted in polyurethane.
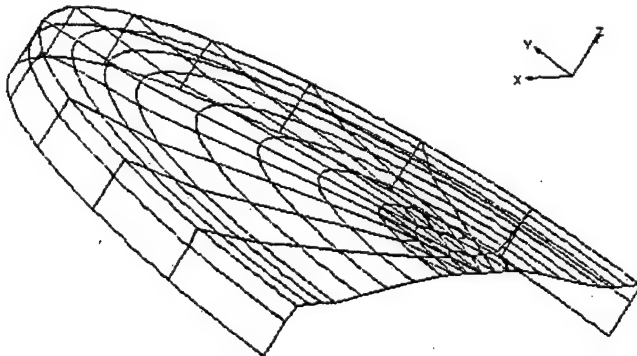

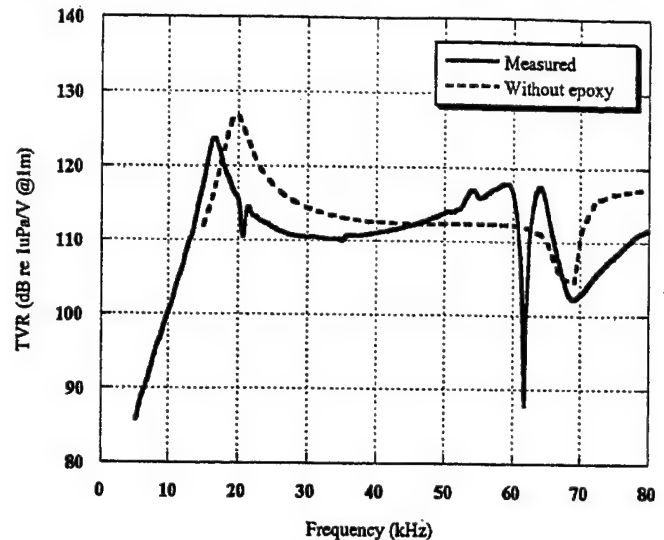Fig. 2. Mesh of the surface elements of a single element.

Fig. 3. Comparison of experimental and calculated TVR of a single element. Computation did not include the epoxy bonding layer.

in Fig. 2. The symmetry plane XOY is grounded and 1 V was applied to the upper side of the ceramic. Because 1 V was applied to a thickness of 0.5 mm, which is half of the thickness of the ceramic, the electric field was actually 1 V/0.5 mm = 2 V/mm. It is equivalent to an applied voltage of 2 V for a 1 mm-thick ceramic. Therefore, what the program calculates is source level (SL). To obtain the TVR, the following equation was used:

$$SL = TVR + 20 \log V. \qquad (4)$$

Here $20 \log V = 6$. Thus, we have to subtract 6 dB from the calculated source level to get TVR. For the same reason, the calculated impedance was multiplied by two to get TVR for a 1 mm-thick ceramic disk.

Because the epoxy thickness is very small compared with the ceramic and the caps, we initially did not include the epoxy layer in the model, assuming it has little effect on the transducer performance. Fig. 3 shows the calculated TVR of a cymbal transducer compared with measurement. Without modeling the glue layer, the calculated resonance frequency was about 20 kHz compared to the measured resonance frequency of 16.6 kHz. The considerable difference in resonance frequency suggests that the epoxy layer increases the effective compliance of the cymbal structure substantially. Therefore, the epoxy layer must be included in the model even at the cost of a larger mesh and considerably increased computation time.

In the next step, the epoxy layer was included in the modeling. Its thickness was assumed to be 40 μm. The calculated TVR is shown in Fig. 4 and compared with the measured values. A nearly perfect match was obtained over a wide frequency range from 10 kHz to 80 kHz. The four peaks at 20 kHz, 34 kHz, 53 kHz, and 62 kHz come from the resonance of the air bubbles in the cured polyurethane and will be ignored in the discussion. The major peak at 17 kHz in the TVR curve corresponds to the first flextensional mode of the caps, which is illustrated in Fig. 5(a).
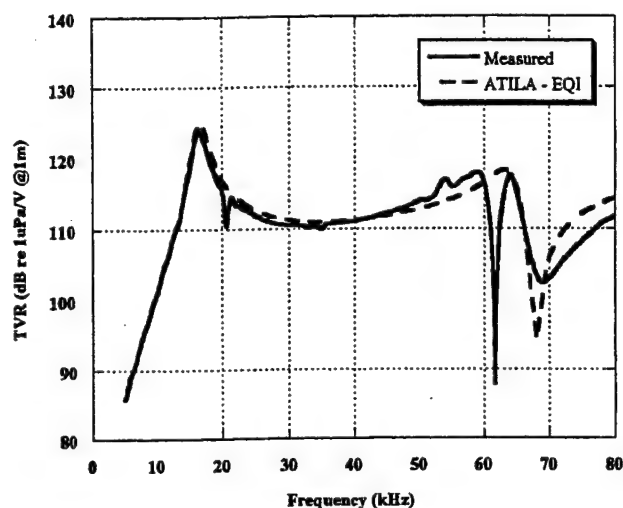
Fig. 4. Calculated and measured TVR of single cymbal modeled more accurately with the bonding layer.
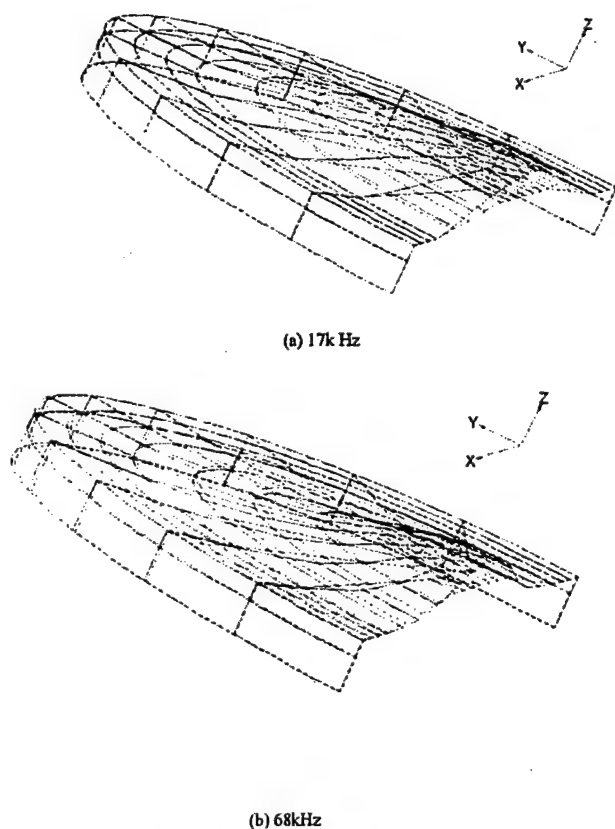

(a) 17k Hz

(b) 68kHz

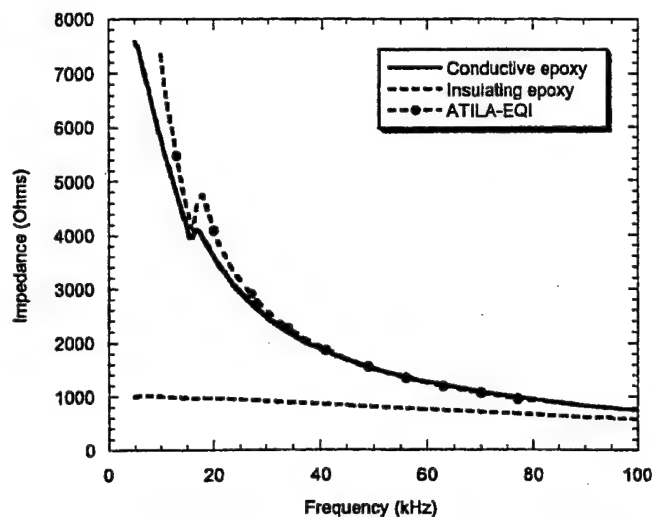Fig. 5. Displaced shape of the cymbal transducer at frequency: (a) 17 kHz, (b) 68 kHz.

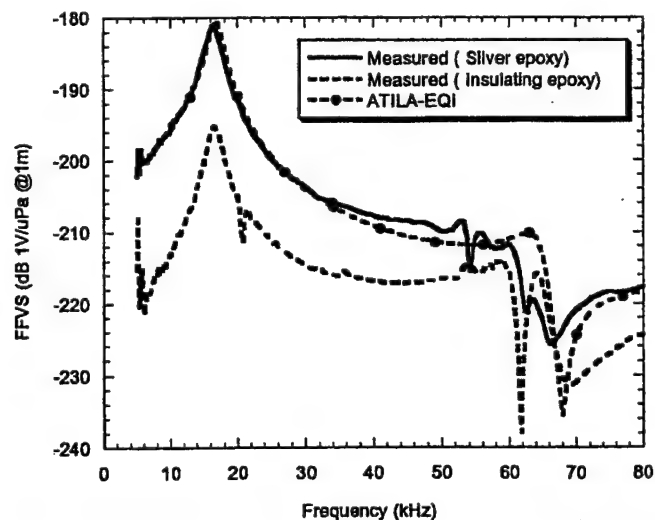Fig. 6. The calculated and measured impedance of a cymbal transducer.

Fig. 7. Calculated FFVS of cymbal transducer based on reciprocity.

There is a sharp dip at about 68 kHz, which originates from the second flextensional mode of the metal caps. As seen from the vibration mode in Fig. 5(b) at this frequency, two portions of the cap vibrated out of phase. The pressures from different portions of the metal caps cancel out, leading to a sharp drop in transmit response.

The calculated impedance of a cymbal transducer is shown in Fig. 6 and compared with the measured impedance. There is a significant difference between the measurement and modeling at low frequencies. Based on reciprocity, the receive response of the cymbal transducer was calculated from the calculated TVR and impedance using the following equation:

$$TVR = FFVS + 20\log\ f - 20\log |Z| + 354. \quad (5)$$

Fig. 7 shows the calculated FFVS of a cymbal transducer compared with measurement. A difference of about
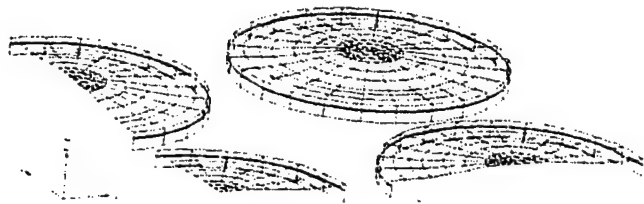
Fig. 8. Meshes of the surface elements of the 3 × 3 array. The center cymbal is in the lower left.

10 dB exists between the modeling and measurement. To explain the discrepancies, it is necessary to examine the experimental conditions. In the modeling, the electric field was applied directly to the face of the PZT disk, and it does not "see" the epoxy layer. In the measurement, the leads were connected to the cap instead of the PZT disk for convenience. The insulating epoxy layer sometimes can cause problems because of poor electrical contact. To verify this idea, another cymbal transducer of the same material and cap geometry was assembled with conductive epoxy. The electrical leads were connected to the flange of the cap in the usual way. The measured impedance and FFVS of the modified cymbal are shown in Fig. 6 and Fig. 7, respectively. In both cases, the modeling and measurement agree very well. It is clear now that poor electrical contact between the cap and ceramic is a weak point in the manufacture of a cymbal transducer. This problem can be solved by placing the epoxy layer under compressive stress, which is difficult to achieve experimentally and may complicate the design. Use of conductive epoxy can alleviate the problem by an order of magnitude. Unfortunately, the conductive epoxy usually has lower bonding strength and is not good for high power transmission. This is a materials problem requiring further attention.

B. Array Modeling

Three symmetry planes exist for the 3 × 3 array; therefore, only one-eighth of the array is modeled. Fig. 8 shows the mesh of the surface elements.

The predicted TVR of a 3 × 3 array with a center-to-center spacing of 15 mm is shown in Fig. 9 and compared with the measured TVR of the array. In both modeling and measurement, the peaks associated with the resonance have disappeared because of the damping associated with acoustic loading. This is a result of strong acoustic interaction between adjacent transducers at resonance. Although all the transducers in the array are electrically driven in phase, the amplitude and phase of the vibration of the transducers are very different, depending on their location in the array. The calculated displacement of the dome of transducers in the array is shown in Fig. 10 and compared with that of a single, individual element. At off-resonance frequencies, the displacement of transducers in the array is pretty much the same as that of a single element. At resonance, the displacement of the center transducer in the array is almost two times larger than that of a single, individual element at this frequency. Because of this
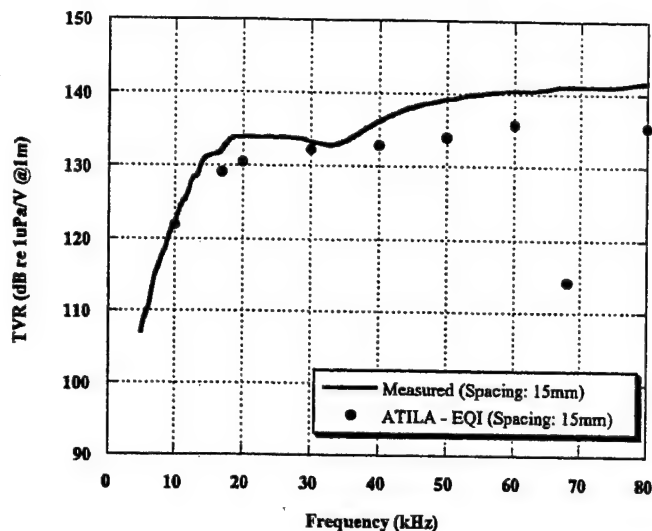

Fig. 9. Predicted TVR of a 3 × 3 cymbal array compared with measurement.
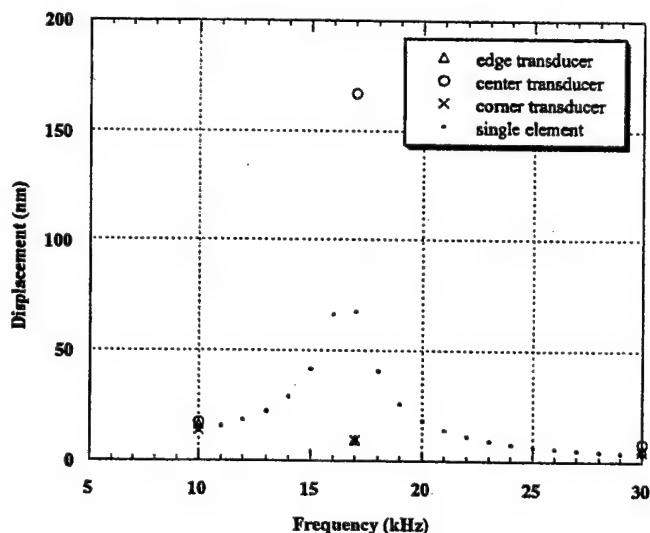

Fig. 10. Calculated displacement of transducers in the array and of a single, individual transducer.

large motion, the stress in the ceramic may exceed the mechanical tolerance and destroy the ceramic. In addition to mechanical failure, the heat generated in the ceramic due to mechanical and dielectric loss may depole the ceramic, leading to a thermal failure.

Fig. 11 shows the calculated displacement field of transducers in the array at the nominal resonance frequency (17 kHz). The corner transducers actually vibrate out of phase with the other transducers in the array. The pressures from different transducers partially cancel as a result of out of phase vibration. The net effect is, the resulting TVR curves are flattened around its nominal resonance and appear to have a broad band response.

Another consequence of array interaction is the improved efficiency of a 3 × 3 cymbal transducer array over
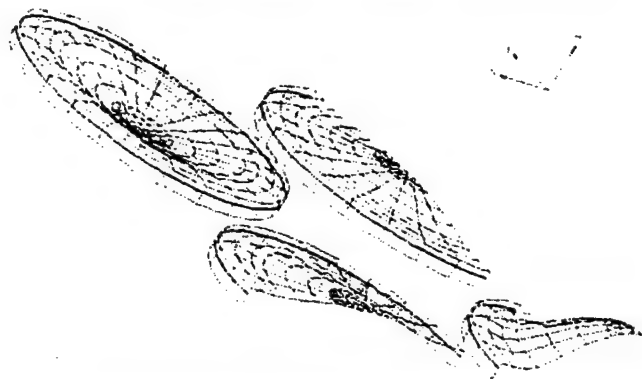
Fig. 11. The displacement fields of the transducer in the 3 × 3 array at 17 kHz (nominal resonance). The center cymbal is in the lower right.
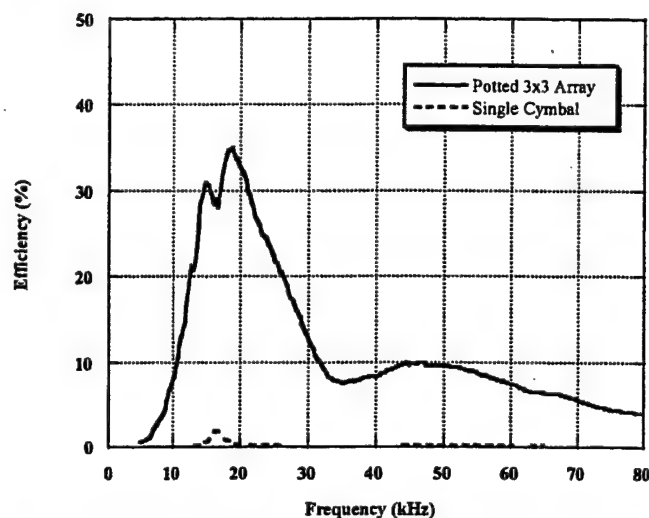

Fig. 13. The reduced motion of transducers in the array as a result of varying the surface geometry.

Fig. 12. Measured efficiency of a single cymbal transducer and of the potted 3 × 3 array.

Fig. 14. Predicted TVR of a 3 × 3 array of transducers with varied surface geometry compared with that of a 3 × 3 array with identical transducers.

an individual cymbal transducer. This is shown in Fig. 12. The array has an efficiency over 30% around nominal resonance, compared with the very small efficiency of the single cymbal transducer.

The calculations indicate that array interaction might be disastrous for a closely packed cymbal array driven at the nominal resonance, but there is a way to avoid this problem. Mutual radiation impedance not only depends on element-to-element spacing and operational wavelength, it also depends on the acoustic properties of the transducer surfaces and the shape of the transducer [3]. Instead of having identical transducers in the array, we slightly varied the cavity depth of the transducers in the array so that the surface geometry of the transducers was different. The cavity depth of the center transducer was maintained at 0.32 mm, and the cavity depths for the corner and edge transducers were 0.28 mm and 0.36 mm, respectively. Fig. 13 shows the calculated displacement of the dome area of the transducers in the array. At nominal resonance the displacement of the center transducer in the array was greatly damped
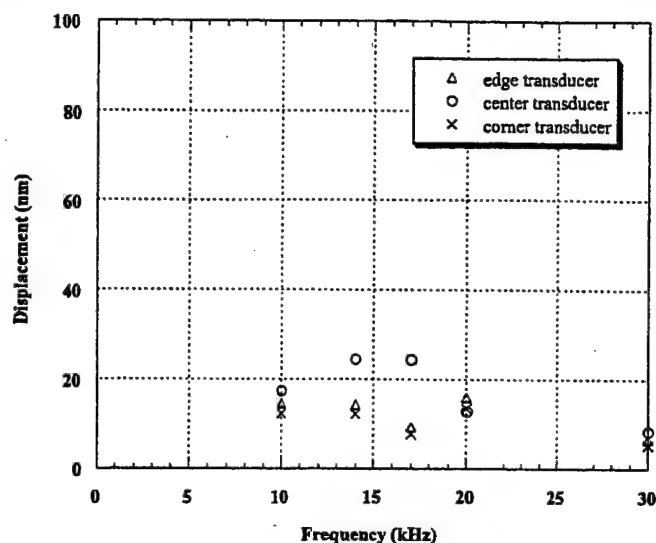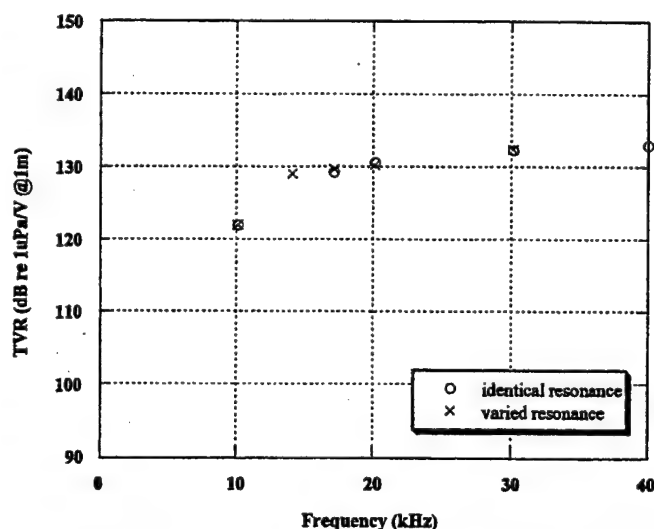
compared with its displacement in an array of identical transducers. It also is much smaller than that of a single, individual cymbal. Therefore, by slightly varying the surface geometry of the transducers in the array, the vibration velocities of the transducers in the array become more uniform, even at resonance, making the array less subject to the aforementioned mechanical and thermal failure. The predicted TVR of this array is nearly identical to the identical-transducer array shown in Fig. 14.

As shown in Fig. 9, the predicted TVR is 2 to 4 dB lower than the measured value above the nominal resonance frequency. This discrepancy is believed to be caused by the polymer matrix used in assembling the array. The potted array structure is actually very similar to the popular 1-3
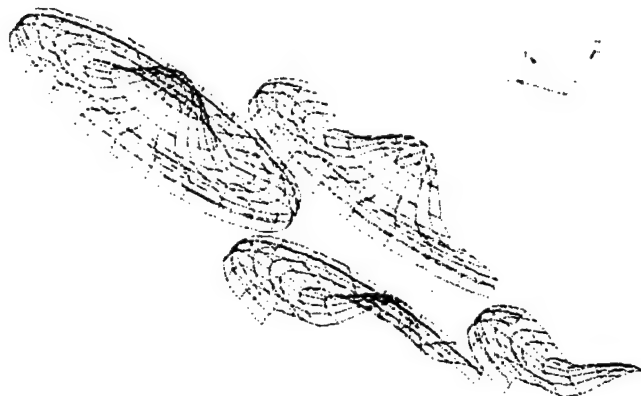
Fig. 15. Displacement field of transducers in the array at 68 kHz.

Fig. 16. Displacement field of transducers in the array at 80 kHz.

composite and has a similar decoupling effect [12] caused by the polymer matrix. As in the 1-3 composite, the radial motion of the ceramic disk is partially suppressed by the polymer matrix, and the axial motion of the caps is not. Therefore, the negative contribution of the radial motion to the sound pressure is reduced. Because the metal caps of the cymbal have an amplified motion in the axial direction, the effective acoustic impedance in the axial direction is reduced, and the polymer may further serve as a matching layer between the cap and water. Therefore, the energy transfer is more efficient in the axial direction than in the lateral direction of the array. The decoupling of the lateral motion of the ceramic from the axial motion and the improved acoustic matching layer increase the output pressure of the array.

The modeling predicts a sharp dip in the TVR curve for 3×3 array at 68 kHz, as shown in Fig. 9. This corresponds to the sharp dip in the TVR curve for a single element. The displacement pattern of the array at this frequency is illustrated in Fig. 15. At this frequency all the transducers have a similar vibration mode to that of a single element. Therefore, a dip in the TVR curve at this frequency is expected, but we did not observe such a dip in the measured TVR. Again, the discrepancy may be ascribed to the polymer matrix that alters the boundary conditions of the transducer elements in the array. Because the metal caps are in close contact with the polymer matrix, the two-nodal point line mode shown in Fig. 15 is not favorable and tends to be suppressed by the polymer matrix. As a result, the TVR is improved in this frequency range.

The vibration mode of transducers in the array at 80 kHz is shown in Fig. 16. The displacement for each transducer in the array is essentially the same with the same phase, suggesting little array interaction at this frequency as a result of large spacing to acoustic wavelength ratio at this frequency.

The calculated beam patterns of the 3×3 array in XOZ plane at various frequencies are shown in Fig. 17. The acoustic axis is the OZ direction. At frequencies up to 80 kHz, the modeling successfully predicts the main lobes and the side lobes in addition to the nulls in the beam pattern.
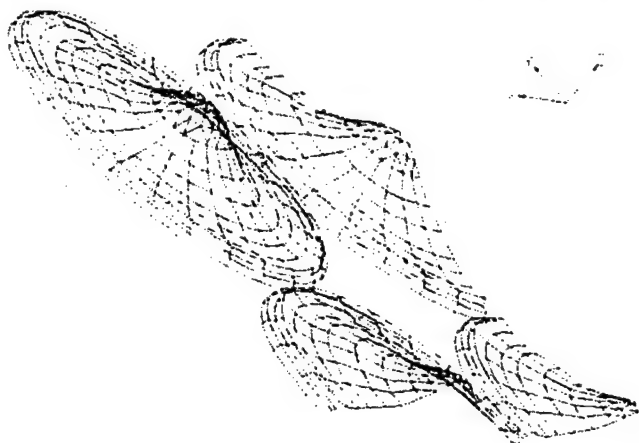
The effect of element center-to-center spacing in the array is shown in Fig. 18. At low frequencies when array interaction is severe, the predicted TVR is very sensitive to the element spacing. At the nominal resonance frequency of 17 kHz, the TVR of the array increases from 124 dB to 133 dB when the element spacing is increased from 13.5 mm to 16 mm. The difference is 9 dB when there is a change in spacing of only 2.5 mm. At higher frequencies, when the wavelength is of the same order of the size of the array (40 kHz), the predicted TVR is less dependent on the spacing.

V. SUMMARY

The coupling of finite element analysis and boundary element method provides an efficient way of modeling underwater transducers and arrays. For a single cymbal transducer, excellent agreement was obtained between calculation and measurement using this technique. The thin epoxy layer used to glue the caps to the ceramic disk has a tremendous effect on the transducer resonance and sensitivity. It is necessary to include the epoxy layer in finite element calculations, even at the cost of fine mesh and long computation time.

The acoustic interaction in the array was analyzed using the program EQI. The vibration modes of the transducers in the array behave very differently from a single, individual transducer at low frequencies where acoustic interaction is important. The vibration magnitude and phase of the transducers are strongly affected by the mutual radiation impedance, which is dependent on surface geometry of the transducers and their locations in the array. As the operational frequency increases, acoustic interaction becomes less severe, and transducers in the array behave more like a single, individual element. In addition to mutual radiation impedance, the vibration of the transducers in the array also is affected by the polymer matrix used in assembling the array. The polymer matrix tends to suppress the undesired vibration modes and improve the performance of the array. The combined finite element analysis and in-
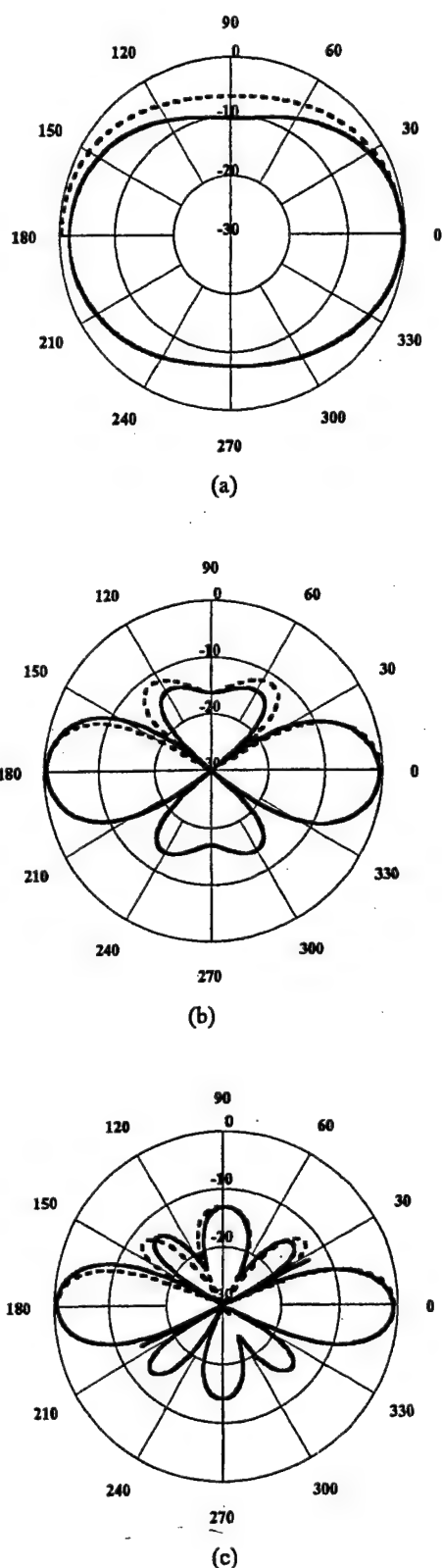
(a)

(b)

(c)

Fig. 17. Predicted beam patterns of the 3 × 3 array compared with the measured beam patterns (a) 20 kHz, (b) 60 kHz, (c) 80 kHz (— measured; − − − ATILA-EQI).
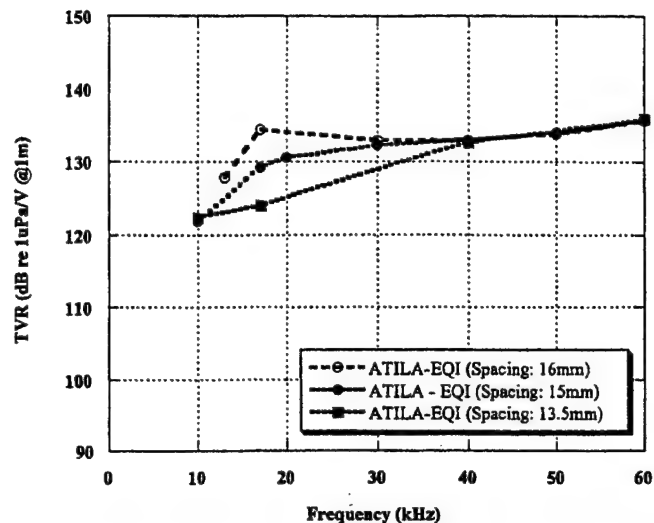

Fig. 18. Effect of element center-to-center spacing on the predicted TVR of a 3 × 3 array.

tegral equation method appear to be an effective way of modeling both single element transducers and arrays.

REFERENCES

[1] A. Dogan, K. Uchino, and R. E. Newnham, "Composite piezo-electric transducers with truncated conical endcaps 'Cymbals'," *IEEE Trans. Ultrason., Ferroelect., Freq. Contr.*, vol. 44, no. 3, pp. 597–605, 1997.

[2] J. F. Tressler, R. E. Newnham, and W. J. Hughes, "Capped ceramic underwater sound projector: The 'cymbal' transducer," *J. Acoust. Soc. Amer.*, vol. 105, no. 2, pp. 591–600, 1999.

[3] C. H. Sherman, "Analysis of acoustic interactions in transducer arrays," *IEEE Trans. Sonics Ultrason.*, vol. SU-13, no. 1, pp. 9–15, 1966.

[4] B. F. Hamonic, O. B. Wilson, and J.-N. Decarpigny, "The design of low-frequency underwater acoustic projectors: Present status and future trends," *IEEE J. Oceanic Eng.*, vol. 16, no. 1, pp. 107–121, 1991.

[5] SWANSON Analysis Systems, Inc., *ANSYS User's Manual*, Revision 5. Houston, PA: SWANSON Analysis Systems, Inc., 1992.

[6] N. N. Abboud, G. L. Wojcik, D. K. Vaughan, J. Mould, D. J. Powell, and L. Nikodym, "Finite element modeling for ultrasonic transducers," in *Proc. Int. Symp. Med. Imaging*, 1998, pp. 19–42.

[7] MAGSOFT Corporation, *ATILA Version 5.1X User's Manual*. Troy, NY: MAGSOFT Corp., 1997.

[8] B. Hamonic, J. C. Debus, J.-N. Decarpigny, D. Boucher, and B. Tocquet, "Analysis of a radiating thin-shell sonar transducer using the finite element method," *J. Acoust. Soc. Amer.*, vol. 86, no. 4, pp. 1245–1253, 1989.

[9] B. Stupfel, B. Lavie, and J.-N. Decarpigny, "Combined integral equation formulation and null-field method for the exterior acoustic problem," *J. Acoust. Soc. Amer.*, vol. 83, no. 3, pp. 927–941, 1988.

[10] ISEN, *EQI User's Manual.* France: ISEN, 1999.

[11] J. Zhang, W. J. Hughes, R. J. Meyer, Jr., K. Uchino, and R. E. Newnham, "Cymbal array: A broad band sound projector," *Ultrasonics,* vol. 37, pp. 523–529, 2000.

[12] K. A. Klicker, J. V. Biggers, and R. E. Newnham, "Composites of PZT and epoxy for hydrostatic transducer applications," *J. Amer. Ceram. Soc.,* vol. 64, no. 1, pp. 5–9, 1981.

Jindong Zhang was born in Nanyang, China on February 1, 1970. He received the B.S. degree in ceramic science and engineering in 1991 from Zhejiang University in China, and the M.S. degree in ceramic engineering in 1996 from Shanghai Institute of Ceramics, Chinese Academy of Sciences. He worked in Dalian Porcelain Insulator Works, China, as an engineer from 1991–1993.

He currently is a Ph.D. student in Intercollege Programs in Materials and The Pennsylvania State University, University Park, PA. His research interests are in electroceramics, piezoelectric actuators, and transducers.

Robert E. Newnham (M'85) was born in Amsterdam, NY, on March 28, 1929. He received the B.S. degree in mathematics in 1950 from Hartwick College, Oneonta, NY; the M.S. degree in physics from the Colorado State University, Fort Collins, CO; a Ph.D. degree in physics and mineralogy from The Pennsylvania State University; and a second doctorate in crystallography from Cambridge University in 1960.

He is ALCOA professor of solid state science and former Associate Director of the Materials Research Lab at The Pennsylvania State University, University Park, PA. His research interests are in structure-property relations, electroceramics, and composite materials for electronic applications.

APPENDIX 39

Cymbal array: a broad band sound projector

Jindong Zhang [a,*], W. Jack Hughes [b], R.J. Meyer Jr. [a], Kenji Uchino [a], Robert E. Newnham [a]

[a] *Materials Research Laboratory, The Pennsylvania State University, University Park, PA 16802, USA*
[b] *Applied Research Laboratory, The Pennsylvania State University, University Park, PA 16802, USA*

Abstract

A prototype 3×3 planar cymbal transducer array was built and tested. The array has a radiating area of $5.5 \, cm \times 5.5 \, cm$ and a thickness of less than 8 mm. The measured transmitting voltage response was above 134 dB re 1 µPa/V @ 1 m and flat over the frequency range of 16 and 100 kHz. Array interaction was analyzed using an equivalent circuit model. The array interaction leads to variations in radiation resistance and velocity of the transducers in the array according to their surroundings in the array. The effect is enhanced overall efficiency and a flat response. © 2000 Elsevier Science B.V. All rights reserved.

1. Introduction

The cymbal transducer was developed by Newnham et al. in the early 1990s [1]. It evolved from the commercially successful moonie patent [2]. The moonie and cymbal transducers consist of a piezoelectric disk (poled in the thickness direction) sandwiched between two metal end caps. The caps contain a shallow cavity on their inner surface. The presence of the cavities allows the caps to be used as a mechanical transformer, which transforms the high impedance, small extensional motion of the ceramic into low impedance, large flexural motion of the shell. According to the shape of the metal caps, this structure is a small Class V flextensional transducer [3]. Compared to the traditional flextensional transducers, which have a complicated design, are usually assembled by hand and are therefore expensive, the fabrication process of the moonie and cymbal is very simple, easy and inexpensive to mass-produce.

The cymbal was originally designed as an actuator, which provides a sizeable displacement as well as a large generative force, bridging the gap between the two most common actuators, bimorph and the multilayer [4]. It was later proposed [5] by Newnham et al. as an underwater transducer, as both sound projector and

hydrophone. As a sound projector, the cymbal transducer is attractive in its low weight, low cost and thin profile and its ability to produce medium to high output power.

Since the cymbal transducer is small compared to the wavelength in water around resonance, it has a very low radiation resistance and a relatively high radiation reactance, which means that the transfer of radiated acoustic power from the surface of the radiator to the water is very inefficient. Since the overall efficiency is the product of the radiation and mechanical transduction efficiencies, the cymbal's overall efficiency would also be low, even if the mechanical transduction rate is high [6]. The high Q and low efficiency of the cymbal transducer make it difficult for the cymbal transducer to find practical applications, and it is necessary to assemble them into arrays to achieve the desired source level and directivity. In assembling arrays, it is always desirable to have the transducer elements close packed in the array to save space.

It is well known that in closely packed arrays, acoustic interactions occur that lead to different acoustic loading on each transducer element, depending on its position in the array [7]. This then results in significant variations in the volume velocity of each array element. These interactions reduce the acoustic output power of the array, and in some extreme cases, a transducer element may have a negative radiation resistance and absorb

* Corresponding author. Tel.: +1-814-863-0180;
fax: +1-814-865-2326.
E-mail address: jxz132@psu.edu (J. Zhang)

acoustic power. The acoustic interactions are especially serious when the transducer elements are small compared to the wavelength and if they have a high efficiency. Since the single cymbal transducer has a low overall efficiency, array interactions may not pose any serious problems in cymbal arrays.

The objectives of this work were to design a planar cymbal transducer array, initially a planar array, and to model and understand the array element interaction in order to optimize the array performance. The information gathered here will be used to design larger conformal arrays for underwater vehicle applications.

2. Experimental

2.1. Single element

The piezoelectric ceramic disks (PKI402, Piezokinetics, Bellefonte, PA) have a thickness of 1 mm and a diameter of 12.7 mm. The PZT disks were poled in the thickness direction. The silver electrodes on the PZT disks were first ground with sandpaper to remove the oxide layer and then cleaned with acetone. Titanium caps were punched from Ti foil of 0.25 mm thickness and shaped using a special die. The shaped caps had a diameter of 12.7 mm. The cavity diameter was 9.0 mm at the bottom and 3.2 mm at the top. The cavity depth was 0.32 mm. The flanges of the Ti caps were ground using sandpaper. The caps were then bonded to the piezoelectric ceramic disk. The bonding material was an Emerson and Cuming insulating epoxy. A ratio of three parts 45 LV epoxy resin to one part 15LV hardener was used. The thickness of the epoxy-bonding layer was approximately 20 μm. The entire assembly was kept under uniaxial stress in a special die for 24 h at room temperature to allow the epoxy time to cure.

2.2. Array fabrication

Single element cymbal transducers were incorporated into a 3×3 square planar array. Each element has a center-to-center spacing of 13.5 mm. Two different schemes were proposed.

2.2.1. PC board technique

The nine cymbals were sandwiched between two copper-clad PC boards each 1.5 mm thick. Holes 11 mm in diameter were drilled equidistant from one another through the boards. Each element had a center-to-center spacing of 13.5 mm. Plastic posts 1.5 mm thick were used to maintain a uniform distance between the upper and lower panels, which were screwed together tightly to keep the transducers in place. The elements were electrically in parallel due to the PC board configuration.
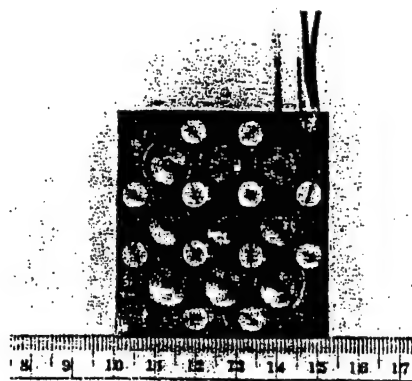
(a)
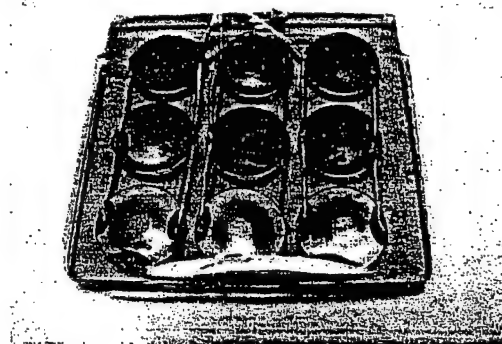
(b)

Fig. 1. Two arrays: (a) the cymbals were sandwiched between two PC boards; (b) the cymbals were potted in polyurethane.

2.2.2. Direct potting technique

The elements in the array were connected electrically in parallel using very fine electrical wire. Conductive epoxy was used to bond the wire to the flange of the cymbal transducers. The assembled cymbal transducer array was then potted in polyurethane with hardness Shore-A 90. Pictures of the two arrays are shown in Fig. 1.

Underwater calibration tests of cymbal transducers were performed at the Applied Research Laboratory at Penn State. The tank measured 5.5 m in depth, 5.3 m in width and 7.9 m in length. A pure tone sinusoidal pulse signal of 2 ms duration was applied to the test transducer, and its acoustic output was monitored with a standard F33 transducer used as a hydrophone. The test transducer and the standard were positioned at a depth of 2.74 m and separated by a distance of 3.16 m. The parameters measured were transmitting voltage response (TVR), free-field voltage sensitivity (FFVS), and directivity pattern.

3. Array modeling

A transducer can be represented by an ABCD transfer matrix, which relates input voltage and current, and the

output force and velocity in the form [8]:

$$\begin{pmatrix} e_j \\ i_j \end{pmatrix} = \begin{pmatrix} A_j & B_j \\ C_j & D_j \end{pmatrix} \begin{pmatrix} f_j \\ v_j \end{pmatrix} \tag{1}$$

where e and i are voltage and current at the electrical terminal, and f and v are the force and velocity at the mechanical (acoustical) terminals, respectively ($j = 1$ to N, N is the number of transducers in the array).

By definition, the force on the jth transducer is

$$f_j = \sum_{m=1}^{N} z_{jm} v_{in}, \tag{2}$$

where z_{jm} is the mutual impedance matrix, which can be calculated from the Pritchard approximation [9].

Substituting Eq. (2) into Eq. (1), we obtain $2N$ linear equations. By solving this linear system, the velocities of each transducer in the array were obtained.

The ABCD parameters could be calculated from lumped equivalent circuit parameters. An equivalent circuit of the cymbal transducer is shown in Fig. 2. Here, C_0 is the clamped capacitance, and N is the electromechanical turns ratio. C represents the mechanical compliance, M the dynamic mass, and R the mechanical impedance. In calculating the ABCD parameters, an effective radiating area was required and was taken to be the surface area of the caps. The equivalent circuit parameters of the cymbal transducer are:

C_0: clamped capacitance, 2.02nF
C: compliance, 9.9×10^{-9} m/N
M: dynamic mass, 8.25 g.

The program 'ARRAY' [10], developed by J.L. Butler, was used to calculate the mutual impedance matrix and the velocities of the transducers in the array.

4. Results and discussion

The TVRs of the two 3×3 arrays with different mounting schemes, the direct potting and PC board case, are shown in Fig. 3. The direct potting array has a significantly higher TVR than its counterpart made with PC board. The transmit response was also flatter over the frequency range of interest because the PC boards impose an anisotropic stress on the flange of the cymbal transducer and partially clamp it, as it did for the single cymbal [11]. This clamping results in lowered TVR and spurious peaks in the transmit response. In
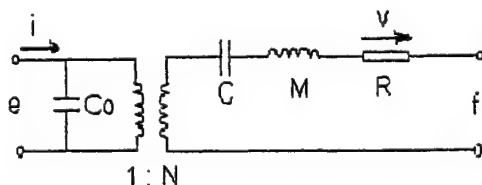

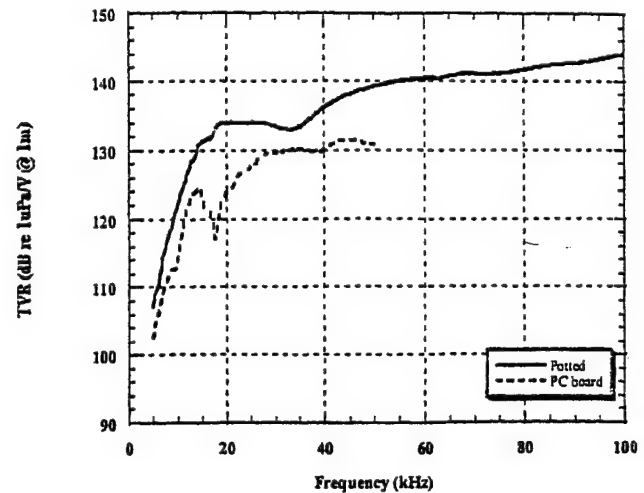Fig. 2. Equivalent circuit of the cymbal transducer.

Fig. 3. Measured transmitting voltage response of 3×3 arrays assembled in two different mounting schemes.

addition, the PC boards lead to abnormal beam patterns over the frequency range of interest. Fig. 4 and Fig. 5 show the measured beam patterns of the two arrays along with predicted beam pattern. In the calculation, we assumed the cymbal transducer functions as a point source. This assumption was valid since a single cymbal transducer under free conditions is omnidirectional up to 60 kHz [11]. At frequencies below the resonance frequency, 15 kHz, each array shows near omnidirectional beam patterns and agrees well with the calculation. As the frequency was increased, the detrimental effect of the PC board was seen clearly as low as 30 kHz. The beam patterns of the PC board sandwiched array shows asymmetric and distorted beam patterns at 30 kHz and above. However, the beam patterns of the potted array were symmetric and agreed well with the calculation, particularly for the main lobes. As no additional boundary conditions were imposed on the transducers in assembling of the array, the beam patterns of the potted array were predictable, which is of great advantage in the design of large sonar transducer arrays.

The introduction of a polyurethane coating along with the thin profile and small size of the cymbal transducer also makes it possible to build a flexible array from the cymbal transducers. It can then be bent to make a conformal cylindrical array, which can be wrapped around the shell of underwater vehicles.

The direct potting array removes any possible interference from fixtures, making an ideal geometry for array analysis. The cymbal is much smaller than a wavelength at resonance, validating the use of the Pritchard approximation to calculate the mutual radiation impedance. In the array modeling, the cymbal transducer was modeled as a dual piston, since the cymbal has two caps. The equivalent circuit parameters used here were all measured except for the electromechanical turns ratio. The turns ratio was calculated from ATILA and is a function of frequency. In this case, a
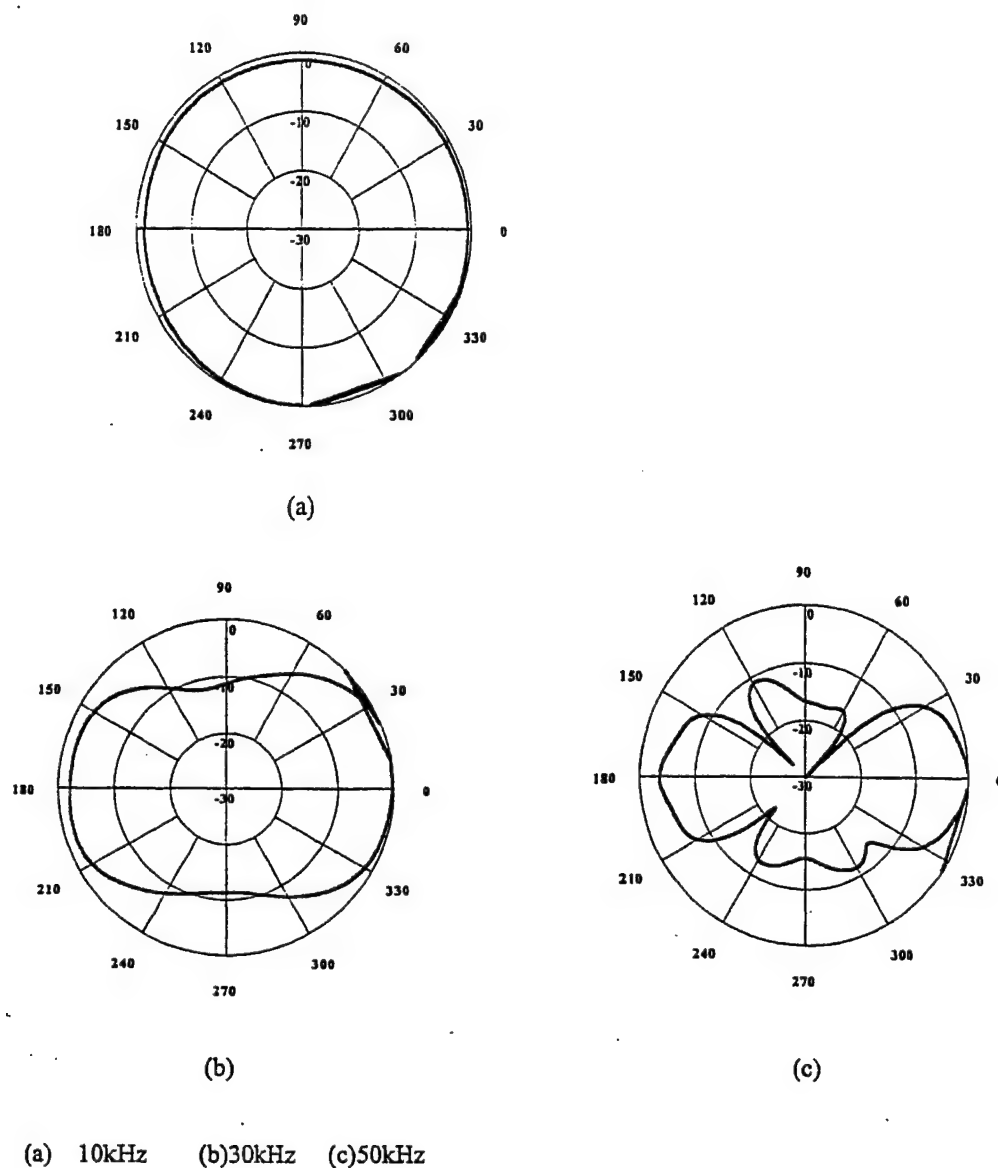
(a)

(b)　　　　　　　　　　　　　　　　　　　(c)

(a)　10kHz　　　(b)30kHz　　(c)50kHz

Fig. 4. Beam patterns of the 3 × 3 array with PC board.

value of 0.11 N/V was adopted for the resonance frequency around 17 kHz. Fig. 6 shows the calculated TVR of a single cymbal transducer. A reasonable agreement between the measurement and calculation was obtained around resonance, validating the use of these equivalent circuit parameters. Fig. 7 shows the calculated TVR for the 3 × 3 planar array; a reasonable agreement was obtained between the calculation and the experiments near resonance.

When a transducer is assembled in an array, the radiation loading on each individual source is different, depending on its position in the array. The single transducer adjusts by changing its velocity. In the 3 × 3 array, the transducers were grouped into three categories due to the symmetry of the array, as shown in Fig. 8.

The normalized radiation resistance (relative to that

of a single element) of each group of transducers in the array is shown in Fig. 9. Near resonance, the normalized radiation resistance of all three groups of transducers is greater than unity. As expected, the radiation resistance of the center transducer oscillates the most with frequency, with quite a low radiation resistance below resonance. This is where the center transducer might have a negative radiation resistance. Fortunately, the single cymbal transducer has a low overall efficiency, and does not possess a negative value in this array. As frequency increases, the radiation resistance of the transducers decreases and approaches unity, indicating less array interaction at high frequencies. Fig. 10 shows the velocities of the three types of transducers near the resonance frequency. The velocities are normalized relative to v_{11}, the velocity of a separate, single cymbal
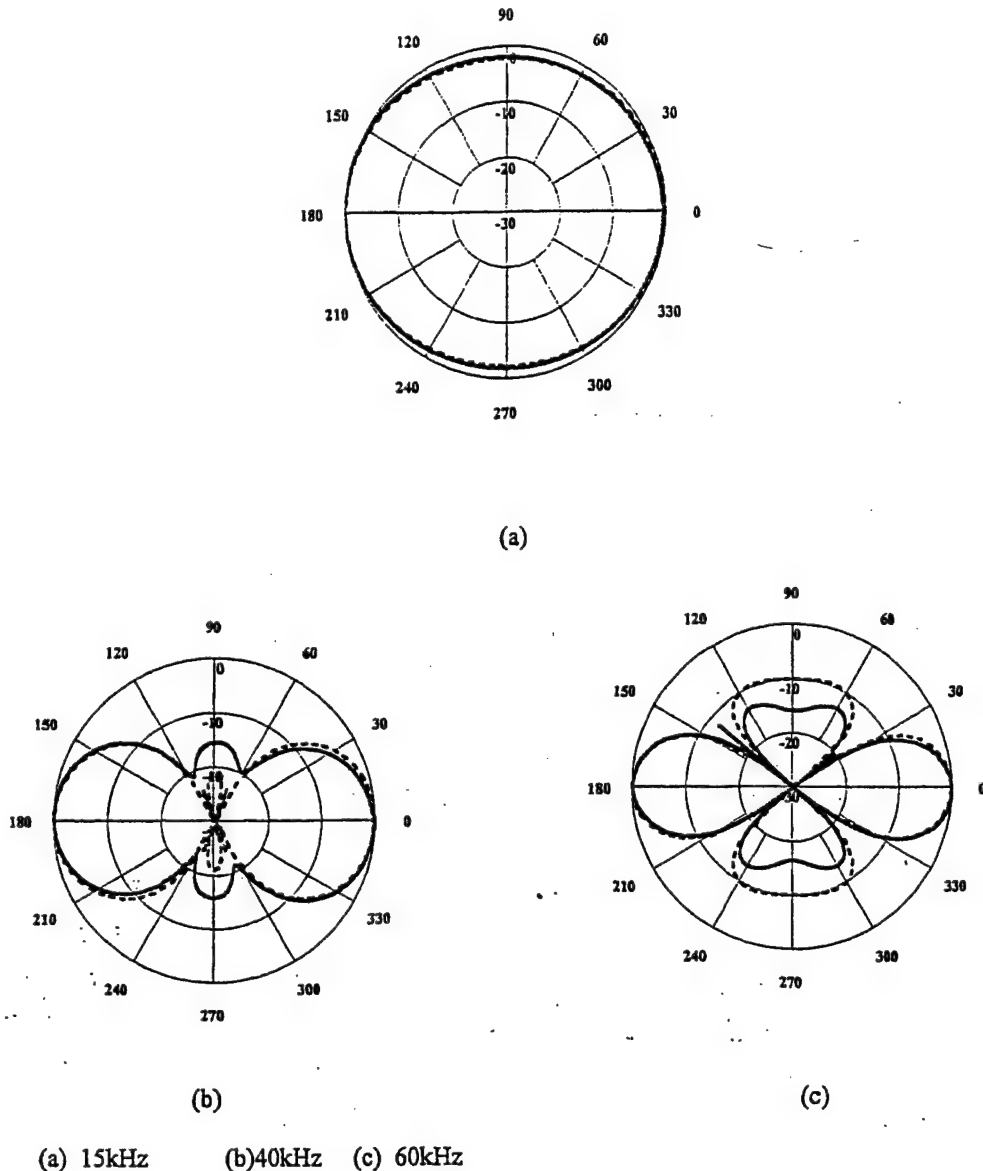
(a)

(b)

(c)

(a) 15kHz   (b)40kHz   (c) 60kHz

Fig. 5. Beam patterns of the potted 3 × 3 array (—: measured; - - -: calculated).

transducer. Due to the increase in radiation compared to a single transducer, the velocities of all three groups were smaller than that of a single cymbal transducer with no acoustic loading. The Group A transducer has the smallest velocity since it has more surrounding transducers than the other groups and 'feels more acoustic loading'. Another consequence of this mutual radiation resistance in the array is the much higher efficiency of an individual cymbal transducer. This is shown in Fig. 11. The array has an efficiency over 30% for this small array, compared to the very small efficiency of the single cymbal transducer.

Fig. 12 shows the normalized velocity of the Group A transducer plotted as a function of spacing between elements. At a spacing of 15 mm. the velocity of the Group A transducer in the array is only 10% of that of

a single transducer, indicating a strong acoustic interaction at a small spacing. Although the strong interaction at this spacing results in small TVR values around resonance frequency, it flattens the transmit response of the array, as shown in Fig. 13. As the spacing increases, the normalized velocity variations among the three group transducers decrease and approach unity, indicating less array interaction. As a result of this, the predicted peak value of the 3 × 3 array increases at the cost of losing the flat TVR response.

5. Conclusions

In assembling arrays, care must be taken not to introduce additional mechanical boundary conditions.
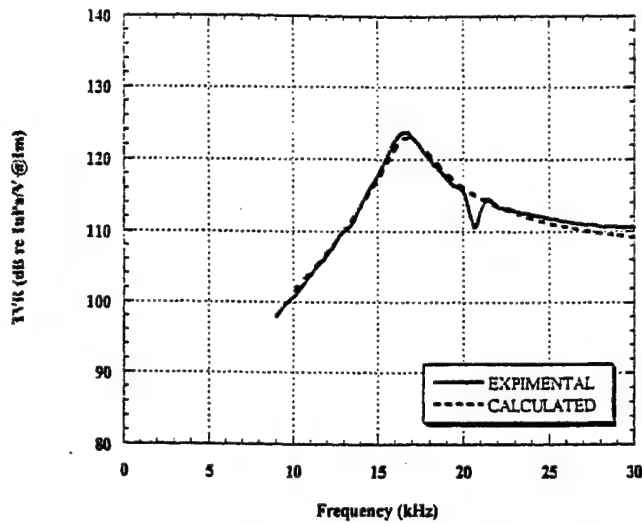
Fig. 6. Calculated and experimental transmitting voltage response of a single cymbal transducer from the equivalent circuit model.
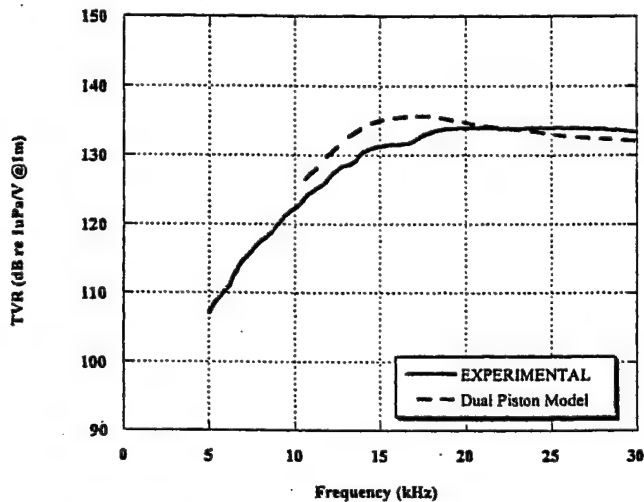

Fig. 9. Normalized radiation resistance of the transducers in the 3×3 array.

Fig. 7. Calculated transmitting voltage response of the potted 3×3 array using the equivalent circuit model.
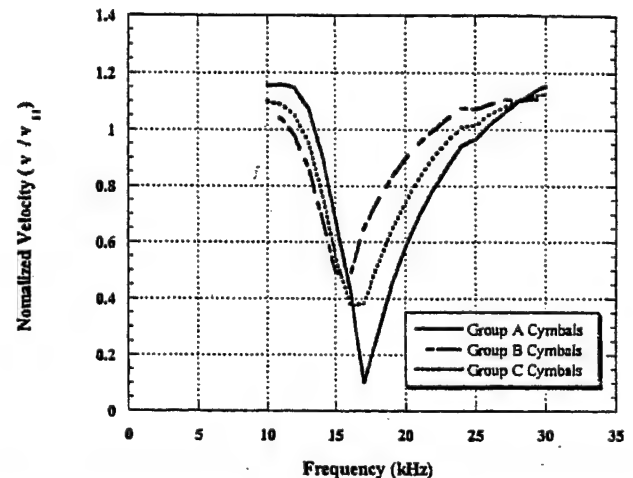
Fig. 10. Normalized velocity of transducers in the array, depending on their surroundings.

The direct potting technique of mounting cymbal transducers in the array does not complicate the mechanical boundary conditions of the transducer in the array and gives more predictable beam patterns. The TVR for the direct potted array exceeds 134 dB re 1 μPa/V @1 m and is flat over the frequency range of interest. A simple equivalent circuit model was successfully used to analyze the array interaction in a small square array. The velocities of the transducer decrease significantly near
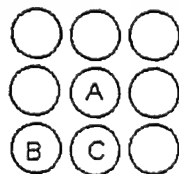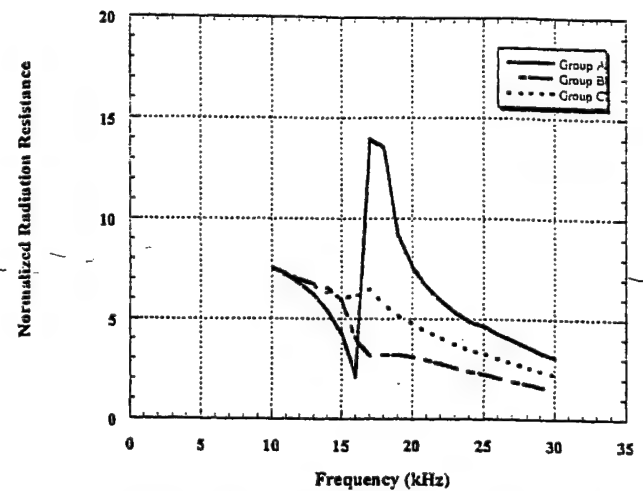

Fig. 8. Group A, B, C transducers in the array.

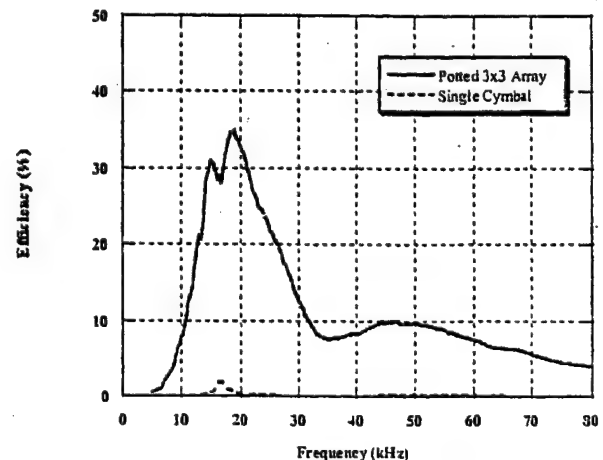

Fig. 11. Measured efficiency of a single cymbal transducer and of the potted 3×3 array.
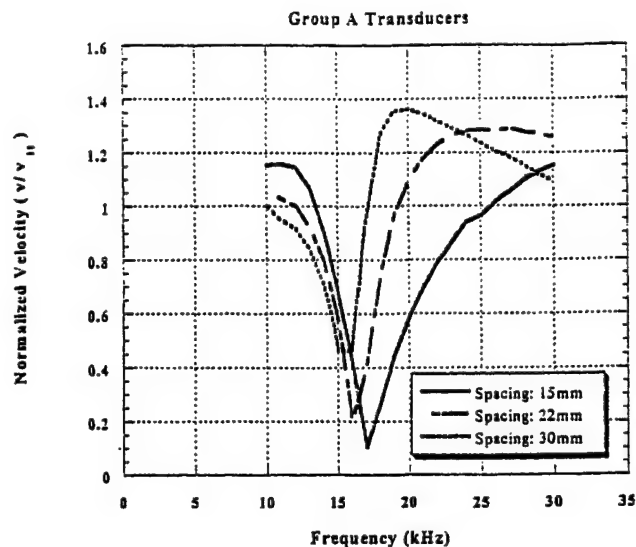
Group A Transducers

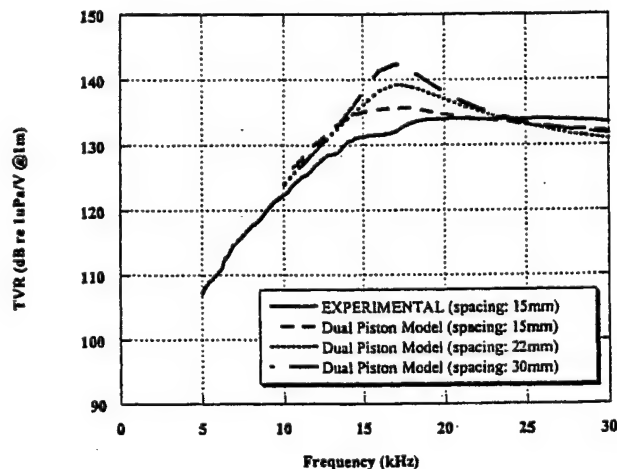Fig. 12. Normalized velocity of group A transducers as a function of frequency and spacing.

Fig. 13. Calculated transmit voltage response of a 3×3 array as a function of center to center spacing.

resonance compared to a single element, depending on the spacing between the elements and their surroundings. The array interaction works to its advantage in the sense that it flattens the transmit response around the resonance frequency, and, more importantly, it enhances the efficiency of the array.

Acknowledgements

References

[1] A. Dogan, Ph.D. thesis, The Pennsylvania State University, 1994.
[2] R.E. Newnham, Q.C. Xu, S. Yoshikawa, Metal electroactive ceramic composite actuators, US Patent, 5,276,657, 4 January 1994.
[3] K.D. Rolt, J. Acoust. Soc. Am. 87 (1990) 1340.
[4] Aydin Dogan, IEEE Trans. UFFC 44 (1997) 597.
[5] J.F. Tressler, R.E. Newnham, W.J. Hughes, J. Acoust. Soc. Am. 105 (1999) 591.
[6] B.F. Hamonic, O.B. Wilson, J.-N. Decarpigny, J.-N. Decarpigny, B. Hamonic, O.B. Wilson Jr. (Eds.), IEEE J. Oceanic Eng. 16 (1991) 107.
[7] C.H. Sherman, IEEE Trans. Sonics Ultrasonics SU 13 (1) (1966) 9.
[8] C. Audoly, J. Acoust. Soc. Am. 89 (1991) 1428.
[9] R.L. Pritchard, J. Acoust. Soc. 32 (1960) 730.
[10] J.L. Butler, User Manual for the Program ARRAY, Image Acoustics, Inc., Cohasset, MA 02025, 1990.
[11] J.D. Zhang, W.J. Hughes, P. Bouchilloux, R.J. Meyer Jr., K. Uchino, R.E. Newnham, Ultrasonics 37 (1999) 387.

APPENDIX 40

A miniature class V flextensional cymbal transducer with directional beam patterns: the double-driver

J. Zhang [a,*], A.C. Hladky-Hennion [b], W. Jack Hughes [c], R.E. Newnham [a]

[a] *Materials Research Laboratory, The Pennsylvania State University, University Park, PA 16802, USA*
[b] *IEMN-Department I.S.E.N., 41 Boulevard Vauban, 59046 Lille, France*
[c] *Applied Research Laboratory, The Pennsylvania State University, University Park, PA 16802, USA*

Abstract

The "double-driver" cymbal, a directional class V flextensional transducer, is described in this paper. Its basic structure is a bilaminar piezoelectric disk with metal caps as mechanical transformers and amplifiers. The directivity was accomplished by exciting the double-driver in a combined flexural and bending mode causing the sound pressure to add in one direction and cancel in the opposite direction. The cardioid beam pattern predicted by finite element modeling agreed well with the experimental measurements. A 3×3 double-driver array was constructed to demonstrate that under optimal conditions the array can provide a directional beam pattern with a front-to-back ratio of more than 20 dB. © 2001 Elsevier Science B.V. All rights reserved.

1. Introduction

Flextensional transducers were first developed in the 1920s and have been used as underwater transducers since the 1950s [1]. They consist of an active piezoelectric or magnetostrictive drive element and a mechanical shell structure. The shell is used as a mechanical transformer which transforms the high-impedance, small extensional motion of the ceramic into a low-impedance, large flexural motion of the shell. According to the shape of the shell, flextensional transducers have been divided into seven classes [2]. During the past decade, two miniaturized versions of the class V flextensional transducer, called the moonie and cymbal were developed at the Materials Research Laboratory at the Pennsylvania State University [3,4]. The moonie and cymbal are small in size, similar to common coins in appearance, with a thin profile and small weight. Most important of all, their bonding and fabrication process are very simple, which makes them inexpensive and easy to mass-produce.

The moonie and cymbal transducers consist of a piezoelectric ceramic disk poled in the thickness direction and sandwiched between two metal end caps. The caps contain a shallow cavity under their inner surface. The presence of the cavities allows the caps to convert and amplify the small radial displacement of the disk into a much larger axial displacement normal to the surface of the caps. When operated underwater this contributes to a much larger acoustic pressure output than would occur in the uncapped ceramic.

The standard moonie and cymbal transducers, along with all other types of flextensional transducers, are generally small compared to the wavelength of sound in the usable frequency range, usually near their first resonance frequency. In addition, most of the radiating surface area of the shells moves in phase, thus the resulting acoustic radiation pattern is nearly omnidirectional resembling an acoustic monopole. The omnidirectional characteristics of flextensional transducers create significant problems in projection transducers and arrays designed to transmit in one direction. At the present time, large baffles are used, or rows of transducers are carefully arranged and phased, to produce the desired beam patterns. This is expensive, time-consuming and cumbersome. To overcome this problem

* Corresponding author. Tel.: +1-814-862-8461; fax: +1-814-865-2326.
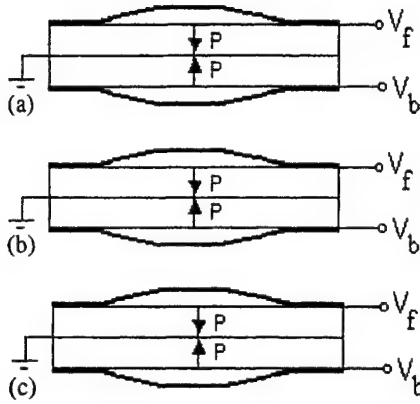*E-mail address:* jindongzhang@hotmail.com (J. Zhang).

Fig. 1. The driving schemes of the double-driver cymbal transducer. (a) Monopole (in phase, same amplitude), $V_b = V_f = V_m$, $\varphi = 0$. (b) Dipole (out of phase, same amplitude), $V_b = -V_d$, $V_f = V_d$, $\varphi = \pi$. (c) Cardioid, $V_b/V_f = (1-R)/(1+R)$, where $R = \mathrm{TVR_m/TVR_d}$, $0 < \varphi < \pi$.

a method has been proposed to generate a directional beam from a class IV flextensional transducer by exciting both an extensional mode and the a bending mode simultaneously [5].

This same idea has been incorporated in the double-driver cymbal described in this paper. A prototype model was constructed from two PZT disks poled through the thickness and bonded together with opposite polarization to form a common ground. Then the back-to-back transducers were sandwiched between two metal caps. To shape the beam pattern, the outer electrodes are driven with different voltages and phases as illustrated in Fig. 1.

2. Principle of operation

A directional beam pattern was achieved through the cancellation of sound pressure in one direction (back side) and addition in the opposite direction (front side). This is accomplished by exciting the double-driver in a combined flexural and bending motion.

When the two sides of the double disk are driven in phase with the same electric field ($V_b = V_f$) as shown in Fig. 1a, a pure flextensional mode is excited, and a near omnidirectional beam pattern (monopole) is obtained. To excite the dipole mode (bending mode of the double-driver), the two transducers are driven with the same electric field but with a phase difference of 180° (Fig. 1b).

In the dipole mode (bending mode) of the double-driver cymbal, the transmit voltage response (TVR) showed two maxima in opposite directions (front and back), but the phase of the TVR output from one lobe is opposite to that from the other. When combined with the omnidirectional mode, this can be used to generate a

directivity pattern which has only one maximum. If the output from the dipole mode is added to the output from a monopole of equal transmitting voltage response, the resulting beam pattern is a cardioid curve with a single maximum [6]. The cancellation procedure follows the method outlined in Ref. [5].

The complex drive conditions shown in Fig. 1c combine the two modes to obtain the directional mode. V_f is the electric field on the front side (up) and V_b represents the electric field on the back side (down). V_m and V_d are the driving fields associated with the monopole and dipole drive conditions.

$$V_f = V_m + V_d \tag{1}$$

$$V_b = V_m - V_d \tag{2}$$

$$\frac{V_b}{V_f} = \frac{1-r}{1+r} \tag{3}$$

where $r = V_d/V_m$.

TVR is related to the voltage by $\mathrm{TVR_b} = p_b/V_b$ and $\mathrm{TVR_f} = p_f/V_f$, where p is the measured sound pressure. To cancel the sound pressure completely in the back side, the pressure amplitudes should be equal, leading to

$$\frac{V_b}{V_f} = \frac{1-R}{1+R} \tag{4}$$

where $R = \mathrm{TVR_m/TVR_d}$.

The complex ratio R is determined from the measured monopole and dipole constant voltage transmitting responses. The equation gives the ratio of the voltages and the phase lag φ on each side of the double-driver cymbal.

3. Computer simulation

The finite element analysis code ATILA was used in modeling the performance of the double-driver cymbal transducer. ATILA was developed at the Acoustics Department at Institut Superieur d'Electronique du Nord (ISEN) to model underwater transducers and has been used successfully in the simulation of flextensional transducers [7]. Modal analysis was carried out to determine the vibration modes, their resonance and anti-resonance frequencies, and associated coupling factors. Through harmonic analysis, the in-air and in-water impedance and displacement field can be computed as a function of frequency, together with the TVR, free field voltage sensitivity and the directivity patterns. In this study, ATILA was primarily used to determine the vibration modes and calculate the TVR and beam pattern of the double-driver cymbal transducers.

Fig. 2 shows the calculated modes of the double-driver cymbal transducer under different driving conditions. In the monopole mode, the two caps vibrate in
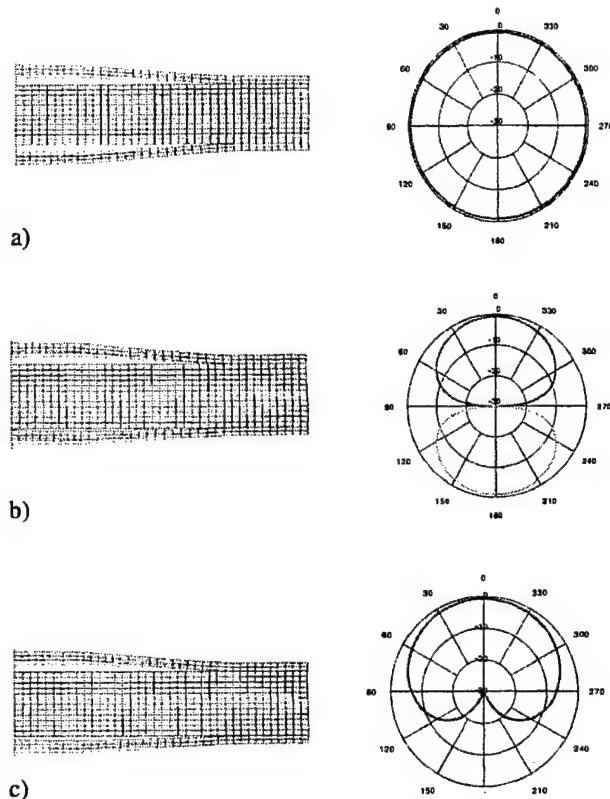
a)

b)

c)

Fig. 2. The vibration modes and predicted beam patterns by ATILA for a double-driver cymbal transducer. (a) Monopole mode; (b) dipole mode; (c) cardioid mode, $V_b/V_f = (1 - R)/(1 + R)$, where $R = TVR_m/TVR_d$.

Table 1
Driving voltages and phases for the directional mode at 20 kHz

	V_f		V_b	
	Amplitude	Phase (degree)	Amplitude	Phase (degree)
ATILA	100	0	73.8	51
Experimental (calculated)	100	164	78	0
Experimental (adjusted)	100	166	72	0

and a diameter of 12.7 mm. The PZT disks were poled in the thickness direction. The PZT disks were first ground with sand paper to remove the oxide layer and then cleaned with acetone. Using conductive epoxy, the PZT disks were then bonded together in pairs with opposite polarization directions.

Titanium caps were punched from Ti foil of 0.25 mm thickness and shaped using a special die. The shaped caps had a diameter of 12.7 mm. The cavity diameter was 9.0 mm at the bottom and 3.2 mm at the top. The cavity depth was 0.2 mm. The flanges of the Ti caps were slightly roughened using sand paper. The caps were then bonded to the piezoelectric ceramic double-driver cymbals. The bonding material is an Emerson and Cuming insulating epoxy. A ratio of three parts 45 LV epoxy resin to one part 15 LV hardener was used. The thickness of the epoxy bonding layer was approximately 20 μm. The entire assembly was kept under uniaxial stress in a special die for 24 h at room temperature to allow the epoxy time to cure.

Underwater calibration tests of single cymbals were performed at the Applied Research Laboratory at Pennsylvania State University. The tank measures 5.5 m in depth, 5.3 m in width and 7.9 m in length. A pure tone sinusoidal pulse signal of 2 ms duration was applied to the test transducer and its acoustic output was monitored with a standard F33 hydrophone. The test transducer and the standard were positioned at a depth of 2.74 m and separated by a distance of 3.16 m. The double-dipper transducers were potted with a polyurethane coating about 0.5 mm thick. The polyurethane layer insulated the cymbal from the conductive water in the water tank. The measured parameters were the mechanical Q, TVR and beam pattern.

phase, and indeed the beam pattern was predicted to be omnidirectional as shown in Fig. 2(a). In the dipole mode, the two caps vibrate out of phase, and the predicted beam pattern Fig. 2(b) is a dipole with two maxima in the front and back directions. The amplitude was the same in the two directions but there was a phase difference of 180°. The TVR amplitudes and phases for the two cases at 20 kHz were also calculated by ATILA, from which the driving conditions for the cardioid mode were calculated using Eq. (1). The driving voltages and phases in ATILA modeling at 20 kHz for the cardioid mode are listed in Table 1 and the corresponding vibration mode is shown in Fig. 2(c). The two caps vibrate with a phase difference, which adds the sound pressure in the forward direction and subtracts in the back direction, thereby producing the desired cardioid beam pattern. The pattern predicted by ATILA is shown in Fig. 2(c).

4. Experimental procedure

The piezoelectric ceramic disks (PKI 552, Piezokinetics Inc., Bellefonte, PA) have a thickness of 1 mm

5. Experimental results and discussion

The double-driver cymbal was first tested in the monopole and dipole modes. The TVR including amplitude, phase and beam pattern were measured at 20 kHz. The measured beam patterns are shown in Fig. 3. A nearly omnidirectional and a dipolar beam pattern
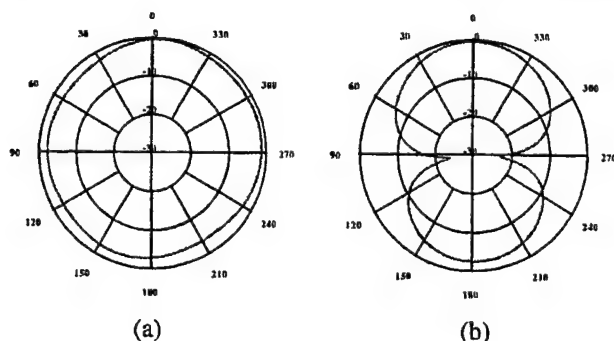
Fig. 3. Measured beam pattern of (a) monopolar mode ($V_f = V_b$, $\varphi = 0$), (b) dipolar mode ($V_f = V_b$, $\varphi = \pi$).

achieve unidirectional beam patterns must be obtained experimentally.

We have demonstrated that a directional beam pattern can be obtained from a double-dipper transducer which is much smaller than a wavelength. With this method, a directional pattern can be obtained at virtually any frequency. However, the TVR amplitude and phases of the double-dipper fluctuates drastically with frequency. As a consequence, the calculated voltage ratios (amplitude and phase) at different frequencies are drastically different, suggesting unique driving conditions at each frequency or a narrow working bandwidth.

were obtained for the monopole and the dipole mode. They agreed well with the ATILA prediction. The driving voltages and phases for the cardioid mode at 20 kHz were calculated from the measured TVR amplitudes and phases for the monopole and dipole case according to Eq. (1) and the values are listed in Table 1. The resulting experimental beam pattern is shown in Fig. 4(a). It is not a perfect cardioid pattern but shows a very directional beam shape. When the driving amplitude and the phase of the back side were adjusted slightly, a nearly perfect cardioid beam pattern shown in Fig. 4(b) was obtained.

The experimentally obtained driving conditions for the cardioid pattern is shown in Table 1 and compared with ATILA computation. The voltage amplitude calculated from ATILA agrees well with the experimental data. However, the calculated phase is significantly different from experimentally obtained values. It is obvious that ATILA can predict the TVR amplitude of the double-driver very well. But the phase of the TVR is complicated by many experimental factors and therefore difficult to predict. Hence, the driving conditions to
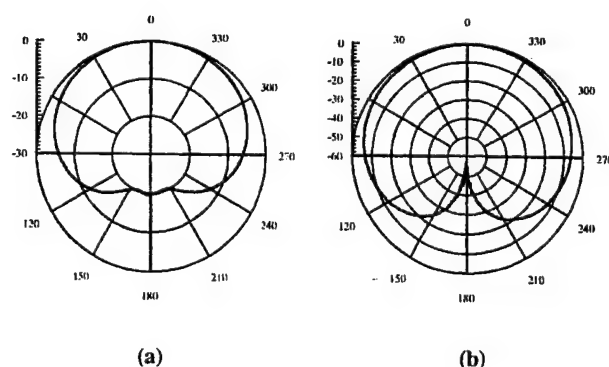

(a)

(b)

(c)

Fig. 5. Measured directional beam patterns of the 3 × 3 double-dipper array at (a) 15 kHz, $V_f = 100$ V, $V_b = 55$ V, $\varphi = 237°$, (b) 20 kHz, $V_f = 100$ V, $V_b = 38$ V, $\varphi = 268°$, (c) 80 kHz. $V_f = 98$ V, $V_b = 100$ V, $\varphi = 332°$.

(a)

(b)

Fig. 4. Measured cardioid pattern: (a) driving voltage calculated according to Eq. (1), $V_f = 100$ V, $V_b = 78$ V, $\varphi = 164°$; (b) driving voltage adjusted to: $V_f = 100$ V, $V_b = 72$ V, $\varphi = 166°$.

This may complicate the driving electronic circuits if the double-dipper is used over a wide frequency range.

A 3×3 planar array of the double-driver was built using the same potting technique and tested without a baffle. It was found that Eq. (4) cannot be used for predicting the driving conditions for the array. The difficulty is most probably caused by array interactions. Because of array interaction, the vibration velocity and phase vary for individual transducers in the array, which complicates the driving conditions. Therefore, the driving voltage and phases for the array were adjusted manually to obtain the desired directivities. The resulting beam patterns of the arrays at 15, 20 and 80 kHz are shown in Fig. 5. In all cases, a front to back ratio of above 20 dB is obtained.

6. Conclusions

A directional class V flextensional transducer is proposed which makes use of the bending mode of a bilaminar ceramic plate. It maintains the advantageous features of conventional cymbal transducers, including thin profile, small size and low cost, while introducing a new mechanism to project sound in one direction. The double-driver cymbal transducer is a promising candidate as directional underwater sound projectors in conformable arrays mounted on underwater vehicles.

References

[1] K.D. Rolt, History of the flextensional electroacoustic transducers, J. Acoust. Soc. Am. 87 (1990) 1340.
[2] W. Jack Hughes, Encyclopedia of Applied Physics, vol. 22, Wiley–VCH, New York, 1998.
[3] Q.C. Xu, S. Yoshikawa, J.R. Belsick, R.E. Newnham, Piezoelectric composites with high sensitivity and high capacitance for use at high pressures, IEEE Trans. UFFC 38 (1991) 634–639.
[4] A. Dogan, K. Uchino, R.E. Newnham, Composite piezoelectric transducers with truncated conical endcaps 'Cymbals', IEEE Trans. UFFC 44 (1997) 597–605.
[5] S.C. Butler, J.L. Butler, A.L. Butler, G.H. Cavanagh, A low frequency directional flextensional transducer, J. Acoust. Soc. Am. 102 (1997) 308–314.
[6] D. Stansfield, Underwater Electroacoustic Transducers, Bath University Press and Institute of Acoustics, 1990.
[7] B. Hamonic, J.C. Debus, J.-N. Decarpigy, D. Boucher, B. Tocquet, Analysis of a radiating thin-shell sonar transducer using the finite element method, J. Acoust. Soc. Am. 86 (1989) 1245–1253.

APPENDIX 41

Flextensional Transducers with Shape Memory Caps for Tunable Devices

R. J. MEYER, JR.* AND R. E. NEWNHAM

The Pennsylvania State University, 254 Materials Research Laboratory, University Park, PA 16802

ABSTRACT: Shape memory alloys were used as caps for the "cymbal" flextensional transducer. The active caps provide a tunable resonance frequency and a damage recovery mechanism associated with the alloy's martensitic phase transformation. These two concepts were investigated and a 25% change in resonance frequency was observed for Ni-Ti alloy caps. It was also demonstrated that complete shape recovery could be achieved after hydrostatic pressures buckled the transducer caps. Cap deformation and recovery were demonstrated with profilometer and d_h measurements.

INTRODUCTION

ELECTROACOUSTIC transducers, converting electrical energy into acoustic energy and vice versa, are the fundamental sound sources in sonar and ultrasound systems. Many types of these transducers have been developed during the last century beginning with the discovery of the piezoelectric effect in 1880. Longitudinal vibrators, flexural disks, moving coils, and spherical shells are a few of the many device configurations used to generate and detect ultrasound. One of the main underwater transducer designs for low frequency applications is the flextensional transducer. Utilizing a piezoceramic acting on a flexing shell, these transducers magnify the motion of the driving element providing higher power outputs than flexural disks. Past improvements in the performance of the flextensional transducers have come at the expense of increased complexity and production costs. Two miniature flextensional transducers, the "Moonie" and "Cymbal," were developed at Penn State to reduce cost and size and are now being tested for use in underwater arrays.

The moonie and cymbal designs, shown in Figure 1, consist of a poled piezoelectric disk bonded to metal end caps having specially designed geometries to accommodate an air cavity between the metal and ceramic (Sugawara et al., 1992; Newnham, Xu and Yoshikawa, 1991; Dogan et al., 1994; Dogan and Newnham, 1998). Increased sensitivity and amplified motions are obtained with these devices due to the conversion of radial stresses into large axial motions. With the moonie and cymbal, improvements in the piezoelectric figure of merit were found to be greater than 250 times larger than uncapped lead zirconate titanate (PZT) (Dogan et al., 1994). Additionally, a large displacement of 40 μm @ 1 kV/mm (compared to 1 μm @ 1 kV/mm for uncapped PZT) with reasonable generative force (approx. 20 N) was obtained for the cymbal. Moonies and cymbals are suitable for many actuator applications and help to bridge the gap between the high-force, low-displacement multilayer structures and the high-displacement, low-force bender type actuators. Compact and inexpensive moonie and cymbal hydrophones have also found many applications including towed undersea arrays, fish finding, underwater imaging and geophysical research.

Ease of fabrication and the ability to tailor performance to the desired application are attractive features of the cymbal design. Resonance frequency, force, displacement and response times of this structure are controlled through the choice of the cap and driver materials, together with the geometry and overall dimensions, thereby accommodating this design to numerous applications. Resonance frequencies have been tailored between 1 kHz to over 100 kHz.

Normally the caps are punched from standard metals such as brass or steel, but in this study we have replaced the passive metal caps with Nitinol shape memory alloys (Buehler, Gilfrich and Wiley, 1963). These "smart" materials provide tunable mechanical properties by utilizing the martensite to austenite phase transformation in which significant changes in elastic modulus take place (SMA-Inc., 1999). A change in modulus can alter the resonant frequency, the speed of sound, and improve acoustic impedance matching. The smart caps also provide additional control of the force and displacement characteristics of the actuator by adjusting cavity depth, cap modulus and even provide cap shape restoration through the shape memory effect. Materials such as Nitinol and both magnetostrictive Metglass™ (METGLAS) and Terfenol-D (Clark and Belson, 1971) can be explored for use as active caps. Ni-Ti shape memory alloys were used here to demonstrate the potential usefulness of active caps.

Shape Memory Effect

The shape memory effect was first discovered in Au-Cd alloys in 1951 (Chang and Read, 1951). Subsequent investi-

---

*Author to whom correspondence should be addressed. E-mail: rmeyer@psu.edu

METGLAS is a registered trademark of the Allied Corporation.
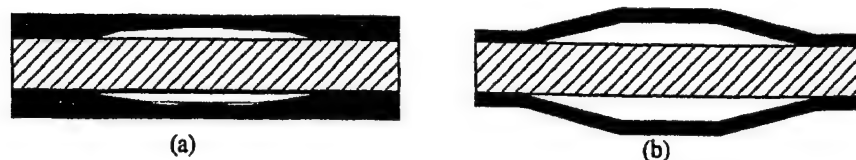
Figure 1. Schematic structure of (a) Moonie and (b) cymbal flextensional transducers. The "driver" (hatched area) and the punched metal caps (solid area) have typical dimensions of 12 mm in diameter and 2 mm thick. Cymbal cap geometry used here was: 320 μm cavity depth, 3 mm dome and a flange width of 1.85 mm.

gations of the Ni-Ti system unearthed the enormous potential of this class of materials in commercial applications (Buehler, Gilfrich and Wiley, 1963). Nitinol, so named for its elemental constituents and founding institution, the Naval Ordnance Laboratory, was found to be particularly useful because of the ease of controlling its martensite to austenite phase transition through small variations in the Ni to Ti ratio. The transition temperature can be adjusted between –200° and 110°C (SMA-Inc., 1999). Other systems exhibiting the shape memory effect or superelasticity, which is also closely related to the martensitic phase transition, include In-Tl, Cu-Zn, Cu-Al-Ni, Fe-Pt, and Fe-Mn-Si alloys (Shimizu and Tadaki, 1987).

The origins of the shape memory effect can be traced to the alloy's crystal structure and the martensitic phase transformation. This phase transformation is diffusionless with atoms moving cooperatively through shear-like mechanisms (Shimizu and Tadaki, 1987). The high temperature austenite phase, or parent phase, is usually cubic with substantial long range order. The low temperature martensite phase has a lower symmetry. The martensite phase essentially consists of twin-related, self-accommodating variants of the high temperature phase. Stressing the material promotes the transformation of some of the variants in the stressing direction either by twinning or de-twinning. During the reverse transformation, the martensite becomes unstable and the crystal structure reverts to the parent phase through a displacive transformation in which the macrosopic strain is recovered. The driving force for this reverse transformation is the difference in chemical free energy between the austenite and the martensite phases. In the case of NiTi alloys, the maximum recoverable strain is approximately 8% (SMA-Inc., 1999). Two-way shape memory can be achieved by "training" the material using cyclic heating and cooling. Training results in the generation of internal stresses, which inhibits self-accommodation thereby reducing the number of possible variants.

In addition to the changes in mechanical properties, the phase transition is also accompanied by changes in thermal conductivity, the coefficients of thermal expansion, and electrical resistivity. Property changes occurring during the austenite-martensite phase transition are usually hysteretic in nature. This hysteresis defines four characteristic temperatures: the austenite start and finish temperatures and the martensite start and finish temperatures.

Young's modulus for NiTi alloys has been reported as highly nonlinear, ranging from 28 to 41 GPa in the martensite phase up to 60 to 90 GPa in the austenite phase (SMA-Inc., 1999). This large change in elastic stiffness together with shape recovery can be exploited in the design of a tunable resonance transducer with impedance matching caps and thermally activated healing.

Tunable Transducers

The idea of tuning a transducer is not a new concept. Several attempts have been made using a liquid backing to adjust the effective thickness of the transducer (Fry, Fry and Hall, 1951; Lanina, 1978). Other researchers have focused on the elastic modulus and its contribution to the resonance frequency. Using the nonlinear elastic properties of rubber and the mechanical bias provided by a stress bolt, a tunable Langevin-type transducer has been explored previously (Blaszkiewicz, 1994; Newnham, Xu and Blaszkiewicz, 1992). Various means of applying mechanical bias were studied with changes in the resonance frequency as large as 200% but the results were difficult to reproduce because of relaxation and permanent deformation in the elastomers. Relaxor ferroelectrics are electrically nonlinear and when combined with rubber add the possibility of using an electrical bias to tailor resonant frequency, acoustic impedance, damping factors and electromechanical coupling coefficients (Newnham, 1991). Previous attempts at combining ferroelectric oxides and shape memory alloys were first explored by depositing sol-gel thin films of PZT onto a shape memory substrate (Blaszkiewicz, 1994; Chen et al., 1992). Several others followed with hopes of achieving a ferroelastic-ferroelectric heterostructure for active damping applications (Mercado and Jardine, 1994). Combinations of these two materials offer a wide range of sensing and actuating possibilities.

The two effects demonstrated in this work are a tunable resonant frequency and a shape recovery or healing mechanism. The active caps made use of the shape memory effect and the temperature dependent elastic properties of Ni-Ti.

Generally, the flextensional resonant frequency is proportional to:

$$f \propto \sqrt{\frac{E}{\rho(1-\sigma)}} \qquad (1)$$

where E is the modulus, ρ is the density and σ is Poisson's ratio (Tressler, 1997). Active caps provide a way of thermally controlling the elastic properties of the composite, and tuning the resonant frequency. Thermally controlled shape change or shape recovery offers two additional applications. For a flextensional transducer, a change in cavity depth by a factor of two has the potential of changing the resonant frequency by more than 30% (Tressler, 1997). Shape recovery also allows transducers with damaged caps to be reused. Modeling of the behavior of these caps allows for application-oriented design of these composite structures.

EXPERIMENTAL PROCEDURE

Cymbal Fabrication

Ni-Ti sheet material was obtained (Alloy B; SMA-Inc.). The SMA sheet was 250 μm thick with an austenite finish temperature between 20° and 40°C. The austenite finish temperature is highly variable and is a function of composition and annealing conditions. Half-inch diameter blanks were cut from the sheet using a hardened steel punch. Two caps were polished to 200 μm thick samples for comparison with standard cymbals. The cymbal shape, illustrated in Figure 1(b), was formed from the blank using machined carbon dies at 500°C for 30 minutes and 30 MPa of pressure. Pressure was maintained throughout the cooling process. Shape setting was conducted under argon atmosphere to prevent oxidation of the carbon dies. Each cap was fabricated with a 320 μm cavity depth, 3 mm top and a flange width of 1.85 mm.

The surface of the flange and piezoceramic were roughened with 600 grit sandpaper to enhance bonding. The lead zirconate titanate ceramics used for these sets of experiments were Navy Type VI (PKI 552; PiezoKinetics Inc.). The ceramic was 12.7 mm in diameter and 1 mm thick. The epoxy used to bond the caps to the ceramic was Emerson and Cuming Epoxy. A ratio of three parts 45LV epoxy resin to one part 15LV resin hardener was used. Bonding was carried out using a screen-printed epoxy layer. During bonding, the ceramic and caps were clamped and the epoxy was allowed to cure in air at 60°C for a minimum of 4 hours.

Cymbal Characterization

The flextensional composites were evaluated using a Hewlett-Packard 4194a Impedance/Gain Phase analyzer to observe the resonance frequency spectrum. The transducers were mounted in a sample holder in which the spring-loaded probes clamp only the flange. The sample holder was modified for recording temperature measurements by allowing a thermocouple to be positioned in close proximity to the sample. Resonance frequency was measured as a function of temperature inside a computer-controlled oven (Delta Design; model 9023). The temperature was adjusted in 5° or 10° increments from –5° to 80°C. Data were collected two min-

utes after the internal thermocouple reached the desired temperature.

To demonstrate the shape recovery mechanism, the transducers were subjected to hydrostatic pressure. The hydrostatic piezoelectric coefficient, d_h, was monitored with reference to a known standard made from monolithic Ca-doped lead titanate. The primary source of failure for the cymbal flextensional transducer under hydrostatic pressures is cavity collapse and is observed as a significant decrease in d_h with more than 20% of the original value irrecoverable (Tressler, 1997). Pressure tolerances depend on cavity depth, cap modulus, and cap thickness.

For testing, the sample and standard were placed in hydraulic fluid inside a hydrostatic pressure vessel. A weak 30 Hz pressure wave is transmitted through the fluid surrounding the sample. The short circuit current from the sample is converted to an equivalent voltage that is monitored by an oscilloscope. Specific details of the test setup have been previously reported (Tressler et al., 1995). Comparison of the voltage of the standard to the sample allows for the calculation of the sample's hydrostatic piezoelectric coefficient through the equation:

$$d_h = \left(\frac{V_{samp}}{V_{std}} \right) \left(\frac{A_{std}}{A_{samp}} \right) d_h^{std}$$

where V is the voltage and A is the area. The sample was remeasured several times to determine its behavior after being subjected to damaging pressures.

Modeling

Finite element modeling was used to simulate the response of the transducer. A half section of the cymbal transducer was modeled with ATILA finite element code. Since the SMA modulus values are highly dependent on material annealing, estimates of the modulus were determined by adjusting input values until the simulated curves matched the observed response. A simple composite model was utilized to reduce computation time.

RESULTS AND DISCUSSION

Resonance Frequency Tuning

Shape memory caps were successfully formed in the austenite phase, and on cooling through the transition, the cymbal shape was retained. Bending the cap and reheating using a hot plate verified the austenite shape setting and the recovery mechanism. Three cymbal transducers were constructed, two with 250 μm thick caps and one with 200 μm thick caps. The admittance spectra for these samples showed the fundamental flextensional resonance frequencies near 25 kHz. No spurious modes were observed indicating uniform bonding.
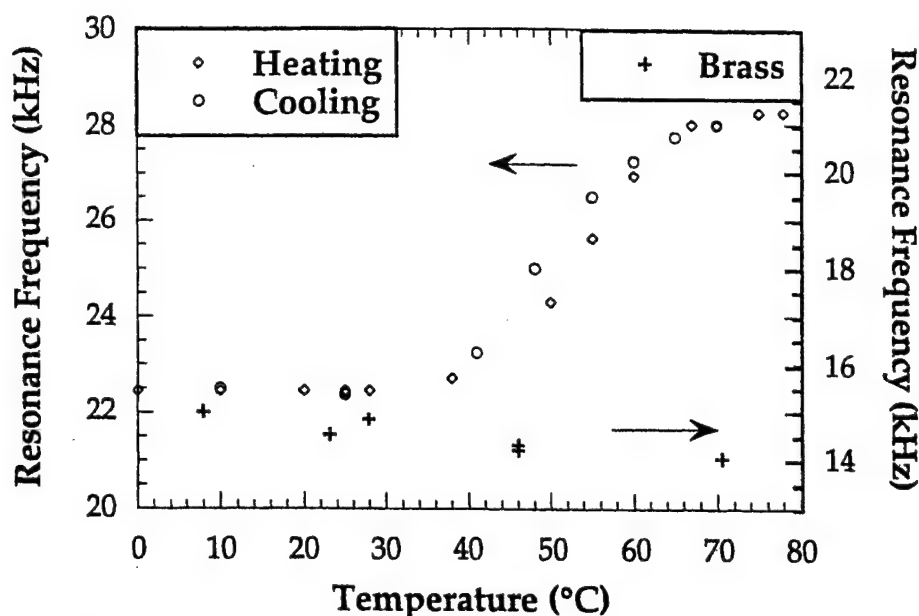
Figure 2. *Flextensional resonance frequency for a cymbal with shape memory caps plotted as a function of temperature for a heating and cooling cycle. A comparison to a brass capped cymbal is also shown.*

To observe the shift in resonance with the change in modulus of the cap material, the resonance frequency was monitored as a function of temperature. The results of this experiment for the 200 μm thick caps are shown in Figure 2. Contrary to most materials, shape memory alloys stiffen as the temperature increases. The flextensional resonance frequency was observed to be approximately 22.5 kHz in the martensite phase and increased to 28.3 kHz in the austenite phase, a total increase of 25.5%. The plot clearly shows the hysteretic nature of the transition. Based on the cooling curve, the austenite finish temperature was observed to fall within the designated range (20° to 40°C) for this material. The martensite finish temperature was approximately 70°C.

The observed hysteresis was reproducible over several cycles when maintaining identical measurement procedures. During heating, if the sample was allowed to equilibrate for longer times, the resonance frequency would shift by traversing the loop to the cooling cycle value. This frequency stabilized after 30 minute dwell times. This stability region is the result of the phase transformation mechanism in which a predictable percentage of conversion takes place. This percent conversion is reproducible and is dependent on the material's processing history.

To compare these frequency changes with those associated with normal thermal expansion, heating experiments were repeated using brass and titanium capped cymbal transducers. Both of these transducers showed a decrease in resonance frequency with 7% and 2% reductions for brass and titanium capped cymbals, respectively over the same temperature range. The behavior of each sample was reproducible over several heating and cooling runs.

ATILA finite element modeling was used to model the observed response. The values of SMA modulus needed to simulate the martensite and austenite resonance frequencies were 40 and 70 GPa, respectively, which fall within the expected range for this material.

Although the change in resonance frequency was significant, it was expected that even larger increases could be achieved. Variations in annealing conditions and variations in composition could be investigated to maximize the difference in modulus between the austenite and martensite phases.

Shape Recovery

The healing ability offered by shape recovery materials was demonstrated by subjecting the transducer to excessive hydrostatic pressures. These experiments simulate the deep ocean environment encountered by underwater transducers. The results of these experiments are depicted in Figure 3. The hydrostatic piezoelectric coefficient, d_h, was initially 4200 pC/N at 0.6 MPa and dropped rapidly at pressures greater than 1.4 MPa. These values are consistent with those measured previously for various cap materials (Tressler, 1997). Subjecting the sample to increasing pressure, the transducer first deforms elastically up to pressures near 2 MPa. This elastic deformation is completely recoverable, however, at pressures greater than 2 MPa, inelastic collapse of the cavity results. The sample was tested to a maximum pressure of 4.8 MPa, which was the upper limit of the measurement equipment. Decreasing the pressure from 4.8 MPa resulted in lower values of the d_h coefficient. Final values for
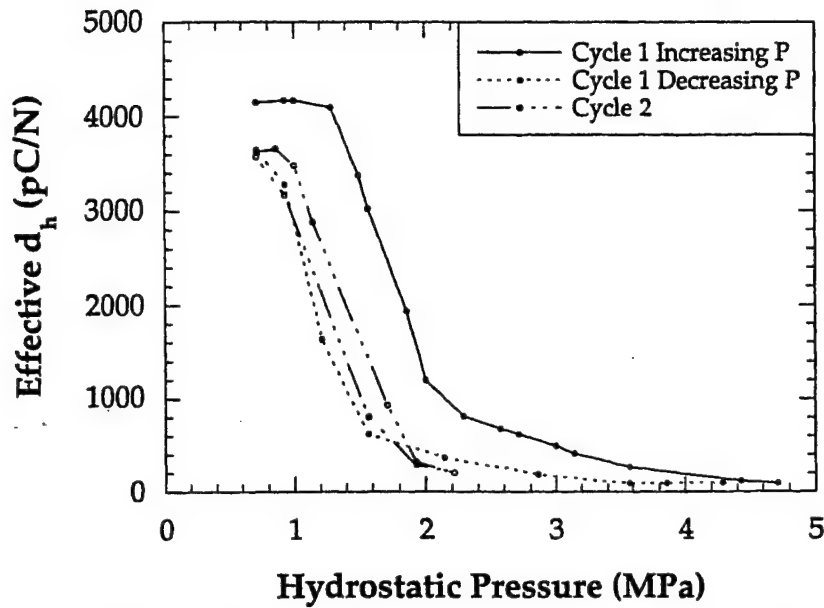
Figure 3. *Effective* d_h *plotted as a function of pressure for an SMA capped cymbal.*
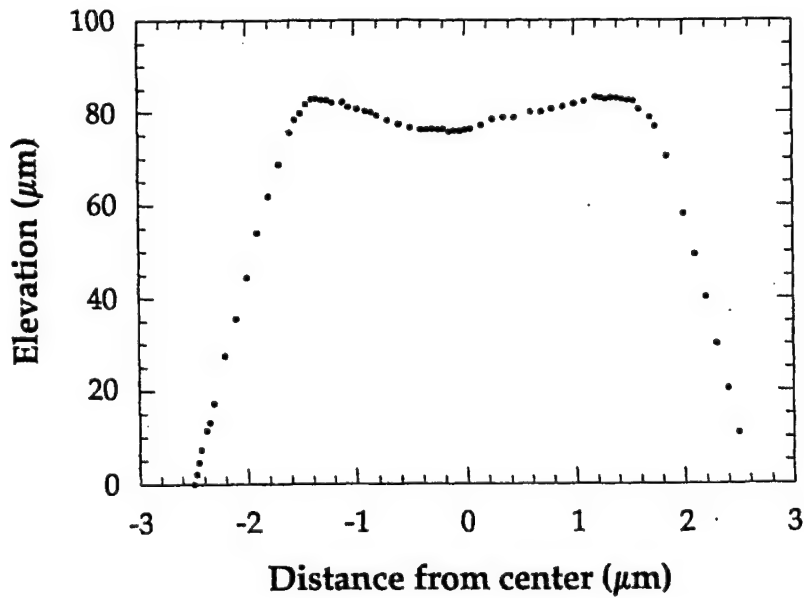

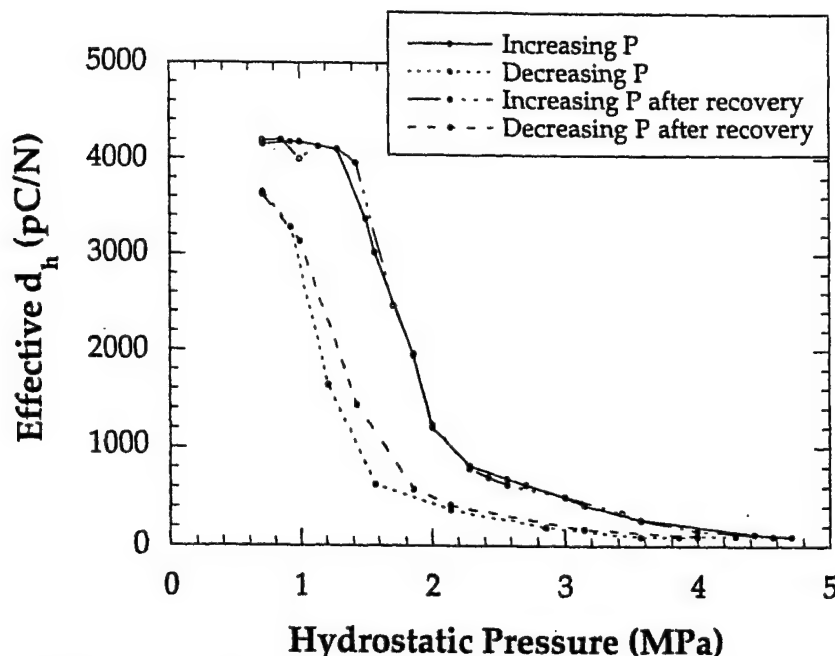**Figure 4.** *Profile of the cap after being subjected to 4.8 MPa hydrostatic pressure.*

Figure 5. *Direct comparison of the effective* d_h *plotted as a function of pressure for the SMA capped cymbal representing the original testing cycle and the recovered sample after heat treatment.*

d_h were 15% lower than the initial value which indicated permanent damage to the transducer. The second cycle shows a steady decline in the magnitude of d_h.

The resonance frequency was monitored from the measured admittance data before and after subjecting the sample to hydrostatic pressure. The flextensional resonance frequency was found to decrease in frequency from 23.65 kHz to 21.63 kHz, with a 24% decline in amplitude. The frequency and amplitude of the radial mode of the ceramic was unchanged. This indicated that the bonding layer remained intact.

To further investigate the deformation of the cap, · the shape of the cap was profiled using a Tencor Instruments Alpha-Step 200 Profilometer. The surface contour across the dimple of the cap is plotted in Figure 4. It can be clearly seen that the cavity has partially collapsed. Since the height of the cap was greater than the maximum elevation of the instrument, the full cap profile was not obtained.

Next, the cap was heated to 80°C, which is above the martensite-to-austenite transition temperature. This temperature is below the maximum operating temperature of the bonding material and the Curie temperature of the ceramic. The resonance frequency after heat treatment returned to its initial value and magnitude. The sample profile returned to its original flat surface and the d_h value was also recovered. Figure 5 compares the 1st cycle for the initial sample and after shape recovery. Thus, the resonance frequency, cap profile, and very close agreement between the d_h values all indicated complete shape recovery.

CONCLUSIONS

Tunable resonance frequency and shape recovery have been demonstrated for cymbal flextensional transducers with Ni-Ti shape memory caps. A resonance frequency shift was achieved and maintained when transforming the SMA from the martensite to the austenite phase. The ability to repair damaged transducers subjected to hydrostatic pressure was also demonstrated by monitoring resonance frequency, cap profile and the hydrostatic piezoelectric coefficient.

ACKNOWLEDGMENTS

REFERENCES

Blaszkiewicz, M. A., 1994. "Tunable Transducers," Ph.D. Thesis in Solid State Science, The Pennsylvania State University.

Buehler, W. J., J. W. Gilfrich and R. C. Wiley, 1963. *J. Appl. Phys.*, Vol. 34, p. 1475.

Chang, L. C. and T. A. Read, 1951. *Trans. AIME*, Vol. 191, p. 47.

Chen, J., Q. Xu, M. Blaszkiewicz, R. Meyer, Jr. and R. E. Newnham, 1992. "Lead Zirconate Titanate Films on Nickel-Titanium Shape Memory Alloys: SMARTIES," *J. Am. Ceram. Soc.*, Vol. 75, p. 2891.

Clark, A. E. and H. S. Belson, 1971. "Magnetostrictive Rare Earth–Fe$_2$ Compounds," *Proc. of the 17th Conf. on Mag. and Mag. Materials, Part II*, Nov.

Dogan, A., Q. Xu, K. Onitsuka, S. Yoshikawa, K. Uchino and R. E. Newnham, 1994. "High Displacement Ceramic-Metal Composite Actuator," *Ferroelectrics*, Vol. 156, pp. 1–6.

Dogan, A. and R. Newnham, 1998. "Metal-Electroactive Ceramic Composite Actuator," U.S. Patent 5,729,077.

Fry, W. J., R. B. Fry and W. Hall, 1951. "Variable Resonant Frequency Crystal Systems," *Journal of the Acoustical Society of America*, Vol. 13, pp. 94–110.

Lanina, E. P., 1978. "Tunable High Frequency High Power Piezoceramic Radiator," *Sov. Phys. Acoust.*, Vol. 24, pp. 207–209.

Mercado, P. G. and A. P. Jardine, 1994. "Thin Film Multilayers of Ferroelastic TiNi-Ferroelectric PZZT: Fabrication and Characterization," *Proc. 2nd International Conf. on Intelligent Materials*, Colonial Williamsburg, VA, Ed. by C. Rogers and G. Wallace, pp. 665–676.

Newnham, R. E., Q. C. Xu and S. Yoshikawa, 1991. "Transformed Stress Direction Acoustic Transducer," U.S. Patent 4,999,819 March.

Newnham, R. E., 1991. "Tunable Transducers: Nonlinear Phenomena in Electroceramics," NIST Special Publication 804, Chemistry of Electronic Ceramic Materials, Proceedings of the Internation Conference held in Jackson, WY, August 17–22, 1990.

Newnham, R. E., Q. C. Xu and M. A. Blaszkiewicz, 1992. U.S. Patent 5,166,907, Nov.

Shimizu, K. and T. Tadaki, 1987. *Shape Memory Alloys*, Ed. H. Funakubo, Gordon and Breach Science Publishers.

SMA-Inc., 1999. Corporate brochure, www.sma-inc.com.

Sugawara, Y., K. Onitsuka, S. Yoshikawa, Q. Xu, R. E. Newnham and K. Uchino, 1992. "Metal Ceramic Composite Actuators," *J. Am. Ceram. Soc.*, Vol. 75, 996.

Tressler, J. F., A. Dogan, J. F. Fernandez, Jr., K. Uchino and R. E. Newnham, 1995. "Capped Ceramic Hydrophones," *IEEE Int. Ultrasonic Symp. Proc.*, Seattle, WA, Vol. 2, pp. 897–900.

Tressler, J. F., 1997. "Capped Ceramic Underwater Sound Projector: The 'Cymbal,' " Ph.D. Thesis, The Pennsylvania State University.

APPENDIX 42

Pre-Focused Lead Titanate >25 MHz Single-Element Transducers from Hollow Spheres

Richard Meyer, Jr., Robert Newnham, *Member, IEEE*, Sedat Alkoy, *Associate Member, IEEE*, Timothy Ritter, *Associate Member, IEEE*, and Joe Cochran, Jr.

Abstract—Miniature lead titanate (PT) hollow spheres with diameters in the 1 to 10 mm range and wall thicknesses of 20 to 120 μm have been fabricated. Shell sections were used as components of pre-focused transducers. Spheres are produced using a new sacrificial core technique that produces hundreds of spheres with a more uniform wall thickness than those produced by earlier methods. Shells produced from these spheres were found to have a wall thickness variation of about 10%.

Despite this variation, bulk properties were estimated from capacitance and impedance data. Shells tested in this work had dielectric constants (1 kHz) near 280 with loss factor of <2% and d_{33} values of 68 pC/N. Thickness coupling coefficients averaged 0.51 with mechanical quality factors of <15. A transducer fabricated from these sections of spheres had a round-trip insertion loss of −20.1 dB at the center frequency of 39.8 MHz and a 6 dB bandwidth of 33%.

I. INTRODUCTION

THE ADVANTAGES of ultrasonic imaging techniques have stimulated broad interest in ultrasonic transducer design and materials optimization. Biomedical imaging technology has become one of the most popular and fastest growing areas in diagnostic healthcare today [1]. Clinical demands for increased resolution and sensitivity to visualize the fine tissue interfaces of the skin, eyes, and vascular structures have pushed the frequencies of ultrasonic transducers far into the megahertz range. Operating requirements for these high frequency medical imaging transducers have led to the development of new transducer materials and novel material fabrication techniques. As the transducer element thickness is decreased to accommodate these high frequencies, the microstructural scale of traditional ceramics is approached, resulting in expensive and time-consuming fabrication processes. Moreover, focusing the ultrasonic beam to obtain improved resolution is also

difficult. In this paper, microsphere technology has been pursued to provide improved performance and low cost alternatives for high frequency ultrasonic backscatter microscopy (UBM) applications.

Previously, hollow spheres of lead zirconate titanate were produced using a coaxial nozzle technique for use as spherical transducers [2]. In addition, small spherical shell sections were used as pre-focused elements for single-element, high frequency transducers designed for UBM applications [3]. These shell sections offered an inexpensive and time-saving alternative to the manufacture of traditional focusing devices such as lens grinding or the ball bearing approach [1], [4]. Moreover, using shells allows for smaller geometries with low f-numbers. Presented here is an extension of this work, which includes improved processing techniques, compositional tailoring, and ultrasonic evaluation.

Processing of the spheres has been improved by implementing a sacrificial core method. This method involves the use of polystyrene balls and a powder slurry. The sphere diameter is controlled by selection of the core size, and the ball rolling time controls the wall thickness. Uniformity and reproducibility have been greatly improved over the coaxial nozzle technique [3]. Another important advantage with this technique is a smaller powder batch size, 100 vs. 1000 gm. This allows easier compositional adjustments and multiple wall thickness trials. One processing run provides thousands of spheres compared with tens of thousands in the coaxial nozzle technique. For the purposes of this study, spheres between 2 and 7 mm in diameter with wall thicknesses between 20 and 120 μm were made. PT compositions were chosen for their large piezoelectric anisotropy, giving nearly pure thickness oscillation. The dielectric constant of PT can be tailored as well through doping concentrations, ultimately allowing for easier electrical impedance matching.

Previous work on PT transducers has shown that the coupling coefficient is relatively independent of resonance frequency, and the low dielectric constant is favorable to PZT compositions for electrical impedance matching [5]. Transducers prepared previously in the 50- and 95-MHz range were focused using a ball bearing technique. Properties were slightly degraded after the fired sheets were bent into spherical sections.

PT transducers have recently been compared with LiNbO$_3$ single crystals, 1-3 composites, and PVDF poly-

mer transducers [6]. PT shows a performance equivalent to LiNbO$_3$ at 50 MHz, demonstrating the promise of ceramic PT single-element transducers for high frequency imaging applications.

This paper describes the production of PT spheres and the fabrication of focused single-element transducers. The properties of the shells along with measurements of a 40-MHz device are presented.

II. EXPERIMENTAL PROCEDURES

A. Hollow Sphere Processing and Characterization

Millimeter-size hollow spheres were produced using a sacrificial core technique using polystyrene spheres under development at the Georgia Institute of Technology. Specific details of the process are unavailable at the present time to retain patent rights, but the process uses sacrificial polystyrene (PS) balls that are tumbled and mixed with a powder slurry. Wall thickness is controlled through rolling time and is monitored by evaluating green density. Diameters are determined though core choice. Several batches of spheres were produced with green densities (including PS core) ranging from 0.05 to 0.5 g/cm^3. Core diameters ranged from 2 to 7 mm. The green PT spheres were calcined at 550°C for 30 min preceeded by a heating rate of 1°C/min. The spheres were then sintered on a bed of lead zirconate titanate powder in a closed container with a compensating lead source (mixture of lead oxide and zirconia powders) at 1300°C for 3 h.

The sintered hollow spheres were then immersed in low melting wax (Crystal bond^{TM}) for polishing into shells as shown in Fig. 1. The spheres were removed and cleaned with acetone after the final aperture size was achieved. The shells were then electroded on both faces using sputtered gold. Coating thickness averaged 30 to 35 nm. Poling of the shell was achieved at 140°C by applying 6.5 MV/m in silicon oil. Capacitance and loss were measured before and after poling. The piezoelectric d$_{33}$ coefficient was also measured using a Berlincourt d$_{33}$ meter (Channel Products).

For the evaluation of the material parameters, guidelines set by the IEEE Standard on Piezoelectricity were adopted [7]. This procedure involves the measurement of the electrical impedance of the sample as a function of frequency and provides a convenient way of determining the piezoelectric properties. Using this methodology, however, the materials were assumed to be lossless, and the parameters were assumed to be real and non-dispersive near resonance.

Resonance characteristics were measured using an impedance/gain phase analyzer (HP 4194A) with an HP41941-B impedance probe adapter. The impedance probe adapter allowed the measurement of impedance up to 100 MHz. Samples were held in a special fixture incorporating spring-loaded gold pins that limited the mechanical loading on the sample. The impedance spectra of the ele-
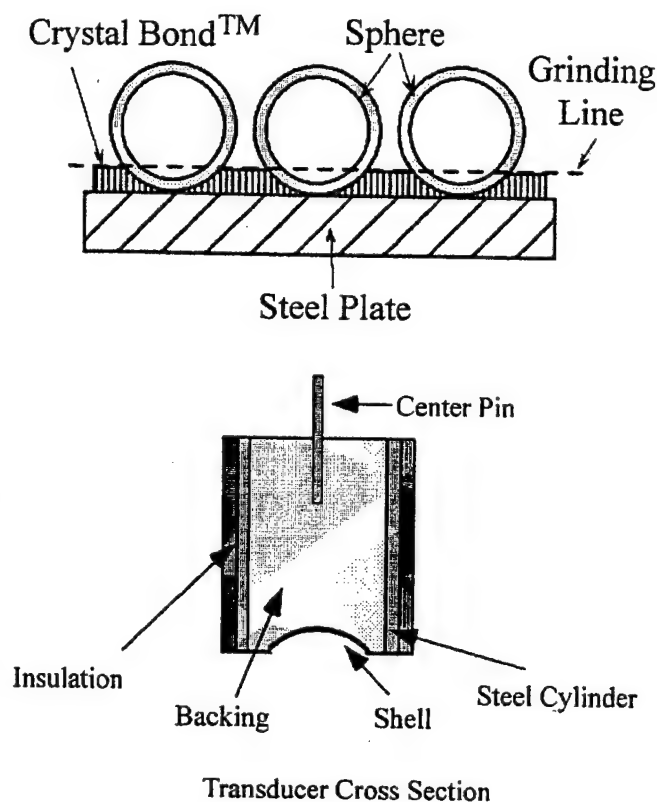

Fig. 1. Shell transducer construction from the sphere to the finished transducer.

ments were analyzed to obtain Q$_m$ and the thickness electromechanical coupling coefficient, k$_t$. Elements with the desired properties were selected for transducer fabrication.

B. Transducer Fabrication and Characterization

Transducers were assembled by placing the elements on Scotch^{TM} tape at the center of a cylindrical housing. The aperture of the element was determined by the desired f-number or to match the 50-Ω electronics. The cylinder was filled with silver-loaded epoxy (Eccobond 3022; Z$_a$ = 6 MRayl) and was allowed to cure at 50°C for at least 4 h. The housing was then insulated by using heat shrink tubing. The front face was isolated from the conductive backing using a thin epoxy layer applied using a syringe needle. The transducer assembly, shown in Fig. 1, was mounted in a sub-miniature co-axial barrel connector (SMA), and the front face was gold-sputtered to complete the ground connection. A thin layer of Parylene C (Z$_a$ = 3.0 MRayls; n = 2150 mm/μs) was deposited by evaporation as an acoustic quarter wave matching layer.

Pulse/echo and insertion loss data were collected using a water tank and a reflecting steel target. Excitation was achieved using a Panametrics model 5900 pulser/receiver. The reflected waveform was received and digitized using a 500-MHz LeCroy oscilloscope. The parameters for the input waveform were 1 μJ energy, 50 Ω damping, 40 dB attenuation, and 40 dB gain. The receive waveform was measured at the focal distance, which was determined by

maximizing the return signal. In a separate experiment, an insertion loss value was obtained at the focal distance at the center frequency using a tone burst by dividing the received voltage by the input voltage. This value was not corrected for attenuation from water or the steel reflector. The actual focal distance was calculated based on the time of flight of the received signal. Electrical tuning was not used for these transducers.

C. Transducer Modeling

Modeling was carried out using PiezoCad software (Sonic Concepts, Woodinville, WA). It was assumed that radial modes were suppressed because of the large piezoelectric anisotropy in lead titanate and that the shell acted in a pure piston mode. Modeled parameters were based on material properties calculated using IEEE methods [7].

This approach allows easy calculations of the effects of backing and matching layers along with electrical tuning if necessary. PiezoCad was used to model input impedance spectra as well as the pulse/echo response and insertion loss. A drawback of this method is that it is only one-dimensional, so the effects of focusing and diffraction are not considered.

III. RESULTS AND DISCUSSION

A. PT Hollow Spheres

PT spheres sintered at 1300°C for 3 h showed the best dielectric characteristics. Depicted in Fig. 2 are SEM images of a polished cross-section and interior grain size showing dense walls and grain sizes between 4 and 5 μm. These photos also show a surface roughness or thickness variation stemming from the green sphere preparation. A 33 to 36% shrinkage of the spheres during firing was observed.

Several different processing runs were examined. Each run provided different wall thicknesses. It was observed that as wall thickness decreased, wall thickness variation increased. For spheres produced with 70- to 90-μm walls, a thickness variation of 10% was found. A variation of 20% was obtained for spheres with 50- to 60-μm walls. This is a significant improvement over the coaxial nozzle technique in which sphere wall thicknesses varied over 300% [3]. Improvements in green sphere preparation are continuing to be made. Average wall thickness values were used in calculations when needed.

Dielectric properties and impedance spectra were obtained for electroded shells resonating between 35 and 50 MHz. Free dielectric constants averaged 280 with loss factors <2%. A piezoelectric d_{33} coefficient of 68 pC/N was obtained for these samples. The impedance spectrum in air of a shell showed only a pure thickness oscillation with $f_p = 50$ MHz. Fig. 3 shows the real part of impedance and admittance from which the parallel and series resonance frequencies were obtained for this 50-MHz sample.
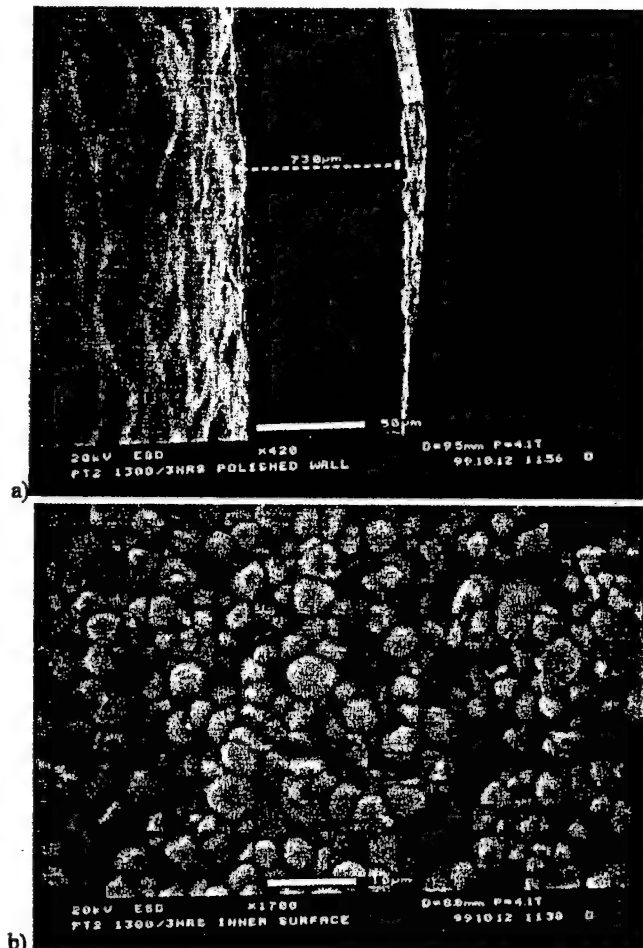

a)

b)

Fig. 2. SEM micrographs of a) a polished wall cross-section (bar = 50 μm) and b) interior grain size (bar = 10 μm) of PT spheres sintered at 1300°C for 3 h.

As can be seen, a broadened peak associated with a thickness variation was obtained. For the samples tested, thickness coupling and mechanical quality factors calculated using IEEE equations [7] resulted in values of 48 to 52% and 6 to 8, respectively. The values for Q vary significantly from typical values reported for PT compositions [8], [9]. Use of the bandwidth approximation for Q resulted in similar numbers [10].

Transducers were built from the shells and evaluated. The construction of these transducers was found to be quite simple. The impedance spectrum was measured in water before testing to verify the activity of the element and is shown in Fig. 4. The receive response in both the time and frequency domain is shown in Fig. 5. This transducer had roughly a 2-mm aperture size and was obtained from a 2.8-mm diameter sphere. A 14-μm Parylene C matching layer was deposited as a matching layer. The center frequency of this transducer was 39.8 MHz with a 6 dB bandwidth of 33%, having upper and lower frequencies of 46.3 and 33.3 MHz, respectively. The observed focal distance was calculated to be 1.43 mm from the time of flight data. The insertion loss at the center frequency was
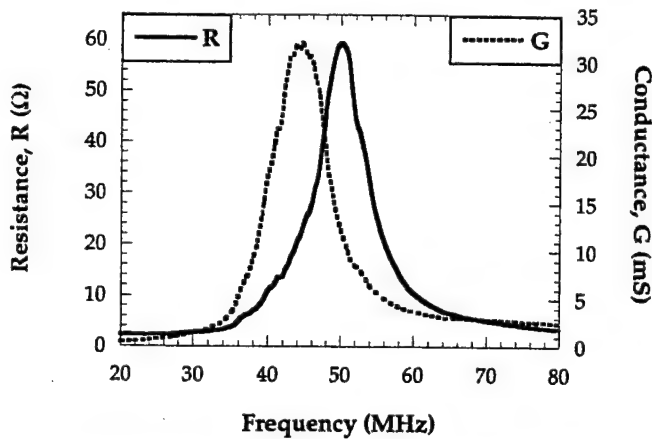
Fig. 3. Resistance and conductance plotted as a function of frequency for the 50-MHz PT shell.
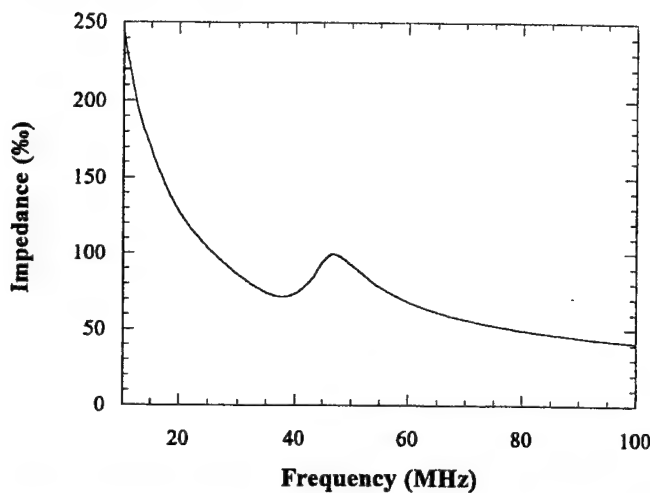

Fig. 4. Impedance spectrum of the finished transducer in water.

Fig. 5. Time (a) and frequency domain plots (b) of the receive response of a 40-MHz PT pre-focused transducer.

calculated from the input and receive signals. The transducer returned 0.775 V of a transmit voltage of 7.86 V at 40 MHz, giving an insertion loss of −20.1 dB. From the impedance plot of the finished transducer, the electrical input impedance at the center frequency was found to be 73 Ω.

Also shown in Fig. 5 is a comparison of the measured waveforms to the simulated waveforms. Modeling of this transducer using PiezoCad gave a receive response centered on 39.5 MHz with a bandwidth of 38%. The input parameters used in the model were based on material properties measured or calculated based on IEEE methods. Good agreement between the simulated and measured responses will allow for optimization of the properties of future transducers based on hollow spheres.

The very low f-number of the present transducer can provide extremely fine lateral resolution in imaging applications. Because the low f-number is achieved without a lens (which often results in acoustic reflections) and with high sensitivity, improved imaging should result. Typical UBM scanning is performed using transducers with mod-
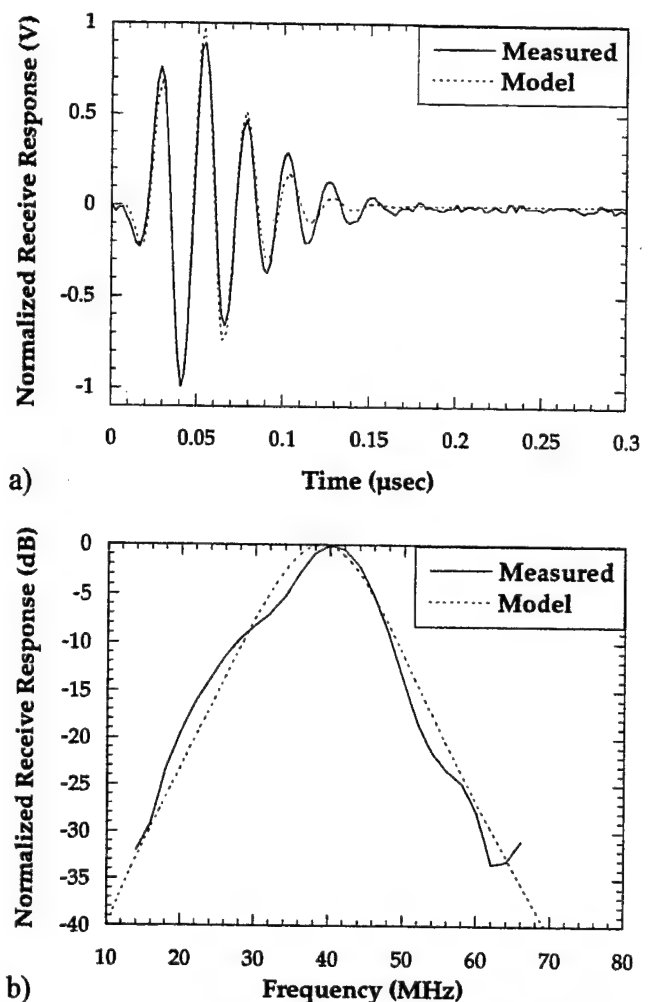
erate f-numbers of approximately 3 to 5. At 40 MHz, this corresponds to a lateral resolution on the order of 120 to 200 μm. With an f-number of 0.7, the PbTiO$_3$ device described previously can achieve a lateral resolution of less than 40 μm. This capability is displayed in Fig. 6, in which the theoretical pulse-echo amplitude response near the focal point is displayed as a contour plot. The limited depth of field resulting from this design can be dealt with by using a B/D scan approach as described by Passman and Ermert [11]. The B/D scan incorporates multiple B-scans each with a limited depth of field. The transducer is first scanned laterally to acquire a single image with a shallow axial depth. The transducer is then indexed axially a distance equal to the transducer's depth of field. Another B-scan is then acquired, this time imaging deeper within the tissue of interest. After repeating this process numerous times, a composite image is formed by combining the multiple scans into a single display.

Production of larger diameter spheres is in progress to provide focal distances suitable for dermatological and ophthalmological applications. Also, spheres with wall
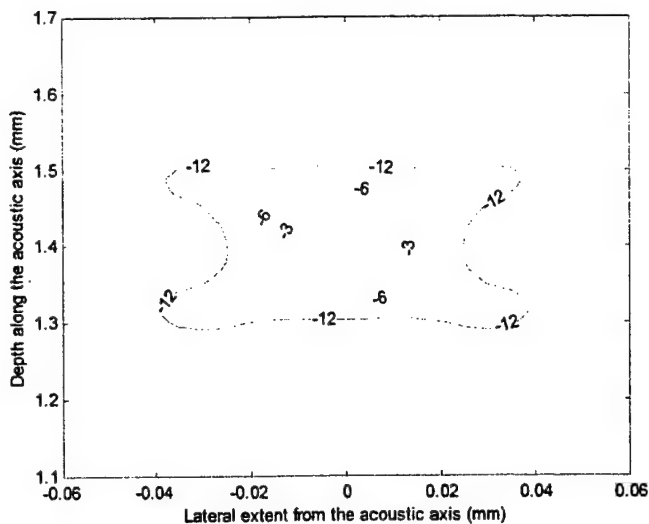
Fig. 6. Contour plot showing the theoretical pulse-echo amplitude response near the focal point. Values are in decibels.

thickness of 10 to 30 μm are now being evaluated for higher frequency applications. Highly focused transducers with the high sensitivities presented here have potential in ultrasonic ablation applications.

IV. CONCLUSIONS

Hollow spheres were successfully produced using PT powders. The sacrificial core method provides a technique for producing more uniform wall thicknesses with a large range of diameters. Techniques for burnout and sintering the green spheres were devised to produce spheres with good dielectric characteristics. Fabrication of shell transducers from these spheres was found to be very simple and time-saving compared with other focusing techniques. High sensitivity was found for these PT transducers, verifying the usefulness of this technique for producing single-element, high frequency devices.

ACKNOWLEDGMENTS

The authors thank Scott Sentz of Channel Industries for advice on PT.

REFERENCES

[1] K. Shung and M. Zipparo, "Ultrasonic transducers and arrays," *IEEE Eng. Med. Biol.*, pp. 20–30, Nov./Dec. 1996.
[2] R. Meyer, Jr., H. Weitzing, Q. Xu, Q. Zhang, J. Cochran, and R. Newnham, "PZT hollow-sphere transducers," *J. Amer. Ceram. Soc.*, vol. 77, no. 6, pp. 1669–1672, 1994.
[3] S. Alkoy, P. Lopath, R. Newnham, A. Hladky, and J. Cochran, "Focused spherical transducers for ultrasonic imaging," in *Proc. IEEE Int. Ultrason. Symp.*, 1997, pp. 991–994.
[4] G. Lockwood, D. Turnbull, and F. Foster, "Fabrication of high frequency spherically shaped ceramic transducers," *IEEE Trans. Ultrason., Ferroelect., Freq. Contr.*, vol. 41, no. 2, pp. 231–235, 1994.
[5] M. Zipparo, K. K. Shung, and T. Shrout, "Piezoceramics for high-frequency (20 to 100 MHz) single-element imaging transducers," *IEEE Trans. Ultrason., Ferroelect., Freq. Contr.*, vol. 44, no. 5, pp. 1038–1048, Sep. 1997.
[6] J. Zhao, C. Alves, K. Snook, J. Cannata, W. Chen, R. Meyer, Jr., S. Ayyappan, R. Ritter, and K. K. Shung, "Performance of 50 MHz transducers incorporating fiber composites, PVDF, PbTiO$_3$, and LiNbO$_3$," in *Proc. IEEE Ultrason. Symp.*, 1999, pp. 1185–1190.
[7] IEEE Standard on Piezoelectricity, ANSI/IEEE Std. 176, 1987.
[8] Company catalog, EDO Corp., Salt Lake City, UT, 1999.
[9] Company catalog, Sensor Technology Ltd., Collingwood, Ontario Canada, 1999.
[10] E. Kuntsal and W. Bunker, "Guidelines for specifying underwater electroacoustic transducers," presented at the UDT-92 Conference, London, England, Jun. 1992.
[11] C. Passman and H. Ermert, "A 100 MHz ultrasound imaging system for dermatologic and ophthalmologic diagnostics," *IEEE Trans. Ultrason., Ferroelect., Freq. Contr.*, vol. 43, no. 4, Jul. 1996.

Richard J. Meyer Jr. was born in Pittsburgh, Pennsylvania on May 7, 1971. He studied ceramic science and engineering and graduated with a B.S. degree in 1993 as the Student Marshal for the Materials Science and Engineering Department. He received his Master's degree in 1995 in Materials at the Materials Research Laboratory under the direction of Thomas Shrout and Shoko Yoshikawa. He completed his Ph.D. in October 1998 with the development of high frequency 1-3 composite transducers.

After graduation, he studied one year as a post-doctoral scholar under the supervision of Dr. Robert E. Newnham and then was promoted to his current position as Research Associate at the Materials Research Laboratory, The Pennsylvania State University. His research interests include ceramic processing, development of undersea and medical ultrasonic devices, and composites materials for actuators and transducers.

Robert E. Newnham (M'85) was born in Amsterdam, New York on March 28, 1929. He received the B.S. degree in mathematics in 1950 from Hartwick College, Oneonta, New York; the M.S. degree in physics from the Colorado State University, Fort Collins, Colorado; a Ph.D. in physics and mineralogy from The Pennsylvania State University; and a second doctorate in crystallography from the Cambridge University, United Kingdom in 1960.

He is ALCOA Professor Emeritus of Solid State Science at The Pennsylvania State University, University Park, Pennsylvania. Previously, he was a staff member of the Laboratory for Insulation Research at the Massachusetts Institute of Technology, Cambridge, Massachusetts. His research interests are in structure-property relations, electroceramics, and composite materials for electronic applications.

Sedat Alkoy (S'96–A'99) was born in Akhisar-Manisa, Turkey on May 10. He received the B.S. degree in metallurgical engineering in 1992 and the M.S. degree in materials science and engineering in 1994, both from the Istanbul Technical University, Istanbul, Turkey. He studied one year at the Drexel University, Philadelphia, Pennsylvania, before joining the Materials Research Laboratory (MRL) at The Pennsylvania State University as a graduate student in 1995. He received the Ph.D. degree in materials science and engineering (Ceramic Science Program) in 1999 from The Pennsylvania State University.

Following his graduate work, he worked as a post-doctoral fellow at MRL-PSU. He is currently on the faculty of the Gebze Institute of Technology, Turkey. His research interests include ceramic processing, ferroelectrics, development, and design and finite element analysis of sensor-actuator systems. He is an Associate Member of the IEEE Ultrasonics, Ferroelectrics, and Frequency Control Society and a member of the American Ceramic Society and the Materials Research Society.

Joe K. Cochran, Jr. is the B. Mifflin Hood Professor in Materials Science and Engineering at the Georgia Institute of Technology, Georgia. He received the B.S. degree in 1965 and the M.S. degree in 1968 from Georgia Institute of Technology and the Ph.D. from The Ohio State University, Ohio in 1971. All degrees were in ceramic engineering. He was an instructor at Georgia Institute of Technology from 1966 to 1968 and has been on the faculty since 1971. He is a Fellow of the American Ceramic Society (ACS), recipient of the Hewit Wilson Award from the SE Section of the ACS, and served as interim director of MSE in 1993.

He developed a process for fabricating hollow spheres from powders. His research interests include processing and properties of ceramic foams, premixed radiant burners, rheology of high solid slurries, fine powder processing, and strength of low density materials. His current focus is hollow spheres and foams from low density metals.

Timothy A. Ritter (A'97) was born in Harrisburg, Pennsylvania on February 19, 1965. He earned his B.S. in mechanical engineering from The Pennsylvania State University, University Park, PA, in 1987 and his M.S. in physics from the University of Connecticut, Storrs, CT, in 1991.

Mr. Ritter is presently a Ph.D. student in the Bioengineering Department at The Pennsylvania State University and serves as a manager of the NIH Resource Center for Medical Ultrasonic Transducer Technology. His research interests are piezoelectric transducers, transducer modeling, and high frequency arrays. He is an Associate Member of the IEEE.

APPENDIX 43

High-dielectric-constant ceramic-powder polymer composites

Y. Bai, Z.-Y. Cheng, V. Bharti, H. S. Xu, and Q. M. Zhang[a]

Materials Research Laboratory, Pennsylvania State University, University Park, Pennsylvania 16802

A ceramic-powder polymer composite, making use of a relaxor ferroelectric polymer that has a high room-temperature dielectric constant as the matrix, is developed. The experimental data show that the dielectric constant of the composites with $Pb(Mg_{1/3}Nb_{2/3})O_3$–$PbTiO_3$ powders can reach more than 250 with weak temperature dependence. In addition, the composites under a proper preparation procedure exhibit a high breakdown field strength (>120 MV/m), leading to a maximum energy storage density of more than 15 J/cm^3. Experimental results also indicate that the high electron irradiation does not have much effect on the dielectric behavior of $Pb(Mg_{1/3}Nb_{2/3})O_3$–$PbTiO_3$ powders, possibly due to the relaxor nature of the ceramic. © *2000 American Institute of Physics.* [S0003-6951(00)04925-1]

By integrating two or more materials with complementary properties, composite materials offer the potential to have performance far beyond those of the constituent materials.[1] For instance; ferroelectric ceramics possess very high dielectric constant but are brittle and have low dielectric strength. On the other hand, polymers are flexible, easy to process with low processing temperature, and possess high dielectric breakdown field. By combining these two, one may be able to develop a new material with high dielectric constant and high breakdown field to achieve high volume efficiency and energy storage density for applications of capacitors and electric energy storage devices. In the past twenty years, a great deal of effort has been devoted to the development of ceramic powder polymer composites (0–3 composites).[2,3] However, due to the low dielectric constant of polymer matrix (usually below 10), the dielectric constant of 0–3 composites developed to date is at the level of about 60 at room temperature.[4–6]

Recent research on P(VDF-TrFE) copolymer found that high energy electron irradiation with proper dosage can increase its room temperature dielectric constant to more than 50 over a relative broad temperature range.[7] In addition, the high energy irradiation converts the copolymer from a normal ferroelectric into a relaxor ferroelectric, which removes the large polarization-field hysteresis under high field, typical in the normal ferroelectric copolymers. These features provide a great opportunity for the development of high dielectric constant 0–3 composites. In this letter, we report the results of the development and characterization of 0–3 composites based on the irradiated copolymer as the polymer matrix. We will show that the composite thus developed has a much-improved dielectric constant. In addition, under a proper processing condition, the breakdown field of the composite can reach more than 120 MV/m.

The P(VDF-TrFE) 50/50 mol% copolymer (purchased from Solvay and Cie, Belgium) was chosen for the polymer matrix since it can be easily converted into a relaxor under relatively low irradiation dose.[7] $Pb(Mg_{1/3}Nb_{2/3})O_3$–$PbTiO_3$ (PMN–PT) ceramic powder (PMN-85, TRS Ceramics, Inc.)

which is also a relaxor ferroelectric with high room temperature dielectric constant was used as filler.[8] The composite was prepared using solution cast method. P(VDF/TrFE) copolymer was dissolved in methyl–ethyl ketone, and a proper amount of PMN–PT ceramic powder (average particle diameter is 0.5 μm) was added into the solution, which was thoroughly mixed with the solvent. The suspension was then poured onto a glass plate to remove the solvent (at room temperature for 1 h), resulting in a composite film of about 15 μm thick. All these were carried out in a clean bench (class 1000). The film was then heated in a vacuum oven at 70 °C for 12 h to further remove any remaining traces of the solvent. Then it was folded to an average area of 3×2 inches and melt pressed at 170 °C (above the melting point of the copolymer) under 15 000 lbs of force, which was used to remove any possible pores in the composite. It was found that only by following this procedure, the breakdown field of the composite can reach more than 120 MV/m. Scanning electron microscopy (SEM) micrograph shows that the composites thus prepared have a uniform ceramic powder distribution in the polymer matrix. The typical thickness of the pressed composite was about 20 μm. Finally, the composite was annealed at 140 °C in vacuum for 12 h and slowly cooled down to room temperature. Composites with volume percentage of the ceramic from 10% to 60% were prepared and irradiated at 120 °C with the energy of the electron source of 2.55 MeV and various dosages (40, 60, and 80 Mrad). It should be noted that for such a high energy the penetration depth of the electron is more than 0.2 mm into a lead plate (more than 90% of the electron energy still remained).[9] Hence, for the composites with 20 μm thickness, the electron will pass through the material without much absorption by the material.

For the electric characterization, the films were cut into small pieces of 5×5 mm and circular gold electrodes with 3 mm radius were sputtered in the center on both sides of each sample. The dielectric properties as a function of temperature were measured at frequencies from 100 to 100 kHz using a dielectric analyzer (DEA 2970, TA Instrument). The frequency dependence of the dielectric constant and loss at a constant temperature was measured by means of an imped-

[a]Electronic mail: qxz1@psu.edu

Appl. Phys. Lett., Vol. 76, No. 25, 19 June 2000
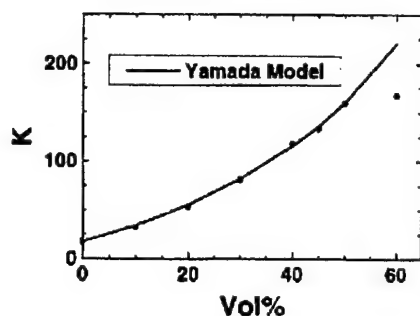
Bai *et al.*   3805

FIG. 1. Variation of the dielectric constant of the composites (before irradiation) with the volume percentage of the ceramic (measured at room temperature and 100 Hz). Dots are data points and solid curve is from Eq. (1).

FIG. 2. Dielectric constant of the composites with 50% volume percentage of ceramic powder under different irradiation doses

ance analyzer (HP 4194A, HP) from 1 kHz to 100 MHz. In order to evaluate the breakdown strength, the sample was immersed in silicon oil and a direct-current (dc) voltage was applied using a high voltage supply (Trek, 610D).

The composites prepared before the irradiation were characterized and Fig. 1 shows the dielectric constant measured at 100 Hz as a function of the volume percentage of ceramic powder (unirradiated). As expected, the dielectric constant increased with the volume fraction of ceramic filler. In the past, there have been many efforts in developing models for 0–3 composites.[10–12] It was found that the expression developed by Yamada *et al.* can fit the data well (solid curve in the figure),

$$K = K_p \left[1 + \frac{nq(K_c - K_p)}{nK_p + (K_c - K_p)(1 + q)} \right], \qquad (1)$$

where K is the dielectric constant of the composite, K_p and K_c are the dielectric constants of the polymer matrix and the ceramic, respectively, q is the volume fraction of ceramic and n is a parameter related to the geometry of ceramic particles.[10] For the copolymer, K_p at room temperature is 17, which is directly measured at 100 Hz. The values of K_c and n obtained from the fitting to Eq. (1) are 1400 and 10.6, respectively (n value is also in agreement with that found in Ref. 10). After irradiated with 40 Mrad, K_p is increased to 46, while n remains the same since it is only related to the geometry of ceramic powders. K_c calculated using Eq. (1) from the dielectric constant of the irradiated composites is 1360. This result indicates that the irradiation does not have a significant effect on the dielectric properties of the ceramic filler. In addition, PMN–PT bulk ceramics with the composition similar to that used in the composite were also irradiated and the dielectric constant before and after the irradiation does not show much change. This could be due to the fact that PMN–PT is a relaxor ferroelectric that already possesses frozen in defects, and therefore, the additional defects induced by the irradiation do not have as much effect in the dielectric properties as that on normal ferroelectric ceramics, where the irradiation effect seems more significant.[13]

Figure 1 also reveals that when volume percent of the ceramic powder increases to 60%, the measured dielectric constant of composite becomes much lower than that predicted from Eq. (1). This is probably caused by two factors. First, the high volume fraction of ceramic filler in composites may result in an increase in porosity. In addition, the high volume percent of ceramic may lead to agglomeration
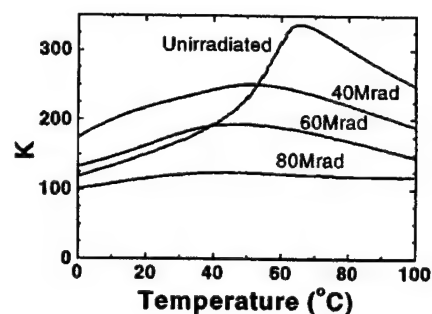
of powders, which results in a nonuniform distribution of the ceramic powder. Therefore, in this study, only the composites with 50% volume fraction of ceramic powder were chosen for further investigation.

Presented in Fig. 2 is the dielectric constant (1 kHz) as a function of temperature for irradiated composites with 50% ceramic volume content. The data shows that over a relatively broad temperature range, the dielectric constant is quite high and exhibits a weak temperature dependence. Furthermore, by adjusting the dosage, the level of the dielectric constant and the flatness of temperature dependence can also be varied, as can be seen in Fig. 2, where the dielectric constant for composites irradiated at different dosages is shown. In comparison, the dielectric constant of unirradiated composite is also presented, which shows a stronger temperature dependence. In addition, the copolymer matrix is still a normal ferroelectric and under high fields the polarization-field curve of the composites exhibits large hysteresis.

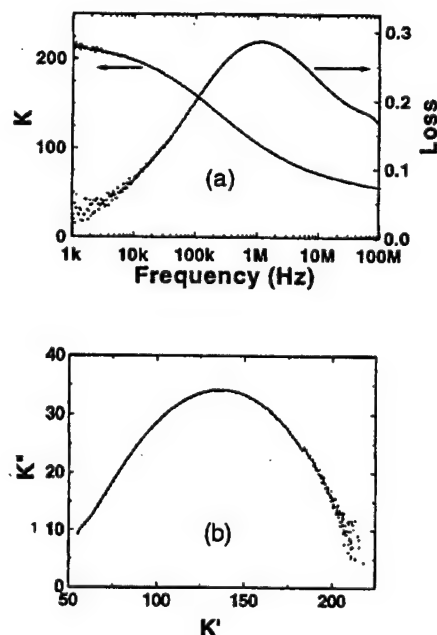Frequency dependence of the room temperature dielec-

FIG. 3. (a) Dielectric properties of the composite with 50% volume percentage of the ceramic powder and irradiated with 40 Mrad doses as a function of frequency measured at room temperature and (b) Cole–Cole plot of the dielectric data where K' and K'' are the real and imaginary part of the dielectric constant.
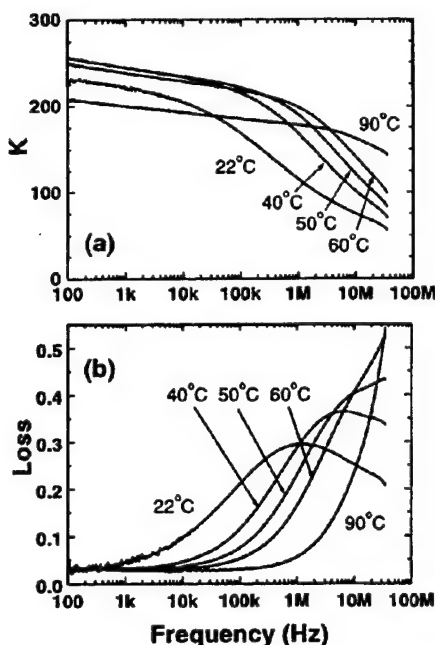
FIG. 4. Dielectric properties measured at different temperature as a function of frequency for the composite with 50% volume percentage of the ceramic powder and irradiated with 40 Mrad doses: (a) the dielectric constant and (b) the dielectric loss.

tric constant and tan δ of the composite irradiated with 40 Mrad at 120 °C are shown in Fig. 3(a). It is evident that the dielectric absorption of the composite with a maximum near 1 MHz is a simple relaxation process, as shown in Fig. 3(b), which can be fitted quite well with the modified Cole–Cole equation[14]

$$K = K_\infty + \frac{\Delta K}{1 + (i\omega\tau)^\alpha}, \tag{2}$$

which yields $K_\infty = 50.832$, $\Delta K = 173.2$, $\alpha = 0.484$, $\tau = 61.69\,\mu s$, indicating that the composite has a dielectric constant of 50 at 100 MHz and this value is comparable to those of current materials used in microwave applications.[15] Moreover, with increased temperatures, the relaxation frequency $1/\tau$ moves progressively to higher frequencies as shown in Fig. 4, resulting in a higher dielectric constant at high frequencies. For instance, the dielectric constant of the composite can be higher than 150 at 10 MHz when measured at 90 °C and above.

We also characterized the irradiated composites for possible applications of electric energy storage devices. In that application, the maximum stored energy density is an important parameter and for a linear dielectric as the composites studied here, the maximum stored energy per unit volume is

$$U = \tfrac{1}{2} K \epsilon_0 E_{max}^2, \tag{3}$$

where K is the relative dielectric constant and E_{max} is the

maximum field, which can be applied to the material (proportional to the breakdown field of the material).[16] For dielectric materials, it is well known that the breakdown field will depend on sample thickness and, in general, will increase as the thickness is reduced (due to the avalanche phenomenon).[17,18] For the thickness studied here ($\sim 20\,\mu m$), the breakdown field for the irradiated copolymer is about 350 MV/m while for the ceramic, it is below 10 MV/m.[18,19] In the 0–3 composites, the complicated geometry makes it difficult to predict exactly the level of the breakdown field and no systematic thickness dependence of the breakdown field was observed. Instead, in this study it was found that the main causes for the breakdown are due to the extrinsic effects such as inclusion of the air bulbs, dust, and residual solvent in the composites. For instance, by preparing the composites in a class 1000 clean bench rather than in a normal environment raised the breakdown field from 80 to 120 MV/m. Using K of 250 and $E_{max} = 120\,MV/m$, Eq. (1) yields that the maximum stored energy of the composite is more than 15 J/cm^3 higher than those reported from the current literatures.[20]

[1] R. E. Newnham, Annu. Rev. Mater. Sci. **16**, 47 (1986).
[2] C. J. Dias and D. K. Das-Gupta, in *Ferroelectric Polymer and Ceramic-Polymer Composites*, edited by D. K. Das-Gupta (Trans Tech Publications Ltd., Switzerland, 1994), p. 217.
[3] C. J. Dias and D. K. Das-Gupta, IEEE Trans. Electr. Insul. **3**, 706 (1996).
[4] K. A. Hanner, A. Safari, R. E. Newnham, and J. Runt, Ferroelectrics **100**, 255 (1989).
[5] R. Gregorio, Jr., M. Cestari, and F. E. Bernardino, J. Mater. Sci. **31**, 2925 (1996).
[6] H. L. W. Chan, W. K. Chan, Y. Zhang, and C. L. Choy, IEEE Trans. Electr. Insul. **5**, 505 (1998).
[7] Q. M. Zhang, V. Bharti, and X. Zhao, Science **280**, 2101 (1998).
[8] L. E. Cross, Ferroelectrics **76**, 241 (1986).
[9] J. G. Trump, R. J. Van de Graaff, and R. W. Cloud, Am. J. Roentgenol. Radium Ther. **40**, 728 (1940).
[10] T. Yamada, T. Ueda, and T. Kitayama, J. Appl. Phys. **53**, 4328 (1982).
[11] D. K. Das-Gupta, Ferroelectrics **118**, 165 (1991).
[12] T. Furukawa, K. Ishida, and E. Fukada, J. Appl. Phys. **50**, 4904 (1979).
[13] J. Gao, L. Zheng, J. Zeng, and C. Lin, Jpn. J. Appl. Phys., Part 1 **37**, 5126 (1998).
[14] B. K. P. Acaife, *Principal of Dielectrics* (Clarendon, Oxford, 1989).
[15] T. Laverghetta, *Microwave Materials and Fabrication Techniques* (Artech House, Boston, 1991).
[16] H. Frohlich, *Theory of Dielectrics* (Oxford University Press, London, 1958), Chap. 1.
[17] R. Gerson and T. C. Marshall, J. Appl. Phys. **30**, 1550 (1959).
[18] J. F. Scott, Ferroelectr. Rev. **1**, 1 (1998).
[19] E. Furman, PhD Thesis, Pennsylvania State University (1987).
[20] E. Aulagner, J. Guillet, G. Seytre, C. Hantouche, P. Le Gonidec, and G. Terzulli, *Proceedings of IEEE Fifth International Conference on Conduction and Breakdown in Solid Dielectrics*, Leicester, UK (IEEE, Piscataway, 1995), p. 423.

APPENDIX 44

Acoustic bandgap formation in a periodic structure with multilayer unit cells

Mingrong Shen† and Wenwu Cao

Materials Research Laboratory, The Pennsylvania State University, University Park,
PA 16802, USA

Abstract. Using the transfer matrix method and Floquet's theorem we have derived the dispersion relation for acoustic wave propagation in a periodic layered structure in which each unit cell contains several sub-layers of different materials. Structures with unit cells containing two, four and six sublayers of different thickness and two types of materials were used as examples for our study. It was found that narrow passbands and broad stopbands could be obtained when the unit cell has more than two sublayers. The calculated results were verified experimentally using glass–water structures containing only one to three cells. Good agreement was obtained between the experimental results and the transfer matrix calculations. Desired bandgap structures can be produced in less than three cells, revealing application potential for the bandgap materials in vibration control devices and acoustic filters.

1. Introduction

In recent years, photonic bandgap materials have been widely studied [1–3]. These materials are made of periodic arrays of two transparent dielectrics. Such a structure can produce stopbands in which electromagnetic waves of certain frequencies cannot propagate, which is analogous to the Bragg reflection of electrons in solids. The study of photonic crystals arouses the interest in phononic (acoustic) bandgap structures because the nature of wave propagation is the same.

Periodic structures exhibiting acoustic bandgaps were predicted theoretically [4–9]. Several theoretical methods have been developed to study the bandgap phenomena, such as the transfer matrix method [6], plane-wave method [7, 8] and effective medium method [9]. There are also a few experimental investigations reported in the literature on this topic [10–12]. The existence of acoustic bandgaps is of interest for many applications, such as elastic/acoustic wave filters, ultrasonic silent blocks (or acoustic passband mirrors), and the concept can also help to improve the efficiency of ultrasonic transducers [13, 14].

All previously reports on wave propagation in periodic acoustic media were focused on layered structures with only two sublayers in each unit cell. In this paper, we use the transfer matrix method and Floquet's theorem to derive the dispersion relations of acoustic waves in layered structures in which each unit cell contains several sublayers of different materials with different thickness. The periodic structures made of two, four and six sublayers of two different materials were selected as demonstration cases

† Permanent address: Physics Department, Suzhou University, Suzhou 215006, People's Republic of China.

for easy comparison with experiments. For finite size periodic structures, Floquet's theorem does not apply and the transmission coefficient spectrum was calculated using the transfer matrix technique; the numerical results were verified by experiments for a system containing only three cells.

2. Dispersion relation for infinite periodic layered structures

Assuming an infinite periodic layered structure in which each unit cell contains M sublayers. The material and thickness of these sublayers are all different. Figure 1 illustrates a unit cell of the infinite periodic layered structure under study. When an acoustic plane wave is incident normal into the structure, we can write the wavefunction inside the mth layer of the nth cell in the following form:
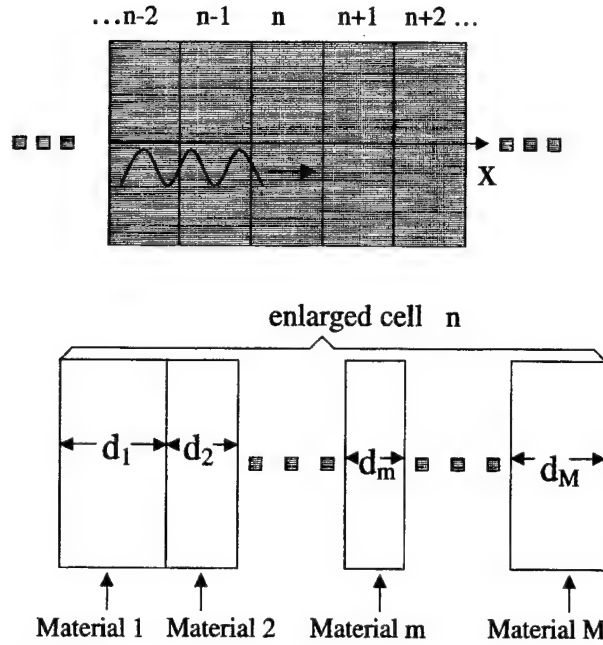
$$\psi_{n,m} = a_{n,m}\, e^{i(2\pi f t - k_m x)} + b_{n,m}\, e^{i(2\pi f t + k_m x)} \qquad (1)$$

where n is the unit cell number and m is the layer number within the nth cell. The first and the second terms on the right-hand side of equation (1) represent the forward and the backward waves, respectively; $k_m = 2\pi f/c_m$ is the wavevector for waves propagating in material m; f is the wave frequency; and c_m is the phase velocity of the acoustic wave in the mth layer.

The continuity requirements for the wavefunction and the stress at the interface between the sublayers in the nth unit cell lead to the following relations among the coefficients $a_{n,j}$, $b_{n,j}$ and $a_{n+1,j}$, $b_{n+1,j}$ [6, 15]

$$\begin{pmatrix} a_{n,j} \\ b_{n,j} \end{pmatrix} = \begin{pmatrix} A & B \\ C & D \end{pmatrix} \begin{pmatrix} a_{n+1,j} \\ b_{n+1,j} \end{pmatrix} \qquad (2)$$

...n-2   n-1   n   n+1   n+2 ...

X

enlarged cell   n

d_1 d_2 d_m d_M

Material 1   Material 2   Material m   Material M

Figure 1. A one-dimensional layered structure with each unit cell consisting of M sublayers of different materials with different thickness.

where the (2×2) transfer matrix is given by

$$\begin{pmatrix} A & B \\ C & D \end{pmatrix} = \prod_{m=1}^{M} \begin{pmatrix} A_m & B_m \\ C_m & D_m \end{pmatrix} \tag{3}$$

with

$$A_m = \frac{z_m + z_{m+1}}{2z_m} e^{i(k_m - k_{m+1})x_m}$$

$$B_m = \frac{z_m - z_{m+1}}{2z_m} e^{i(k_m - k_{m+1})x_m}.$$

In equation (3) C_m and D_m are the complex conjugates of B_m and A_m respectively, $z_m = \rho_m v_m$ is the acoustic impedance with ρ_m and v_m the density and velocity of the mth sublayer, respectively, and x_m is the coordinate of the interface between the mth and $(m + 1)$th sublayers. Equation (3) includes the acoustic properties of all layers in one unit cell.

According to Floquet's theorem, for an infinite one-dimensional periodic system, the coefficients $a_{n,j}$ and $b_{n,j}$ for the same material in different unit cells must be the same except a phase shift, i.e.,

$$\begin{pmatrix} a_{n,j} \\ b_{n,j} \end{pmatrix} = \begin{pmatrix} a_{n+1,j} \\ b_{n+1,j} \end{pmatrix} e^{-ikd} \tag{4}$$

where k is the effective wavevector for waves propagating in the whole structure and d is the unit cell size (period).

Using (2) and (4) we can derive the dispersion relation for the whole structure,

$$k = \frac{1}{d} \arccos \left(\frac{1}{2}(A + D) \right). \tag{5}$$

Equation (5) has been obtained in periodic layered structures with two sublayers in each unit cell [15]. For the multiplayer
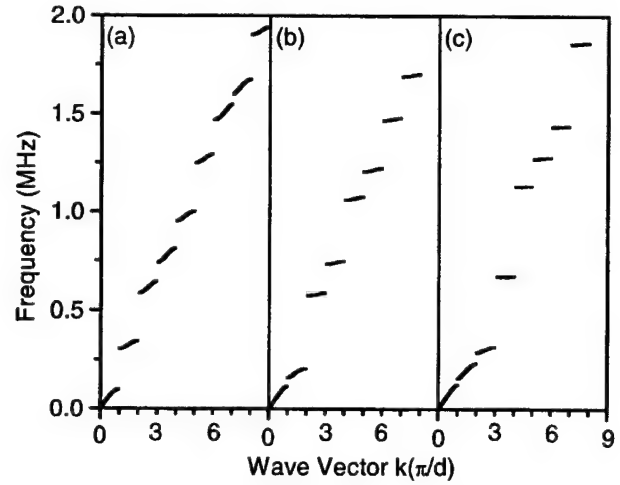
Figure 2. Dispersion relations for infinite multilayer periodic structures: (a) two sublayers in each unit cell, $d_1 = 3.690$ mm (glass) and $d_2 = 2.310$ mm (water); (b) four sublayers in each unit cell, $d_1 = 1.230$ mm (glass), $d_2 = 1.010$ mm (water), $d_3 = 2.460$ mm (glass) and $d_4 = 1.300$ mm (water); (c) six sublayers in each unit cell, $d_1 = 1.230$ mm (glass), $d_2 = 0.650$ mm (water), $d_3 = 1.230$ mm (glass) and $d_4 = 1.155$ mm (water), $d_5 = 1.230$ mm (glass), $d_6 = 0.505$ mm (water).

unit cell situation, the quantity $(A + D)$ in (5) can be obtained directly from (3):

$$A + D = \prod_{h=1}^{M} \cos(k_h d_h) - \sum_{h=1}^{M-1} \sum_{j=h+1}^{M} \left(\frac{z_h}{z_j} + \frac{z_j}{z_h} \right)$$

$$\times \left[\prod_{k=h,j} \sin(k_k d_k) \right] \prod_{l(\neq h,j)=1}^{M} \cos(k_l d_l)$$

$$+ \sum_{h=1}^{M-3} \sum_{j=h+2}^{M-1} \sum_{k=h+1}^{j-1} \sum_{l=j+1}^{M} \left(\frac{z_h z_j}{z_l z_k} + \frac{z_l z_k}{z_h z_j} \right)$$

$$\times \left[\prod_{m=h,j,k,l} \sin(k_m d_m) \right] \left[\prod_{n(\neq h,j,k,l)=1}^{M} \cos(k_n d_n) \right]$$

$$- \sum_{h=1}^{M-5} \sum_{j=h+2}^{M-3} \sum_{k=h+4}^{M-1} \sum_{l=h+1}^{j-1} \sum_{m=j+1}^{k-1} \sum_{n=k+1}^{M} \left(\frac{z_h z_j z_k}{z_l z_m z_n} + \frac{z_l z_m z_n}{z_h z_j z_k} \right)$$

$$\times \left[\prod_{p=h,j,k,l,m,n} \sin(k_p d_p) \right] \prod_{q(\neq h,j,k,l,m,n)=1}^{M} \cos(k_q d_q)$$

$$+ \sum_{h=1}^{M-7} \sum_{j=h+2}^{M-5} \sum_{k=h+4}^{M-3} \sum_{l=h+6}^{M-1} \sum_{m=h+1}^{j-1} \sum_{n=j+1}^{k-1} \sum_{p=k+1}^{l-1} \sum_{q=l+1}^{M}$$

$$\times \left(\frac{z_h z_j z_k z_l}{z_m z_n z_p z_q} + \frac{z_m z_n z_p z_q}{z_h z_j z_k z_l} \right) \left[\prod_{r=h,j,k,l,m,n,p,q} \sin(k_r d_r) \right]$$

$$\times \prod_{s(\neq h,j,k,l,m,n,p,q)=1}^{M} \cos(k_s d_s) - \cdots \tag{6}$$

where the subscripts h, j, k, l, m, n, p, q, r and s are all integers. When there are two, four and six sublayers in a unit cell, (6) is truncated at the second, third and fourth terms, respectively, and the specific forms of $(A + D)$ are given in the appendix.

In figure 2, we show the calculated dispersion relations for acoustic waves propagating through infinite periodic

1151

layered structures with each unit cell containing two, four and six sublayers. The sublayers were made of two materials with different thickness and arranged alternately within the unit cell. The properties of the two materials are: (1) glass with a density of 2459 kg m^{-3} and a phase velocity of 5660 m s^{-1} and (2) distilled water with a density 1000 kg m^{-3} and a phase velocity of 1480 m s^{-1}. In each case, the volume ratio between the glass and the water was kept constant, and the cell period was kept at $d = 6.0$ mm. Figure 2(a) is a typical dispersion relation for an infinite periodic one-dimensional structure formed by unit cells of two sublayers. The piecewise dispersion curves represent the passbands while the gaps are the stopbands. If the unit cell contains four sublayers of water and glass, narrow passbands are produced, as shown in figure 2(b), except the first two passbands. Extremely narrow passbands appear if the unit cell is divided into six different sublayers as shown in figure 2(c). Many passbands become almost a straight line perpendicular to the frequency axis. Although the number of passbands for the cases shown in figures 2(a)–(c) remains unchanged in the frequency range 0–2 MHz, the bandwidth ratio between the stopbands and passbands increases significantly from 2.69 for the case in figure 2(a) to 6.08 for the case in figure 2(b) and to 6.97 for the case in figure 2(c). In other words, bandgaps become much wider when we subdivide the unit cell into non-equivalent sublayers. The only exceptions are the first passband and the first stopband, they become wider and narrower, respectively, when the unit cell is divided into more sublayers.

The Floquet condition equation (4) is valid only for infinite systems, which does not reflect the experimental situation since the measured structures are always finite in size. For a finite system, the dispersion relation can be obtained by the transfer matrix technique defined in [6]: Band structures are not fully developed for a finite system; therefore, it is more meaningful to look at the frequency spectrum of the transmission coefficient.
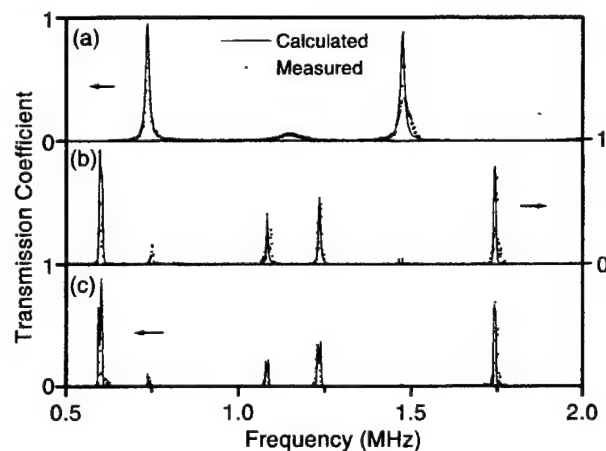
3. Frequency spectrum of the transmission coefficient of multi-sublayer periodic structures of finite size

We select glass and water as the base material for convenience in experimental testing. A dissipation factor was introduced in the calculations through adding a small imaginary component to the phase velocity in glass, i.e. $c_g = (5660 + 10i)$ m s^{-1}. Each test structure contains only one to three cells with each cell contains two, four and six sublayers of glass and water in an alternating arrangement. The transfer matrix technique defined in [6] for a finite system was used to calculate the acoustic band structure.

The experiments were conducted in a water tank using a set-up similar to that described in [12, 13]. Two broadband ultrasonic transducers with centre frequency of 1.5 MHz were used to cover the frequency range of 0.5–2 MHz, one as the transmitter and the other as the receiver. The nominal active diameter of the transducers is 12 mm. The transmitting transducer was driven by a DPR35 Pulser/Receiver and the received signal was fed to a digital oscilloscope (Tektronix TDS 460A with fast Fourier transform analysis capabilities).
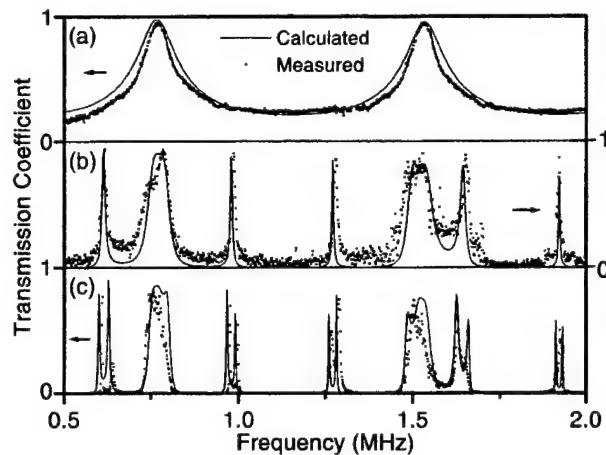
Figure 3. Calculated and measured transmission coefficients as functions of frequency for finite periodic structures containing two sublayers in the unit cell. The thickness values of the two sublayers are the same as those in figure 2(a): (a) a structure with only one unit cell, (b) a structure with two unit cells and (c) a structure with three unit cells.
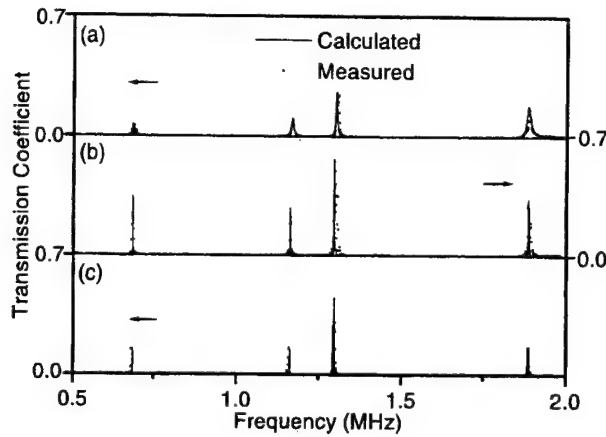

Figure 4. Calculated and measured transmission coefficients as functions of frequency for finite structures containing four sublayers in the unit cell. The thickness values of the four sublayers are the same as those in figure 2(b): (a) a structure with only one unit cell, (b) a structure with two unit cells and (c) a structure with three unit cells.

A ten-signal average scheme was used to improve the signal-to-noise ratio and the reference signal of water was subtracted in the data processing stage.

Figure 3 shows the calculated and measured frequency spectra of the transmission coefficient for structures consisting of one, two and three cells with each unit cell containing only one layer of glass and one layer of water. Good agreement was obtained between the measured and calculated spectra of the transmission coefficient. Gibbs-type oscillations are seen in the passband for the case shown in figure 3(c), which is consistent with that of [12].

Figure 4 is for the case with four sublayer unit cells, i.e., two layers of water and two layers of glass arranged alternately in the cell. The unit cell size and the volume ratio of the two types of materials were kept the same as the case shown in figure 3. It is interesting to note that a band structure with two narrow passbands can be seen with only one unit

Figure 5. Calculated and measured transmission coefficients as functions of frequency for finite structures containing six sublayers in the unit cell. The thickness values of the six sublayers are the same as those in figure 2(c): (a) a structure with only one cell, (b) a structure with two cells and (c) a structure with three unit cells.

cell. The results also suggest that two unit cells appear to be enough to provide well defined bandgaps (figure 4(b)). This is a significant finding because the total thickness of the structure allowed in real applications is always limited.

The band structure of the six sublayers unit cell systems (i.e. three layers of water and three layers of glass) is shown in figure 5. The period and the volume ratio of the two types of materials were kept the same as for the cases shown in figures 3 and 4. Narrower passbands than those of figures 3 and 4 were obtained in the frequency range of 0.5–2 MHz, which is consistent with the dispersion relation for an infinite system (figure 2(c)). The predicted small peak centred at about 1.38 MHz has a very weak intensity and could not be detected in the experiments.

4. Conclusions

Acoustic bandgaps produced by periodic structures originate from multiple reflections at the interface due to the impedance mismatch between the adjacent materials. In this investigation, we subdivided the unit cell into several different sublayers, which can alter the band structures. Using the transfer matrix method and Floquet's theorem, the dispersion relations were derived for infinite periodic structures with the unit cell containing arbitrary number of sublayers made of different materials with different thickness. Numerical calculations were performed for the cases with unit cells containing two, four and six sublayers made of glass and water. The results showed that narrow passbands are produced when the unit cell is subdivided into more than four sublayers. The ratio of the total stopband width versus passband width increases significantly from the case of two sublayer cells to the case of six sublayer cells. These theoretical results were confirmed by the measurements of the frequency spectrum of the transmission coefficient for several finite structures. Our results showed that it is possible to produce high-quality acoustic filters with very narrow passbands using less than three cells when the unit cell is subdivided into more than four layers.

Appendix

The expression of $(A + D)$ in equation (6) for different numbers of sublayers in one unit cell.

(1) Each cell contains two sublayers:

$$A + D = \cos(k_1d_1)\cos(k_2d_2)$$
$$+ \frac{1}{2}\left(\frac{z_1}{z_2} + \frac{z_2}{z_1}\right)\sin(k_1d_1)\sin(k_2d_2). \tag{A1}$$

(2) Each cell contains four sublayers:

$$A + D = \cos(k_1d_1)\cos(k_2d_2)\cos(k_3d_3)\cos(k_4d_4)$$
$$- \frac{1}{2}\left(\frac{z_1}{z_2} + \frac{z_2}{z_1}\right)\sin(k_1d_1)\sin(k_2d_2)\cos(k_3d_3)\cos(k_4d_4)$$
$$- \frac{1}{2}\left(\frac{z_2}{z_3} + \frac{z_3}{z_2}\right)\sin(k_2d_2)\sin(k_3d_3)\cos(k_1d_1)\cos(k_4d_4)$$
$$- \frac{1}{2}\left(\frac{z_3}{z_4} + \frac{z_4}{z_3}\right)\sin(k_3d_3)\sin(k_4d_4)\cos(k_1d_1)\cos(k_2d_2)$$
$$- \frac{1}{2}\left(\frac{z_1}{z_3} + \frac{z_3}{z_1}\right)\sin(k_1d_1)\sin(k_3d_3)\cos(k_2d_2)\cos(k_4d_4)$$
$$- \frac{1}{2}\left(\frac{z_2}{z_4} + \frac{z_4}{z_2}\right)\sin(k_2d_2)\sin(k_4d_4)\cos(k_1d_1)\cos(k_3d_3)$$
$$+ \frac{1}{2}\left(\frac{z_1z_3}{z_2z_4} + \frac{z_2z_4}{z_1z_3}\right)\sin(k_1d_1)\sin(k_2d_2)$$
$$\times \sin(k_3d_3)\sin(k_4d_4). \tag{A2}$$

(3) Each cell contains six sublayers:

$$A + D = \cos(k_1d_1)\cos(k_2d_2)\cos(k_3d_3)\cos(k_4d_4)\cos(k_5d_5)$$
$$\times \cos(k_6d_6) - \frac{1}{2}\left(\frac{z_1}{z_2} + \frac{z_2}{z_1}\right)\sin(k_1d_1)\sin(k_2d_2)$$
$$\times \cos(k_3d_3)\cos(k_4d_4)\cos(k_5d_5)\cos(k_6d_6)$$
$$- \frac{1}{2}\left(\frac{z_2}{z_3} + \frac{z_3}{z_2}\right)\sin(k_2d_2)\sin(k_3d_3)\cos(k_1d_1)\cos(k_4d_4)$$
$$\times \cos(k_5d_5)\cos(k_6d_6) - \frac{1}{2}\left(\frac{z_3}{z_4} + \frac{z_4}{z_3}\right)\sin(k_3d_3)$$
$$\times \sin(k_4d_4)\cos(k_1d_1)\cos(k_2d_2)\cos(k_5d_5)\cos(k_6d_6)$$
$$- \frac{1}{2}\left(\frac{z_1}{z_3} + \frac{z_3}{z_1}\right)\sin(k_1d_1)\sin(k_3d_3)\cos(k_2d_2)\cos(k_4d_4)$$
$$\times \cos(k_5d_5)\cos(k_6d_6) - \frac{1}{2}\left(\frac{z_2}{z_4} + \frac{z_4}{z_2}\right)\sin(k_2d_2)$$
$$\times \sin(k_4d_4)\cos(k_1d_1)\cos(k_3d_3)\cos(k_5d_5)\cos(k_6d_6)$$
$$- \frac{1}{2}\left(\frac{z_1}{z_4} + \frac{z_4}{z_1}\right)\sin(k_1d_1)\sin(k_4d_4)\cos(k_2d_2)\cos(k_3d_3)$$
$$\times \cos(k_5d_5)\cos(k_6d_6) - \frac{1}{2}\left(\frac{z_1}{z_5} + \frac{z_5}{z_1}\right)\sin(k_1d_1)$$
$$\times \sin(k_5d_5)\cos(k_2d_2)\cos(k_3d_3)\cos(k_4d_4)\cos(k_6d_6)$$
$$- \frac{1}{2}\left(\frac{z_1}{z_6} + \frac{z_6}{z_1}\right)\sin(k_1d_1)\sin(k_6d_6)\cos(k_2d_2)\cos(k_3d_3)$$

$$\times \cos(k_4 d_4)\cos(k_5 d_5) - \frac{1}{2}\left(\frac{z_2}{z_5}+\frac{z_5}{z_2}\right)\sin(k_2 d_2)$$

$$\times \sin(k_5 d_5)\cos(k_1 d_1)\cos(k_3 d_3)\cos(k_4 d_4)\cos(k_6 d_6)$$

$$-\frac{1}{2}\left(\frac{z_2}{z_6}+\frac{z_6}{z_2}\right)\sin(k_2 d_2)\sin(k_6 d_6)\cos(k_1 d_1)\cos(k_3 d_3)$$

$$\times \cos(k_4 d_4)\cos(k_5 d_5) - \frac{1}{2}\left(\frac{z_3}{z_5}+\frac{z_5}{z_3}\right)\sin(k_3 d_3)$$

$$\times \sin(k_5 d_5)\cos(k_1 d_1)\cos(k_2 d_2)\cos(k_4 d_4)\cos(k_6 d_6)$$

$$-\frac{1}{2}\left(\frac{z_3}{z_6}+\frac{z_6}{z_3}\right)\sin(k_3 d_3)\sin(k_6 d_6)\cos(k_1 d_1)\cos(k_2 d_2)$$

$$\times \cos(k_4 d_4)\cos(k_5 d_5) - \frac{1}{2}\left(\frac{z_4}{z_5}+\frac{z_5}{z_4}\right)\sin(k_4 d_4)$$

$$\times \sin(k_5 d_5)\cos(k_1 d_1)\cos(k_2 d_2)\cos(k_3 d_3)\cos(k_6 d_6)$$

$$-\frac{1}{2}\left(\frac{z_4}{z_6}+\frac{z_6}{z_4}\right)\sin(k_4 d_4)\sin(k_6 d_6)\cos(k_1 d_1)\cos(k_2 d_2)$$

$$\times \cos(k_3 d_3)\cos(k_5 d_5) + \frac{1}{2}\left(\frac{z_5}{z_6}+\frac{z_6}{z_5}\right)\sin(k_5 d_5)$$

$$\times \sin(k_6 d_6)\cos(k_1 d_1)\cos(k_2 d_2)\cos(k_3 d_3)\cos(k_4 d_4)$$

$$+\frac{1}{2}\left(\frac{z_1 z_3}{z_2 z_4}+\frac{z_2 z_4}{z_1 z_3}\right)\sin(k_1 d_1)\sin(k_2 d_2)\sin(k_3 d_3)$$

$$\times \sin(k_4 d_4)\sin(k_5 d_5)\cos(k_6 d_6) + \frac{1}{2}\left(\frac{z_1 z_3}{z_2 z_6}+\frac{z_2 z_6}{z_1 z_3}\right)$$

$$\times \sin(k_1 d_1)\sin(k_2 d_2)\sin(k_3 d_3)\sin(k_6 d_6)\cos(k_4 d_4)$$

$$\times \cos(k_5 d_5) + \frac{1}{2}\left(\frac{z_2 z_5}{z_1 z_4}+\frac{z_1 z_4}{z_2 z_5}\right)\sin(k_1 d_1)\sin(k_2 d_2)$$

$$\times \sin(k_4 d_4)\sin(k_5 d_5)\cos(k_3 d_3)\cos(k_6 d_6)$$

$$+\frac{1}{2}\left(\frac{z_3 z_5}{z_1 z_4}+\frac{z_1 z_4}{z_3 z_5}\right)\sin(k_1 d_1)\sin(k_3 d_3)\sin(k_4 d_4)$$

$$\times \sin(k_5 d_5)\cos(k_2 d_2)\cos(k_6 d_6) + \frac{1}{2}\left(\frac{z_2 z_6}{z_1 z_4}+\frac{z_1 z_4}{z_2 z_6}\right)$$

$$\times \sin(k_1 d_1)\sin(k_2 d_2)\sin(k_4 d_4)\sin(k_6 d_6)\cos(k_3 d_3)$$

$$\times \cos(k_5 d_5) + \frac{1}{2}\left(\frac{z_3 z_6}{z_1 z_4}+\frac{z_1 z_4}{z_3 z_6}\right)\sin(k_1 d_1)\sin(k_3 d_3)$$

$$\times \sin(k_4 d_4)\sin(k_6 d_6)\cos(k_2 d_2)\cos(k_5 d_5)$$

$$+\frac{1}{2}\left(\frac{z_2 z_6}{z_1 z_5}+\frac{z_1 z_5}{z_2 z_6}\right)\sin(k_1 d_1)\sin(k_2 d_2)\sin(k_5 d_5)$$

$$\times \sin(k_6 d_6)\cos(k_3 d_3)\cos(k_4 d_4) + \frac{1}{2}\left(\frac{z_3 z_6}{z_1 z_5}+\frac{z_1 z_5}{z_3 z_6}\right)$$

$$\times \sin(k_1 d_1)\sin(k_3 d_3)\sin(k_5 d_5)\sin(k_6 d_6)\cos(k_2 d_2)$$

$$\times \cos(k_4 d_4) + \frac{1}{2}\left(\frac{z_4 z_6}{z_1 z_5}+\frac{z_1 z_5}{z_4 z_6}\right)\sin(k_1 d_1)\sin(k_4 d_4)$$

$$\times \sin(k_5 d_5)\sin(k_6 d_6)\cos(k_2 d_2)\cos(k_3 d_3)$$

$$+\frac{1}{2}\left(\frac{z_3 z_5}{z_2 z_4}+\frac{z_2 z_4}{z_3 z_5}\right)\sin(k_2 d_2)\sin(k_3 d_3)\sin(k_4 d_4)$$

$$\times \sin(k_5 d_5)\cos(k_1 d_1)\cos(k_6 d_6) + \frac{1}{2}\left(\frac{z_3 z_6}{z_2 z_4}+\frac{z_2 z_4}{z_3 z_6}\right)$$

$$\times \sin(k_2 d_2)\sin(k_3 d_3)\sin(k_4 d_4)\sin(k_6 d_6)\cos(k_1 d_1)$$

$$\times \cos(k_5 d_5) + \frac{1}{2}\left(\frac{z_3 z_6}{z_2 z_5}+\frac{z_2 z_5}{z_3 z_6}\right)\sin(k_2 d_2)\sin(k_3 d_3)$$

$$\times \sin(k_5 d_5)\sin(k_6 d_6)\cos(k_1 d_1)\cos(k_4 d_4)$$

$$+\frac{1}{2}\left(\frac{z_4 z_6}{z_2 z_5}+\frac{z_2 z_5}{z_4 z_6}\right)\sin(k_2 d_2)\sin(k_4 d_4)\sin(k_5 d_5)$$

$$\times \sin(k_6 d_6)\cos(k_1 d_1)\cos(k_3 d_3) + \frac{1}{2}\left(\frac{z_4 z_6}{z_3 z_5}+\frac{z_3 z_5}{z_4 z_6}\right)$$

$$\times \sin(k_3 d_3)\sin(k_4 d_4)\sin(k_5 d_5)\sin(k_6 d_6)\cos(k_1 d_1)$$

$$\times \cos(k_2 d_2) - \frac{1}{2}\left(\frac{z_1 z_3 z_5}{z_2 z_4 z_6}+\frac{z_2 z_4 z_6}{z_1 z_3 z_5}\right)\sin(k_1 d_1)$$

$$\times \sin(k_2 d_2)\sin(k_3 d_3)\sin(k_4 d_4)\sin(k_5 d_5)\sin(k_6 d_6).$$

$$(A3)$$

References

[1] Yablonovitch E 1987 *Phys. Rev. Lett.* **58** 2059
John S 1987 *Phys. Rev. Lett.* **58** 2486
[2] Soukoulis C M 1993 Photonic band gaps and localization
(NATO ASI, Ser. B, vol 308) (New York: Plenum)
Ho K M, Chan C T and Soukoulis C M 1990 *Phys. Rev. Lett.*
65 3152
Leung K M and Liu Y F 1990 *Phys. Rev. Lett.* **65** 2646
Sigalas M M, Economou E N and Kafesaki M 1994
Phys. Rev. B **50** 3393
[3] Sheng P (ed) 1990 *Scattering and Localization of Classical
Waves in Random Media* (Singapore: World Scientific)
[4] Sigalas M M and Economou E N 1992 *J. Sound Vib.* **158** 337
[5] Kushwaha M S, Halevi P, Dobrzynski L and
Djafari-Rouhani B 1993, *Phys. Rev. Lett.* **71** 2022
[6] Cao W and Qi W K 1995 *J. Appl. Phys.* **78** 4627
[7] Kushwaha M S and Djafari-Rouhani B 1998 *J. Appl. Phys.*
84 4677
[8] Potel C and Belleval J F 1993 *J. Acoust. Am.* **93** 2669
[9] Sigalas M M and Economou E N 1996 *Europhys. Lett.* **36** 241
[10] Martinez-Sala R, Sancho J, Sanchez J V, Gomez V, Llinares J
and Meseguer F 1995 *Nature* **378** 241
[11] Montero de Espinosa F R, Jimenez E and Torres M 1998
Phys. Rev. Lett. **80** 1208
[12] James R, Woodley S M, Dyer C M and Humphrey V F 1995
J. Acoust. Soc. Am. **97** 2041
[13] Parmley S, Zobrist T, Clough T, Perez-Moller A, Makela M
and Yu R 1995 *Appl. Phys. Lett.* **67** 777
[14] Weaver R L 1990 *Wave Motion* **12** 129
Weaver R L 1993 *Phys. Rev.* B **47** 1077
[15] Wang Y, Schmidt E and Auld B A 1986 *Proc. IEEE 1986
Ultrasonic Symp.* p 685

APPENDIX 45

Fabrication and characterization of three-dimensional periodic ferroelectric polymer-silica opal composites and inverse opals

T.-B. Xu, Z.-Y. Cheng,[a) and Q. M. Zhang
Materials Research Laboratory, The Pennsylvania State University, University Park, Pennsylvania 16802

R. H. Baughman, C. Cui, A. A. Zakhidov, and J. Su[b)
Honeywell International, 101 Columbia Road, Morristown, New Jersey 07962

Using a high temperature solution infiltration process, ferroelectric poly(vinylidene fluoride-trifluoroethylene) copolymer is infiltrated into three-dimensional (3D) periodic opal lattices with the silica opal diameters of 180, 225, and 300 nm to form periodic composite structures. By etching out the silica opal, inverse copolymer opals can be fabricated, which retains the 3D periodic structure of the original silica opal lattice. In addition to the optical observation, x-ray diffraction and dielectric study were carried out to characterize the change in the ferroelectric behavior of the composites and inverse opals. Although the copolymer in the composites and inverse opals remains ferroelectric, the ferroelectric transition in the composites and inverse opal becomes diffused and moves to a lower temperature, which is due to the random stress introduced by the irregular voids and interfaces and may be made use of to facilitate the transformation of the copolymer into a relaxor. These results suggest the feasibility of using ferroelectric copolymer to form 3D photonic crystals. © *2000 American Institute of Physics.* [S0021-8979(00)04713-7]

I. INTRODUCTION

This article reports the experimental results on the change of transitional behaviors of ferroelectric poly(vinylidene fluoride-trifluoroethylene) [P(VDF-TrFE)] copolymer infiltrated in three-dimensional periodic SiO_2 opals and in the inverse opal. The motivation for this study is to examine the feasibility of using ferroelectric polymer to form three-dimensional (3D) periodic structure for field tunable photonic crystals.[1–3] One of the interesting issues in the research of photonic crystals is how to tune the band structure over a large wavelength range.[4,5] This can be achieved by tuning the refractive index of the lattice with an external electric field or magnetic field. However, in most of the dielectric materials the change of refractive index with these fields is relatively small, typically on the order of 10^{-3},[6] which may not provide a large enough change required for the tuning of the band structure of the lattice. Another approach to tuning the band structure is to use the lattice strain of the crystal, which can be induced by external fields.[4,5] Recently, we reported the finding that a massive electrostrictive strain, ~5%, can be induced in high energy electron irradiated P(VDF-TrFE) copolymers.[7] As has been shown recently in theoretical studies, such a large lattice strain can induce a large change in the band structure of photonic crystals.[4,5]

A photonic crystal made of these P(VDF-TrFE) copolymers may be realized by infiltrating these polymers into three dimensional periodic SiO_2 opal to form a composite, then etching out the SiO_2 and filling the replica (inverse opal made of polymers) with high dielectric constant fluids. As a first step in this direction, in this article we investigate the method to infiltrate the copolymer into 3D silica opals and how the ferroelectric transitional behaviors in this class of polymers are influenced by the SiO_2 opal matrix and interfaces.

When infiltrated into SiO_2 matrix, P(VDF-TrFE) copolymers will experience mechanical constraints and finite dimensions due to the opal structures. For a ferroelectric polymer, it is well known that the ferroelectric properties are sensitive to the external stress, interface conditions, and finite size effect. Therefore, the infiltrated P(VDF-TrFE) copolymer-SiO_2 opal composites also provide an interesting system for the study of these effects on the ferroelectric behavior of the polymers.

In this article, the fabrication process for the P(VDF-TrFE) infiltrated silica opal composite and for the three-dimensional ordered pure copolymer replica (inverse opal) is reported first. Then the results from x-ray and dielectric measurement, which are used to characterize the changes in the structures and transitional behaviors in the copolymer, are presented.

II. EXPERIMENT

The details on the fabrication process and properties of the silica opal used in this investigation have been reported in Ref. 8. Three different silica opals with the diameter of the silica sphere of 180, 225, and 300 nm were used in this study. Based on the results of the electrostrictive behavior of P(VDF-TrFE) copolymers, the copolymer with 55 mol% of VDF was chosen to be infiltrated into silica opal which has a fcc lattice structure.[7,8] The copolymer pellets were purchased

[a)]Author to whom correspondence should be addressed; electronic mail: zxc7@psu.edu

[b)]Current address: Advanced Materials and Processing, NASA-Langley Research Center, Hampton, VA 23681.

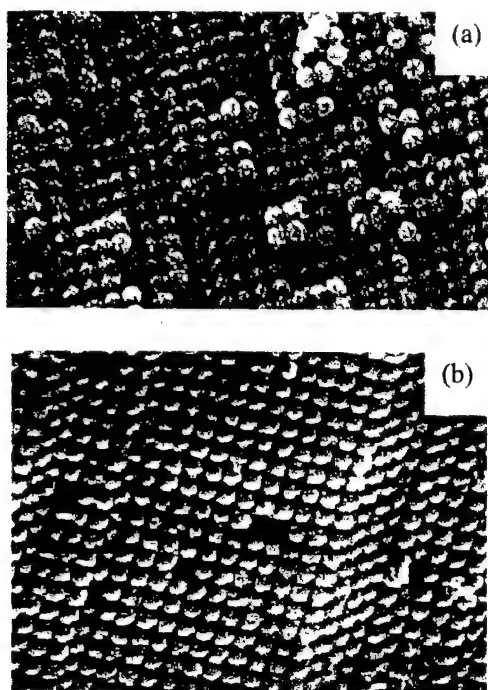406   J. Appl. Phys., Vol. 88, No. 1, 1 July 2000

Xu *et al.*

FIG. 1. SEM micrograph from fractured surface of (a) pure opal of 300 nm in diameter and (b) copolymer-opal composite where the diameter of the opal is 225 nm.

composite was further evacuated to vacuum at an elevated temperature (near the melting point of the copolymer) to ensure a nearly complete filling of the copolymer into the opal. As shown by the scanning electron microscopy (SEM) micrograph taken from the fractured surface in the middle section of infiltrated opal samples thus prepared (opal-polymer composites) (Fig. 1), the copolymer indeed fills the voids of the opal lattice. The density measurement of the composites indicates that more than 90% of the voids are filled by the copolymer. For the comparison, a pure 55/45 copolymer bulk sample was also prepared using the same solvent and sample preparation procedure.

A freestanding three-dimensional periodic polymer structure (copolymer inverse opal) can be obtained by etching out the silica in the composites using 24% aqueous hydrofluoric acid (HF) for 20 h (near by 100% of silica was removed). Under a white light, the copolymer inverse opal shows the similar color pattern as the original opal when immersed in water (Fig. 2). The color display is due to the Bragg diffraction from the periodic lattice.[11] The results indicate that the copolymer inverse opal retains the periodicity of the original opal. The color observed in Fig. 2 depends on the crystal domain orientation with respect to the light source and observer. For the copolymer inverse opal, it was ob-

from Ktech Corp. NM. For such a fcc lattice, there are two different voids existing between silica spheres: one has an opening of about 0.4D and the other has a smaller opening of about 0.2D, where D is the diameter of the silica sphere.[9] In order to infiltrate the copolymer into these narrow spaces, a high temperature solution infiltration process was developed.

The solvent used was cyclohexanone which has a high solubility for P(VDF-TrFE) copolymers. In order to minimize the influence of the solvent, a high concentration solution (50 wt.% of copolymer) was made and it was found that at this concentration the copolymer can be dissolved completely when solution temperatures are higher than 100 °C. The infiltration was carried out at a temperature between 155 and 160 °C, which is slightly above the boiling point of the solvent (~155 °C) and also higher than the melting point of the copolymer (based on the differential scanning calorimetry (DSC) measurement with a scanning rate of 10 °C/min, the melting point for the copolymer studied here is ~147 °C).[10] At these temperatures, the solution exhibits very low viscosity required for the infiltration. In the infiltration process, the opal and solution were kept in a closed glass system that has a water cooled condenser at the top to recycle the solvent. The filling of the opal by the solution can be monitored by observing the change in the transparency of the opal when cooled down to room temperature. A complete infiltration should result in a highly transparent opal-solution system at room temperature. It was found that after 16 h of infiltration, the opal-solution system became completely transparent. After that, the glass system was opened while still being kept at high temperature for another 4 h to let the solvent evaporate and copolymer fill into the opal (filling in the space occupied by the solvent). The copolymer-opal
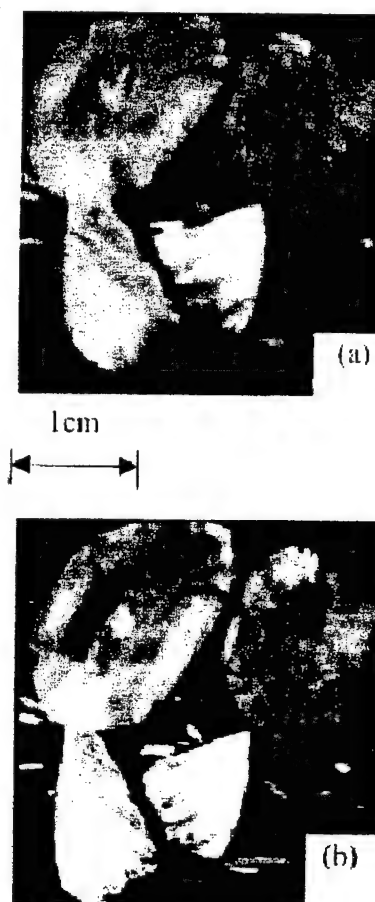

1 cm

FIG. 2. (Color) Display of several inverse opals under white incident light at different observation angles. There is a large color change between the pictures in (a) and (b), which is due to the Bragg diffraction from the periodic lattice.
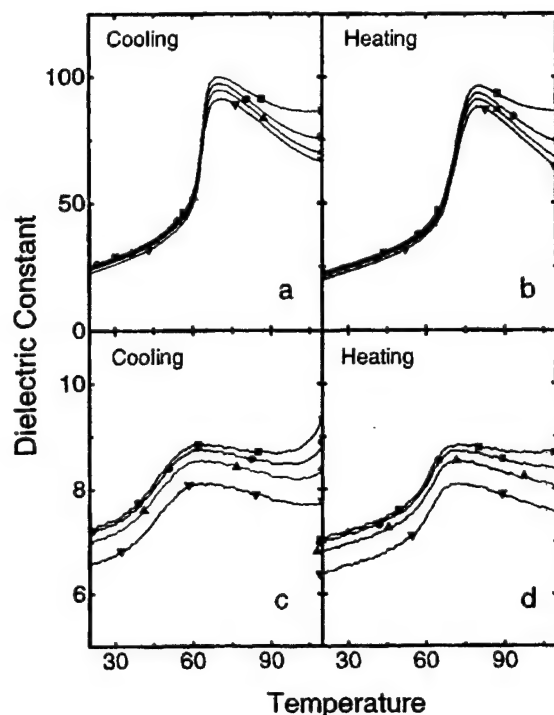
FIG. 3. Dielectric constant as a function of temperature of (a) and (b) for pure copolymer and (c) and (d) for copolymer-opal composite where the diameter of the opal is 300 nm. The data were taken from cooling [(a) and (c)] and heating [(b) and (d)] scans. The curves from top to bottom in each figure correspond to the dielectric constant measured at different frequencies: 1 kHz (squares), 2 kHz (dots), 4 kHz (triangles), and 10 kHz (inverse triangles).

FIG. 4. Dielectric constant (10 kHz) as a function temperature of composites and pure copolymer to show the temperature shift in the PE-FE transition. The solid line is for the pure copolymer, dot, dash, and dash dot are the data from the composites with the opal diameter of 180, 225, and 300 nm, respectively.

served that the color displayed changes as the observation angle was varied [Figs. 2(a) and 2(b)], indicating that it is from 3D periodic structure.[11]

The x-ray diffraction of the opal-copolymer composites and copolymer inverse opal was taken to characterize any changes in the copolymer structure. The measurement was carried out at room temperature by a Scintag diffractometer (model PAD-V) with Ni filtered Cu $K\alpha$ radiation. For the same composite, the x-ray measurement was repeated several times on different samples to ensure the reproducibility of the data. For the dielectric constant measurement of opal-copolymer composites, gold electrodes were sputtered on both surfaces of the samples and the dielectric constant was measured using a dielectric analyzer (TA Instrument, model No. 2970) in the temperature range from −60 to 110 °C with a scanning rate of 2 °C/min. In order to observe any hysteresis associated with the ferroelectric-paraelectric (PE-FE) transition, both heating and cooling scans were performed in the dielectric measurement.

III. DIELECTRIC PROPERTIES AND X-RAY DIFFRACTION DATA

The temperature dependence of the dielectric properties of the pure 55/45 copolymer and the three copolymer-opal composites fabricated are presented in Figs. 3 and 4. The data reveal that there is a large drop in the dielectric constant in the composites compared with the pure copolymer. This is
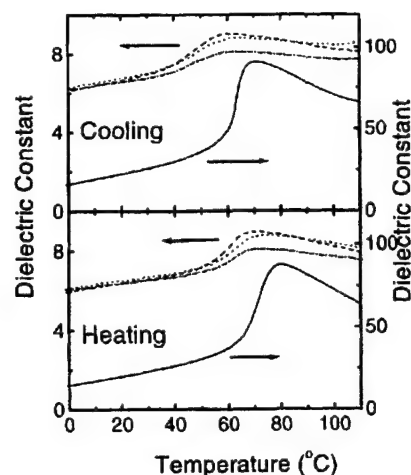
due to the small dielectric constant of the silica, which is 3.9; in the silica opal-copolymer composite, silica occupies about 74% volume of the total composite.[9]

For a composite structure such as the one studied here, there is no simple relationship between the dielectric constant of the composite and properties of the constituents. Here we compare the dielectric constants measured at 10 kHz, which do not have a significant contribution from the space charge effect, with those predicted from several simple models or empirical relation (Table I). In Table I, the calculated dielectric constants are obtained from the series model, parallel model, and the logarithmic mixing law.[12,13] In the series model, the silica opal and copolymer are assumed to be electrically in series, which should underestimate the dielectric constant of the composite. On the other hand, in the parallel model, the two constituents are assumed to be electrically parallel, which overestimates the dielectric constant of the composite. In addition, it has been observed that in many ceramic powder-polymer composites where the high dielectric constant ceramic forms isolated inclusions in a three-dimensionally connected low dielectric constant matrix, the logarithmic mixing law can describe quite well the dependence of the dielectric constant K of the composite on the properties of the constituents[13]

TABLE I. Measured dielectric constants at 10 kHz for the pure copolymer and the composites with different opal sizes. The data were taken at 20 °C during heating and cooling, respectively.

Materials	Heating	Cooling
Pure copolymer	23.0	25.3
300 nm opal	7.06	7.24
225 nm opal	7.03	7.24
180 nm opal	7.30	7.50
Parallel model	8.93	9.53
Series model	5.09	5.12
Logarithmic mixing Law [Eq. (1)]	6.29	6.46

$$\log K = v_1 \log K_1 + (1 - v_1) \log K_2, \qquad (1)$$

where K_1 and K_2 are the dielectric constants and v_1 and v_2 are the volume fractions of the two constituents, respectively. For the composite system studied here, both the high dielectric constant polymer and low dielectric constant opal form 3D linked phases which are different from the power-matrix composite and hence, Eq. (1) may also underestimate the dielectric constant of the composite here. Indeed, as can be seen from the table, both the series model and logarithmic mixing law underestimate the dielectric constant of the composites, while the parallel model overestimates the dielectric constant value. These results verify that the copolymer has nearly completely infiltrated the silica opal to form a three-dimensionally connected structure.

What is more interesting in the data in Fig. 4 is that there is a large shift in the dielectric constant peak associated with PE-FE transition, which is about 75 °C (averaged PE-FE temperature from the heating and cooling cycles). The PE-FE transition temperature drops about 10 °C in the composites compared with pure copolymer. In addition, the dielectric constant peak becomes much broader in the composites. Besides these, the frequency dispersion of the dielectric constant in the composites is also much different from that in the pure copolymer. At high temperature, the strong dispersion in both composite and pure copolymer is related to the conducting behavior of the material possibly due to the residual solvent trapped in the material. That is why the dielectric constant, especially at low frequency, may increase with temperature at a higher temperature. The lower the temperature is, the smaller is the contribution of the conducting behavior to the dielectric constant. In addition, in the ferroelectric phase, the electric carriers may be trapped at the domain wall or the surface of the crystalline area due to the strong spontaneous polarization. Therefore, the contribution of the conductivity to the dielectric dispersion is very small at the temperatures lower than FE-PE transition. The small dispersion observed in the pure copolymer at low temperature originates from the α-relaxation process.[14] However, at low temperature, a much strong dispersion was observed in the composites. The dispersion observed here in the composites is presumably due to the space charge phenomenon because of the large difference in the dielectric constant and loss between the silica and copolymer which exists at all the temperatures.[15] That is why the dispersion in composites before and after phase transition is very similar.

Several effects in the composite can cause such a drop in PE-FE transition temperature in the copolymer. For the copolymers in the opal matrix, due to the difference of the thermal expansion coefficients between the two materials (copolymer has a higher thermal expansion coefficient),[14,16] there exists a tensile stress in the copolymer when cooled down from the fabrication temperature to room temperature. This tensile force would favor the high temperature phase (favor the phase with a large unit cell volume and for the copolymer here, the paraelectric phase has larger unit cell volume than that of the ferroelectric phase).[14] As a result, this will shift the PE-FE temperature to a lower temperature.[17] On the other hand, when trapped in the silica opal
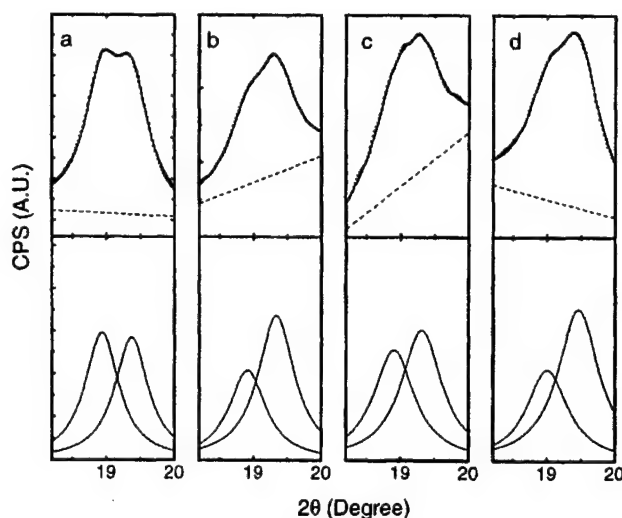

FIG. 5. X-ray diffraction of (200, 110) reflections of (a) pure copolymer, (b) copolymer-opal composite with the opal diameter of 300 nm, (c) composite with the opal diameter of 180 nm, and (d) the pure copolymer inverse opal from the composite with opal diameter of 300 nm. The top panels are the experimental data (dots) and fitting to the data (solid lines) where the dashed lines are background signals. In (b) and (c), there is a large reflection peak due to SiO_2 opal at 2θ angle just above 20° which causes the change in the background signals. The bottom panels are details of the fitting of two-peak structure (the parameters are listed in Table II) to the x-ray data.

matrix, the growth of crystalline phase of the copolymer will be subjected to the constraints of the opal matrix, which is different from the natural growth conditions when there are no constraints. These constraints may act as a "random" field that reduces the crystalline ordering and coherence of the polarization. Consequently, the transition will also be moved to a lower temperature and the transition region will be broadened. From the broadening of the observed dielectric peak, it is clear that this random defect effect exists in the copolymer of the composites.

In order to assess how large the effect of the thermal expansion coefficient mismatch between the silica opal and infiltrated copolymer is, an x-ray diffraction experiment was conducted to measure the possible lattice constant change of the copolymers in composites compared with the pure copolymer. The data for (110, 200) reflections is presented in Fig. 5 and fitting parameters to the data are listed in Table II. The observed two-peak structure of the x-ray data in the pure copolymer shown in the figure is consistent with the early observation. The lower angle peak is caused by the hexagonal packing of 3/1-helical chains generated by Trans-gauche and Trans-gauché defects, which are due to the presence of domain pattern and the higher angle peak is from the regu-

TABLE II. Summary of the x-ray results.

Materials	Lower angle peak		Higher angle peak	
	Center	FWHM	Center	FWHM
Pure copolymer	18.938	0.619	19.377	0.633
300 nm opal copolymer	18.919	0.650	19.334	0.650
180 nm opal copolymer	18.907	0.749	19.315	0.749
Inverse copolymer opal	19.008	0.933	19.421	0.933

larly packed trans-planar chains (β phase).[14,18] The data in Fig. 5 reveal that there is a slight lattice expansion and also broadening in the peak width for the copolymer in the composites compared with the pure copolymer, especially in the composite with 180 nm size silica opal.

From the data in Table II, the lattice strain can be calculated from the change of the peak position of the higher angle peak between the pure copolymer and the copolymer in the composite, which yields a strain of 2.2×10^{-3} for 300 nm and 3.2×10^{-3} for 180 nm size silica opal composites, respectively. Assuming an isotropic tensile stress exerted to the copolymer and a Poisson's ratio of 0.38 for the crystalline phase, the tensile stress will be 58 and 83 MPa for the two composites, respectively, if the external tensile stress is the only cause for the observed change in the lattice constant. In the calculation, the elastic modulus data were taken from Ref. 19.

For a ferroelectric single crystal, the change of the PE-FE transition temperature with external stress can be evaluated through the electrostrictive coefficient[17]

$$\Delta T = 2\epsilon_0 C Q \Delta \sigma, \qquad (2)$$

where ΔT is the shift of the PE-FE transition temperature, ϵ_0 is permittivity in free space, C is Curie–Weiss constant, σ is the applied stress, and Q is electrostrictive coefficient. If assuming an isotropic stress, the electrostrictive coefficient Q in Eq. (2) should be Q_h, the hydrostatic electrostrictive coefficient, which for the single crystal copolymer is about -1 m^4/C^2.[14] Using $C = 3500$ obtained earlier,[20] one would get $\Delta T = 3.6$ and $5.1\,^{\circ}$C for the 300 and 180 nm silica opal-copolymer composites. Therefore, on the order of magnitude the results here are consistent with the fact that the stress due to the thermal expansion mismatch is partially responsible for the observed shift of the PE-FE transition temperature. This is also consistent with the data in Fig. 4, where in spite of the large drop in the transition temperature in the composite the thermal hysteresis in the composites, which is measured by the difference in the transition temperatures between the data taken from the heating cycle and the data taken from the cooling cycle, is nearly the same as that in the pure copolymer.

The existence of the tensile stress in the copolymers when in silica opal matrix was further confirmed by the change of the lattice constant of the inverse copolymer opal, i.e., the 3D copolymer structure without opal. As shown in Table II, the (110, 200) reflections in the inverse copolymer opal move to a higher angle and the peak becomes even broader. This change in the peak position in the inverse copolymer opal reflects the contraction of the lattice in the directions perpendicular to the polymer chain. Hence, in the inverse copolymer opal, it might be the surface tension due to the free surfaces which causes the observed lattice contraction. The broadening of the peak width in the copolymer-opal composites and inverse copolymer opal are due to the random stress induced by the opal matrix and finite size of the system.

IV. SUMMARY

In summary, a high temperature solution infiltration process was developed to infiltrate P(VDF-TrFE) copolymer into 3D silica opal lattice. The experimental results show that this method is effective in fabricating a copolymer-opal composite and inverse copolymer opal where the copolymer can nearly completely fill the voids in the silica opal and the inverse copolymer opal retains the 3D periodic structure of the original silica opal lattice.

The dielectric and x-ray data performed in the composites and inverse copolymer opal reveal that the copolymer remains in the ferroelectric state, but with a substantial amount of disordering in the copolymer lattice. This disordering causes the broadening of the dielectric peak associated with FE-PE transition and the lowering of the transition temperature. In addition, the existence of the interfaces (either in copolymer-silica opal composites or in the inverse copolymer opal) induces external stresses to the copolymer, also resulting in the changes of FE-PE transition temperature and lattice constant of the copolymer crystallites. These effects may be used to facilitate the conversion of the copolymer from a normal ferroelectric into a relaxor ferroelectric with large electrostrictive strain, as has been observed recently in high energy electron irradiated P(VDF-TrFE) copolymer, where the irradiation introduces random defects to convert the copolymer into a relaxor.[7]

ACKNOWLEDGMENT

[1] S. John, Phys. Rev. Lett. **58**, 2486 (1987); Phys. Today **44**, 32 (1991).
[2] E. Yablonovitch and K. M. Leng, Nature (London) **391**, 667 (1998).
[3] J. D. Joannopoulos, R. Meade, and J. Winn, *Photonic Crystals: Molding the Flow of Light* (Princeton University Press, Princeton, NJ, 1995).
[4] K. Busch and S. John, Phys. Rev. E **58**, 3896 (1998); Phys. Rev. Lett. **83**, 967 (1999).
[5] A. Figotin, Y. A. Godin, and I. Vitebsky, Phys. Rev. B **57**, 2841 (1998).
[6] J. Wilson and J. F. B. Hawkes, *Optoelectronics, An Introduction* (Prentice–Hall, New York, 1988), Chap. 3, p. 183.
[7] Q. M. Zhang, V. Bharti, and X. Zhao, Science **280**, 2101 (1998).
[8] A. A. Zakhidov, R. H. Baughman, Z. Igbal, C. Cui, I. Khayrullin, S. O. Dantas, J. Marti, and V. G. Ralchenko, Science **282**, 897 (1998).
[9] L. Suchow, in *Solid State Chemistry and Physics*, edited by P. F. Weller (Dekker, New York, 1973), Vol. 1, Chap. 2.
[10] F. J. Balta, A. G. Arche, T. A. Ezquerra, C. S. Cruz, F. Batallan, B. Frick, and E. L. Cabarcos, Prog. Polym. Sci. **18**, 1 (1993).
[11] J. V. Sanders, Nature (London) **204**, 1151 (1964).
[12] R. E. Newnham, Annu. Rev. Mater. Sci. **16**, 47 (1987).
[13] H. S. Nalwa, *Ferroelectric Polymers* (Dekker, New York, 1995), Chap. 11.
[14] T. Furukawa, Phase Transit. **18**, 143 (1989).
[15] B. K. P. Scaife, *Principals of Dielectrics* (Clarendon, London, 1989), pp. 105–107.
[16] D. N. Nikogosyan, *Properties of Optical and Laser Related Materials, A Handbook* (Wiley, New York, 1997), Chap. 3.
[17] F. Jona and G. Shirane, *Ferroelectric Crystals* (Pergamon, Oxford, 1962), Chap. 4.
[18] A. J. Lovinger, in *Developments in Crystalline Polymers*, edited by D. C. Bassett (Applied Science, London, 1982), Chap. 5.
[19] K. Omote, H. Ohigashi, and K. Koga, J. Appl. Phys. **81**, 2760 (1997).
[20] V. Bharti, Z.-Y. Cheng, S. Gross, T.-B. Xu, and Q. M. Zhang, Appl. Phys. Lett. **75**, 2653 (1999).

TRANSDUCER STUDIES

Piezoelectric Transformers

APPENDIX 46

PIEZOELECTRIC TRANSFORMERS
- New Perspective -

K. UCHINO, B. KOC, P. LAORATANAKUL
and A. VÁZQUEZ CARAZO
International Center for Actuators and Transducer
Materials Research Laboratory, The Pennsylvania State University
University Park, PA 16802, USA

Piezoelectric transformers have been commercialised for the backlight inverters of laptop computers nowadays. For further high power applications, we developed new PZT based piezoelectric ceramics with the maximum vibration velocity of 0.9 msec. Regarding the design, two new transformers, disk shaped and glass sandwiched types, have advantages over the conventional Rosen type in terms of high voltage step-up ratio and high isolation resistance, respectively. For the application area, we studied on piezoelectric actuator drive system, using piezoelectric transformers, aiming at active vibration control on a helicopter.

Keywords: PZT ceramics, piezoelectric transformer, power supply, vibration control

1. INTRODUCTION

One of the bulkiest components in information processing equipment (such as laptop computers) is the power supply, especially the electromagnetic transformer used in the power supply. Losses such as skin effect, thin wire loss and core loss of the electromagnetic transformer increase rapidly as the size of the transformer is reduced. Therefore, it is difficult to realize miniature low profile electromagnetic transformers with high efficiency. To the contrary, high efficiency, small size, no electromagnetic noise are some of the attractive features of piezoelectric transformers (PTs), making them more suitable for miniaturized power inverter components such as lighting up the cold cathode fluorescent lamp behind a color liquid crystal displays or generating high voltage for air-cleaners [1].

1

The original design to transform an input ac voltage to step up or step down using converse and direct piezoelectric properties of ceramic materials was proposed by Rosen [2]. The principle of this type of transformer is to excite a piezoelectric element (Fig. 1 top) at its mechanical resonance frequency. Applying an electrical input to one part of the piezoelectric element (left top electrode) generates a mechanical vibration and then this mechanical vibration is re-converted into electrical voltage from the other part (right edge electrode) of the piezoelectric plate. The voltage step-up ratio for unloaded condition (open circuited) is provided by

$$r \propto k_{31} k_{33} \, Q_m \, (L/t), \tag{1}$$

where L and t are the electrode gap distances for the input and output parts, respectively. Note that increasing in length/thickness ratio, electromechanical coupling factors and/or mechanical quality factor is the key to the step-up ratio increase. This transformer was utilized on trial in the color TVs in 1970's.
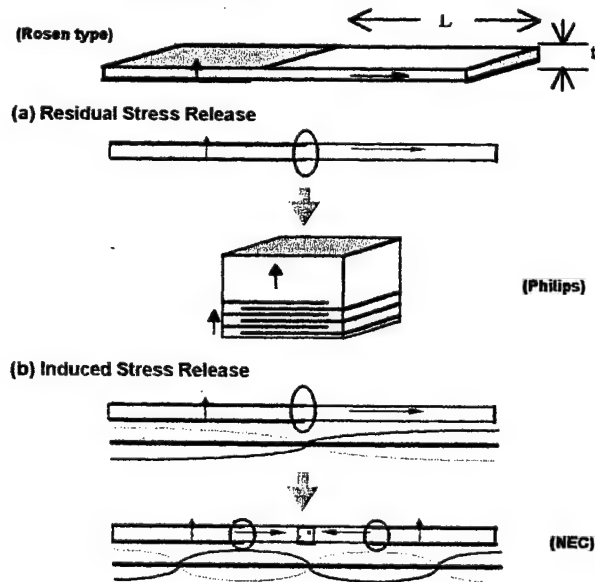
Fig. 1 New piezoelectric transformer designs improved from the Rosen type. (a) multilayer type, and (b) 3rd mode type.

However, the initial Rosen type had a reliability problem; that is, easy mechanical breakdown at the center position due to the coincidence of the residual stress cencentration (through the poling process) and the

2

vibration nodal point (highest induced stress). In addition to improved mechanically tough ceramic materials, by using a multilayer type without generating any poling direction mismatch (Philips Components, NEC [3]), or by redesigning the electrode configuration and exciting a 3rd longitudinal vibration mode of the rectangular plate (NEC) [4], the piezo-transformers shown in Fig. 1 have been commercialized as a back-light inverter for the LCDs.

In order to improve the transformer performance, various proposals have been made: improvement in piezoceramics with higher mechanical toughness and low loss/high Q_m; selection of a vibration mode and an electrode configuration to separate the nodal point from the maximum residual stress point; selection of a vibration mode with higher electromechanical coupling. This paper reviews, first, the recent development of high power piezoelectrics, then describes the present design problems and some possible solutions. We introduce our two new designs, a disk type and a stack type. Finally, we propose a new piezoelectric actuator system driven by piezoelectric transformers.

2. HIGH POWER PIEZOELECTRICS

One of the serious problems in the present transformers is their heat generation. The conventional piezo-ceramics have the limitation in the maximum vibration velocity (v_{max}), more than which all the additionally input electrical energy converts into heat, rather than into mechanical energy. The typical rms value of v_{max} for the commercialized materials, defined by the temperature rise of 20 °C from the room temperature, is around 0.3 m/sec for the rectangular k_{31} samples [5]. Pb(Mn,Sb)O$_3$ (PMS) - lead zirconate tatanate (PZT) ceramics with the v_{max} of 0.62 m/sec have been reported [6]. By doping rare-earth ions such as Yb, Eu and Ce additionally into the PMS-PZT, we recently developed the high power piezoelectrics, which can exhibit the v_{max} up to 0.9 m/sec. Compared with commercially available piezoelectrics, one order of magnitude higher input electrical energy and out mechanical energy can be expected for this new material without generating significant temperature rise.

3. NEW TRANSFORMER DESIGNS

One of the drawbacks of piezo-transformers is a significant reduction of the step-up ratio (Eq. (1)) under an electrical load. This is mainly due to the impedance mismatch between the load and the output impedance

3

of the transformer (i.e., capacitance C_{out}). For instance, a capacitive load C_L (= C_{out}) divides the step-up ratio r by two. Thus, several designs have been proposed in order to increase the step-up ratio.

3.1 Multilayer Transformer
NEC developed a multilayer type transformer as shown in Fig. 2, where a higher voltage step up ratio was realized in proportion to the number of layers in the input part [4].
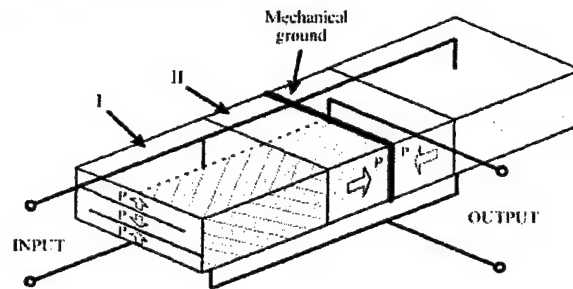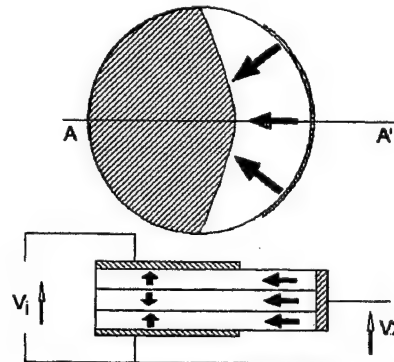

Fig. 2 Multilayer type piezoelectric transformer (NEC).

Fig. 3 Disk shape piezoelectric transformer with curved electrodes.
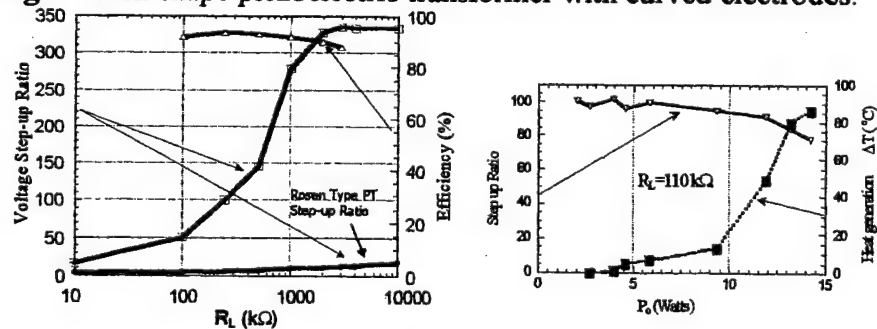
Fig. 4 Characteristics in the disk shape piezoelectric transformer.

4

3.2 Disk Shape Transformer

Disk type transformers in Fig. 3 have advantages over the Rosen type: usage of k_p and k_{15} (due to the curved electrode configuration) instead of k_{31} enhances the step-up ratio, and usage of curved electrodes reduces the stress concentration [7].

Figure 4 shows transformer characteristics for the disk type with 1" in diameter and 1.5 mm in total thickness. Note that a very high voltage step-up ratio 300 (10 times higher than the Rosen type) under unloaded condition can be obtained by sustaining an efficiency more than 90%. The maximum power (20°C temperature rise) is 9 W. We demonstrated lighting up the 2W CCFL directly by 500V without using an additional booster coil.

3.3 Stack Type Transformer

Face International developed a simple stacked piezo-transformer as shown in Fig. 5, which enhanced the power capability by several times of the Rosen-type transformers [8]. During the bonding process, the different thermal conductivity of the involved materials introduces a remained pre-stress in the transformer, which is the key to enhancement of its power capabilities. Power rates higher than 80W with efficiencies around 95% have already been demonstrated.
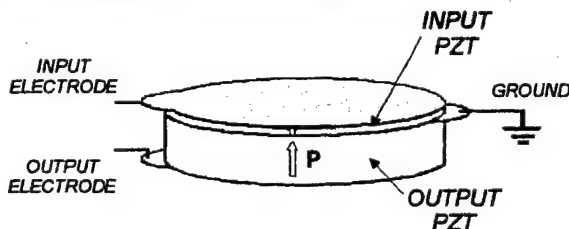

Fig. 5 Stack type power transformer (Face International).
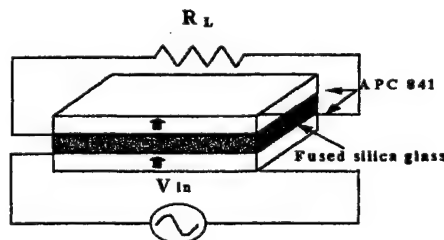

Fig. 6 Construction of a new multistack type transformer for a step-down transformer.

5

A stacked piezo-transformer with a glass plate shown in Fig. 6 is operated in the thickness extensional mode. The merits include complete electric isolation (i.e., floating) owing to the sandwiched glass between the input and output piezo-plates, and high energy density owing to a high operating frequency. Using the 2nd thickness vibration mode at 1.69 MHz, we developed a step-down transformer for the AC adapter.

4. APPLICATIONS

Piezoelectric transformers are classified into basically two groups: resonance and off-resonance types. The off-resonance type is for step-down transformers for precisely measuring a high voltage such as 30 kV or a high current on the electric power transmission lines [9]. The resonance type is further divided into two groups: step-up types typically used as high-voltage inverters for the LCD back-light, and step-down types used as AC adapters (i.e., DC-DC converters) [10].

We propose here a new application, that is, driving piezoelectric actuators. The basic concept is illustrated in Fig. 7. When we tune the transformer operating frequency exactly to the same frequency of an ultrasonic motor's resonance (for example, making a ring transformer, using the same size piezo-ring as the ultrasonic motor), we may use it as a drive system, or fabricate a transformer-integrated motor. When we couple a rectifier with the transformer, we can drive a multilayer or bimorph piezoelectric actuator.
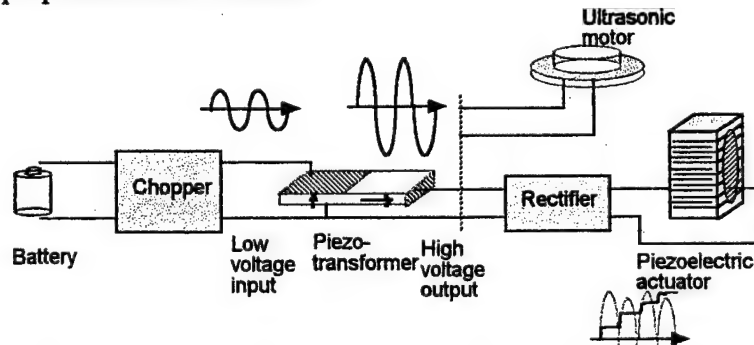

Fig. 7 Basic concept of piezo-actuator drive systems (AC or pseudo DC) using a piezoelectric transformer.

In the following, we introduce a compact drive system with piezoelectric transformers for a multilayer piezoelectric actuator, aiming at active vibration control on a helicopter. In this sort of

6

military application, we need to realize a compact, light-weight and electromagnetic-noise free system with keeping quick response (minimum 200Hz). For this sake, we have chosen a multilayer piezoelectric device as an actuator, and piezo-transformers (rather than electromagnetic transformers) as drive system components. Figure 8 summarizes our compact drive system for piezoelectric actuator control, using piezoelectric transformers.

We have targeted to develop two kinds of power supplies with piezo-transformers driven by a helicopter battery $24V_{DC}$: one is a high voltage DC power supply (100-1000V, 90W) for driving the piezoelectric actuator, and the other is an AC adapter ($\pm 15V_{DC}$, 0.1-0.5W) for driving the supporting circuitry. We utilized large and small multi-stacked piezo-transformer elements both with an insulative glass layer between the input and output parts for ensuring the complete floating condition, for the high power supply and the adapter, respectively. The used actuator was supplied from Tokin Corp., which has the size of $10 \times 10 \times 20 mm^3$, and is capable to generate a 16µm displacement under the maximum voltage of 100V.
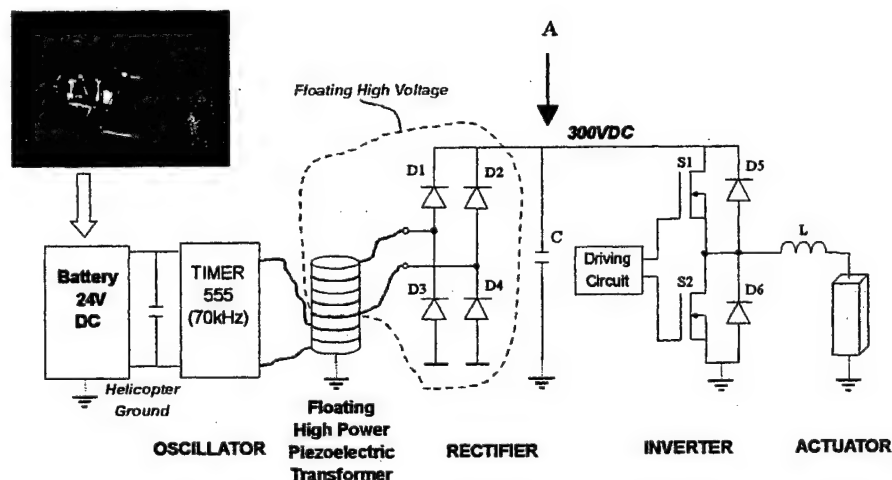

Fig. 8 Compact drive system for piezoelectric actuator control.

We initially tried to drive the actuator by applying the rectified high voltage directly after the power transformer (i.e., voltage at the point A in Fig. 8). However, because of a very slow response during a rising or falling voltage process(~1 sec), we decided to use this rectified voltage

7

as a constant high DC voltage, and additionally use a power amplifier to control the voltage applied to the actuator. Among various power amplifier families [11], we have chosen a Class-D switching amplifier (see the inverter in Fig. 8), because it has some advantages over the other switching and linear amplifiers, such as permitting amplitude and frequency control and realizing fast actuation response of the actuator by chopping a DC voltage. The voltage level generated in the transformer was 300V for the input voltage of 75V applied through a timer 555 (Fig. 8).

The signal from a PWM (pulse width modulation) driving circuit (Fig. 9) was applied to two power MOSFET's of the half bridge. Thus, the constant $300V_{DC}$ voltage from the piezo-transformer was chopped, and control of frequency and magnitude was achieved. This output voltage was applied to the piezo-actuator through a filtering inductance of 100mH [12]. The PWM carrier frequency was chosen as 40kHz, which is below the mechanical resonance frequency of the used piezo-actuator (~60kHz). Figure 10 shows the displacement curves of the actuator driven by the newly developed power amplifier. The displacement was directly measured with an eddy current sensor. As seen in this figure, the displacement $\pm1.5\mu m$ was controlled by $\pm20V$ applied voltage. This drive system could be used at least up to 500Hz, which is sufficient for the active vibration control on a helicopter.
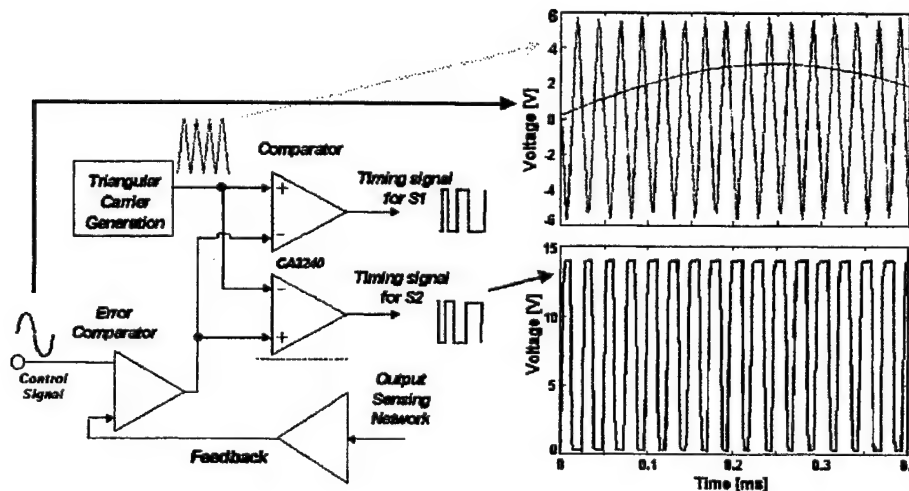
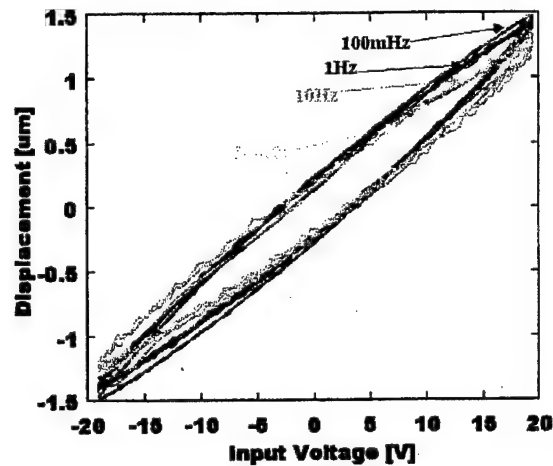**Fig. 9** Pulse width modulation circuit for driving the power amplifier.

8

Fig. 10 Displacement curves of the piezoelectric actuator driven by the newly developed power amplifier.

5. SUMMARY AND FUTURE

1. Piezoelectric transformers have the advantages over electromagnetic types in miniaturization, no electromagnetic noise generation, and high efficiency.

2. New high-power piezoceramics have been developed based on PZT-$Pb(Mn_{1/3}Sb_{2/3})O_3$ doped with Yb, Eu, Ce. The maximum vibration velocity 0.9 m/s is triple higher than the commercialized materials.

3. Using k_p and k_{15}, circular piezo-transformers have been designed, with characteristics; voltage step-up ratio – 10 times of the Rosen type; stress distribution - more uniform than the Rosen type. Using k_{33}, we also developed thickness, float mode piezo-transformer with voltage step-down characteristics which is suitable to the driving circuit power supply.

4. Using piezoelectric transformers, a drive system of a piezo-actuator has been developed, aiming at active vibration control on a helicopter. We manufactured a variable high voltage, DC - slow AC power supply for driving a piezoelectric multilayer actuator, and a constant low voltage DC power supply for the circuit drive.

As future work, we still need more reliable high power piezoelectrics with v_{max} up to 1m/sec and high fracture toughness, better transformer designs with higher efficiency and step-up voltage/current ratio, better designs for the drive circuits, aiming at expanding application areas.

9

References

1. T. Yoshida, "Technology Trend of Piezoelectric Devices," Tokin Technical Review, **24**, p.1-9 (1997).
2. C. A. Rosen, "Ceramic Transformers and Filters," Proc. Electronic Component Symp., p. 205-211 (1956).
3. NEC, "Thickness Mode Piezoelectric Transformer," US Patent No. 5,118,982 (1992).
4. S. Kawashima, O. Ohnishi, H. Hakamata, S. Tagami, A. Fukuoka, T. Inoue and S. Hirose, "Third order longitudinal mode piezoelectric ceramic transformer and its application to high-voltage power inverter," IEEE Int'l Ultrasonic Symp. Proc., Nov. (1994).
5. S. Hirose, S. Takahashi, K. Uchino, M. Aoyagi and Y. Tomikawa, "Measuring Methods for High-Power Characteristics of Piezoelectric Materials," Proc. Mater. for Smart Systems, Mater. Res. Soc. Vol.**360**, p.15-20 (1995).
6. S. Takahashi, Y. Sasaki, S. Hirose and K. Uchino, "Electromechanical Properties of $PbZrO_3$-$PbTiO_3$-$Pb(Mn_{1/3}Sb_{2/3})O_3$ Ceramics under Vibration-Level Change," Mat. Res. Soc. Symp. Proc. Vol.**360**, p.305-310 (1995).
7. B. Koc and K. Uchino, "A Disk Type Piezoelectric Transformer with Crescent Shape Input Electrodes," Proc. Piezoelectric Materails: Adv. in Sci. Tech. and Appl., p.375-382 (2000).
8. R. P. Bishop, Face International, Multilayer Piezoelectric Transformer," US Patent No. 5,834,882 (1998)
9. A. Vázquez Carazo and R. Bosch, "Piezoelectric Non-Resonant Transformer to Measure High Voltage," J. European Ceram. Soc. **19**, 1275-79 (1999).
10. T. Zaitsu, Y. Fuda, Y. Okabe, T. Ninomiya, S. Hamamura, and M. Katsuno, "New Piezoelectric Transformer Converter for AC-Adapter," Proc. IEEE APEC'97, Vol.**2**, p.568-572, Feb. (1997).
11. N. O. Sokal, "RF Power Amplifier, Classes A through S," Proc. Electron. Ind. Forum of New England, p. 179-252 (1997).
12. Motorola, "Actuator Drive and Energy Recovery System," US Patent No. 5,691,592 (1997).

APPENDIX 47

A DISK TYPE PIEZOELECTRIC TRANSFORMER WITH CRESCENT SHAPE INPUT ELECTRODES

BURHANETTIN KOC AND KENJI UCHINO
International Center for Actuators and Transducers
Materials Research Laboratory
The Pennsylvania State University, University Park PA 16802

Abstract

For most PZT based piezoelectric materials the shear mode coupling constant is twice as large as the transverse mode coupling. From this motivation, a new circular piezoelectric transformer was designed. Non-concentric input electrodes and non-uniform output poling lead to the usage of shear mode piezoelectric effect at (3,0) radial mode resonance frequency. A prototype three layered transformer with 25.4-mm in diameter and 1.5 mm in thickness, operating at 153 kHz, was fabricated and its characteristics were measured. Characteristics, such as efficiency, step-up ratio and temperature rise of the proposed transformer are presented.

1. Introduction

One of the bulkiest components in information processing equipment (such as note-book-type personal computers) is the power supply, specifically the electromagnetic transformer used in power supply. Losses such as skin effect, thin wire loss and core loss of the electromagnetic transformer increase rapidly as the size of the transformer is reduced. Therefore, it is difficult to realize miniature low profile electromagnetic transformers with high efficiency.

High efficiency, small size, no electromagnetic noise are some of the attractive features of piezoelectric transformers making them more suitable for miniaturized power inverter elements such as lighting up the cold cathode fluorescent lamp (CCFL) behind a color liquid crystal displays (LCD) or generating high voltage for air-cleaners.

The original design to transform an input ac voltage to step up or step down using converse and direct piezoelectric properties of ceramic materials was proposed by Rosen [1]. The principle of this type of transformer is to excite a piezoelectric element (Figure 1) at its mechanical resonance frequency. Applying an electrical input to one part of the piezoelectric element generates a mechanical vibration and then this mechanical vibration is converted into electrical voltage from the other part of the piezoelectric plate.

376

The initial Rosen type transformer had major reliability problem, which is the easy mechanical breakdown at the center position due to the coincidence of the residual stress concentration and the vibration nodal point. In addition to improved mechanically tough ceramic materials, by redesigning the electrode configuration and exciting a third longitudinal resonance mode of the rectangular plate, the piezoelectric transformer shown in Figure 2a was commercialized by NEC in 1994 for miniaturized back-light inverter to light up the cold cathode fluorescent lamp (CCFL) behind a color liquid crystal displays (LCD) [2].
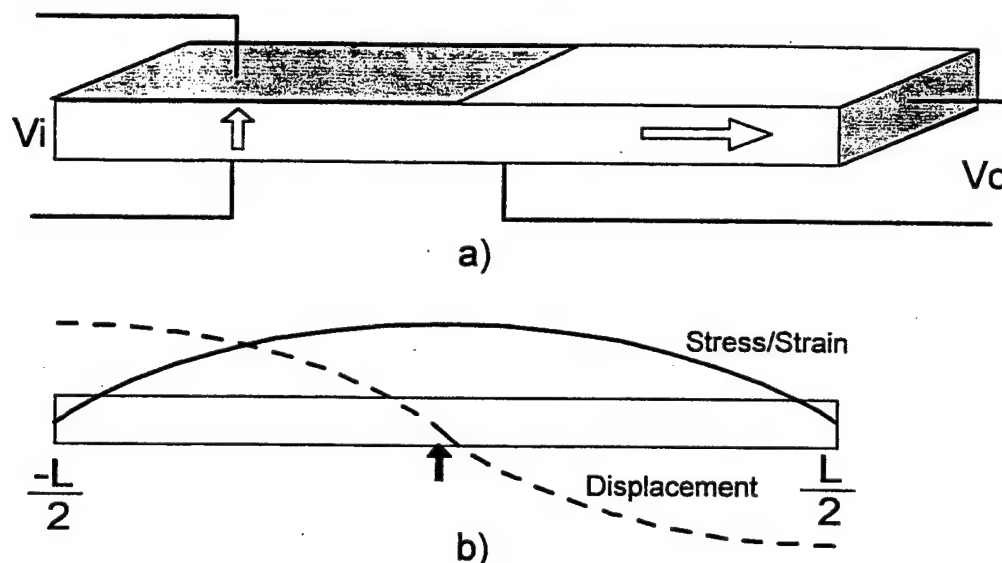
Figure 1. a) Rosen type piezoelectric transformer, b) Stress/strain and displacement distribution at first longitudinal resonance mode.

Another third mode transformer shown in Figure 2b was commercialized, recently, by Mitsui-Sekka to use it also for miniaturized power inverter element [3]. In addition to no electromagnetic noise generation, small size and high efficiency are some of the advantages of the piezoelectric transformers over the electromagnetic types particularly for computer applications.

The third mode transformers have some advantages over original Rosen type first mode transformer, such as follows:
i) for the third mode transformer, stress concentration on the bar is separated into three different points which makes the transformer mechanically stronger. The electric field and stress concentration are not at the same point on the piezoelectric bar, while for the first mode transformer, the maximum stress and nodal point are at the center of the piezoelectric bar that makes the transformer mechanically weaker. This is the major problem of the first mode transformer. Moreover, in order to get higher efficiency the transformer has to be clamped only at a nodal point. Because the third mode transformers have three nodal points on the bar, they can be clamped at two points

easily without affecting the vibration modes. Therefore, third mode transformers can be packaged more safely.

ii)   the third mode transformers are more efficient (96%) than the first mode transformers (90 %).

iii) impedance matching of the third mode transformer with CCFL is better than the first mode transformer.
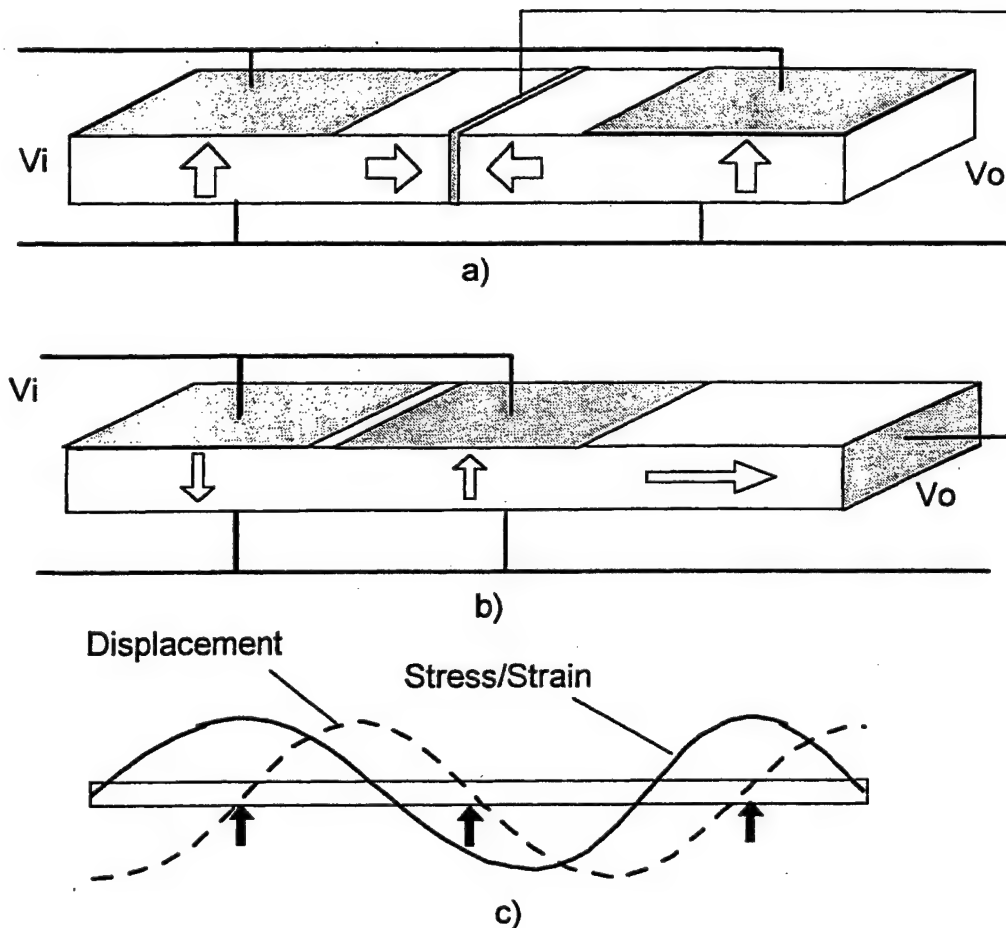

Figure 2. Structures of the third mode piezoelectric transformers, proposed by (a) NEC, (b) Mitsui-Sekka, (c) stress/strain and displacement distribution.

For most PZT based piezoelectric materials, the shear mode coupling constant is twice as large as the transverse mode coupling. From this motivation, a new disk type piezoelectric transformer was designed and it will be introduced in the following section.

2. Disk Type Piezoelectric Transformer

All the rectangular type transformers explained in the previous section are using the transverse mode coupling constant (k_{31}) of the piezoelectric materials. For most piezoelectric materials, however, the shear mode coupling constant (k_{15}) is twice as large as the transverse mode coupling constant (k_{31}). From this motivation, we designed a new circular piezoelectric transformer, which uses shear (k_{15}) or planar (k_p) mode coupling constants of the piezoelectric effect (Fig 3). The transformer is operating at the third radial resonance frequency of the piezoelectric disk.
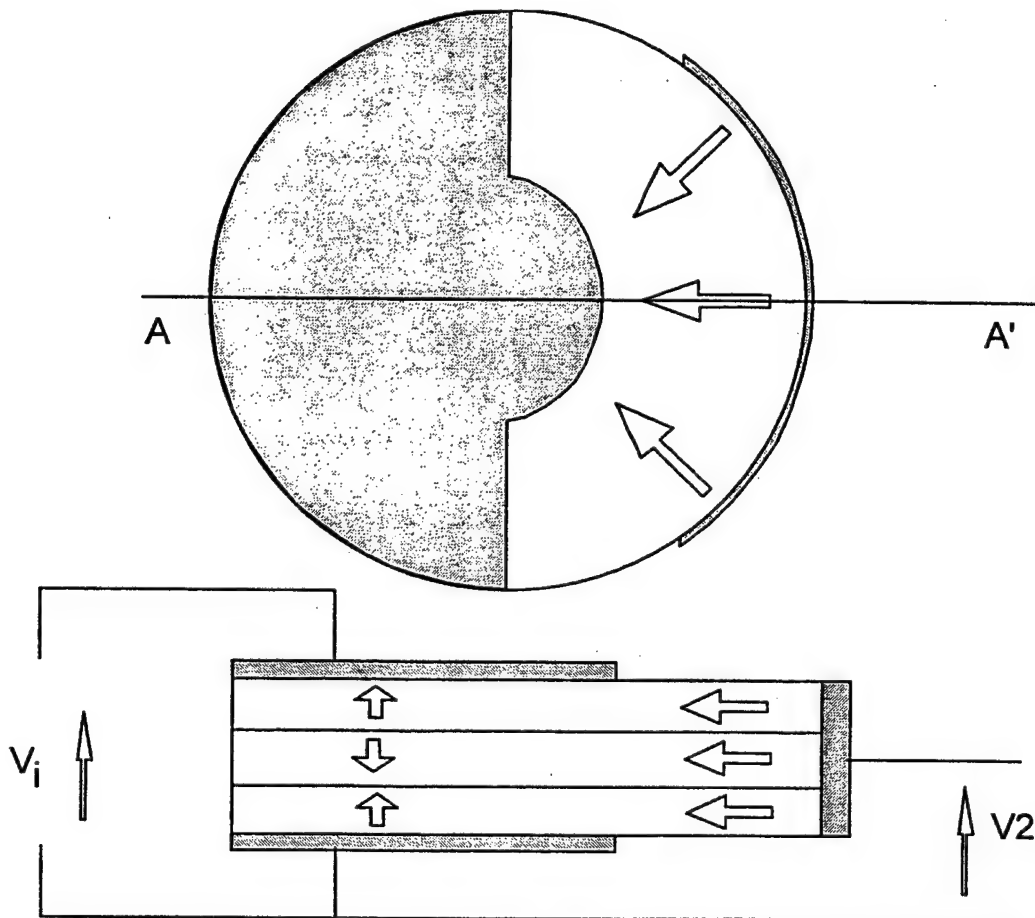
Figure 3. Newly designed circular type piezoelectric transformer structure.

The behavior of the transformer was modeled using ATILA finite element software. The fundamental and third harmonic mode shapes and potential fields are shown in Figures 4 and 5. When the transformer is driven at the first radial resonance frequency it uses planar mode coupling constant effectively. If the transformer is driven at the third

harmonic radial frequency, it uses shear mode coupling coefficient. This can be seen from the mode shape and potential field shown in Figure 5.
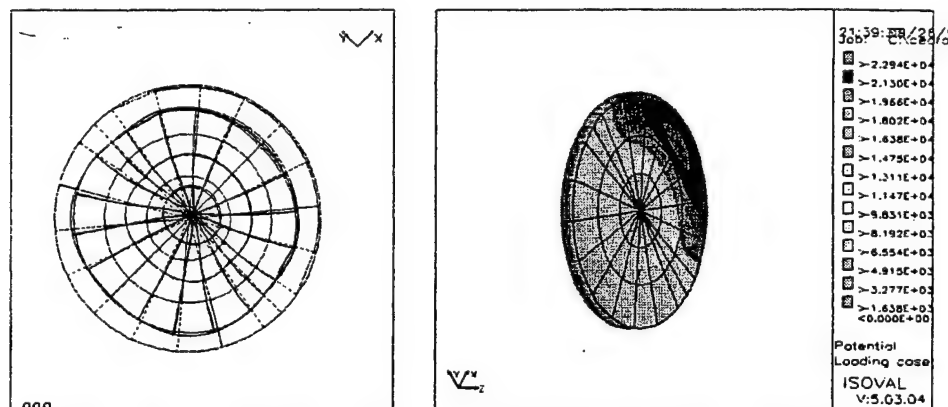

Figure 4. First mode potential field and displacement shape of the circular transformer (67 kHz FEM calculations using ATILA©).
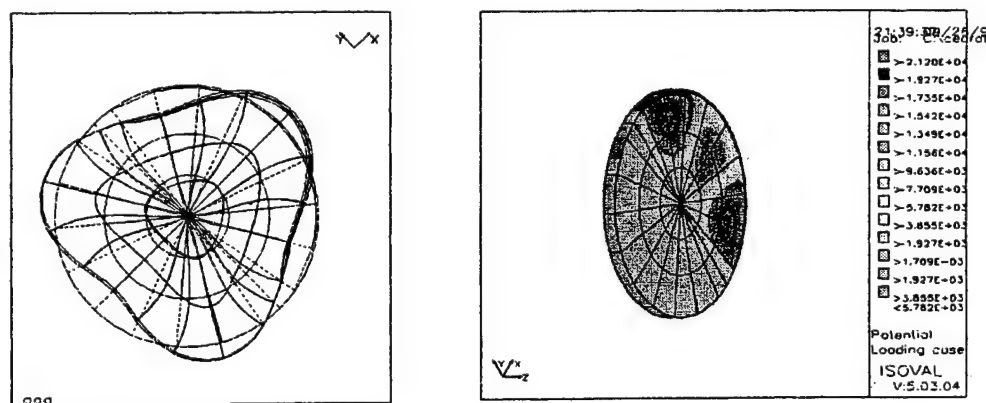

Figure 5. Third mode potential field and displacement shape of the circular transformer (152 kHz FEM calculations using ATILA©).

3. Experimental

The transformer structure shown in Figure 4 was fabricated using commercially available piezoelectric ceramic material (APC International, USA). Hard piezoelectric ceramic disks 25.4 mm in diameter and 0.5 mm in thickness were sputtered with

platinum electrodes according to the proposed electrode configuration. The transformer was subjected to a polarization treatment by applying a DC voltage of 3.0 kV/mm at 150 °C across the input and output electrical terminals. Three identical single layer transformers were then stacked using adhesive epoxy as the last step of the fabrication process.

In order to clarify the operating frequency of the transformer, the input (output terminal open-circuited) and output admittance spectra were measured and the results are shown in Figure 6. The possible operating frequencies of the transformer are first three radial mode resonance frequencies of which both input and output terminals can excite. The best performance was obtained when the transformer was driven at the third mode resonance frequency.
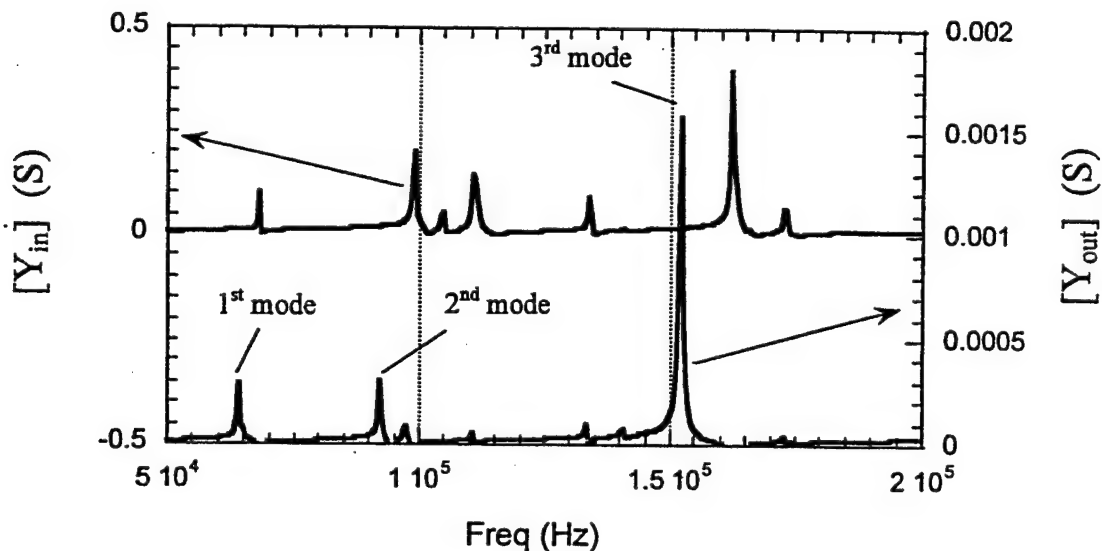

Figure 6. Input and output admittance spectrum.

The transformer low field voltage step-up ratio and efficiency were measured for different resistive loads and the results are shown in Figure 7. The output power on the resistive loads was 1.5 Watts and the transformer was driven around 153 kHz. When measuring the efficiency, the operating frequency of the transformer was tuned so that the maximum efficiency could be obtained for different resistive loads. The efficiency for a resistive load ranging from 100 to 1200 kΩ is found to be around 90 %. For the same range of load resistance, the voltage step up ratio was increased from 70 to 320. These primary results clearly indicate that the proposed transformer can realize a step up ratio and power high enough to light up the cold cathode fluorescent lamp (CCFL) for back-lights in color liquid crystal displays (LCD) when it is operated at the third mode resonance frequency.
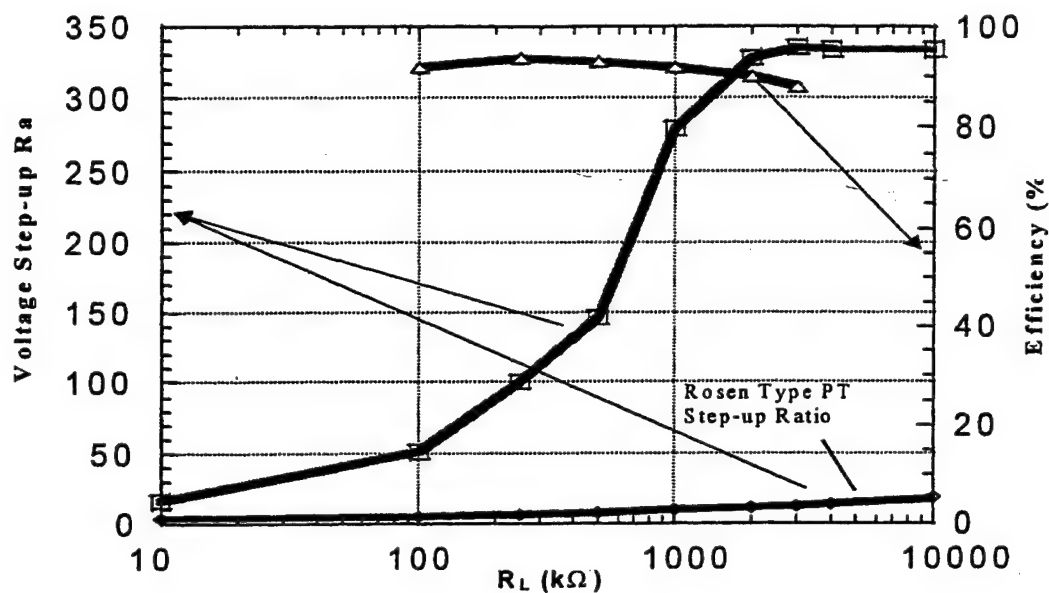
Figure 7. Step-up ratio and efficiency as a function of load resistance.

Figure 8 shows the output/input voltage step-up ratio and temperature rise of the piezoelectric transformer with variable output power for a constant resistive load of 110 $k\Omega$. Temperature rise for a 110 $k\Omega$ resistive load is not significant up to 10 Watts of output power. When the output power is further increased, the temperature of the transformer was observed to increase by more than 80 °C from room temperature. The transformer step-up ratio, however, decreased gradually from 100 to 70 for the same load condition.
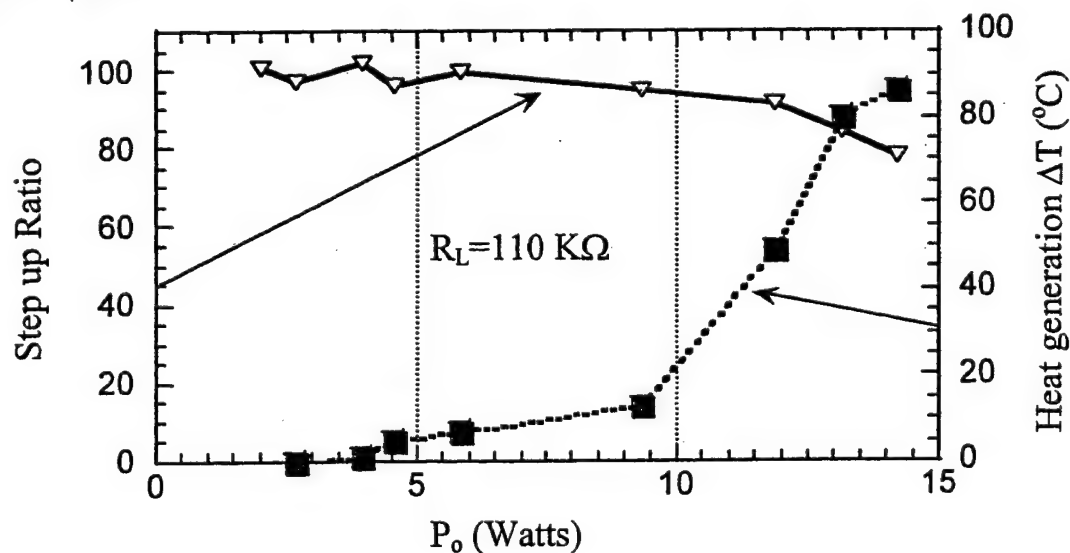

Figure 8. Step-up Ratio and Temperature rise as a function of output power on a resistive load.

382

4. Conclusions

A new disk type piezoelectric transformer design was proposed using three layered commercially available hard piezoelectric disks. Non-concentric input electrodes and non-uniform output poling lead to the usage of shear mode piezoelectric effect at (3,0) radial mode resonance frequency. A prototype three layered transformer of 25.4-mm in diameter and 1.5 mm in thickness, operating at 153 kHz, was fabricated and its characteristics were measured. The transformer can generate enough step-up ratio and power to light up CCFL for back-light of color liquid crystal displays (LCD) when it is operated at the third mode resonance frequency.

Heat generation and step up ratio as a function of output power was also investigated. Temperature rise for a 110 kΩ resistive load is not significant up to 10 Watts range of output power. When the output power was further increased the temperature of the transformer increased more than 80 °C from room temperature. The transformer step-up ratio however decreased gradually from 100 to 70 for the same load condition.

Acknowledgements

5. References

1. Rosen, C.A. (1959), Electromechanical Application, in H.W. Katz (eds), *Solid State Magnetic and Dielectric Devices*, New York: Wiley, pp. 171-229.
2. Kawashima, S., Ohnishi, O., Hakamata, H., Tagami, S., Fukuoka, A., Inoue, T. and Hirose, S. (1994) Third Order Longitudinal Mode Piezoelectric Ceramic Transformer and its Application to High-Voltage Inverter, *IEEE Int. Ultrasonic Symp,* Cannes, 525-530.
3. Kanayama, K., Maruko, N. and Saigoh, H. (1998) Development of the Multilayer Alternately Poled Piezoelectric Transformers, *Jpn. J. Appl. Phys.* Vol. 37, pp.2891-2895, 1998.
4. Tsuchiya, H. and Fukami, T. (1986) Design and Principles for Multilayer Piezoelectric Transformers, *Ferroelectrics,* **68,** 225-234.

TRANSDUCER STUDIES

High Power Level Materials

APPENDIX 48

Loss Mechanisms in Piezoelectrics: How to Measure Different Losses Separately

Kenji Uchino, *Member, IEEE,* and Seiji Hirose, *Member, IEEE*

Abstract—Losses in piezoelectrics are considered in general to have three different mechanisms: dielectric, mechanical, and piezoelectric losses. This paper deals with the phenomenology of losses first, then how to measure these losses separately in experiments. We found that heat generation at off-resonance is caused mainly by dielectric loss $\tan \delta'$ (i.e., P-E hysteresis loss), not by mechanical loss, and that a significant decrease in mechanical Q_m with an increase of vibration level was observed in resonant piezoelectric ceramic devices, which is due to an increase in the extensive dielectric loss, not in the extensive mechanical loss. We propose the usage of the antiresonance mode rather than the conventional resonance mode, particularly for high power applications because the mechanical quality factor Q_B at an antiresonance frequency is larger than Q_A at a resonance frequency.

I. INTRODUCTION

LOSS or hysteresis in piezoelectrics exhibits both merits and demerits. For positioning actuator applications, hysteresis in the field-induced strain provides a serious problem and, for resonance actuation such as ultrasonic motors, loss generates significant heat in the piezoelectric materials. Further, in consideration of the resonant strain amplified in proportion to a mechanical quality factor, low (intensive) mechanical loss materials are preferred for ultrasonic motors. On the contrary, for force sensors and acoustic transducers, a low mechanical quality factor Q_m (which corresponds to high mechanical loss) is helpful to widen a frequency range for receiving signals.

Haerdtl [1] wrote a review article on electrical and mechanical losses in ferroelectric ceramics. Losses are considered to consist of four portions: domain wall motion; fundamental lattice portion, which also should occur in domain-free monocrystals; microstructure portion, which occurs typically in polycrystalline samples; and conductivity portion in highly ohmic samples. However, in the typical piezoelectric ceramic case, the loss due to the domain wall motion exceeds the other three contributions significantly. They reported interesting experimental results on the relationship between electrical and mechanical losses in piezoceramics, $Pb_{0.9}La_{0.1}(Zr_{0.5}Ti_{0.5})_{1-x}Me_xO_3$, where

Me represents the doped ions Mn, Fe, or Al and x varied between 0 and 0.09. However, they measured the mechanical losses on poled ceramic samples, while the electrical losses on unpoled samples, i.e., in a different polarization state. Thus, they completely neglected piezoelectric losses.

As far as we know, not much research effort has been put into systematic studies of the loss mechanisms in piezoelectrics, particularly in high-voltage and high-power ranges. Because not many comprehensive descriptions can be found in previous reports, this paper will clarify the loss mechanisms in piezoelectrics phenomenologically, describe heat generation processes and high power characteristics, and discuss the resonance and antiresonance vibration modes from a viewpoint of a quality factor.

Although Ikeda [2] described part of the formulas of this paper in his textbook, he totally neglected the piezoelectric losses, which have been found not to be neglected in our investigations. We derive the full descriptions of the losses in this paper. It is also worth noting that we have changed the terminologies "extrinsic" and "intrinsic" losses used in our previous presentations and papers to "intensive" and "extensive" losses, respectively, in this paper.

II. LOSS AND HYSTERESIS IN THE POLARIZATION CURVE

A. Relation Between Hysteresis and Dissipation Factor

Let us start first with loss and hysteresis in the electric displacement D (nearly equal to polarization P) vs. electric field E curve without considering the electromechanical coupling. Fig. 1(a) shows an example of a P-E hysteresis curve. When the D (or P) traces a different line with increased and decreased applied electric field E, it is called hysteresis.

When the hysteresis is not very large, the electric displacement D can be expressed by using a slight phase lag to the applied electric field. The hysteresis curve shows an ellipse in this case. Assuming that the electric field oscillates at a frequency $f(= \omega/2\pi)$ as

$$E^* = E_0 e^{j\omega t}, \tag{1}$$

the induced electric displacement also oscillates at the same frequency under the steady state, but with some time phase delay δ':
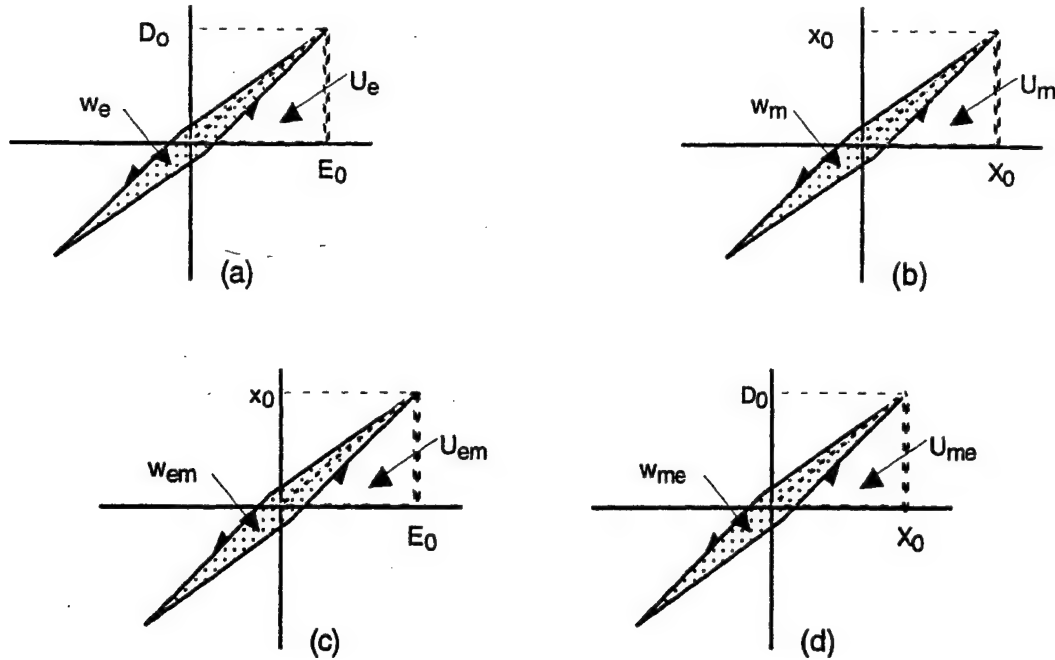
$$D^* = D_0 e^{j(\omega t - \delta')}. \tag{2}$$

Fig. 1. (a) D vs. E (stress free), (b) x vs. X (short-circuit), (c) x vs. E (stress free), and (d) D vs. X (open-circuit) curves with a slight hysteresis in each relation.

If we express the relation between $D*$ and $E*$ as:

$$D^* = \varepsilon^* \varepsilon_0 E^*, \qquad (3)$$

where the complex dielectric constant ε^* is:

$$\varepsilon^* = \varepsilon' - j\varepsilon'', \qquad (4)$$

and where

$$\varepsilon''/\varepsilon' = \tan\delta'. \qquad (5)$$

Note that the negative connection in (4) comes from the time "delay," and that $\varepsilon'\varepsilon_0 = (D_0/E_0)\cos\delta'$ and $\varepsilon''\varepsilon_0 = (D_0/E_0)\sin\delta'$.

The area w_e corresponds to the consumed loss energy during an electric field cycle per unit volume of the dielectrics and can be related in isotropic dielectrics with ε'' or $\tan\delta'$ as follows:

$$w_e = -\int \mathbf{D} d\mathbf{E} = -\int_0^{2\pi/\omega} \mathbf{D}(d\mathbf{E}/dt)\, dt = \pi E_0 D_0 \sin\delta'$$
$$= \pi\varepsilon''\varepsilon_0 E_0^2 = \pi\varepsilon'\varepsilon_0 E_0^2 \tan\delta'. \qquad (6)$$

When there is no phase delay ($\delta' = 0$), $w_e = 0$; i.e., the electrostatic energy stored in the dielectric will be recovered completely after a full cycle (100% efficiency). However, when there is a phase delay, the loss w_e will be accompanied per cycle, and the dielectric material generates heat. The $\tan\delta'$ is called dielectric dissipation factor.

In consideration of the stored electrostatic energy during a half cycle from $-E_0$ to $E_0 [= 4\,U_e$, which is illustrated as an area in Fig. 1(a)] provided by:

$$4\,U_e = (1/2)(2\,E_0)(2\,\varepsilon'\varepsilon_0 E_0) = 2\,\varepsilon'\varepsilon_0 E_0^2, \qquad (7)$$

the dissipation factor $\tan\delta'$ can be experimentally obtained by:

$$\tan\delta' = (1/2\pi)\,(w_e/U_e). \qquad (8)$$

Note that w_e is the hysteresis in a full cycle and U_e is the stored energy in a quarter of a cycle.

B. Temperature, Electric Field, and Frequency Dependence of P-E Hysteresis

Fig. 2, 3, and 4 show temperature, electric field and frequency dependence of the dissipation factor $\tan\delta'$ calculated from the P-E hysteresis loss measured under stress-free conditions for a PZT-based ceramic. Experimental details are in [3]. The loss $\tan\delta'$ decreases gradually with increasing temperature, but it is rather insensitive to frequency. On the contrary, the $\tan\delta'$ increases initially in proportion to the applied electric field, exhibiting a saturation above a certain electric field. After reaching the saturation, i.e., more than 0.1 of $\tan\delta'$, this complex physical quantity treatment should not be used. The value for $E = 0$ (solid triangle mark in the figure) was obtained with an impedance analyzer.

III. GENERAL CONSIDERATION OF LOSS AND HYSTERESIS

A. Theoretical Formulas

Let us expand the above discussion into more general cases, i.e., piezoelectric materials. We will start from the Gibbs free energy G expressed by:
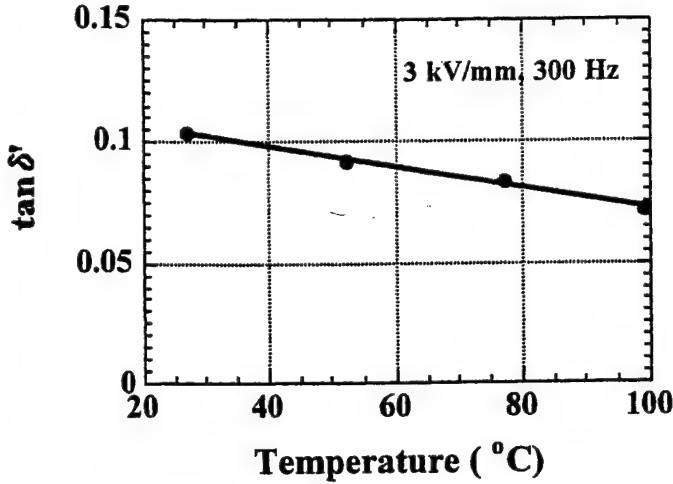
$$dG = -x\,dX - D\,dE - S\,dT, \qquad (9)$$

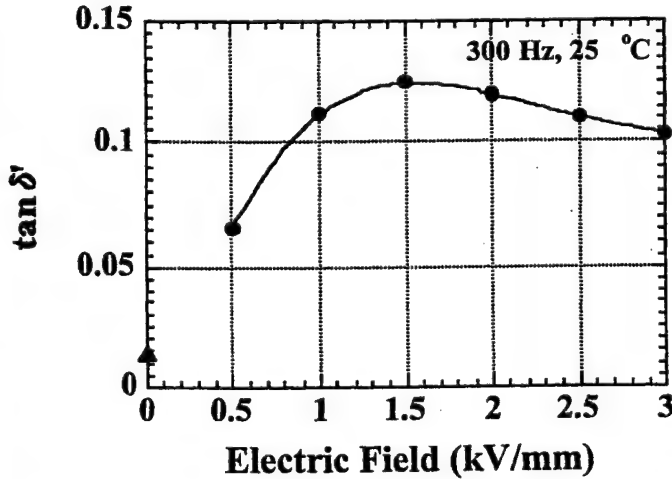Fig. 2. Loss $\tan \delta'$ as a function of sample temperature (3 kV/mm, 300 Hz).

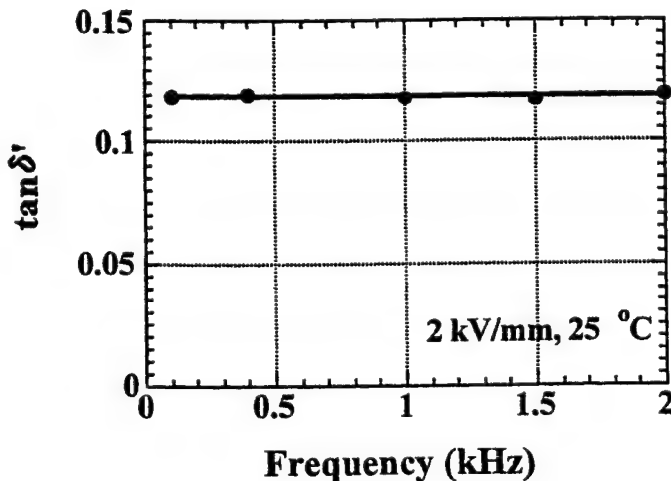Fig. 3. Loss $\tan \delta'$ as a function of electric field ($T = 25°C$, f = 300 Hz).

Fig. 4. Loss $\tan \delta'$ as a function of frequency ($T = 25°C$, $E = 2$ kV/mm).

or

$$G = -(1/2)\,s^{E}X^2 - d\,X\,E - (1/2)\,\varepsilon^{X}\varepsilon_0\,E^2.$$
(10)

Here, x is strain, X is stress, D is electric displacement, E is electric field, S is enthalpy, and T is temperature. (10) is the energy expression in terms of intensive (i.e., externally controllable) physical parameters X and E. Temperature dependence is carried into the elastic compliance s^{E}, the dielectric constant ε^{X} and the piezoelectric constant d. We will obtain the following two piezoelectric equations:

$$x = -(\partial G/\partial X) = s^{E}X + d\,E,$$
(11)

$$D = -(\partial G/\partial E) = d\,X + \varepsilon^{X}\varepsilon_0 E.$$
(12)

Note that thermodynamical equations and the consequent piezoelectric equations [(9)–(12)] cannot yield a delay-time-related loss without taking into account irreversible thermodynamic equations or dissipation functions, in general. However, the latter considerations are mathematically equivalent to the introduction of complex physical constants into the phenomenological equations, if the loss can be treated as a perturbation.

Therefore, we will introduce complex parameters ε^{X*}, s^{E*}, and d* in order to consider the hysteresis losses in dielectric, elastic, and piezoelectric coupling energy:

$$\varepsilon^{X*} = \varepsilon^{X}(1 - j\tan\delta'),$$
(13)

$$s^{E*} = s^{E}(1 - j\tan\phi'),$$
(14)

$$d^* = d(1 - j\tan\theta'),$$
(15)

where θ' is the phase delay of the strain under an applied electric field, or the phase delay of the electric displacement under an applied stress. Both delay phases should be exactly the same if we introduce the same complex piezoelectric constant d* into (11) and (12). δ' is the phase delay of the electric displacement to an applied electric field under a constant stress (e.g., zero stress) condition, and ϕ' is the phase delay of the strain to an applied stress under a constant electric field (e.g., short-circuit) condition. We will consider these phase delays as "intensive" losses.

Fig. 1(a)–(d) correspond to the model hysteresis curves for practical experiments: D vs. E curve under a stress-free condition, x vs. X under a short-circuit condition, x vs. E under a stress-free condition, and D vs. X under an open-circuit condition for measuring charge (or under a short-circuit condition for measuring current), respectively. Notice that these measurements are easily conducted in practice.

In a similar fashion to the previous section, the stored energies and hysteresis losses for pure dielectric and elastic energies can be calculated as:

$$U_e = (1/2)\varepsilon^{X}\varepsilon_0 E_0^2,$$
(16)

$$w_e = \pi\varepsilon^{X}\varepsilon_0 E_0^2 \tan\delta',$$
(17)

$$U_m = (1/2)\,s^{E}X_0^2,$$
(18)

$$w_m = \pi s^{E}X_0^2 \tan\phi'.$$
(19)

The electromechanical loss, when measuring the induced strain under an electric field, is more complicated. Let us calculate the stored energy U_{em} during a quarter electric field cycle (i.e., 0 to E_0) , first:

$$U_{em} = - \int x\, dX = (1/2)(x_0^2/s^E) = (1/2)(dE_0)^2/s^E$$
$$= (1/2)(d^2/s^E)E_0^2. \qquad (20)$$

Replacing d and s^E by $d^* = d(1 - j\tan\theta')$ and $s^{E*} = s^E(1 - j\tan\phi')$, we obtain

$$U_{em} = (1/2)(d^2/s^E)E_0^2, \qquad (21)$$

and

$$w_{em} = \pi(d^2/s^E)\, E_0^2\, (2\tan\theta' - \tan\phi'). \qquad (22)$$

Note that the strain vs. electric field measurement seems to provide the piezoelectric loss $\tan\theta'$ directly; however, the observed loss should include an additional elastic loss because the strain should be delayed to the initial stress, which is needed to calculate energy.

Similarly, when we measure the induced charge under stress, the stored energy U_{me} and the hysteresis loss w_{me} during a quarter and a full-stress cycle, respectively, are obtained as:

$$U_{me} = (1/2)(d^2/\varepsilon_0\varepsilon^X)\, X_0^2, \qquad (23)$$

and

$$w_{me} = \pi(d^2/\varepsilon_0\varepsilon^X)\, X_0^2\, (2\tan\theta' - \tan\delta'). \qquad (24)$$

Hence, from the measurements of D vs. E and x vs. X, we obtain $\tan\delta'$ and $\tan\phi'$, respectively, and either the piezoelectric (D vs. X) or converse piezoelectric measurement (x vs. E) provides $\tan\theta'$ through a numerical subtraction.

So far, we have discussed the "intensive" dielectric, mechanical, and piezoelectric losses. In order to consider real physical meanings of the losses, we will introduce the "extensive" losses [2]. When we start from the energy expression in terms of extensive (material's own) physical parameters x and D, that is,

$$dA = X\, dx + E\, dD - S\, dT, \qquad (25)$$

we can obtain the piezoelectric equations as follows:

$$X = (\partial A/\partial x) = c^D x - h\, D, \qquad (26)$$
$$E = (\partial A/\partial D) = -h\, x + \kappa^x\kappa_0\, D. \qquad (27)$$

We introduce the extensive dielectric, elastic, and piezoelectric losses as:

$$\kappa^{x*} = \kappa^x(1 + j\tan\delta), \qquad (28)$$
$$c^{D*} = c^D(1 + j\tan\phi), \qquad (29)$$
$$h^* = h(1 + j\tan\theta). \qquad (30)$$

It is notable that the permittivity under a constant strain (e.g., zero strain or completely clamped) condition, ε^{x*} and the elastic compliance under a constant electric displacement (e.g., open-circuit) condition, s^{D*} can be provided as an inverse value of κ^{x*} and c^{D*}, respectively. Thus, using exactly the same losses in (28) and (29),

$$\varepsilon^{x*} = \varepsilon^x(1 - j\tan\delta), \qquad (31)$$
$$s^{D*} = s^D(1 - j\tan\phi), \qquad (32)$$

we will consider these phase delays again as "extensive" losses.

Here, we consider the physical property difference between the boundary conditions: E constant and D constant, or X constant and x constant. When an elecric field is applied on a piezoelectric sample as illustrated in the top of Fig. 5, this state will be equivalent to the superposition of the following two steps; the sample is completely clamped and the field E_0 is applied (pure electrical energy $(1/2)\varepsilon^x\varepsilon_0 E_0^2$ is input); and keeping the field at E_0, the mechanical constraint is released (additional mechanical energy $(1/2)(d^2/s^E)\, E_0^2$ is necessary). The total energy should correspond to the total input electrical energy $(1/2)\varepsilon^X\varepsilon_0 E_0^2$; thus, we obtain the relation,

$$\varepsilon_0\varepsilon^X = \varepsilon_0\varepsilon^x + (d^2/s^E). \qquad (33)$$

Similarly, from the bottom of Fig. 5,

$$s^E = s^D + (d^2/\varepsilon_0\varepsilon^X). \qquad (34)$$

Hence, we obtain the following equations:

$$\varepsilon^x/\varepsilon^X = (1 - k^2), \qquad (35)$$
$$s^D/s^E = (1 - k^2), \qquad (36)$$

where

$$k^2 = d^2/(s^E\, \varepsilon_0\varepsilon^X). \qquad (37)$$

Similarly,

$$\kappa^X/\kappa^x = (1 - k^2), \qquad (38)$$
$$c^E/c^D = (1 - k^2), \qquad (39)$$

where

$$k^2 = h^2/(c^D\, \kappa^x\kappa_0). \qquad (40)$$

This k is called the electromechanical coupling factor, and is the same as the k in (37), because the equation $d^2/(s^E\varepsilon_0\varepsilon^X) = h^2/(c^D\kappa^x\kappa_0)$ can be verified mathematically. We define the k as a real number in this manuscript.

In order to obtain the relationships between the intensive and extensive losses, the following three equations are essential:

$$\varepsilon_0\varepsilon^X = [\kappa^x\kappa_0\, (1 - h^2/(c^D\, \kappa^x\kappa_0))]^{-1}, \qquad (41)$$
$$s^E = [c^D\, (1 - h^2/(c^D\, \kappa^x\kappa_0))]^{-1}, \qquad (42)$$
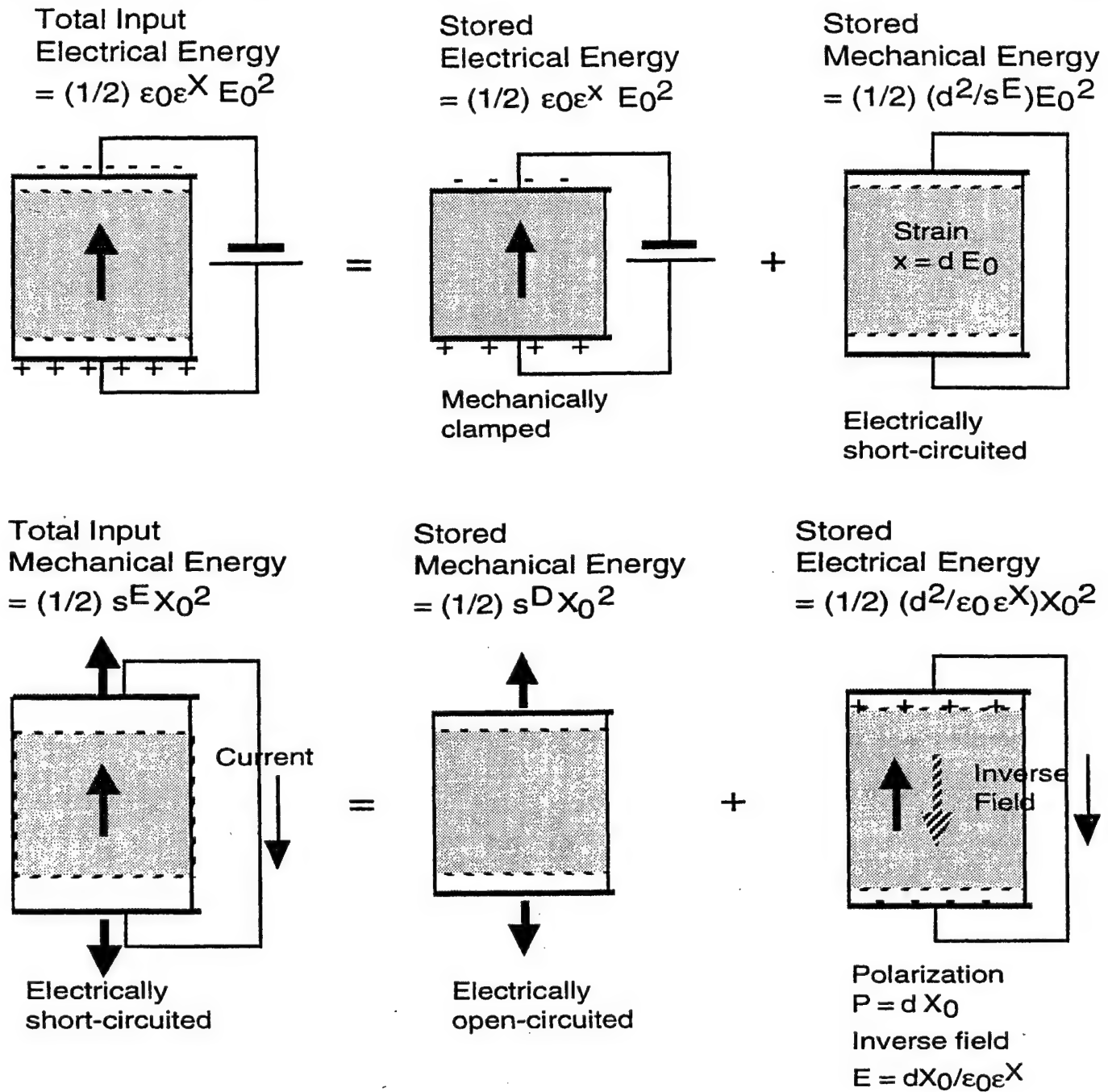$$d = [h^2/(c^D\, \kappa^x\kappa_0)]\, [h\, (1 - h^2/(c^D\, \kappa^x\kappa_0))]^{-1}. \qquad (43)$$

Total Input Electrical Energy $= (1/2)\,\varepsilon_0\varepsilon^X\,E_0^2$

Stored Electrical Energy $= (1/2)\,\varepsilon_0\varepsilon^x\,E_0^2$

Stored Mechanical Energy $= (1/2)\,(d^2/s^E)E_0^2$

Mechanically clamped

Strain $x = d\,E_0$

Electrically short-circuited

Total Input Mechanical Energy $= (1/2)\,s^E X_0^2$

Stored Mechanical Energy $= (1/2)\,s^D X_0^2$

Stored Electrical Energy $= (1/2)\,(d^2/\varepsilon_0\varepsilon^X)X_0^2$

Current

Electrically short-circuited

Electrically open-circuited

Polarization $P = d\,X_0$
Inverse field $E = d X_0/\varepsilon_0\varepsilon^X$

Inverse Field

Fig. 5. Conceptual figure for explaining the relation between ε^X and ε^x, s^E, and s^D.

Replacing the parameters in (41)–(43) by the complex parameters in (13)–(15), (28)–(30), we obtain the relationships between the intensive and extensive losses:

$$\tan\delta' = (1/(1-k^2))[\tan\delta + k^2(\tan\phi - 2\tan\theta)], \tag{44}$$

$$\tan\phi' = (1/(1-k^2))[\tan\phi + k^2(\tan\delta - 2\tan\theta)], \tag{45}$$

$$\tan\theta' = (1/(1-k^2))[\tan\delta + \tan\phi - (1+k^2)\tan\theta], \tag{46}$$

where k is the electromechanical coupling factor defined by either (37) or (40), and here as a real number. It is im-

portant that the intensive dielectric and elastic losses are mutually correlated with the extensive dielectric, elastic, and piezoelectric losses through the electromechanical coupling k^2, and that the denominator $(1-k^2)$ comes basically from the ratios, $\varepsilon^x/\varepsilon^X = (1-k^2)$ and $s^D/s^E = (1-k^2)$, and this real part reflects to the dissipation factor when the imaginary part is divided by the real part. Also note that, depending on the vibration mode, the definition of electromechanical coupling k can be changed such as $k^2 = d^2/(s^D\,\varepsilon_0\varepsilon^X)$.
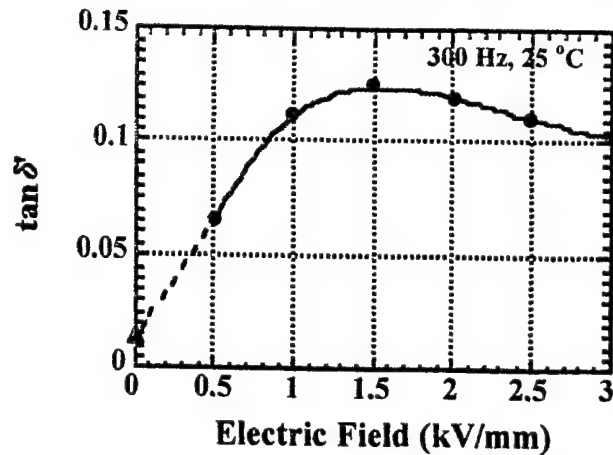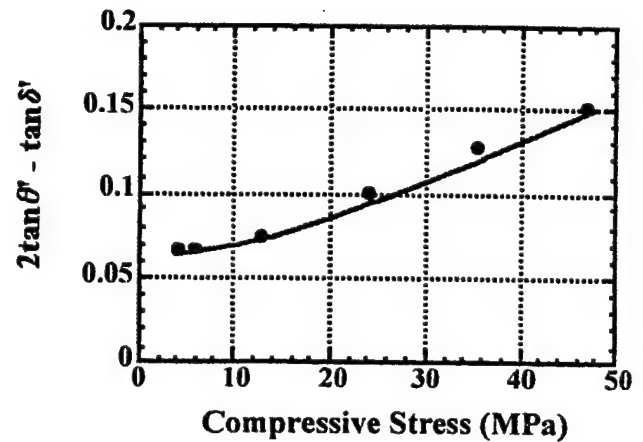
(a)
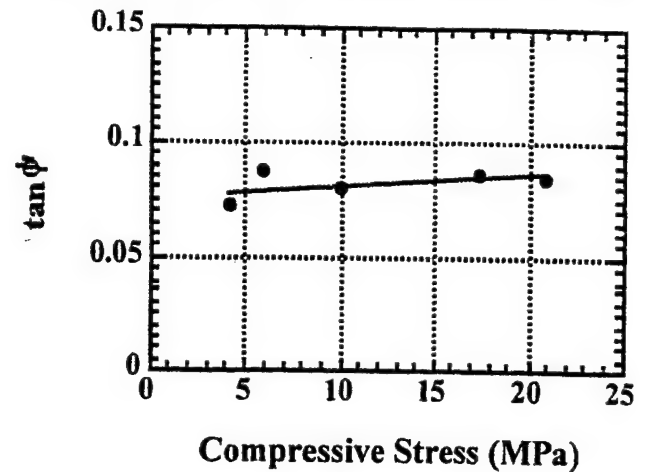
(b)
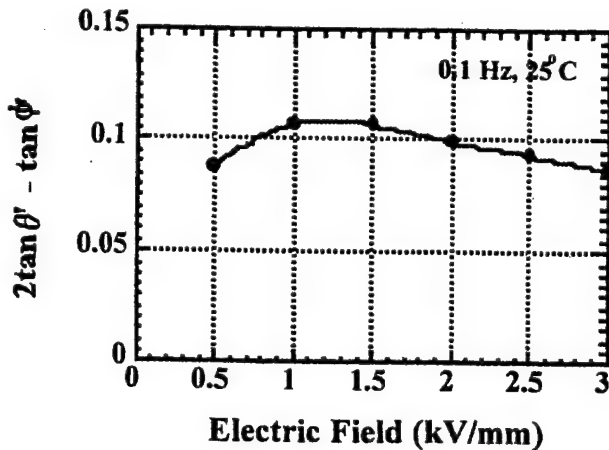
(c)

(d)

Fig. 6. Dissipation factors determined from (a) D vs. E (stress free), (b) x vs. X (short-circuit), (c) x vs. E (stress free), and (d) D vs. X (open-circuit) curves for a PZT-based actuator.

B. Experimental Example

Fig. 6 shows "intensive" dissipation factors determined from Fig. 6(a) D vs. E (stress free), Fig. 6(b) x vs. X (short-circuit), Fig. 6(c) x vs. E (stress free), and Fig. 6(d) D vs. X (open-circuit) curves for a soft PZT-based multilayer actuator used for Figs. 2, 3, and 4. The details on the experiments will be reported in the successive papers. Fig. 7 shows the result for the piezoelectric loss $\tan\theta'$. We used the correlation factor between electric field and compressive stress given averagely by $X = (\varepsilon_0 \varepsilon^X / s^E)^{1/2} E$.

From Figs. 6 and 7, we can calculate the "extensive" losses as shown in Fig. 8. Note that the piezoelectric losses

$\tan\theta'$ and $\tan\theta$ are not as small as previously believed, but they are comparable to the dielectric and elastic losses and increase gradually with the field or stress. Also it is noteworthy that the extensive dielectric loss $\tan\delta$ increases significantly with an increase of the intensive parameter (i.e., the applied electric field), and the extensive elastic loss $\tan\phi$ is rather insensitive to the intensive parameter, i.e., the applied compressive stress.

When similar measurements to Figs. 1(a) and (b), but under constrained conditions—that is, D vs. E, under a completely clamped state, and x vs. X, under an open-circuit state, respectively—we can expect smaller hystereses, that is, extensive losses, $\tan\delta$ and $\tan\phi$. These mea-
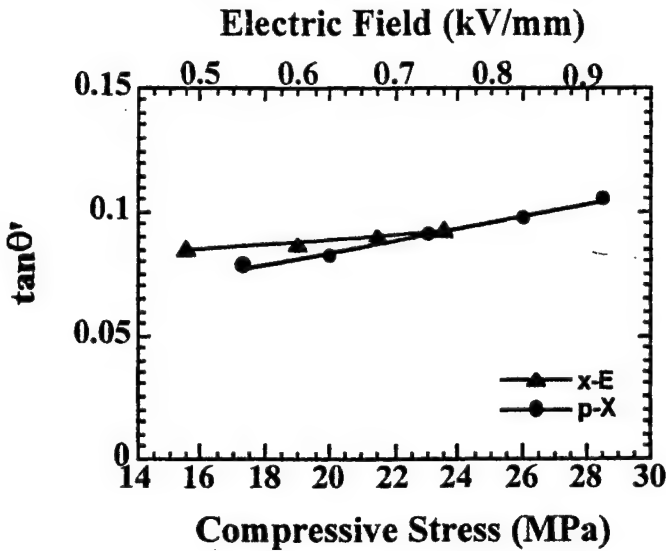
Electric Field (kV/mm)

Fig. 7. Extrinsic piezoelectric dissipation factor $\tan\theta'$ as a function of electric field or compressive stress, measured for a PZT-based actuator.

surements seem to be alternative methods to determine the three losses separately; however, they are rather difficult in practice.

IV. LOSS AND HEAT GENERATION

Heat generation in various types of PZT-based actuators has been studied under a relatively large electric field applied (1 kV/mm or more) at an off-resonance frequency, and a simple analytical method was established to evaluate the temperature rise, which is very useful for the design of piezoelectric high-power actuators. Heat generation in a resonating piezoelectric sample is discussed in the next section.

Zheng et al. [3] reported the heat generation from various sizes of multilayer type piezoelectric ceramic actuators. Fig. 9 shows the temperature change with time in the actuators when driven at 3 kV/mm and 300 Hz. Fig. 10 plots the saturated temperature as a function of V_e/A, where V_e is the effective volume (electrode overlapped part) and A is the surface area. This linear relation is reasonable because the volume V_e generates the heat, and this heat is dissipated through the area A. Thus, if we need to suppress the temperature rise, a small V_e/A design is preferred.

According to the law of energy conservation, the rate of heat storage in the piezoelectric resulting from heat generation and dissipation effects can be expressed as:

$$q_g - q_{out} = V \rho c \, (dT/dt), \qquad (47)$$

assuming uniform temperature distribution in the sample. V, ρ, c are total volume, density, and specific heat, respectively. The heat generation is considered to be caused by losses. Thus, the rate of heat generation (q_g) in the piezo-

electric can be expressed as:

$$q_g = u f V_e, \qquad (48)$$

where u is the loss of the sample per driving cycle per unit volume, f is the driving frequency, and V_e is the effective volume where the ceramic is activated. According to the measuring condition, this u corresponds to the intensive dielectric loss w_e of (17), which consists of the extensive dielectric loss $\tan\delta$ and the electromechanical and piezoelectric combined loss ($\tan\phi - 2\tan\theta$) in the previous section:

$$u = w_e = \pi\varepsilon^X\varepsilon_0 E_0^2 \tan\delta'$$
$$= [1/(1-k^2)][\tan\delta + k^2(\tan\phi - 2\tan\theta)]\pi\varepsilon^X\varepsilon_0 E_0^2. \qquad (49)$$

Note that we do not need to add w_{em} explicitly, because the corresponding electromechanical loss is already included implicitly in w_e.

When we neglect the conduction heat transfer, the rate of heat dissipation (q_{out}) from the sample is the sum of the rates of heat flow by radiation (q_r) and convection (q_c):

$$q_{out} = q_r + q_c$$
$$= \sigma e A(T^4 - T_0^4) + h_c A(T - T_0), \qquad (50)$$

where σ is the Stehan-Boltzmann constant, e is the emissivity of the sample, h_c is the average convective heat transfer coefficient, and A is the sample surface area. Thus, (47) can be written in the form:

$$u \, f \, V - A \, k(T)(T - T_0) = V \rho c(dT/dt), \qquad (51)$$

where

$$k(T) = \sigma e(T^2 + T_0^2)(T + T_0) + h_c \qquad (52)$$

is defined as the overall heat transfer coefficient. If we assume that $k(T)$ is relatively insensitive to temperature change, the solution to (51) for the piezoelectric sample temperature is given as a function of time (t):

$$T - T_0 = [u \, f \, V_e/k(T) \, A] \, [1 - e^{-t/\tau}], \qquad (53)$$

where the time constant τ is expressed as:

$$\tau = \rho c V/k(T)A. \qquad (54)$$

As $t \to \infty$, the maximum temperature rise in the sample becomes:

$$\Delta T = u \, f \, V_e/k(T) \, A. \qquad (55)$$

As $t \to 0$, the initial rate of temperature rise is:

$$(dT/dt) = u \, f \, V_e/\rho c \, V = \Delta T/\tau. \qquad (56)$$

Figs. 11 and 12 show the dependence of $k(T)$ on applied electric field and frequency. Because $k(T)$ is not really constant, we can calculate the total loss u of the piezoelectric
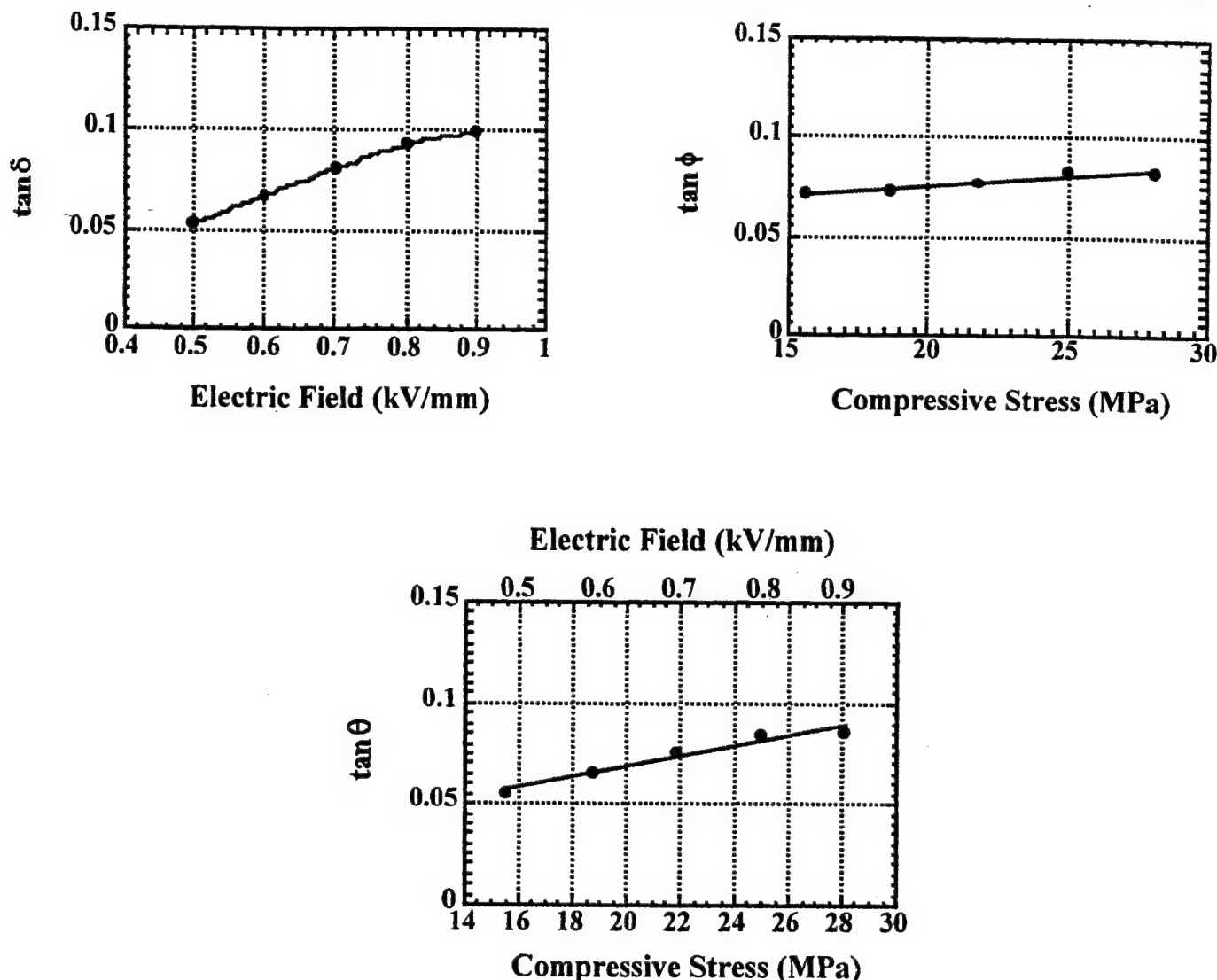
Fig. 8. Intrinsic loss factors $\tan\delta$, $\tan\phi$, and $\tan\theta$ as a function of electric field or compressive stress, measured for a PZT-based actuator.

more precisely through (56). The calculated results are shown in Table I. The experimental data of P-E hysteresis losses under a stress-free condition also are listed for comparison. It is seen that the P-E hysteresis intensive loss agrees well with the total loss contributing to the heat generation under an off-resonance drive.

V. Losses at a Piezoelectric Resonance

So far, we have considered the losses for a quasi-static or off-resonance state. Problems in ultrasonic motors that are driven at the resonance frequency include significant distortion of the admittance frequency spectrum due to nonlinear behavior of elastic compliance at a high vibration amplitude, and heat generation that causes a serious degradation of the motor characteristics through depoling of the piezoceramic. Therefore, the ultrasonic motor requires a very hard-type piezoelectric with a high mechanical quality factor Q_m, leading to the suppression of heat generation. It is also notable that the actual mechanical

vibration amplitude at the resonance frequency is directly proportional to this Q_m value.

A. Losses at a Piezoelectric Resonance

1. Piezoelectric Resonance Without Loss: Let us first review the longitudinal mechanical vibration of a piezoceramic plate without loss through the transverse piezoelectric effect (d_{31}) as shown in Fig. 13 [4]. Assuming that the polarization is in the z-direction and the x-y planes are the planes of the electrodes, the extentional vibration in the x direction is represented by the following dynamic equation:

$$\rho(\partial^2 u/\partial t^2) = F = (\partial X_{11}/\partial x) + (\partial X_{12}/\partial y) + (\partial X_{13}/\partial z),$$
$$(57)$$

where u is the displacement of the small volume element in the ceramic plate in the x-direction and ρ is the density. When the plate is very long and thin, X_2 and X_3 may be

TABLE I

Loss and Overall Heat Transfer Coefficient for PZT Multilayer Samples ($E = 3$ kV/mm, f = 300 Hz).

Actuator	$4.5 \times 3.5 \times 2$ mm	$7 \times 7 \times 2$ mm	$17 \times 3.5 \times 1$ mm
Total loss ($\times 10^3$ J/m^3) $u = \dfrac{\rho cv}{fv_e}\left(\dfrac{dT}{dt}\right)_{t \to 0}$	19.2	19.9	19.7
$P - E$ hysteresis loss ($\times 10^3$ J/m^3)	18.5	17.8	17.4
k(T) (W/m^{2}K)	38.4	39.2	34.1

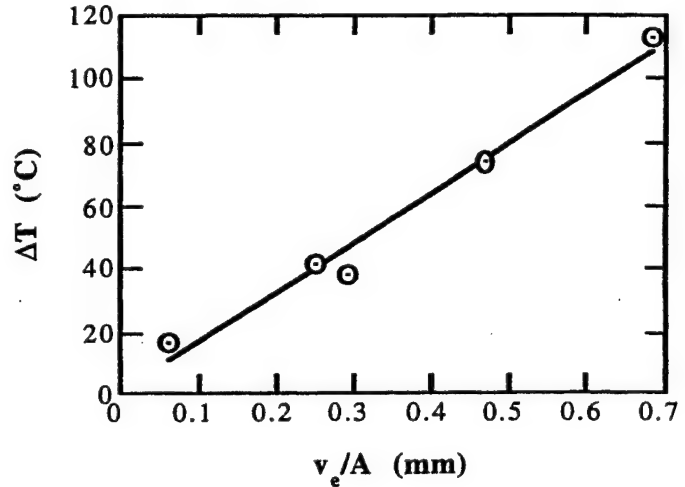Fig. 9. Temperature rise for various actuators while driven at 300 Hz and 3 kV/mm.

Fig. 10. Temperature rise vs. V$_e$/A (3 kV/mm, 300 Hz), where V$_e$ is the effective volume generating the heat and A is the surface area dissipating the heat.

set equal to zero through the plate, and the relation between stress, electric field (only E_z exists), and the induced strain is given by:

$$X_1 = x_1/s_{11}^E - (d_{31}/s_{11}^E)E_z. \qquad (58)$$

Introducing (58) into (57) and allowing for $x_1 = \partial u/\partial x$ and $\partial E_z/\partial x = 0$ (due to the equal potential on each electrode), leads to a harmonic vibration equation:

$$-\omega^2 \rho s_{11}^E u = \partial^2 u/\partial x^2. \qquad (59)$$

Here, ω is the angular frequency of the drive field. Substituting a general solution $u = u_1(x)e^{j\omega t} + u_2(x)e^{-j\omega t}$ into (58), and with the boundary condition $X_1 = 0$ at x = 0 and L (sample length), a solution can be obtained as shown in (60) and (61) (top of next page). Here, v is the sound velocity in the piezoceramic, which is given by:

$$v = 1/\sqrt{\rho s_{11}^E}. \qquad (62)$$

Because the total current is given by (63) (top of next page) and using (60), the admittance for the mechanically free sample is calculated to be (64) (top of next page), where w is the width, L is the length, t is the thickness of the sample, and V is the applied voltage. ε_3^{LC} is the permittivity in a longitudinally clamped sample, which is given by:

$$\varepsilon_0\varepsilon_3^{LC} = \varepsilon_0\varepsilon_3^X - (d_{31}^2/s_{11}^E) = \varepsilon_0\varepsilon_3^X(1 - k_{31}^2). \qquad (65)$$

The final transformation is provided by the definition,

$$k_{31} = d_{31}/\sqrt{s_{11}^E\varepsilon_0\varepsilon_3^X}. \qquad (66)$$

When the drive frequency is much lower than the resonance, taking $\omega \to 0$ (64) leads to Y = $(j\omega wL/t)\varepsilon_3^X$ (corresponding to the static capacitance). The piezoelectric resonance is achieved when the admittance becomes infinite or the impedance is zero. The resonance frequency f$_R$ is calculated from (64), and the fundamental f$_R$ is given by:

$$f_R = v/2L = 1/\left(2L\sqrt{\rho s_{11}^E}\right). \qquad (67)$$

However, the antiresonance state is generated for zero admittance or infinite impedance:

$$(\omega_A L/2v)\cot(\omega_A L/2v) = -d_{31}^2/\varepsilon_3^{LC}s_{11}^E = -k_{31}^2/\left(1 - k_{31}^2\right). \qquad (68)$$

The resonance and antiresonance states are described by the following intuitive model [4]. In a high electromechanical coupling material with k almost equal to 1, the resonance or antiresonance states appear for $\tan(\omega L/2v) = \infty$ or 0 [i. e., $\omega L/2v = (m - 1/2)\pi$ or $m\pi$ (m: integer)], respectively. The strain amplitude x_1 distribution for each state [calculated using (60)] is illustrated in Fig. 14. In the

$$\text{(strain)} \quad \partial u/\partial x = x_1 = d_{31}E_z[\sin\omega(L-x)/v + \sin(\omega x/v)]/\sin(\omega L/v), \tag{60}$$

$$\text{(total displacement)} \quad \Delta L = \int_0^L x_1 dx = d_{31}E_z L(2v/\omega L)\tan(\omega L/2v) \tag{61}$$

$$i = j\omega w \int_0^L D_3\,dx = j\omega w \int_0^L \left[(\varepsilon_0\varepsilon_3^x - d_{31}^2/s_{11}^E)E_z + (d_{31}/s_{11}^E)x_1\right]\,dx, \tag{63}$$

$$\begin{aligned} Y &= (1/Z) = (i/V) = (i/E_z t) \\ &= (j\omega w L/t)\varepsilon_0\varepsilon_3^{LC}\left[1 + (d_{31}^2/\varepsilon_0\varepsilon_3^{LC}s_{11}^E)(\tan(\omega L/2v)/(\omega L/2v))\right], \end{aligned} \tag{64}$$
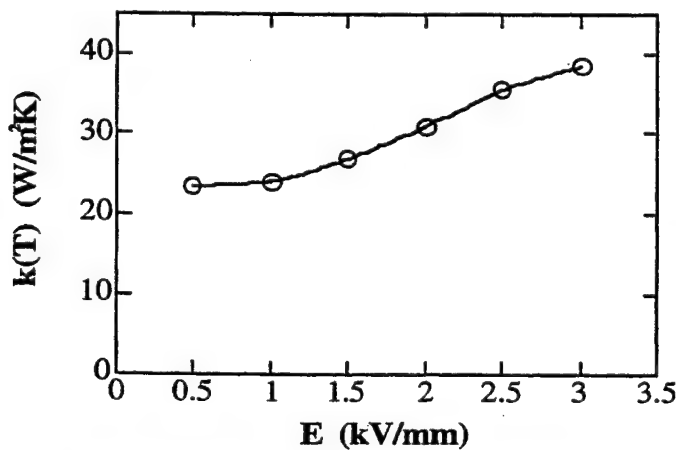

Fig. 11. $k(T)$ as a function of applied electric field (400 Hz, data from the actuator with dimensions of 7 mm × 7 mm × 2 mm).

Fig. 12. Overall heat transfer coefficient $k(T)$ as a function of frequency.

resonance state, large strain amplitudes and large capacitance changes (called motional capacitance) are induced, and the current can easily flow into the device. Note that, for a loss-free piezoelectric, the strain is calculated to be infinite in (60). However, at the antiresonance, the strains induced in the device cancel each other completely, resulting in no capacitance change, and the current cannot flow easily into the sample. Both ends of the plate correspond to the nodal points, which do not generate any motion to be used for actuators. Thus, for a high k material, the first antiresonance frequency f_A should be twice as large as the first resonance frequency f_R.

In a typical case, where $k_{31} = 0.3$, the antiresonance state varies from the above-mentioned mode and becomes closer to the resonance mode. The low-coupling mate-
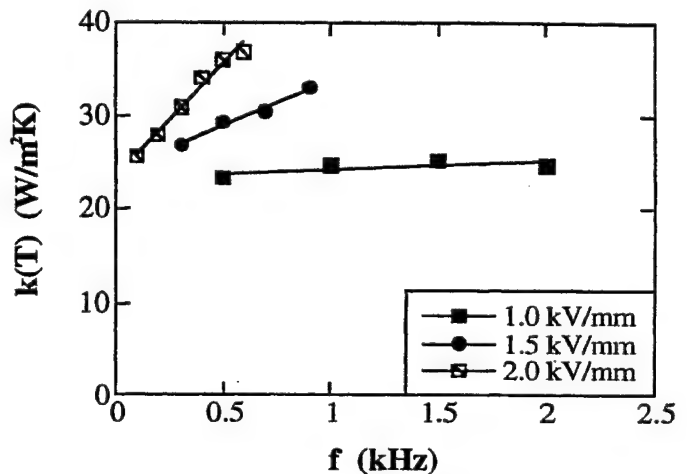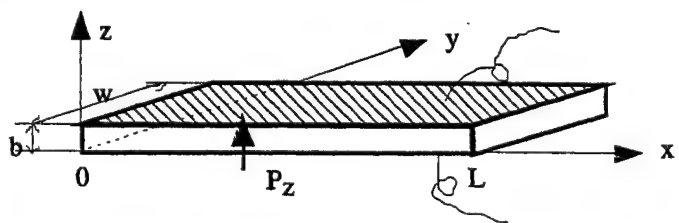

Fig. 13. Longitudinal vibration through the transverse piezoelectric effect (d_{31}) in a rectangular plate.

Resonance

m = 1

Antiresonance
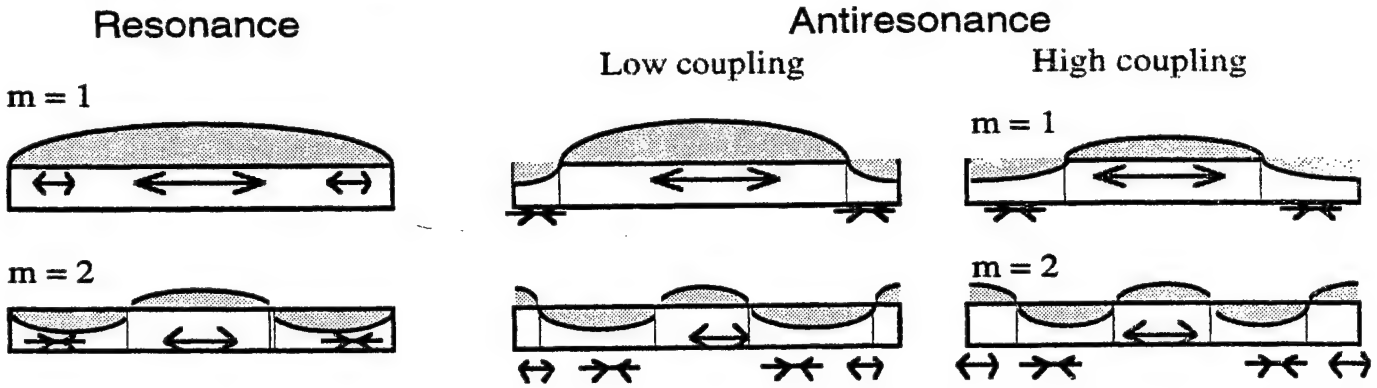### Low coupling
High coupling

m = 2

m = 1

m = 2

Fig. 14. Strain generation in the resonance or antiresonance state. The strain magnitude is plotted in the vertical axis as a function of the x coordinate.

rial exhibits an antiresonance mode in which capacitance change due to the size change is compensated completely by the current required to charge up the static capacitance (called damped capacitance). Thus, the antiresonance frequency f_A will approach the resonance f_R.

When $(f_A - f_R)$ is not very large due to a small electromechanical coupling, we can derive the following approximate expression for f_A. Assuming that $\omega_A - \omega_R$ is much smaller than $\omega_R (= \pi v/L)$, and

$$(\omega_A L/2v) \cot[(\omega_A - \omega_R)L/2v - \pi/2] = -k_{31}^2/ \left(1 - k_{31}^2\right). \tag{69}$$

Thus,

$$\omega_A = (\pi v/L)[1 + (4/\pi^2)K_{31}^2], \tag{70}$$

where we introduced a new parameter K_{31} as:

$$K_{31}^2 = k_{31}^2/(1 - k_{31}^2). \tag{71}$$

It is notable that, for a piezoelectric sample with a typical k_{31} value, the two ends of the plate are not the nodal points; that is, we can expect rather large displacements, which can be applied for ultrasonic motors.

2. Piezoelectric Resonance with Losses: Now we will introduce the complex parameters into the admittance curve around the resonance frequency, in a similar way to the previous section: $\varepsilon_3^{X*} = \varepsilon_3^X(1 - j\tan\delta')$, $s_{11}^{E*} = s_{11}^E(1 - j\tan\phi')$, and $d_{31}^* = d(1 - j\tan\theta')$ into (64) [see (72); next page]. For (72),

$$C_0 = (wL/t)\varepsilon_0\varepsilon_3^X, \tag{73}$$

$$C_d = (1 - k_{31}^2)C_0. \tag{74}$$

Note that the loss for the first term (damped conductance) is represented by the "extensive" dielectric loss $\tan\delta$, not by the intensive loss $\tan\delta'$. Taking into account

$$v^* = 1/\sqrt{\rho s_{11}^E(1 - j\tan\phi')} = v(1 + (1/2)j\tan\phi'), \tag{75}$$

we further calculate $1/\tan(\omega L/2v^*)$ with an expansion-series approximation around $(\omega L/2v) = \pi/2$. The resonance state is defined in this case for the maximum admittance point, rather than the infinite Y.

We will use new frequency parameters,

$$\Omega = \omega L/2v, \Delta\Omega = \Omega - \pi/2(\ll 1). \tag{76}$$

Because $\omega L/2v^* = (\pi/2 + \Delta\Omega)[1 - (1/2)j\tan\phi']$,

$$1/\tan(\omega L/2v^*) = -\Delta\Omega + j(\pi/4)\tan\phi'. \tag{77}$$

Thus, using $K_{31}^2 = k_{31}^2/(1 - k_{31}^2)$, the motional admittance Y_m is approximated around the first resonance frequency by (78) (top of next page). The maximum Y_m is obtained at $\Delta\Omega = 0$:

$$Y_m^{max} = (8/\pi^2)\,\omega_0\,C_d\,K_{31}^2\,(\tan\phi')^{-1}. \tag{79}$$

In order to obtain the mechanical quality factor, let us obtain $\Delta\Omega$, which provides $Y_m^{max}/\sqrt{2}$. Because $\Delta\Omega = (\pi/4)\tan\phi'$ is obtained,

$$Q_m = \Omega_0/2\Delta\Omega = (\pi/2)/2(\pi/4)\tan\phi' = (\tan\phi')^{-1}. \tag{80}$$

This verifies the already used relation, $Q_m = (\tan\phi')^{-1}$.

Here, the displacement amplification also is considered. From (61), also by using the complex parameters, (81) is true (see top of next page). The maximum displacement u_{max} is obtained at $\Delta\Omega = 0$:

$$u_{max} = (8/\pi^2)\,d_{31}\,E_z L(\tan\phi')^{-1}. \tag{82}$$

The maximum displacement at the resonance frequency is $(8/\pi^2)\,Q_m$ times larger than that at a nonresonance frequency $(d_{31}E_z L)$.

In a brief summary, we obtained an already used knowledge: when we observe the admittance or displacement spectrum as a function of drive frequency, and obtain the mechanical quality factor Q_m estimated from $Q_m = \omega_0/2\Delta\omega$, where $2\Delta\omega$ is a full width of the 3 dB down (i.e., $1/\sqrt{2}$) of the maximum value at $\omega = \omega_0$, we can obtain the intensive mechanical loss $\tan\phi'$.

B. Equivalent Circuit

The equivalent circuit for the piezoelectric actuator is represented by a combination of L, C, and R. Fig. 15(a)

$$
\begin{aligned}
Y &= Y_d + Y_m \\
&= (j\omega wL/t)\varepsilon_0\varepsilon_3^X(1-k_{31}^2)[1-j(1/(1-k_{31}^2))(\tan\delta'+k_{31}^2(\tan\phi'-2\tan\theta'))] \\
&\quad + (j\omega wL/t)\varepsilon_0\varepsilon_3^Xk_{31}^2[1-j(2\tan\theta'-\tan\phi')][\tan(\omega L/2\,v^*)/(\omega L/2v^*)] \\
&= j\omega C_0(1-k_{31}^2)[1-j(1/(1-k_{31}^2))(\tan\delta'+k_{31}^2(\tan\phi'-2\tan\theta'))] \\
&\quad + j\omega C_0k_{31}^2[1-j(2\tan\theta'-\tan\phi')][\tan(\omega L/2v^*)/(\omega L/2v^*)] \\
&= j\omega C_d(1-j\tan\delta) + j\omega C_dK_{31}^2[1-j(2\tan\theta'-\tan\phi')][\tan(\omega L/2v^*)/(\omega L/2v^*)],
\end{aligned}
\tag{72}
$$

$$
\begin{aligned}
Y_m &= j\omega C_d\,K_{31}^2[1-j(2\tan\theta'-\tan\phi')][\tan(\omega L/2v*)/(\omega L/2v^*)] \\
&= j\omega_0 C_d\,K_{31}^2[1-j(2\tan\theta'-\tan\phi')]/[(-\Delta\Omega+j(\pi/4)\tan\phi')(\pi/2)(1-(1/2)j\tan\phi')] \\
&= j(8/\pi^2)\omega_0 C_d\,K_{31}^2[(1+j(3/2)\tan\phi'-2\tan\theta')]/[(-(4/\pi)\Delta\Omega+j\tan\phi')].
\end{aligned}
\tag{78}
$$

$$
\begin{aligned}
u(L) &= d_{31}^*E_zL(2v^*/\omega L)\tan(\omega L/2v^*) \\
&= 2d_{31}(1-j\tan\theta')\,E_zL[v(1+(1/2)j\tan\phi')/\omega L]\tan(\omega L/2v^*) \\
&= 2d_{31}(1-j\tan\theta')\,E_zL[v(1+(1/2)j\tan\phi')/\omega_0L]/(-\Delta\Omega+j(\pi/4)\tan\phi').
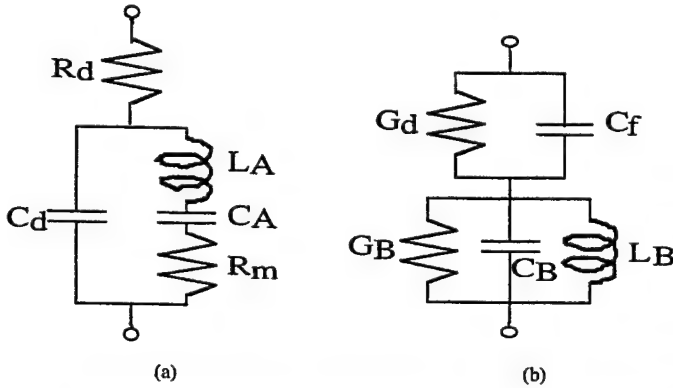\end{aligned}
\tag{81}
$$

Fig. 15. Equivalent circuit of a piezoelectric device for the resonance (a) and the antiresonance (b).

The total resistance $R_A(=R_d+R_m)$ should correspond to the loss $\tan\phi'$, which is composed of the extensive mechanical loss $\tan\phi$ and dielectric/piezoelectric coupled loss $(\tan\delta-2\tan\theta)$ (45). Thus, intuitively speaking, R_d and R_m correspond to the extensive dielectric and mechanical losses, respectively. Note that we introduced an additional resistance R_d to explain a large contribution of the dielectric loss when a vibration velocity is relatively large. Precisely speaking, the above description is not very true. The details will be reported in a forthcoming paper. In contrast, the equivalent circuit for the antiresonance state of the same actuator is shown in Fig. 15(b), which has high impedance.

C. Losses as a Function of Vibration Velocity

Fig. 16 shows the mechanical Q_m vs. basic composition x at two effective vibration velocities $v_0 = 0.05$ m/s and 0.5 m/s for $Pb(Zr_xTi_{1-x})O_3$ doped with 2.1 at.% of Fe [5]. The decrease in mechanical Q_m with an increase of vibration level is minimum around the rhombohedral-tetragonal morphotropic phase boundary (52/48). In other words, the smallest Q_m material at a small vibration level becomes the best at a large vibration level, and the data obtained by a conventional impedance analyzer with a small voltage/power does not provide data relevant to high power materials.

shows an equivalent circuit for the resonance state, which has very low impedance. Taking into account (72), we can understand that C_d and R_d correspond to the electrostatic capacitance (for a longitudinally clamped sample in the previous case, not a free sample) and the clamped (or "extensive") dielectric loss $\tan\delta$, respectively, and the components L_A and C_A in a series resonance circuit are related to the piezoelectric motion. For example, in the case of the longitudinal vibration of the above rectangular plate through d_{31}, these components are represented approximately by

Let us consider the degradation mechanism of the mechanical quality factor Q_m with increasing vibration velocity. Fig. 17 shows an important notion on heat generation from the piezoelectric material [6]. The damped and mo-
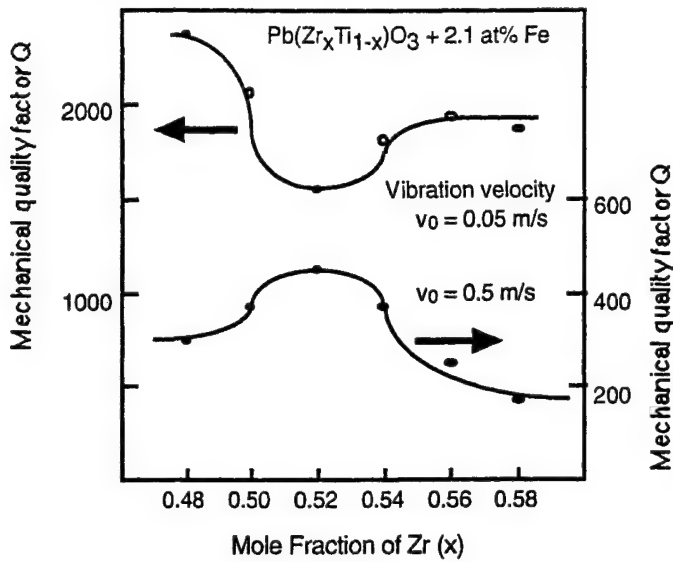
$$
L_A = (\rho/8)(Lb/w)(s_{11}^{E2}/d_{31}^2),
\tag{83}
$$

$$
C_A = (8/\pi^2)(Lw/b)(d_{31}^2/s_{11}^E).
\tag{84}
$$

Fig. 16. Mechanical Q_m versus basic composition x at two effective vibration velocities $v_0 = 0.05$ m/s and 0.5 m/s for $Pb(Zr_xTi_{1-x})O_3$ doped with 2.1 at.% of Fe.

Fig. 17. Vibration velocity dependence of the resistances R_d and R_m in the equivalent electric circuit for a PZT sample.

tional resistances, R_d and R_m, in the equivalent electrical circuit of a PZT sample are separately plotted as a function of vibration velocity. Note that R_m, mainly related to the extensive mechanical loss, is insensitive to the vibration velocity; and R_d, related to the extensive dielectric loss, increases significantly around a certain critical vibration velocity. Thus, the resonance loss at a small vibration velocity is mainly determined by the extensive mechanical loss which provides a high mechanical quality factor Q_m, and with increasing vibration velocity, the extensive dielectric loss contribution significantly increases. After R_d exceeds R_m, we started to observe heat generation.

Tashiro *et al.* [7] observed the heat generation in a rectangular piezoelectric plate during a resonating drive. Even though the maximum electric filed is not very large, heat is generated due to the large induced strain/stress at the resonance. The maximum heat generation was observed at the nodal point of the resonance vibration, at which the maximum strain/stress are generated. This observation supports that the heat generation in a resonating sample is attributed to the intensive elastic loss $\tan \phi'$. This is not contradictory to the result in Section IV, in which a high-voltage was applied at an off-resonance frequency. We concluded there that the heat is originated from the intensive dielectric loss $\tan \delta'$. In consideration that both the "intensive" dielectric and mechanical losses are composed of the "extensive" dielectric and mechanical losses, and that the extensive dielectric loss $\tan \delta$ changes significantly with the external electric field and stress, the major contribution to the heat generation seems to come from the "extensive" dielectric loss. Further investigations are needed for the microscopic explanations of this phenomenon.
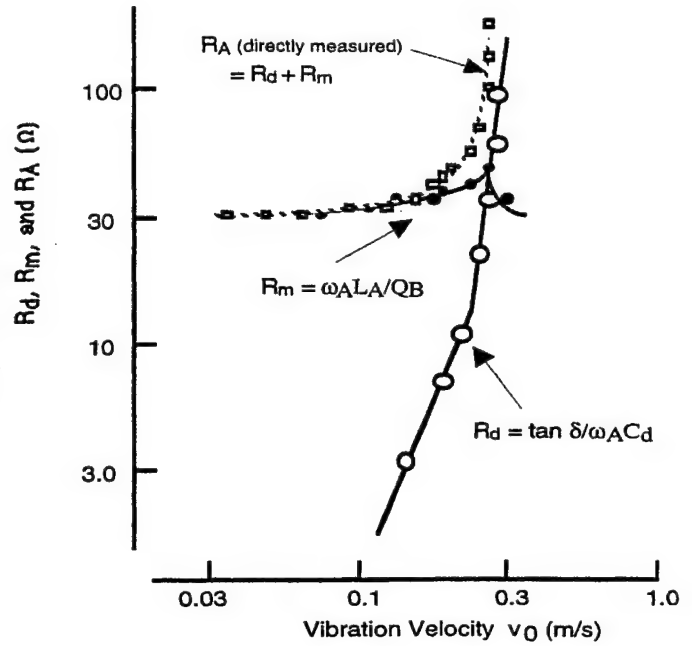
VI. LOSSES AT RESONANCE AND ANTIRESONANCE MODES

A. Losses at a Piezoelectric Antiresonance State

We consider here the losses at the antiresonance frequency in comparison with the resonance mode. The antiresonance mode is obtained at a frequency that provides the minimum value of admittance Y, instead of zero of Y for the loss-free case. Taking an approximation technique on (72) around the antiresonance frequency ω_A, similar to the previous section, we obtain:

$$\Omega_A = \omega_A L/2v, \Delta\Omega = \Omega - \Omega_A (\ll 1). \quad (85)$$

If k_{31} is not very large, the following relationship is obtained:

$$\Omega_A = \omega_A L/2v = (\pi/2)(1 + (4/\pi^2) k_{31}^2). \quad (86)$$

In the following approximation, however, this relation is not used; but we will neglect the higher order of $\Delta\Omega$ and $\tan \phi'$ in (72), yielding (87) (top of next page). Taking into account (88) and (89) (top of next page), where

$$K_{31}^2 = k_{31}^2/(1 - k_{31}^2). \quad (90)$$

Then, Y^{min} can be obtained at $\Delta\Omega = 0$:

$$Y^{min} = \omega C_d (1/2) \tan \phi' (\Omega_A^2 + K_{31}^2 + K_{31}^4)/K_{31}^2. \quad (91)$$

$\sqrt{2} Y^{min}$ can be obtained at:

$$\Delta\Omega = (1/2) \Omega_A \tan \phi'. \quad (92)$$

$$Y = j\omega C_d \left\{ 1 + (k_{31}^2/(1 - k_{31}^2)) \tan[(\Omega_A + \Delta\Omega)(1 - j(1/2)\tan\phi')]/ \right.$$
$$\left. [(\Omega_A + \Delta\Omega)(1 - j(1/2)\tan\phi'). \right. \tag{87}$$

$$\tan[(\Omega_A + \Delta\Omega)(1 - j(1/2)\tan\phi')]$$
$$= [(\Omega_A^2 - K_{31}^2\Delta\Omega + j(1/2)\Omega_A \tan\phi' K_{31}^2]/[(-K_{31}^2 - \Omega_A\Delta\Omega) - j\Omega_A(1/2)\Omega_A \tan\phi'], \tag{88}$$

$$Y = j\omega C_d(\Omega_A^2 + K_{31}^2 + K_{31}^4)[-\Delta\Omega + j(1/2)\Omega_A \tan\phi']/$$
$$[-K_{31}^2\Omega_A - (\Omega_A^2 + K_{31}^2)\Delta\Omega + j(1/2)\Omega_A \tan\phi'(\Omega_A^2 + K_{31}^2)], \tag{89}$$

Thus, mechanical quality factor at the antiresonance can be obtained as:

$$Q_m = \Omega_A/2\Delta\Omega = (\tan\phi')^{-1}. \tag{93}$$

Q_m at the antiresonance could be verified to be equal to Q_m at the resonance ($= (\tan\phi')^{-1}$) in the first approximation neglecting the higher order terms more than $(\Delta\Omega)^2$, $(\tan\phi')^2$ etc. However, this result shows a discrepancy with the experimental results as discussed below. Further higher order approximation analysis will be required.

B. Experimental Results

Fig. 18 illustrates mechanical quality factors, Q_A, Q_B and the temperature rise for the resonance (A-type) and the antiresonance (B-type) modes for a rectangular-shaped hard PZT resonator plotted as a function of vibration velocity [6]. The sample size is indicated in Fig. 18 (43 mm × 7 mm × 2 mm). Note that an "effective" vibration velocity v_0 is a material's constant independent of the sample size, and it is defined as $\sqrt{2}\pi f u_{max}$ where f is the resonance or antiresonance frequency and u_{max} is the maximum vibration amplitude of the piezoelectric device [8]. Again it is noteworthy that the mechanical quality factor decreases significantly above a certain critical vibration velocity (0.1 m/s), at which a steep temperature rise starts. We have suggested that the heat generation is mainly attributed to the extensive dielectric loss rather than the mechanical loss. Note also that Q_B is higher than Q_A over the entire vibration velocity range, and that the temperature rise of the sample is less for the B-type resonance (antiresonance) than for the A-type resonance for the same vibration level. This indicates an intriguing idea that the antiresonance mode should be superior to the conventional resonance mode, particularly for high-power applications such as ultrasonic motors. In a typical piezoelectric material with k_{31} around 30%, the plate edge is not a vibration nodal point and can generate a large vibration velocity.
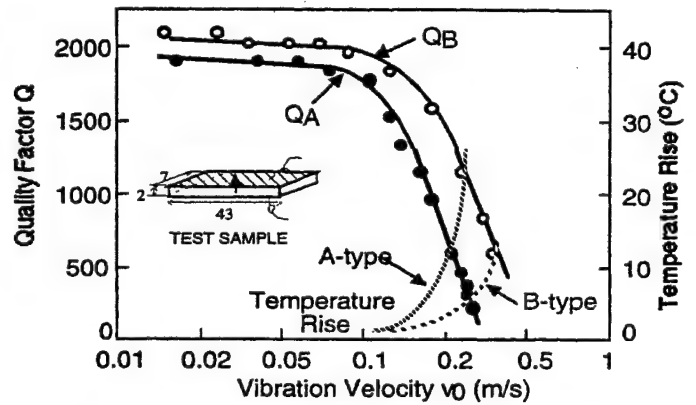

Fig. 18. Vibration velocity dependence of the quality factor Q (Q_A, Q_B) and temperature rise for both A (resonance) and B (antiresonance) type resonances of a longitudinally vibrating PZT ceramic transducer through the transverse piezoelectric effect d_{31}.

VII. CONCLUSIONS

Various techniques for measuring the electric, mechanical, and piezoelectric coupling losses separately have been discussed:

- D vs. E, x vs. X, x vs. E and D vs. X curves for dielectric, mechanical, and piezoelectric losses,
- heat generation at a resonance or an off-resonance frequency for an intensive mechanical or dielectric loss,
- resonance/antiresonance technique for intensive and extensive mechanical losses, respectively.

By combining the above methods, we can investigate the loss mechanisms in practical piezoelectric materials.

The piezoelectric losses $\tan\theta'$ and $\tan\theta$ are not as small as previously believed, but they are comparable to the dielectric and elastic losses in soft PZTs. Also, it is noteworthy that the extensive dielectric loss $\tan\delta$ increases significantly with an increase of the intensive parameter, i.e., the applied electric field; and the extensive elastic loss $\tan\phi$ is rather insensitive to the intensive parameter, i.e., the applied compressive stress.

Heat generation is caused mainly by the intensive dielectric loss $\tan \delta'$ (i.e., P-E hysteresis loss) for an off-resonance state under a high-drive, electric field, and by the intensive mechanical loss $\tan \phi'$ for a resonance state. Both situations are attributed to the large "extensive dielectric loss" enhanced by a large external electric field or stress. In order to suppress the temperature rise practically, a transducer design with larger surface area is recommended (for example, a tube rather than a rod).

A significant decrease in mechanical Q_m with an increase of vibration level was observed in resonant piezoelectric ceramic devices, and the data obtained by a conventional impedance analyzer with a small voltage/power do not provide data relevant to high-power materials.

Because the mechanical quality factor Q_B at an antiresonance frequency is larger than Q_A at a resonance frequency, the antiresonance mode seems to be superior to the conventional usage of the resonance mode, particularly for high-power applications such as ultrasonic motors.

Because the above conclusions were derived from only a limited number of PZT-based soft and hard piezoelectrics, it is too early to generalize these conclusions. Further investigations are highly required.

REFERENCES

[1] K. H. Haerdtl, *Ceram. Int.*, vol. 8, pp. 121–127, 1982.
[2] T. Ikeda, *Fundamentals of Piezoelectric Materials Science.* Tokyo: Ohm Publication, 1984, p. 83.
[3] J. Zheng, S. Takahashi, S. Yoshikawa, K. Uchino, and J.W.C. de Vries, *J. Amer. Ceram. Soc.*, vol. 79, pp. 3193–3198, 1996.
[4] K. Uchino, *Piezoelectric Actuators and Ultrasonic Motors.* Boston: Kluwer, 1997, p. 197.
[5] S. Takahashi and S. Hirose, *Jpn. J. Appl. Phys.*, vol. 32, pp. 2422–2425, 1993.
[6] S. Hirose, M. Aoyagi, Y. Tomikawa, S. Takahashi, and K. Uchino, *Proc. Ultrason.*, Edinburgh, 1995, pp. 184–187.
[7] S. Tashiro, M. Ikehiro, and H. Igarashi, *Jpn. J. Appl. Phys.*, vol. 36, pp. 3004–3009, 1997.
[8] K. Uchino, J. Zheng, A. Joshi, Y. H. Chen, S. Yoshikawa, S. Hirose, S. Takahashi, and J.W.C. de Vries, *J. Electroceram.*, vol. 2, pp. 33–40, 1998.

Kenji Uchino (M'89), one of the pioneers in piezoelectric actuators, is the Director of International Center for Actuators and Transducers and Professor of Electrical Engineering at The Pennsylvania State University.

After being awarded his Ph.D. degree from Tokyo Institute of Technology, Japan, Uchino became a research associate in the Physical Electronics Department at this Institute. He then joined the Sophia University, Japan, as an associate professor in physics in 1985. He moved to Penn State in 1991. He also was involved with the Space Shuttle Utilizing Committee in NASDA, Japan, during 1986–1988, and he was the Vice President of NF Electronic Instruments during 1992–1994. He is the Chairman of the Smart Actuator/Sensor Study Committee, sponsored by Japanese MITI. He is also the executive associate editor for the *Journal of Advanced Performance Materials* (Kluwer Academic) and the associate editor of the *Journal of Intelligent Materials Systems and Structures* (Technomic), and the *Japanese Journal of Applied Physics*.

His research interests are in solid state physics, especially dielectrics, ferroelectrics, and piezoelectrics, including basic research on materials, device designing, and fabrication processes, as well as development of solid state actuators for precision positioners, ultrasonic motors, etc. He has authored 270 papers, 31 books, and has 16 patents in the ceramic actuator area.

He is a recipient of the Outstanding Research Award from Penn State Engineering Society (1996), Academic Scholarship from Nissan Motors Scientific Foundation (1990), Best Movie Memorial Award at Japan Scientific Movie Festival (1989), and the Best Paper Award from the Japanese Society of Oil/Air Pressure Control (1987). He also is a Fellow of the American Ceramic Society and a member of the IEEE.

Seiji Hirose received the B.S. degree in electronics in 1971 from Yamagata University, Yonezawa, Japan, and the Ph.D. degree in 1989 from Tohoku University, Sendai, Japan. Since April 1971, he has been with the Yamagata University, Yonezawa, Japan, where he is a professor of electronics and information engineering.

His research interest is in the high-power characteristics of the piezoelectric material and the piezoelectric transformer.

Dr. Hirose is a member of the Acoustical Society of Japan, the Material Society of America, and IEEE.

APPENDIX 49

LOSS MECHANISMS IN PIEZOELECTRICS
-- Extrinsic and Intrinsic Losses --

K. Uchino, J. Zheng, Y.H. Chen, X. Du, S. Hirose*, S. Takahashi**
International Center for Actuators and Transducers, Materials Research Laboratory, The
Pennsylvania State University, University Park, Pa 16802, kenjiuchino@psu.edu
*Faculty of Engineering, Yamagata University, Yonezawa 992, Japan,
**Research and Development Group, NEC Corporation, 4-1-1 Miyazaki, Miyamae-ku, Kawasaki
216, Japan

ABSTRACT

Losses in piezoelectrics are considered in general to have three different mechanisms; dielectric, mechanical and piezoelectric losses. This paper deals with the phenomenology of losses, first, then how to measure these losses separately in experiments.

INTRODUCTION

Loss or hysteresis in piezoelectrics exhibits both merits and demerits. For positioning actuator applications, hysteresis in the field-induced strain provides a serious problem, and for resonance actuation such as ultrasonic motors, loss generates significant heat in the piezoelectric materials. Further, in consideration of the resonant strain amplified in proportion to a mechanical quality factor, low (extrinsic) mechanical loss materials are preferred for ultrasonic motors [1-3]. On the contrary, for force sensors and acoustic transducers, high mechanical loss, which corresponds to a low mechanical quality factor Q_m, is essential to widen a frequency range for receiving signals.

However, not much research effort has been put into systematic studies of the loss mechanisms in piezoelectrics, particularly in high voltage and high power range [4-6]. Since not many comprehensive descriptions can be found in previous reports [7], this paper will clarify the loss mechanisms in piezoelectrics phenomenologically, first, then how to measure these losses separately in experiments.

GENERAL CONSIDERATION OF LOSS AND HYSTERESIS

Extrinsic Losses

We will start from the Gibbs free energy G in a piezoelectric material expressed by

$$dG = - x\, dX - D\, dE - S\, dT, \tag{1}$$

and

$$G = - (1/2)\, s^E X^2 - d\, X\, E - (1/2)\, \varepsilon^X \varepsilon_0\, E^2. \tag{2}$$

Here, x is strain, X, stress, D, electric displacement, E, electric field, S, enthalpy and T is temperature. Equation (2) is the energy expression in terms of intensive physical parameters (externally controllable parameters) X and E. Temperature dependence is carried into the elastic compliance s^E, the dielectric constant ε^X and the piezoelectric constant d. We will obtain the following two piezoelectric equations:

$$x = - (\partial G/\partial X) = s^E X + d\, E, \tag{3}$$
$$D = - (\partial G/\partial E) = d\, X + \varepsilon^X \varepsilon_0\, E. \tag{4}$$

Note that thermodynamical equations and the consequent piezoelectric equations (Eqs. (1)-(4)) cannot yield a loss, without taking into account irreversible thermodynamic equations or dissipation functions, in general. However, the latter considerations are mathematically equivalent to the introduction of complex physical constants into the phenomenological equations, if the loss can be treated as a perturbation.

Therefore, we will introduce complex parameters ε^{X*}, s^{E*}, and d^* in order to consider the hysteresis losses in electric, elastic and piezoelectric coupling energy :

$$\varepsilon^{X*} = \varepsilon^X(1 - j \tan \delta'), \tag{5}$$

$$s^{E*} = s^E(1 - j \tan \phi'), \tag{6}$$

$$d^* = d(1 - j \tan \theta'). \tag{7}$$

Note that the negative connection in Eqs. (5)-(7) come from the time "delay." θ' is the phase delay of the strain under an applied electric field, or the phase delay of the electric displacement under an applied stress. Both delay phases should be exactly the same if we introduce the same complex piezoelectric constant d^* into Eqs.(3) and (4). δ' is the phase delay of the electric displacement to an applied electric field under a constant stress (i.e., zero stress) condition, and ϕ' is the phase delay of the strain to an applied stress under a constant electric field (i.e., short-circuit) condition. We will consider these phase delays as "extrinsic" losses.

Figures 1(a) - 1(d) correspond to the model hysteresis curves for practical experiments: D vs. E curve under a stress-free condition, x vs. X under a short-circuit condition, x vs. E under a stress-free condition and D vs. X under an open-circuit condition for measuring charge (or under a short-circuit condition for measuring current), respectively.

The stored energies and hysteresis losses for pure electrical and mechanical energies can be calculated as:

$$U_e = (1/2) \varepsilon^X \varepsilon_0 E_0^2, \tag{8}$$

$$w_e = \pi \varepsilon^X \varepsilon_0 E_0^2 \tan \delta' ; \tag{9}$$

$$U_m = (1/2) s^E X_0^2, \tag{10}$$

$$w_m = \pi s^E X_0^2 \tan \phi' . \tag{11}$$

The electromechanical loss, when measuring the induced strain under an electric field, is more complicated, because the field vs. strain domain cannot be used for directly calculating the energy. Let us calculate the stored energy U_{em} during a quarter electric field cycle (i.e., 0 to E_0) , first :
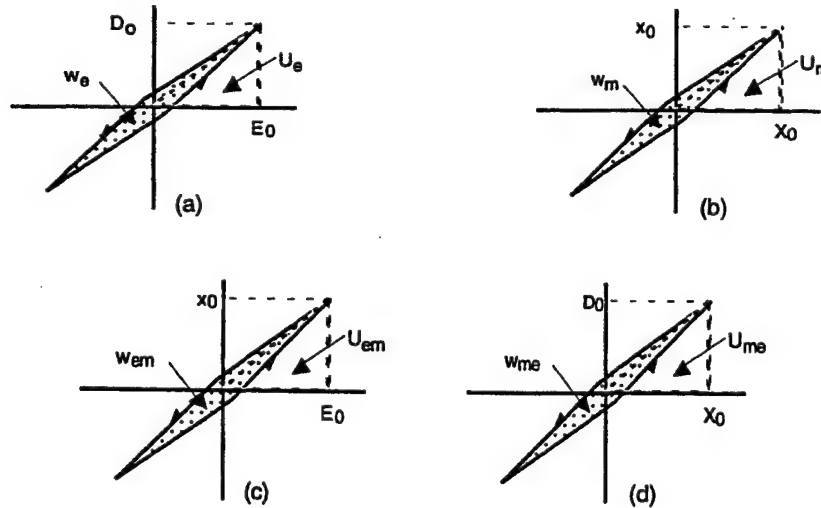

Fig.1   (a) D vs. E (stress free), (b) x vs. X (short-circuit), (c) x vs. E (stress free) and (d) D vs. X (open-circuit) curves with a slight hysteresis in each relation.

$$U_{em} = -\int x \, dX = (1/2) \, (x_0^2/s^E) = (1/2) \, (dE_0)^2/s^E$$
$$= (1/2) \, (d^2/s^E)E_0^2 \qquad (12)$$

Replacing d and s^E by $d^* = d \, (1 - j \tan \theta')$ and $s^{E*} = s^E(1 - j \tan \phi')$, we obtain

$$U_{em} = (1/2) \, (d^2/ \, s^E) \, E_0^2, \qquad (13)$$

and

$$w_{em} = \pi \, (d^2/ \, s^E) \, E_0^2 \, (2 \tan\theta' - \tan\phi'). \qquad (14)$$

Note that the strain vs. electric field measurement seems to provide the piezoelectric loss $\tan\theta'$ directly, however, the observed loss should include an additional elastic loss because the strain should be delayed to the initial stress, which is needed to calculate energy.

Similarly, when we measure the induced charge under stress, the stored energy U_{me} and the hysteresis loss w_{me} during a quarter and a full stress cycle, respectively, are obtained as

$$U_{me} = (1/2) \, (d^2/ \, \varepsilon_0\varepsilon^X) \, X_0^2, \qquad (15)$$

and

$$w_{me} = \pi \, (d^2/ \, \varepsilon_0\varepsilon^X) \, X_0^2 \, (2 \tan\theta' - \tan\delta'). \qquad (16)$$

Hence, from the measurements of D vs. E and x vs. X, we obtain $\tan\delta'$ and $\tan\phi'$, respectively, and either the piezoelectric (D vs. X) or converse piezoelectric measurement (x vs. E) provides $\tan \theta'$ through a numerical subtraction.

Intrinsic Losses

So far, we discussed the "extrinsic" electric, mechanical and piezoelectric losses. In order to consider real physical meanings of the losses, we will introduce the "intrinsic" losses. When we start from the energy expression in terms of extensive physical parameters (material's intrinsic parameters) x and D, that is,

$$dA = X \, dx + E \, dD - S \, dT, \qquad (17)$$

we can obtain the piezoelectric equations as follows:

$$X = (\partial A/\partial x) = c^D \, x - h \, D, \qquad (18)$$
$$E = (\partial A/\partial D) = - \, h \, x + \kappa^X\kappa_0 \, D. \qquad (19)$$

We introduce the intrinsic electric, mechanical and piezoelectric losses as

$$\kappa^{X*} = \kappa^X \, (1 + j \tan \delta), \qquad (20)$$
$$c^{D*} = c^D \, (1 + j \tan \phi), \qquad (21)$$
$$h^* = h \, (1 + j \tan \theta). \qquad (22)$$

It is notable that the permittivity under a constant strain (i. e., zero strain or completely clamped) condition, ε^{X*} and the elastic compiance under a constant electric displacement (i. e., open-circuit) condition, s^{D*} can be provided as an inverse value of κ^{X*} and c^{D*}, respectively. Thus, using the exactly the same losses in Eqs. (20) and (21),

$$\varepsilon^{X*} = \varepsilon^X(1 - j \tan \delta), \qquad (23)$$
$$s^{D*} = s^D(1 - j \tan \phi), \qquad (24)$$

We will consider these phase delays again as "intrinsic" losses.

27

Here, we consider the physical property difference between the boundary conditions; E constant and D constant, or X constant and x constant. When an elecric field is applied on a piezoelectric sample as illustrated in the top of Fig. 2, this state will be equivalent to the superposition of the following two steps: first, the sample is completely clamped and the field E_0 is applied (pure electrical energy $(1/2)\, \varepsilon^X \varepsilon_0\, E_0^2$ is input); second, keeping the field at E_0, the mechanical constraint is released (additional mechanical energy $(1/2)\, (d^2/s^E)\, E_0^2$ is necessary). The total energy should correspond to the total input electrical energy $(1/2)\, \varepsilon^X \varepsilon_0\, E_0^2$; thus, we obtain the relation,

$$\varepsilon_0 \varepsilon^X = \varepsilon_0 \varepsilon^x + (d^2/s^E), \tag{25}$$

Similarly, from the bottom of Fig. 2,

$$s^E = s^D + (d^2/\varepsilon_0 \varepsilon^X). \tag{26}$$

Hence, we obtain the following equations:

$$\varepsilon^x / \varepsilon^X = (1 - k^2), \tag{27}$$
$$s^D / s^E = (1 - k^2), \tag{28}$$

where

$$k^2 = d^2/(s^E\, \varepsilon_0 \varepsilon^X). \tag{29}$$
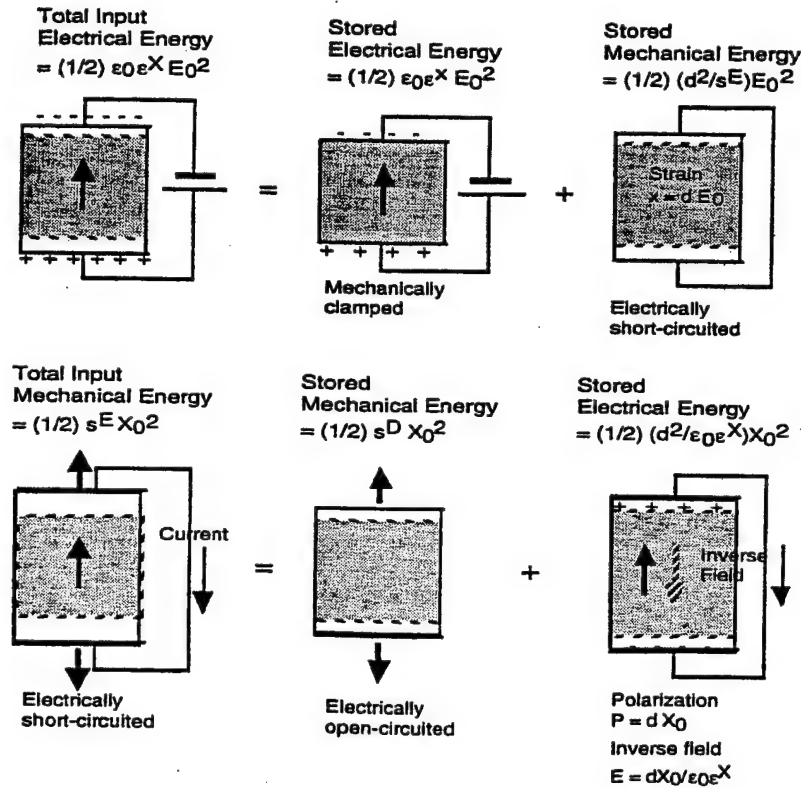
Fig. 2 Conceptual figure for explaining the relation between ε^X and ε^x, s^E and s^D.

Similarly,

$$\kappa^X / \kappa^X = (1 - k^2), \tag{30}$$
$$c^E / c^D = (1 - k^2), \tag{31}$$

where

$$k^2 = h^2/(c^D \kappa^X \kappa_0). \tag{32}$$

This k is called the *electromechanical coupling factor*, and is the same as the k in Eq. (29), because the equation $d^2/(s^E \varepsilon_0 \varepsilon^X) = h^2/(c^D \kappa^X \kappa_0)$ can be verified mathematically. We define the k as a real number in this manuscript.

In order to obtain the relationships between the extrinsic and intrinsic losses, the following three equations are essential:

$$\varepsilon_0 \varepsilon^X = [\kappa^X \kappa_0 (1 - h^2/(c^D \kappa^X \kappa_0))]^{-1}, \tag{33}$$
$$s^E = [c^D (1 - h^2/(c^D \kappa^X \kappa_0))]^{-1}, \tag{34}$$
$$d = [h^2/(c^D \kappa^X \kappa_0)] [h (1 - h^2/(c^D \kappa^X \kappa_0))]^{-1}. \tag{35}$$

Replacing the parameters in Eqs. (33) - (35) by the complex parameters in Eqs. (5) - (7), (20) - (22), we obtain the relationships between the extrinsic and intrinsic losses:

$$\tan \delta' = (1/(1 - k^2))[\tan \delta + k^2(\tan \phi - 2 \tan \theta)], \tag{36}$$
$$\tan \phi' = (1/(1 - k^2))[\tan \phi + k^2(\tan \delta - 2 \tan \theta)], \tag{37}$$
$$\tan \theta' = (1/(1 - k^2))[\tan \delta + \tan \phi + (1 + k^2) \tan \theta], \tag{38}$$

where k is the electromechanical coupling factor defined by either Eq. (29) or Eq. (32), and here as a real number. It is important that the extrinsic dielectric and elastic losses are mutually correlated with the intrinsic dielectric, elastic and piezoelectric losses through the electromechanical coupling k^2, and that the denominator $(1 - k^2)$ comes basically from the ratios, $\varepsilon^x / \varepsilon^X = (1 - k^2)$ and $s^D/s^E = (1 - k^2)$, and this real part reflects to the dissipation factor when the imaginary part is devided by the real part.

EXPERIMENTAL RESULTS

Figure 3 shows "extrinsic" dissipation factors determined from (a) D vs. E (stress free), (b) x vs. X (short-circuit), (c) x vs. E (stress free) and (d) D vs. X (open-circuit) curves for a PZT based soft multilayer actuator. Figure 4 shows the result for the piezoelectric loss $\tan\theta'$. We used the correlation factor between electric field and compressive stress given averagely by $X = (\varepsilon_0 \varepsilon^X/s^E)^{1/2} E$.

From Figs. 3 and 4, we can calculate the "intrinsic" losses as shown in Fig. 5. Note that the piezoelectric losses $\tan\theta'$ and $\tan\theta$ are not so small as previously believed, but comparable to the dielectric and elastic losses, and increase gradually with the field or stress. The experimental details will be reported in the successive papers.

When similar measurements to Figs. 1(a) and 1.(b), but under constrained conditions; that is, D vs. E under a completely clamped state, and x vs. X under an open-circuit state, respectively, we can expect smaller hystereses; that is, intrinsic losses, $\tan\delta$ and $\tan\phi$. These measurements seem to be alternative methods to determine the three losses separately, however, they are rather difficult in practice.
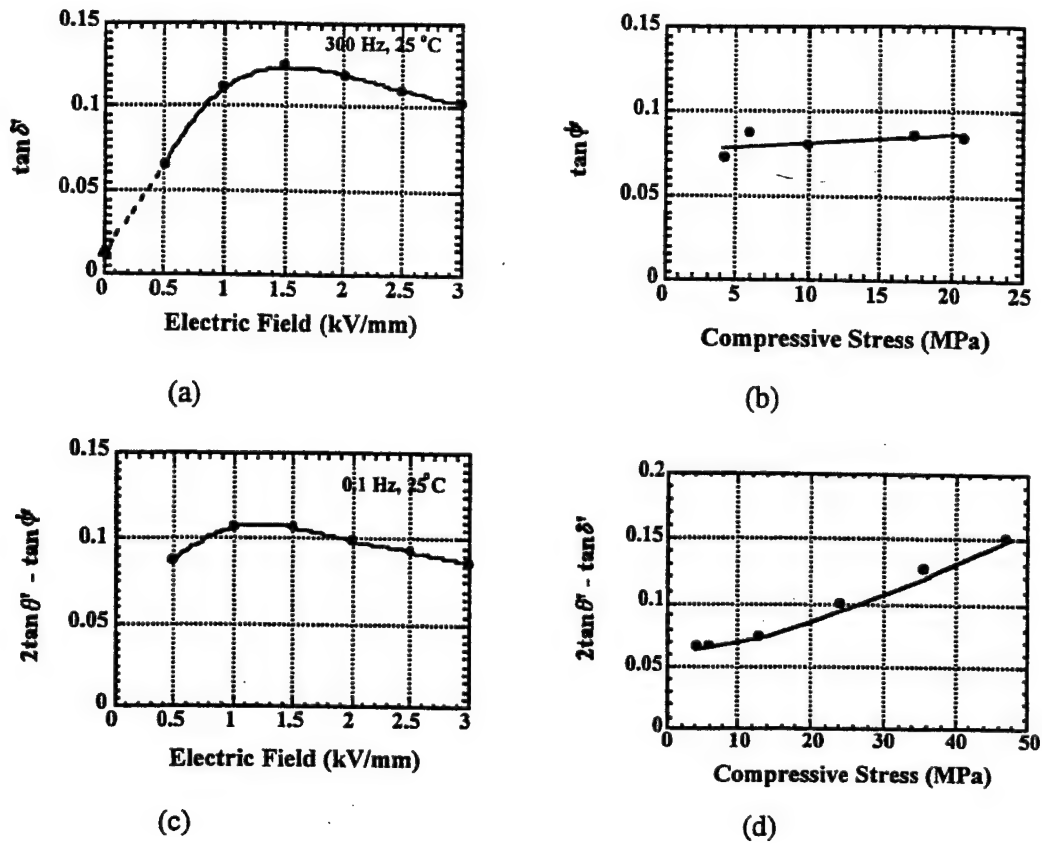
Fig.3 Dissipation factors determined from (a) D vs. E (stress free), (b) x vs. X (short-circuit), (c) x vs. E (stress free) and (d) D vs. X (open-circuit) curves for a PZT based actuator.
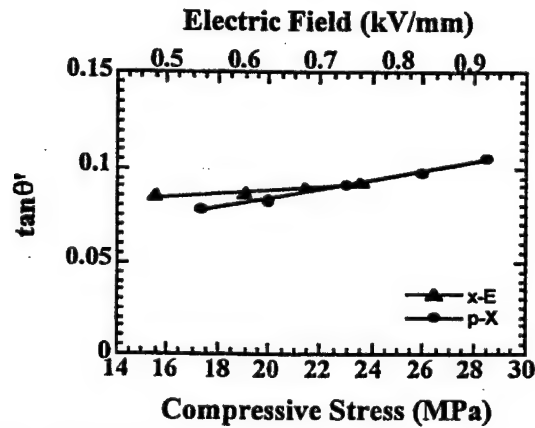

Fig.4 Extrinsic piezoelectric dissipation factor $\tan\theta'$ as a function of electric field or compressive stress, measured for a PZT based actuator.
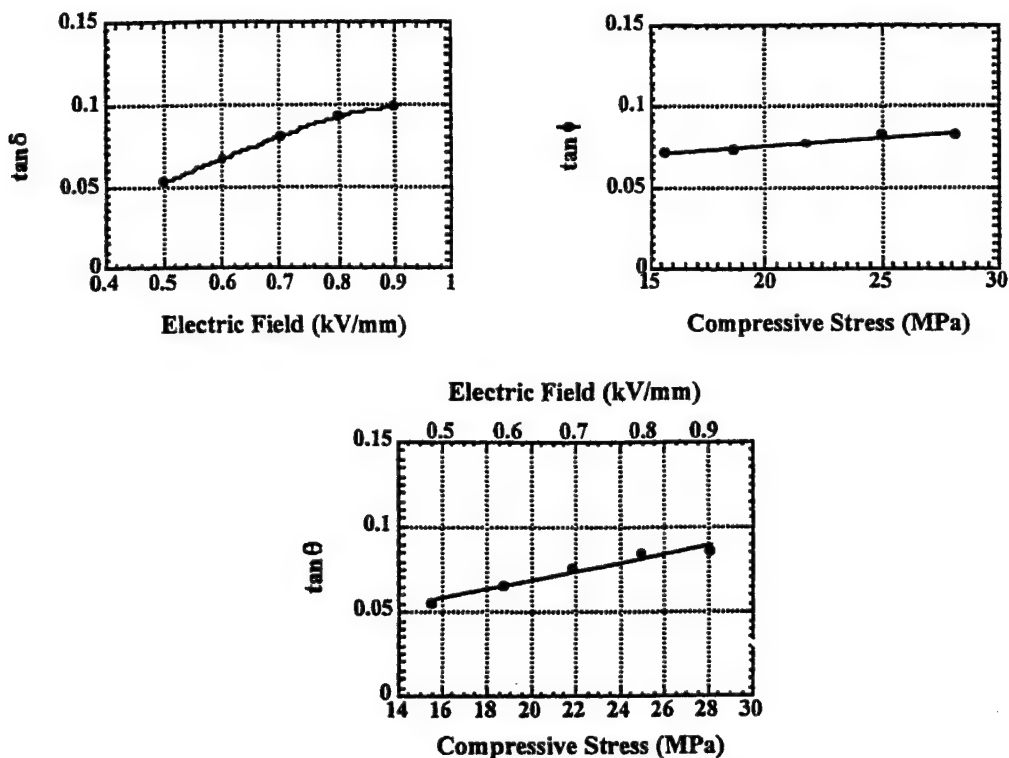
Fig.5 Intrinsic loss factors, tanδ, tanφ, and tanθ as a function of electric field or compressive stress, measured for a PZT based actuator.

CONCLUSIONS

Theoretical and experimental techniques for measuring the extrinsic and intrinsic electric, mechanical and piezoelectric coupling losses separately have been discussed. We found that the piezoelectric loss is not so small as believed by the previous researchers.

This research was sponsored by the Office of Naval Research through the MURI program, Grant No. N00014-96-1-1173.

REFERENCES

1. K. Uchino, J. Zheng, A. Joshi, Y. H. Chen, S. Yoshikawa, S. Hirose, S. Takahashi and J. W. C. de Vries, J. Electroceramics, **2**, 33-40 (1998).
2. S. Takahashi and S. Hirose, Jpn. J. Appl. Phys., **32**, 2422-2425 (1993).
3. S. Hirose, M. Aoyagi, Y. Tomikawa, S. Takahashi and K. Uchino, Proc. Ultrasonics Int'l '95, Edinburgh, pp. 184-87 (1995).
4. K. H. Haerdtl, Ceram. Int'l., **8**, 121-127 (1982).
5. P. Gerthsen, K. H. Haerdtl and N. A. Schmidt, J. Appl. Phys. **51**, 1131-1134 (1980).
6. J. Zheng, S. Takahashi, S. Yoshikawa, K. Uchino and J. W. C. de Vries, J. Amer. Ceram. Soc., **79**, 3193-98 (1996).
7. T. Ikeda, Fundamentals of Piezoelectric Materials Science, (Ohm Publication Company, Tokyo, 1984), pp. 83.

APPENDIX 50

LOSS MECHANISMS IN PIEZOELECTRICS AND RESONANCE/ANTIRESONANCE

Kenji Uchino, Jiehui Zheng, Yun-Han Chen and Xiaohong Du
International Center for Actuators and Transducers
Materials Research Laboratory, The Pennsylvania State University
University Park, Pa 16802

Seiji Hirose
Faculty of Engineering, Yamagata University, Yonezawa 992, Japan

ABSTRACT

Losses in piezoelectrics are considered in general to have three different mechanisms; dielectric, mechanical and piezoelectric losses. This paper deals with the phenomenology of losses, first, then how to measure these losses separately in experiments. We found that heat generation is caused mainly by dielectric loss tan δ' (i. e. P-E hysteresis loss), not by mechanical loss, and that a dramatical decrease in mechanical Q_m with an increase of vibration level was observed in resonant piezoelectric ceramic devices, which is due to an increase in the intrinsic dielectric loss, not in the intrinsic mechanical loss. Finally, we propose the usage of the antiresonance mode rather than the conventional resonance mode, particularly for high power applications, since the mechanical quality factor Q_B at an antiresonance frequency is larger than Q_A at a resonance frequency.

INTRODUCTION

Loss or hysteresis in piezoelectrics exhibits both merits and demerits. For positioning actuator applications, hysteresis in the field-induced strain provides a serious problem, and for resonance actuation such as ultrasonic motors, loss generates significant heat in the piezoelectric materials. Further, in consideration of the resonant strain amplified in proportion to a mechanical quality factor, low (extrinsic) mechanical loss materials are preferred for ultrasonic motors. On the contrary, for force sensors and acoustic transducers, high mechanical loss, which corresponds to a low mechanical quality factor Q_m, is essential to widen a frequency range for receiving signals.

However, not much research effort has been put into systematic studies of the loss mechanisms in piezoelectrics, particularly in high voltage and high power range. Since not many comprehensive descriptions can be found in previous reports, this paper will clarify the loss mechanisms in piezoelectrics phenomenologically, describe heat generation processes and high power characteristics, and ,finally, discuss the resonance and antiresonance vibration modes from a viewpoint of a quality factor.

LOSS AND HYSTERESIS IN THE POLARIZATION CURVE
Relation between Hysteresis and Dissipation Factor

Let us start with loss and hysteresis in the electric displacement D (nearly equal to polarization P) vs. electric field E curve without considering the electromechanical coupling. Figure 1 shows an example P-E hysteresis curve. When the D (or P) traces a different line with increased and decreased applied electric field E, it is called *hysteresis*.

When the hysteresis is not very large, the electric displacement D can be expressed by using a slight phase lag to the applied electric field. Assuming that the electric field oscillates at a frequency f $(= \omega/2\pi)$ as

$$E^* = E_0 \, e^{j\omega t}, \tag{1}$$

the induced electric displacement oscillates also at the same frequency under the steady state, but with some time phase delay δ:
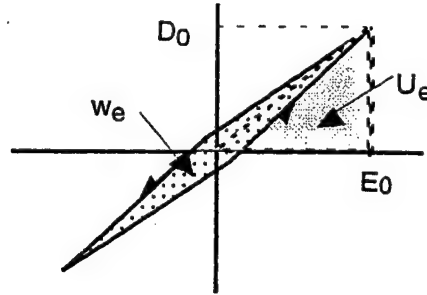
$$D^* = D_0 \, e^{j(\omega t - \delta)}. \tag{2}$$

Fig.1   D (or P) vs. E hysteresis curve.

If we express the relation between D^* and E^* as

$$D^* = \varepsilon^* \varepsilon_0 \, E^*, \tag{3}$$

where the complex dielectric constant ε^* is

$$\varepsilon^* = \varepsilon' - j \, \varepsilon'', \tag{4}$$

and where

$$\varepsilon'' / \varepsilon' = \tan \delta . \tag{5}$$

Note that the negative connection in Eq.(4) comes from the time "delay", and that $\varepsilon' \varepsilon_0 = (D_0/E_0) \cos \delta$ and $\varepsilon'' \varepsilon_0 = (D_0/E_0) \sin \delta$.

The area w_e corresponds to the consumed loss energy during an electric field cycle per unit volume of the dielectrics, and can be related in isotropic dielectrics with ε'' or $\tan \delta$ as follows:

$$w_e = - \int D \, dE = - \int_0^{2\pi/\omega} D \, (dE/dt) \, dt \tag{6}$$

Substituting the real parts in Eqs.(1) and (2) into Eq.(6),

$$w_e = \int_0^{2\pi/\omega} D_0 \cos(\omega t - \delta) \, (E_0 \, \omega \sin\omega t) \, dt$$

$$= E_0 \, D_0 \, \omega \sin \delta \int_0^{2\pi/\omega} \sin^2 \omega t \, dt = \pi \, E_0 \, D_0 \sin \delta \qquad (7)$$

Or

$$w_e = \pi \, \varepsilon'' \varepsilon_0 \, E_0^2 = \pi \, \varepsilon' \varepsilon_0 \, E_0^2 \tan \delta \qquad (8)$$

When there is no phase delay ($\delta = 0$), $w_e = 0$; i. e. the electrostatic energy stored in the dielectric will be recovered completely after a full cycle (100% efficiency). However, when there is a phase delay, the loss w_e will be accompanied per cycle, and the dielectric material generates heat. The tan δ is called *dissipation factor*, and its inverse value $Q = 1/tan\delta$ is called *electrical quality factor*.

In consideration of the stored electrostatic energy during a half cycle from - E_0 to E_0 (= 4 U_e, which is illustrated as an area in Fig. 1) provided by

$$4 \, U_e = (1/2)(2 \, E_0)(2 \, D_0 \cos \delta)$$
$$= 2 \, E_0 \, D_0, \qquad (9)$$

the dissipation factor tan δ can be experimentally obtained by

$$\tan \delta = (1/2\pi) (w_e / U_e). \qquad (10)$$

Note that w_e is the hysteresis in a full cycle and U_e is the stored energy in a quarter of cycle.

<u>Temperature, Electric Field and Frequency Dependence of P-E Hysteresis</u>

Figures 2, 3 and 4 show temperature, electric field and frequency dependence of the dissipation factor tan δ' calculated from the P-E hysteresis loss measured under stress free condition for a PZT-based ceramic.[1] The loss tan δ' decreases gradually with increasing temperature, but is rather insensitive to frequency. On the contrary, the tan δ' increases initially in proportion to the applied electric field, exhibiting a saturation above a certain electric field. The value for E = 0 (solid traangle mark in the figure) was obtained with an impedance analyzer.
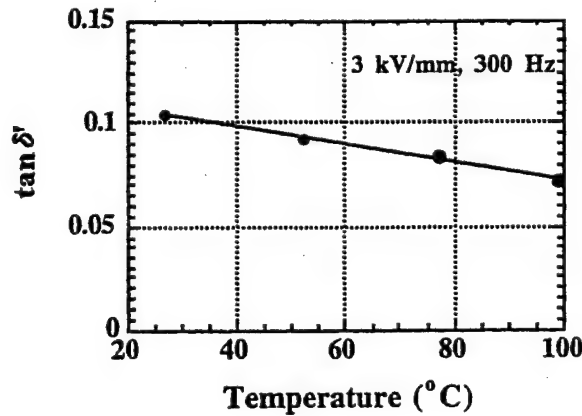

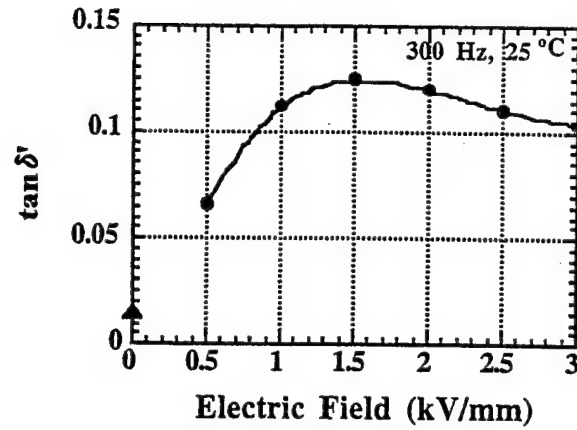Fig.2 Loss tan δ' as a function of sample temperature (3 kV/mm, 300 Hz).

Electronic Ceramic Materials and Devices

Fig.3   Loss tan δ' as a function of electric field (T = 25°C, f = 300 Hz).
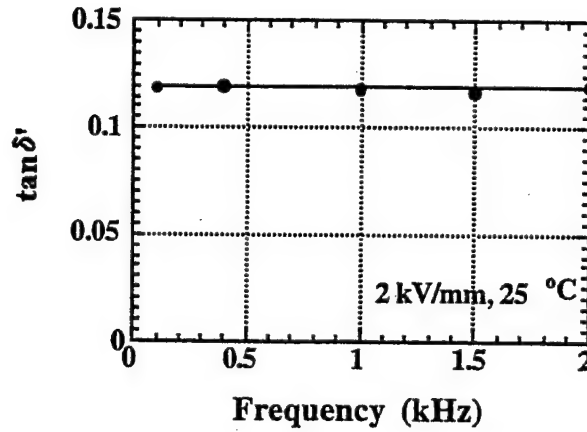
Fig.4   Loss tan δ' as a funtion of frequency (T = 25°C, E = 2 kV/mm).

GENERAL CONSIDERATION OF LOSS AND HYSTERESIS

Let us expand the above discussion into more general cases; i.e., piezoelectric materials. We will start from the Gibbs free energy G expressed by

$$dG = - x \, dX - D \, dE - S \, dT, \tag{11}$$

or

$$G = - (1/2) \, s^E \, X^2 - d \, X \, E - (1/2) \, \varepsilon^X \varepsilon_0 \, E^2. \tag{12}$$

Here, x is strain, X, stress, D, electric displacement, E, electric field, S, enthalpy and T is temperature. Temperature dependence is carried into the elastic compliance s^E, the dielectric

Electronic Ceramic Materials and Devices

constant ε^X and the piezoelectric constant d. We will obtain the following two piezoelectric equations:

$$x = - (\partial G/\partial X) = s^E X + d E , \tag{13}$$

$$D = - (\partial G/\partial E) = d X + \varepsilon^X \varepsilon_0 E . \tag{14}$$

Thermodynamical equations and the consequent piezoelectric equations (Eqs. (11)-(14)) cannot yield a delay-time related loss, without taking into account irreversible thermodynamic equations or dissipation functions. However, the latter considerations are mathematically equivalent to the introduction of complex physical constants into the phenomenological equations.

Therefore, we will introduce complex parameters ε^{x*}, s^{D*}, ε^{X*}, s^{E*} and d^* in order to consider the hysteresis losses in electric, elastic and piezoelectric coupling energy :

$$\varepsilon^{x*} = \varepsilon^x(1 - j \tan \delta), \tag{15}$$
$$\varepsilon^{X*} = \varepsilon^X(1 - j \tan \delta'), \tag{16}$$
$$s^{D*} = s^D(1 - j \tan \phi), \tag{17}$$
$$s^{E*} = s^E(1 - j \tan \phi'), \tag{18}$$
$$d^* = d(1 - j \tan \theta). \tag{19}$$

θ is the phase delay of the strain under an applied electric field, or the phase delay of the electric displacement under an applied stress. Both delay phases should be exactly the same if we introduce the same complex piezoelectric constant d^* into Eqs.(13) and (14). δ is the phase delay of the electric displacement to an applied electric field under a constant strain (i.e., zero strain or completely clamped) condition, and ϕ is the phase delay of the strain to an applied stress under a constant electric displacement (i.e., open-circuit) condition. We will consider these phase delays as "intrinsic" losses. With this assumption, we can calculate the dissipation factors for ε^{X*} (permittivity measured under constant stress) and s^{E*} (elastic compliance measured under constant electric filed) which correspond to "extrinsic" losses. When an elecric field is applied on a piezoelectric sample as illustrated in the top of Fig. 5, this state will be equivalent to the superposition of the following two steps: first, the sample is completely clamped and the field E_0 is applied (pure electrical energy $(1/2) \varepsilon^x \varepsilon_0 E_0^2$ is input); second, keeping the field at E_0, the mechanical constraint is released (additional mechanical energy $(1/2) (d^2/s^E) E_0^2$ is necessary). The total energy should correspond to the total input electrical energy $(1/2) \varepsilon^X \varepsilon_0 E_0^2$; thus, we obtain the relation,

$$\varepsilon_0 \varepsilon^X = \varepsilon_0 \varepsilon^x + (d^2/s^E), \tag{20}$$

Similarly, from the bottom of Fig. 5,

$$s^E = s^D + (d^2/\varepsilon_0 \varepsilon^X). \tag{21}$$

Replacing $\varepsilon^X, \varepsilon^x, s^E, s^D, d$ in Eqs. (20) and (21) by the complex parameters in Eqs. (15) - (19), we obtain :

$$\varepsilon^X / \varepsilon^x = 1/(1 - k^2), \tag{22}$$

$$s^E/s^D = 1/(1 - k^2), \tag{23}$$

$$\tan \delta' = (1/(1 + k^2))[\tan \delta + k^2(2 \tan \theta - \tan \phi)], \tag{24}$$

$$\tan \phi' = (1/(1 + k^2))[\tan \phi + k^2(2 \tan \theta - \tan \delta)], \tag{25}$$

where

$$k^2 = d^2/(s^E \varepsilon_0 \varepsilon^X). \tag{26}$$

This k is called the *electromechanical coupling factor*, and defined here as a real number. It is important that the extrinsic dielectric and elastic losses are mutually correlated with the intrinsic dielectric, elastic and piezoelectric losses through the electromechanical coupling k^2, and that the denominator $(1 + k^2)$ comes basically from the $\varepsilon^X / \varepsilon^x$ ratio and this real part reflects to the dissipation factor when the imaginary part is devided by the real part. Also note that depending on the vibration mode, the definition of electromechanical coupling k can be changed such as $k^2 = d^2/(s^D \varepsilon_0 \varepsilon^X)$.
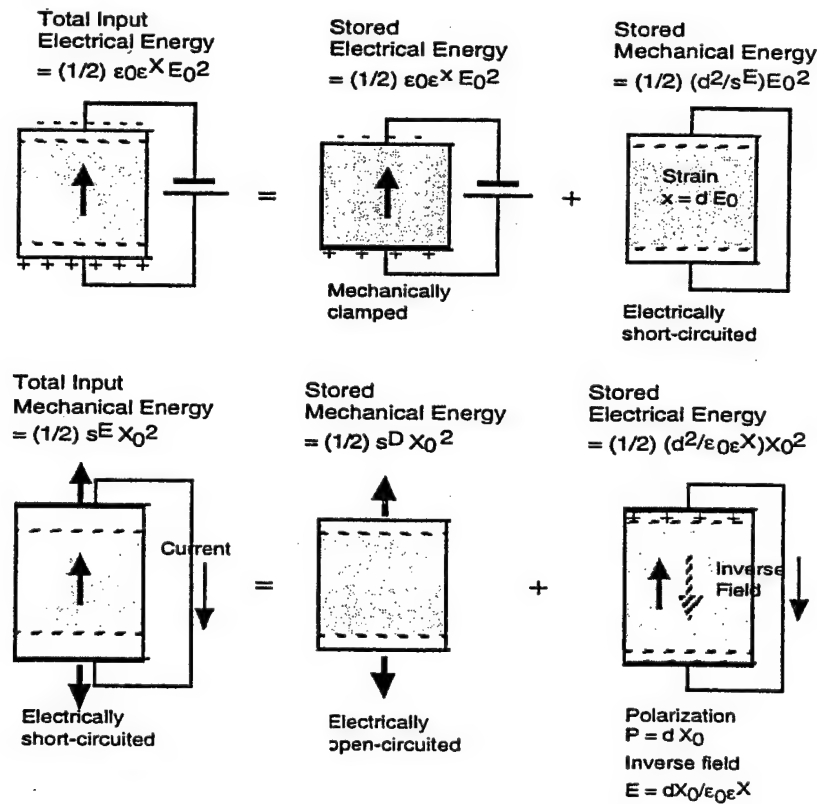

Fig. 5 Conceptual figure for explaining the relation between ε^X and ε^x, s^E and s^D.

Electronic Ceramic Materials and Devices

Figures 6(a) - 6(d) correspond to the model hysteresis curves for practical experiments: D vs. E curve under a stress-free condition, x vs. X under a short-circuit condition, x vs. E under a stress-free condition and D vs. X under an open-circuit condition for measuring charge (or under a short-circuit condition for measuring current), respectively.

In a similar fashion to the previous section, the stored energies and hysteresis losses for pure electrical and mechanical energies can be calculated as:

$$U_e = (1/2) \, \varepsilon^X \varepsilon_0 \, E_0^2, \tag{27}$$

$$w_e = \pi \, \varepsilon^X \varepsilon_0 \, E_0^2 \tan \delta', \tag{28}$$

$$U_m = (1/2) \, s^E \, X_0^2, \tag{29}$$

$$w_m = \pi \, s^E \, X_0^2 \tan \phi'. \tag{30}$$

The electromechanical loss, when measuring the induced strain under an electric field, is more complicated. Let us calculate the stored energy U_{em} during a quarter electric field cycle (i.e., 0 to E_0), first :

$$U_{em} = - \int x \, dX = (1/2) \, (x_0^2/s^E) = (1/2) \, (dE_0)^2/s^E$$
$$= (1/2) \, (d^2/s^E)E_0^2 \tag{31}$$

Replacing d and s^E by $d^* = d(1 - j \tan \theta)$ and $s^{E*} = s^E(1 - j \tan \phi)$, we obtain

$$U_{em} = (1/2) \, (d^2/ \, s^E) \, E_0^2, \tag{32}$$

and

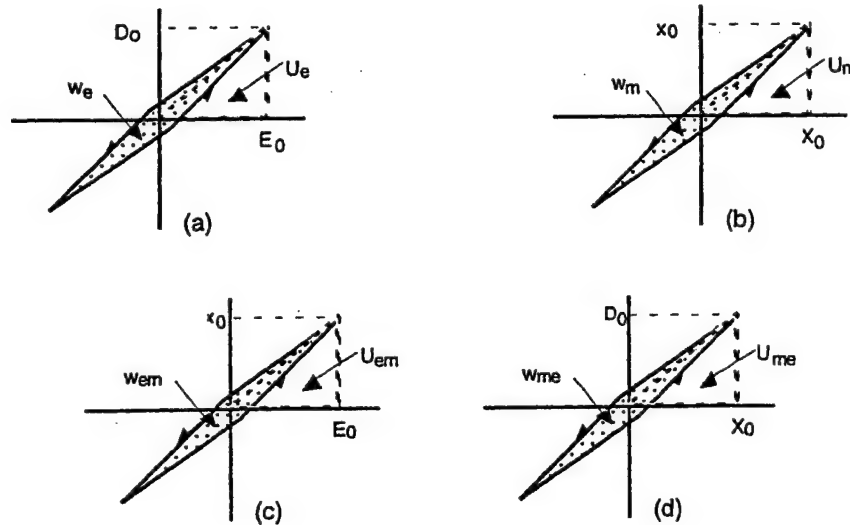$$w_{em} = \pi \, (d^2/ \, s^E) \, E_0^2 \, (2 \tan\theta - \tan\phi'). \tag{33}$$

Fig.6 (a) D vs. E (stress free), (b) x vs. X (short-circuit), (c) x vs. E (stress free) and
(d) D vs. X (open-circuit) curves with a slight hysteresis in each relation.

Note that the strain vs. electric field measurement seems to provide the piezoelectric loss $\tan\theta$ directly, however, the observed loss should include an additional elastic loss because the strain should be delayed to the initial stress, which is needed to calculate energy.

Similarly, when we measure the induced charge under stress, the stored energy U_{me} and the hysteresis loss w_{me} during a quarter and a full stress cycle, respectively, are obtained as

$$U_{me} = (1/2) (d^2/ \varepsilon_0 \varepsilon^X) X_0^2, \tag{34}$$

and

$$w_{me} = \pi (d^2/ \varepsilon_0 \varepsilon^X) X_0^2 (2 \tan\theta - \tan\delta'). \tag{35}$$

Hence, from the measurements of D vs. E and x vs. X, we obtain $\tan\delta'$ and $\tan\phi'$, respectively, and either the piezoelectric (D vs. X) or converse piezoelectric measurement (x vs. E) provides $\tan\theta$ through a numerical subtraction.
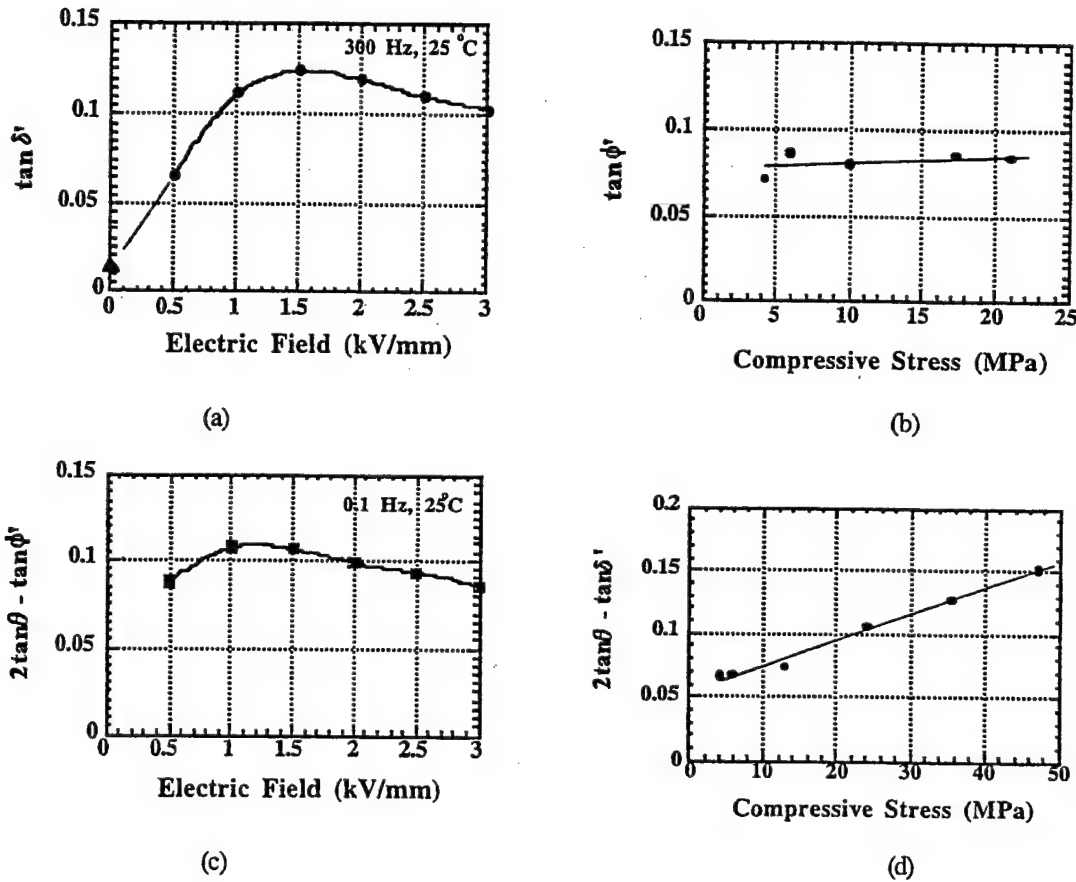

Fig.7 Dissipation factors determined from (a) D vs. E (stress free), (b) x vs. X (short-circuit), (c) x vs. E (stress free) and (d) D vs. X (open-circuit) curves for a PZT based actuator.
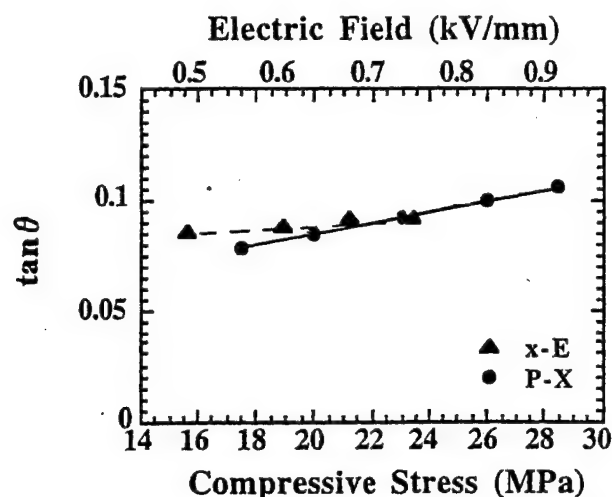
Fig.8 Piezoelectric dissipation factor tanθ as a function of electric field or compressive stress, measured for a PZT based actuator.

Figure 7 shows dissipation factors determined from (a) D vs. E (stress free), (b) x vs. X (short-circuit), (c) x vs. E (stress free) and (d) D vs. X (open-circuit) curves for a PZT based actuator. Figure 8 shows the result for the piezoelectric loss tanθ. We used the correlation factor between electric field and compressive stress given averagely by $X = (\varepsilon_0 \varepsilon^X / s^E)^{1/2} E$. Note that the piezoelectric loss tanθ is not so small as previously believed, but comparable to the dielectric or elastic loss, and is insensitive to the field or stress. The experimental details will be reported in the successive papers.

When similar measurements to Figs. 6(a) and 6.(b), but under constrained conditions; that is, D vs. E under a completely clamped state, and x vs. X under an open-circuit state, respectively, we can expect smaller hystereses; that is, intrinsic losses, tanδ and tanφ. These measurements are alternative methods to determine the three losses separately.

LOSS AND HEAT GENERATION

Heat genration in various types of PZT-based actuators has been studied under a relatively large electric field applied (1 kV/mm or more) at an off-resonance frequency, and a simple analytical method was established to evaluate the temperature rise, which is very useful for the design of piezoelectric high-power actuators.

Zheng et al. reported the heat generation from various sizes of multilayer type piezoelectric ceramic actuators.[1] Figure 9 shows the temperature change in the actuators when driven at 3 kV/mm and 300 Hz, and Fig. 10 plots the saturated temperature as a function of V_e/A, where V_e is the effective volume (electrode overlapped part) and A is the surface area. This linear relation is reasonable because the volume V_e generates the heat and this heat is dissipated through the area A. Thus, if we need to suppress the temperature rise, a small V_e/A design is preferred.

According to the law of energy conservation, the rate of heat storage in the piezoelectric resulting from heat generation and dissipation effects can be expressed as

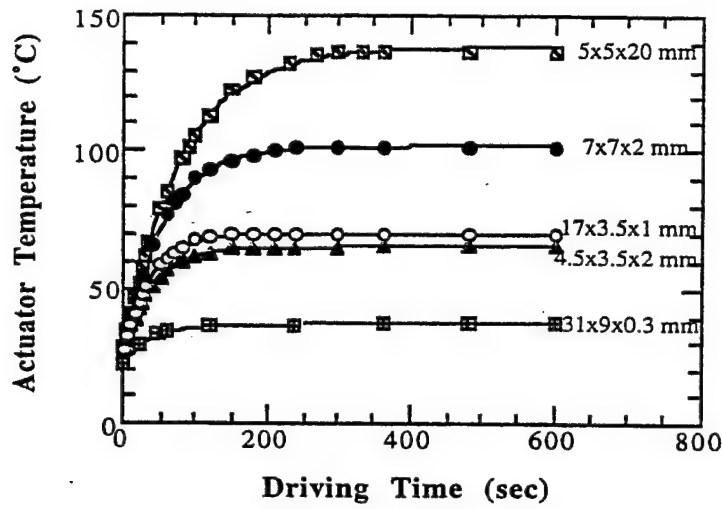$$q_g - q_{out} = V \rho c (dT/dt), \tag{36}$$

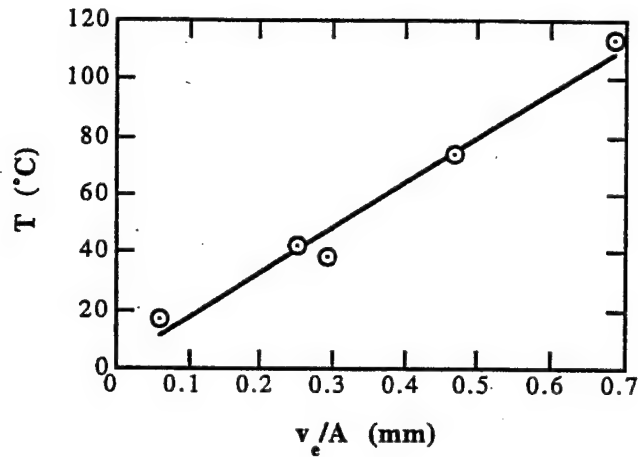Fig.9 Temperature rise for various actuators while driven at 300 Hz and 3 kV/mm.

Fig.10 Temperature rise versus V_e/A (3 kV/mm, 300 Hz), where V_e is the effective volume generating the heat and A is the surface area dissipating the heat.

assuming uniform temperature distribution in the sample. V, ρ, c are total volume, density and specific heat, respectively. The heat generation is considered to be caused by losses. Thus, the rate of heat generation (q_g) in the piezoelectric can be expressed as

$$q_g = u\, f\, V_e, \qquad\qquad (37)$$

where u is the loss of the sample per driving cycle per unit volume, f, the driving frequency, and V_e is the effective volume where the ceramic is activated. According to the measuring condition,

Electronic Ceramic Materials and Devices

this u corresponds to w_e of Eq. (28), which consists of the intrinsic electrical loss $\tan \delta$ and the electromechanical loss ($2 \tan\theta - \tan\phi'$) in the previous section:

$$u = w_e = \pi \varepsilon^X \varepsilon_0 E_0^2 \tan \delta'$$
$$= (1/(1 + k^2))[\tan \delta + k^2(2 \tan \theta - \tan \phi)] \pi \varepsilon^X \varepsilon_0 E_0^2. \qquad (38)$$

Note that we do not need to add w_{em} explicitly, because the corresponding electromechanical loss is already included implicitly in w_e.

When we neglect the conduction heat transfer, the rate of heat dissipation (q_{out}) from the sample is the sum of the rates of heat flow by radiation (q_r) and convection (q_c):

$$q_{out} = q_r + q_c$$
$$= \sigma e A(T^4 - T_0^4) + h_c A(T - T_0), \qquad (39)$$

where σ is the Stehan-Boltzmann constant, e is the emissivity of the sample, h_c is the average convective heat transfer coefficient, and A is the sample surface area.

Thus, Eq.(36) can be written in the form:

$$u f V - A k(T) (T - T_0) = V \rho c (dT/dt), \qquad (40)$$

where

$$k(T) = \sigma e(T^2 + T_0^2)(T + T_0) + h_c \qquad (41)$$

is defined as the overall heat transfer coefficient. If we assume that k(T) is relatively insensitive to temperature change, the solution to Eq.(40) for the piezoelectric sample temperature is given as a function of time (t):

$$T - T_0 = [u f V_e/ k(T) A] [1 - e^{-t/\tau}], \qquad (42)$$

where the time constant τ is expressed as

$$\tau = \rho c V/k(T)A. \qquad (43)$$

As $t \to \infty$, the maximum temperature rise in the sample becomes

$$\Delta T = u f V_e/ k(T) A. \qquad (44)$$

As $t \to 0$, the initial rate of temperature rise is

$$(dT/dt) = u f V_e/\rho c V = \Delta T / \tau . \qquad (45)$$

Figures 11 and 12 show the dependence of k(T) on applied electric field and frequency. Since k(T) is not really constant, we can calculate the total loss u of the piezoelectric through Eq.(45). The calculated results are shown in Table I. The experimental date of P-E hysteresis losses under a stress-free condition are also listed for comparison. It is seen that the P-E hysteresis extrinsic loss agrees well with the total loss contributing to the heat generation.
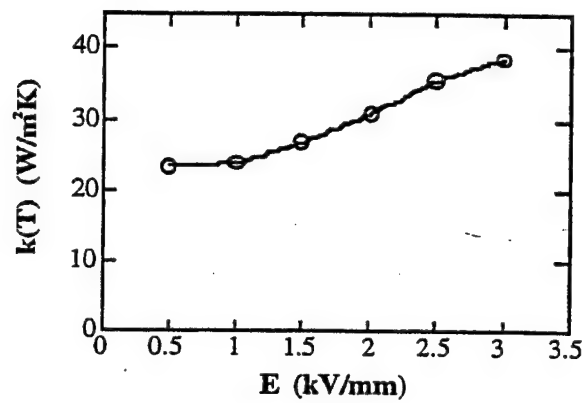
Fig.11 k(T) as a function of applied electric field (400 Hz, data from the actuator with dimensions of 7 mm x 7 mm x 2 mm).
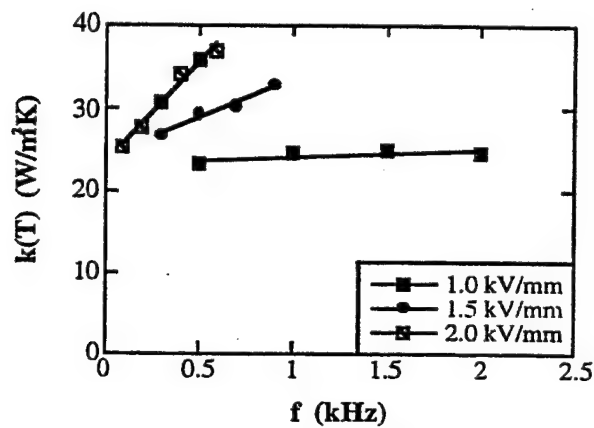

Fig.12 Overall heat transfer coefficient k(T) as a function of frequency.

Table I Loss and overall heat transfer coefficient for PZT multilayer samples
(E = 3 kV/mm, f = 300 Hz).

Actuator	4.5x3.5x2 mm	7x7x2 mm	17x3.5x1 mm
Total loss ($\times 10^3$ J/m^3) $u = \dfrac{\rho c v}{f v_e}\left(\dfrac{dT}{dt}\right)_{t->0}$	19.2	19.9	19.7
P-E hysteresis loss ($\times 10^3$ J/m^3)	18.5	17.8	17.4
k(T) (W/m^{2}K)	38.4	39.2	34.1

Electronic Ceramic Materials and Devices

LOSSES AT A PIEZOELECTRIC RESONANCE

So far, we have considered the losses for a quasi-static or off-resonance state. Problems in ultrasonic motors which are driven at the resonance frequency include significant distortion of the admittance frequency spectrum due to nonlinear behavior of elastic compliance at a high vibration amplitude, and heat generation which causes a serious degradation of the motor characteristics through depoling of the piezoceramic. Therefore, the ultrasonic motor requires a very hard type piezoelectric with a high mechanical quality factor Q, leading to the suppression of heat generation. It is also notable that the actual mechanical vibration amplitude at the resonance frequency is directly proportional to this Q value.

Losses at a Piezoelectric Resonance
Piezoelectric resonance without loss

Let us consider the longitudinal mechanical vibration of a piezo-ceramic plate through the transverse piezoelectric effect (d_{31}) as shown in Fig. 13. Assuming that the polarization is in the z-direction and x-y planes are the planes of the electrodes, the extentional vibration in the x direction is represented by the following dynamic equation :

$$(\partial^2 u/\partial t^2) = F = (\partial X_{11}/\partial x) + (\partial X_{12}/\partial y) + (\partial X_{13}/\partial z), \tag{46}$$

where u is the displacement of the small volume element in the ceramic plate in the x-direction. When the plate is very long and thin, X_2 and X_3 may be set equal to zero through the plate, and the relations between stress, electric field (only E_z exists) and the induced strain are given by :

$$X_1 = x_1/s_{11}{}^E - (d_{31}/s_{11}{}^E)E_z. \tag{47}$$

Introducing Eq.(47) into Eq.(46), and allowing for $x_1=\partial u/\partial x$ and $\partial E_z/\partial x=0$ (due to the equal potential on each electrode), leads to a harmonic vibration equation :

$$- \omega^2\rho\, s_{11}{}^E u = \partial^2 u/\partial x^2 . \tag{48}$$

Here, ω is the angular frequency of the drive field, and ρ is the density. Substituting a general solution $u=u_1(x)e^{j\omega t}+u_2(x)e^{-j\omega t}$ into Eq.(47), and with the boundary condition $X_1 = 0$ at $x = 0$ and L (sample length), the following solutions can be obtained:

(strain) $\quad \partial u/\partial x = x_1 = d_{31}E_z [\sin\omega(L-x)/v + \sin(\omega x/v)] /\sin(\omega L/v), \tag{49}$

(total displacement) $\quad \Delta L = \int_0^L x_1 dx = d_{31}E_z L\, (2v/\omega L)\, \tan(\omega L/2v). \tag{50}$
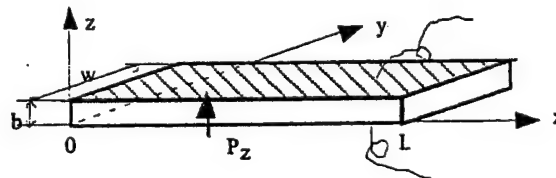

Fig.13   Longitudinal vibration through the transverse piezoelectric effect (d_{31}) in a rectangular plate.

Here, v is the sound velocity in the piezoceramic which is given by

$$v = 1/\sqrt{\rho\, s_{11}{}^E}. \tag{51}$$

Since the total current is given by :

$$i = j\omega w \int_0^L D_3\, dx = j\omega w \int_0^L [(\varepsilon_0\varepsilon_{33}{}^X - d_{31}{}^2/s_{11}{}^E)E_z + (d_{31}/s_{11}{}^E)x_1]\, dx, \tag{52}$$

and using Eq. (49), the admittance for the mechanically free sample is calculated to be:

$$Y = (1/Z) = (i/V) = (i/E_z t)$$
$$= (j\omega w L/t)\,\varepsilon_0\varepsilon_{33}{}^{LC}[1 + (d_{31}{}^2/\varepsilon_0\varepsilon_{33}{}^{LC}s_{11}{}^E)(\tan(\omega L/2v)/(\omega L/2v)], \tag{53}$$

where w is the width, L the length, t the thickness of the sample, and V the applied voltage. $\varepsilon_{33}{}^{LC}$ is the permittivity in a longitudinally clamped sample, which is given by

$$\varepsilon_0\varepsilon_{33}{}^{LC} = \varepsilon_0\varepsilon_{33}{}^X - (d_{31}{}^2/s_{11}{}^E)$$
$$= \varepsilon_0\,\varepsilon_{33}{}^X(1 - k_{31}{}^2). \tag{54}$$

The final transformation is provided by the definition,

$$k_{31} = d_{31}/\sqrt{s_{11}{}^E\,\varepsilon_0\varepsilon_{33}{}^X}. \tag{55}$$

When the drive frequency is much lower than the resonance, taking $\omega \to 0$ in Eq. (53) leads to $Y = (j\omega w L/t)\,\varepsilon_{33}{}^X$ (corresponding to the normal capacitance). The piezoelectric resonance is achieved where the admittance becomes infinite or the impedance is zero. The resonance frequency f_R is calculated from Eq. (53), and the fundamental frequency is given by

$$f_R = v/2L = 1/(2L\sqrt{\rho\, s_{11}{}^E}). \tag{56}$$

On the other hand, the antiresonance state is generated for zero admittance or infinite impedance:

$$(\omega_A L/2v)\cot(\omega_A L/2v) = -d_{31}{}^2/\varepsilon_{33}{}^{LC}s_{11}{}^E = -k_{31}{}^2/(1 - k_{31}{}^2). \tag{57}$$

The resonance and antiresonance states are described by the following intuitive model.[2] In a high electromechanical coupling material with k almost equal to 1, the resonance or antiresonance states appear for $\tan(\omega L/2v) = \infty$ or 0 [i. e., $\omega L/2v = (m-1/2)$ or m (m: integer)], respectively. The strain amplitude x_1 distribution for each state [calculated using Eq. (49)] is illustrated in Fig. 14. In the resonance state, large strain amplitudes and large capacitance changes (called *motional capacitance*) are induced, and the current can easily flow into the device. Note that for a loss-free piezoelectric the strain is calculated to be infinite in Eq. (49). On the other hand, at antiresonance, the strain induced in the device compensates completely, resulting in no capacitance change, and

the current cannot flow easily into the sample. Thus, for a high k material the first antiresonance frequency f_A should be twice as large as the first resonance frequency f_R.

In a typical case, where $k_{31} = 0.3$, the antiresonance state varies from the above-mentioned mode and becomes closer to the resonance mode. The low-coupling material exhibits an antiresonance mode where capacitance change due to the size change is compensated completely by the current required to charge up the static capacitance (called *damped capacitance*). Thus, the antiresonance frequency f_A will approach the resonance f_R.
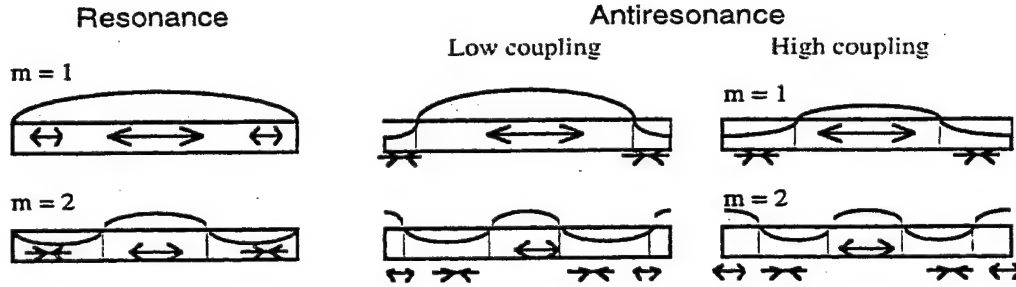

Fig.14   Strain generation in the resonance or antiresonance state.

When $(f_A - f_R)$ is not very large due to a small electromechanical coupling, we can derive the following approximate expression for f_A. Assuming that $\omega_A - \omega_R$ is much smaller than ω_R (= $\pi v /L$),

$$(\omega_A L/2v) \cot (\omega_A - \omega_R)L/2v - \pi/2) = -(\omega_A L/2v)\sin(\omega_A - \omega_R)L/2v)/\cos(\omega_A - \omega_R)L/2v)$$

Thus,

$$\omega_A = (\pi v/L)[1 + (4/\pi^2) K_{31}^2], \tag{59}$$

where we introduced a new parameter K_{31} as

$$K_{31}^2 = k_{31}^2 / (1 - k_{31}^2). \tag{60}$$

It is notable that for a piezoelectric sample with a typical k_{31} value, the two ends of the plate are not the nodal points, that is, we can expect rather large displacements, which can be applied for ultrasonic motors.

Piezoelectric resonance with losses

First, we will discuss the admittance curve. Similar to the treatment in Section 3, we will introduce the complex parameters $\varepsilon_{33}^{X*} = \varepsilon_{33}^X(1 - j \tan \delta')$, $s_{11}^{E*} = s_{11}^E(1 - j \tan \phi')$, and $d_{31}^* = d(1 - j \tan \theta)$ into Eq. (53):

$Y = Y_d + Y_m$

$\quad = (j\omega wL/t)\varepsilon_0\varepsilon_{33}{}^X(1 - k_{31}{}^2)[1 - j\,(1/(1-k_{31}{}^2))((\tan\delta' - k_{31}{}^2(2\tan\theta - \tan\phi'))]$

$\quad + (j\omega wL/t)\varepsilon_0\varepsilon_{33}{}^X k_{31}{}^2\,[(1 - j(2\tan\theta - \tan\phi')][(\tan(\omega L/2\,v^*))/(\omega L/2\,v^*)]$

$\quad = j\omega C_d\,[1 - j\,(1/(1 - k_{31}{}^2))((\tan\delta' - k_{31}{}^2(2\tan\theta - \tan\phi'))]$

$\quad + j\omega C_d\,K_{31}{}^2[(1-j(2\tan\theta-\tan\phi')][(\tan(\omega L/2v^*))/(\omega L/2v^*)]$

$\quad = j\omega C_d\,(1 - j\tan\delta) + j\omega C_0\,k_{31}{}^2[(1-j(2\tan\theta-\tan\phi')][(\tan(\omega L/2v^*))/(\omega L/2v^*)],$ (61)

where

$C_0 = (wL/t)\,\varepsilon_0\varepsilon_{33}{}^X,$ (62)

$C_d = (1 - k_{31}{}^2)\,C_0.$ (63)

Note that the loss for the first term (damped conductance) is represented by the intrinsic electric loss $\tan\delta$, not by the extrinsic loss $\tan\delta'$. Taking into account

$v^* = 1/\sqrt{\overline{\rho\,s_{11}{}^E(1 - j\tan\phi')}} = v\,(1 + (1/2)\,j\tan\phi'),$ (64)

we further calculate $1/(\tan(\omega L/2v^*)$ with an expansion-series approximation around $(\omega L/2v) = \pi/2$. The resonance state is defined in this case for the maximum admittance point, rather than the infinite Y. We will use new frequency paremeters,

$\Omega = \omega L/2\,v,\ \Delta\Omega = \Omega - \pi/2\ (\ll 1).$ (65)

Since $\omega L/2\,v^* = (\pi/2 + \Delta\Omega)\,[1 - (1/2)\,j\tan\phi'],$

$1\,/\,(\tan(\omega L/2v^*) = -\Delta\Omega + j\,(\pi/4)\tan\phi'.$ (66)

Thus, assuming $K_{31}{}^2 = k_{31}{}^2/(1-k_{31}{}^2)$, Y_m is approximated aound the first resonance frequency by

$Y_m = j\omega C_d\,K_{31}{}^2\,[(1-j(2\tan\theta-\tan\phi')][(\tan(\omega L/2v^*))/(\omega L/2v^*)]$

$= j\omega_0 C_d\,K_{31}{}^2\,[(1-j(2\tan\theta-\tan\phi')]/[(-\Delta\Omega+j(\pi/4)\tan\phi')(\pi/2)(1-(1/2)j\tan\phi')]$

$= j(\pi^2/8)\,\omega_0 C_d\,K_{31}{}^2\,[(1+j((3/2)\tan\phi'-2\tan\theta)]/[(-\,(4/\pi)\Delta\Omega+j\tan\phi').$ (67)

The maximum Y_m is obtained at $\Delta\Omega = 0$:

$Y_m{}^{max} = (\pi^2/8)\,\omega_0\,C_d\,K_{31}{}^2\,(\tan\phi')^{-1}.$ (68)

In order to obtain the mechanical quality factor, let us obtain $\Delta\Omega$ which provides $Y_m{}^{max}/\sqrt{2}$. Since $\Delta\Omega = (\pi/4)\tan\phi'$ is obtained,

$Q_m = \Omega_0\,/2\Delta\Omega = (\pi/2)/\,2\,(\pi/4)\tan\phi' = (\tan\phi')^{-1}.$ (69)

This verifies the ready-used relation, $Q_m = (\tan\phi')^{-1}$.

Electronic Ceramic Materials and Devices

Next, the displacement amplification is considered. From Eq. (50) also by using the complex parameters:

$$u(L) = d_{31}{}^* E_z L \, (2v^*/\omega L) \tan(\omega L/2v^*)$$
$$= 2d_{31}(1\text{-}j \tan\theta) \, E_z L \, [v(1+(1/2) \, j \tan\phi') /\omega L] \tan(\omega L/2 \, v^*)$$
$$= 2d_{31}(1\text{-}j \tan\theta) \, E_z L \, [v(1+(1/2) \, j \tan\phi') /\omega_0 L] / (\text{-} \Delta\Omega + j(\pi/4)\tan \phi'). \tag{70}$$

The maximum displacement u_{max} is obtained at $\Delta\Omega = 0$:

$$u_{max} = (\pi^2/8) \, d_{31} \, E_z L \, (\tan \phi')^{-1}. \tag{71}$$

The maximum displacement at the resonance frequency is $(\pi^2/8) \, Q_m$ times larger than that at a non-resonance frequency $(d_{31}E_z L)$.

In a brief summary, when we observe the admittance or dislpacement spectrum as a function of drive frequency, and obtain the mechanical quality factor Q_m estimated from $Q_m = \omega_0/2\Delta\omega$, where $2\Delta\omega$ is a full width of the 3 dB down (i.e., $1/\sqrt{2}$) of the maximum value at $\omega = \omega_0$, we will obtain the extrinsic mechanical loss $\tan \phi'$.

Equivalent Circuit

The equivalent circuit for the piezoelectric acuator is represented by a combination of L, C and R. Figure 15 (a) shows an equivalent circuit for the resonance state, which has very low impedance. Taking into account Eq. (61), we can understand that C_d and R_d correspond to the electrostatic capacitance (for a longitudinally clamped sample in the previous case) and the clamped (or intrinsic) dielectric loss $\tan \delta$, respectively, and the components L_A and C_A in a series resonance circuit are related to the piezoelectric motion. For example, in the case of the longitudinal vibration of the above rectangular plate through d_{31}, these components are represented by

$$L_A = (\rho / 8)(Lb / w)(s_{11}{}^{E2} / d_{31}{}^2), \tag{72}$$

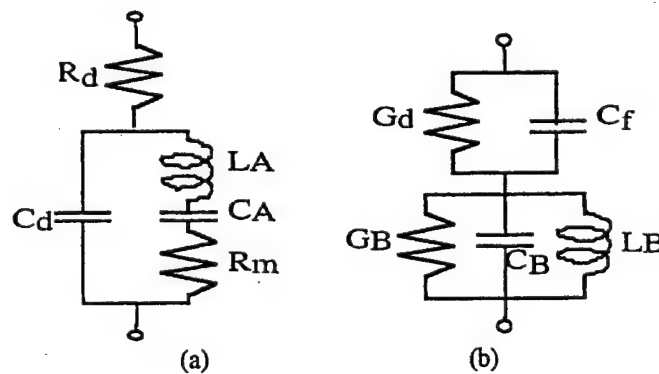$$C_A = (8 / \pi^2)(Lw / b)(d_{31}{}^2 / s_{11}{}^E). \tag{73}$$

Fig.15 Equivalent circuit of a piezoelectric device for the resonance (a) and the antiresonance (b).

The total resistance R_A (= R_d + R_m) should corresponds to the loss tan ϕ', which is composed of the intrinsic mechanical loss tan ϕ and piezoelectric/dielectric coupled loss (2tan θ - tan δ) (see Eq. (25)). Thus, roughly speaking, R_m corresponds to the intrinsic mechanical loss. Note that we introduced an additional resistance R_d to explain a large contribution of the dielectric loss when a vibration velocity is relatively large. In contrast, the equivalent circuit for the antiresonance state of the same actuator is shown in Fig. 15 (b), which has high impedance.

Losses as a Function of Vibration Velocity

Figure 16 shows the mechanical Q_m versus basic composition x at two effective vibration velocities v_0=0.05 m/s and 0.5 m/s for Pb(Zr_xTi_{1-x})O_3 doped with 2.1 at.% of Fe.[3] The decrease in mechanical Q_m with an increase of vibration level is minimum around the rhombohedral-tetragonal morphotropic phase boundary (52/48). In other words, the smallest Q material at a small vibration level becomes the best at a large vibration level, and the data obtained by a conventional impedance analyzer with a small voltage/power does not provide data relevant to high power materials.
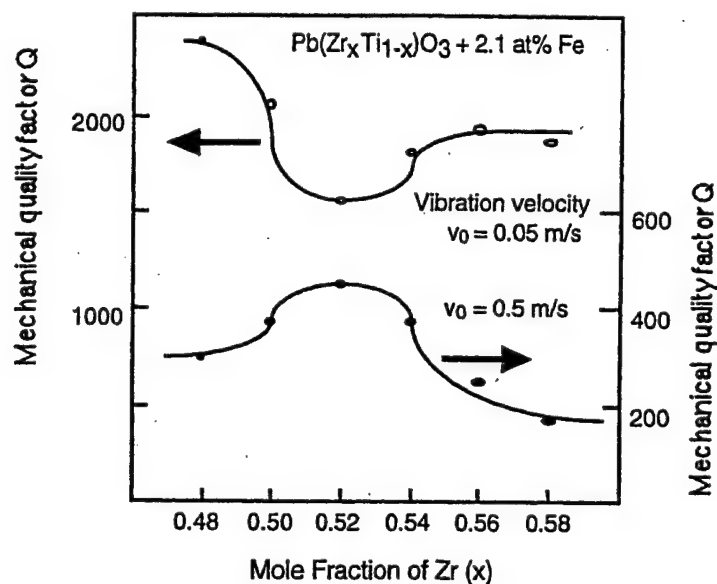

Fig.16   Mechanical Q_m versus basic composition x at two effective vibration velocities v_0=0.05 m/s and 0.5 m/s for Pb(Zr_xTi_{1-x})O_3 doped with 2.1 at.% of Fe.

Let us consider here the degradation mechanism of the mechanical quality factor Q_m with increasing vibration velocity. Figure 17 shows an important notion on heat generation from the piezoelectric material.[3] The damped and motional resistances, R_d and R_m, in the equivalent electrical circuit of a PZT sample are separately plotted as a function of vibration velocity. Note that R_m, mainly related to the mechanical loss, is insensitive to the vibration velocity, while R_d, related to the dielectric loss, increases significantly around a certain critical vibration velocity. Thus, the resonance loss at a small vibration velocity is mainly determined by the intrinsic

mechanical loss which provides a high mechanical quality factor Q_m, and with increasing vibration velocity, the intrinsic dielectric loss contribution significantly increases. After R_d exceeds R_m, we started to observe heat generation. Thus, we can conclude that heat generation is caused mainly by dielectric loss tan δ' (i. e. P-E hysteresis loss); this is not contradictory to the result in Section 4 where a high-voltage drive was conducted at an off-resonance frequency.
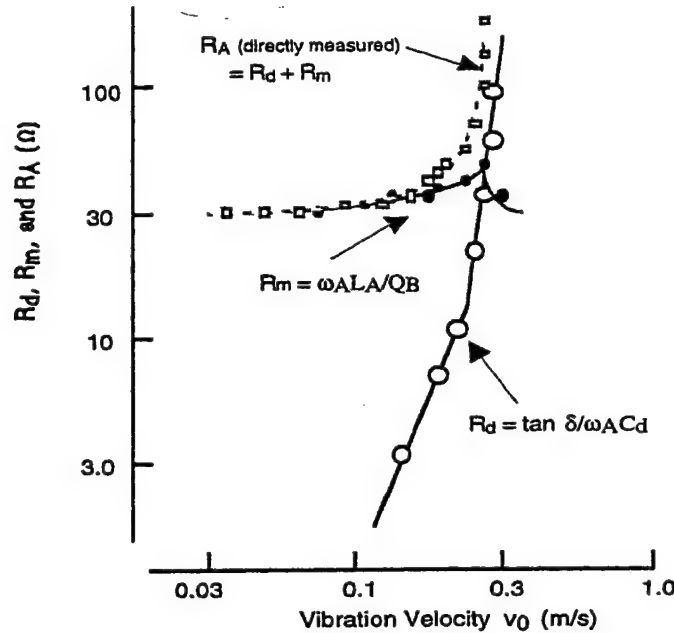

Fig.17 Vibration velocity dependence of the resistances R_d and R_m in the equivalent electric circuit for a PZT sample.

LOSSES AT RESONANCE AND ANTIRESONANCE MODES
Losses at a Piezoelectric Antiresonance State

We will consider the losses at the antiresonance frequency in comparison with the resonance mode. The antiresonance mode is obtained at a frequency which provides the minimum value of admittance Y, instead of zero of Y for the loss-free case. Taking an approximation technique on Eq. (61) around the antiresonance frequency ω_A, similar to the previous section, we obtain:

$$\Omega_A = \omega_A L/2 \ v, \ \Delta\Omega = \Omega - \Omega_A \ (<<1) . \tag{74}$$

If k_{31} is not very large, the following relationship is obtained:

$$\Omega_A = \omega_A L/ 2v = (\pi/2) \ (1 + (4/\pi^2) \ k_{31}^2) \tag{75}$$

In the following approximation, however, this relation is not used, but we will neglect the higher order of $\Delta\Omega$ and tan ϕ' in Eq. (61):

Electronic Ceramic Materials and Devices   97

$$Y = j\omega C_d\{1 + (k_{31}^2/(1-k_{31}^2)) \tan[(\Omega_A+\Delta\Omega) (1- j (1/2) \tan\phi')]/$$
$$[(\Omega_A+\Delta\Omega) (1- j (1/2) \tan\phi')]\}. \tag{76}$$

Taking into account

$$\tan[(\Omega_A+\Delta\Omega) (1- j (1/2) \tan\phi')]$$
$$= [(\Omega_A^2-K_{31}^2\Delta\Omega+ j(1/2)\Omega_A\tan\phi' K_{31}^2] / [(-K_{31}^2- \Omega_A\Delta\Omega) -j\Omega_A (1/2)\Omega_A \tan\phi'], \tag{77}$$

$$Y = j\omega C_d [- (\Omega_A^2+K_{31}^2+K_{31}^4)\Delta\Omega - j(1/2)\Omega_A\tan\phi' (\Omega_A^2-K_{31}^2-K_{31}^4) /$$
$$[- K_{31}^2 \Omega_A - (\Omega_A^2+K_{31}^2)\Delta\Omega - j(1/2)\Omega_A \tan\phi' (\Omega_A^2- K_{31}^2)], \tag{78}$$

where

$$K_{31}^2 = k_{31}^2/(1 - k_{31}^2) \tag{79}$$

Then, Y^{min} can be obtained at $\Delta\Omega = 0$:

$$Y^{min} = \omega C_d (1/2) \tan\phi' (\Omega_A^2- K_{31}^2 - K_{31}^4)/K_{31}^2. \tag{80}$$

$\sqrt{2} Y^{min}$ can be obtained at

$$\Delta\Omega = (1/2) \Omega_A \tan\phi' (\Omega_A^2-K_{31}^2-K_{31}^4) /(\Omega_A^2+K_{31}^2+K_{31}^4). \tag{81}$$

Thus, mechanical quality factor at the antiresonance can be obtained as:

$$Q = \Omega_A /2\Delta\Omega = [(\Omega_A^2+K_{31}^2+K_{31}^4)/(\Omega_A^2-K_{31}^2-K_{31}^4)] (\tan\phi')^{-1}. \tag{82}$$

Since $(\Omega_A^2+K_{31}^2+K_{31}^4)/(\Omega_A^2-K_{31}^2-K_{31}^4)$ is larger than 1, Q_m can be verified to be larger than Q_m at the resonance $(= (\tan\phi')^{-1})$. When k_{31} is small, using Eq. (75) and neglecting k_{31}^4 or higer orders, Q is approximated as

$$Q = (1 + (8/\pi^2) k_{31}^2) (\tan\phi')^{-1}. \tag{83}$$

Note that this Q is equal to the inverse value of the intrinsic mechanical loss, $(\tan\phi)^{-1}$.

Experimental Results

Figure 18 illustrates mechanical quality factors, Q_A, Q_B and the temperature rise for the resonance (A-type) and the antiresonance (B-type) modes for a rectangular-shape har PZT resonator plotted as a function of vibration velocity.[4] The sample size is indicated in the figure (43 mm x 7 mm x 2 mm). Note that an "effective" vibration velocity v_0 is a material's constant independent of the sample size, and is defined as $\sqrt{2} \pi f u_{max}$ where f is the resonance or antiresonance frequency and u_{max} is the maximum vibration amplitude of the piezoelectric device.[5] It is again noteworthy that the mechanical quality factor decreases dramatically above a certain critical

vibration velocity (0.1 m/s), where a steep tempreature rise starts. We have suggested that the heat generation is mainly attributed to a P-E hysteresis loss rather than the pure mechanical loss.[1] Note also that Q_B is higher than Q_A over the entire vibration velocity range, and that the temperature rise of the sample is less for the B-type resonance (antiresonance) than for the A-type resonance for the same vibration level. This indicates an interesting idea that the antiresonance mode should be superior to the conventional resonance mode, particularly for high power applications such as ultrasonic motors. In a typical piezoelectric material with k_{31} around 30 %, the plate edge is not a vibration nodal point and can generate a large vibration velocity.
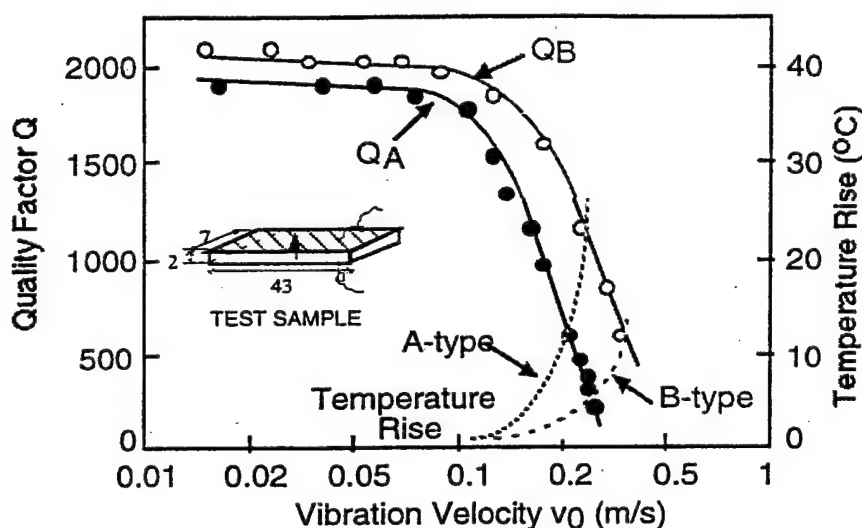

Fig.18 Vibration velocity dependence of the quality factor Q and temperature rise for both A (resonance) and B (antiresonance) type resonances of a longitudinally vibrating PZT ceramic transducer through transverse piezoelectric effect d_{31}.

CONCLUSIONS

(1) Various techniques for measuring the electric, mechanical and piezoelectric coupling losses separately have been discussed:

(a) D vs. E, x vs. X, x vs. E and D vs. X curves for electric, mechanical and piezoelectric losses
(b) heat generation at an off-resonance frequency for an extrinsic electrical loss
(c) resonance/antiresonance technique for intrinsic electric and extrinsic mechanical losses

By combining the above methods, we can investigate the loss mechanisms in practical piezoelectric materials.

(2) Heat generation is caused mainly by dielectric loss tan δ' (i.e., P-E hysteresis loss), not by mechanical loss. In order to suppress the temperature rise, a transducer design with larger surface area is recommended (for example, a tube rather than a rod).

(3) A dramatical decrease in mechanical Q_m with an increase of vibration level was observed in resonant piezoelectric ceramic devices, and the data obtained by a conventional impedance analyzer with a small voltage/power does not provide data relevant to high power materials.

Electronic Ceramic Materials and Devices   99

(4) Since the mechanical quality factor Q_B at an antiresonance frequency is larger than Q_A at a resonance frequency, the antiresonance mode seems to be superior to the conventional usage of the resonance mode, particularly for high power applications such as ultrasonic motors.

REFERENCES

[1] J. Zheng, S. Takahashi, S. Yoshikawa, K. Uchino and J. W. C. de Vries, J. Amer. Ceram. Soc., **79**, 3193-98 (1996).

[2] K. Uchino, Piezoelectric Actuators and Ultrasonic Motors, (Kluwer Academic Publishers, Boston, 1997), pp. 197.

[3] S. Takahashi and S. Hirose, Jpn. J. Appl. Phys., **32**, 2422-2425 (1993).

[4] S. Hirose, M. Aoyagi, Y. Tomikawa, S. Takahashi and K. Uchino, Proc. Ultrasonics Int'l '95, Edinburgh, pp. 184-87 (1995).

[5] K. Uchino, J. Zheng, A. Joshi, Y. H. Chen, S. Yoshikawa, S. Hirose, S. Takahashi and J. W. C. de Vries, J. Electroceramics, **2**, 33-40 (1998).

For a general reference textbook:

[6] T. Ikeda, Fundamentals of Piezoelectric Materials Science, (Ohm Publication Company, Tokyo, 1984), pp. 83.

APPENDIX 51

Doping Effects in $Pb(Mg_{1/3}Nb_{2/3})O_3$-$PbTiO_3$ Ceramics for High Power Transduction Applications

Yun-Han Chen[1], Senji Hirose[2], Dwight Viehland[3] and Kenji Uchino[1]

[1]International Center for Actuators and Transducers, Material Research Laboratory
The Pennsylvania State University, University Park, PA 16802
[2]Yamagata University, Yonezawa-shi, Yamagata 992, Japan
[3]Code 2132; Naval Undersea Warfare Center, Newport, RI 02835

Abstract

Piezoelectric ceramics are potential high-power electro-acoustic sources, and have been studied for many years. However, when these devices are driven under high level vibration, the electromechanical characteristics depart significantly due to the loss and nonlinear behavior in terms of elastic and dielectric properties. In this paper, we present results concerning the development of modified $Pb(Mg_{1/3}Nb_{2/3})O_3$-$PbTiO_3$ (PMN-PT) ceramics for high-power application. We have focused efforts on base PMN-PT compositions close to the morphotropic phase boundary. Different mono-doping have been studied to understand the doping effects on the properties of PMN-PT ceramics and, moreover, to improve the properties for the high-power application. Of all the substitutents investigated in this study, Mn-doping was found the only one to improve the properties of PMN-PT significantly for high-power application by reducing the total loss (including mechanical loss as well as the dielectric loss), yet keeping the coupling factor constant. This work is supported by Office of Naval Research.

Introduction

Piezoelectric ceramics are potential high-power electro-acoustic sources, and have been studied for many years. However, there are still some serious problems, such as the durability of the materials, and the fact that the piezoelectric data obtained for a small applied electric field becomes less relevant as the field is increased far above the general characterization condition[1,2]. Presently, the lead zirconate titanate (PZT) family of ceramics with some acceptor-type doping (Hard PZT) are the most widely used for this kind of application owing to their excellent dielectric and piezoelectric properties at the morphotropic phase boundary with the coexistence of tetragonal and rhombohedral phases, allowing increased domain reorientability and easier polarization as well as the low dielectric loss and high mechanical quality factor, Q_m, which is the inverse of the mechanical loss. However, in hard PZT, the coupling factor k is quite low and the loss still increases very fast under high-level driving[1]. Thus, investigation of other potential high k materials with more stable and reliable loss properties is important for transduction application.

The perovskite lead magnesium niobate $Pb(Mg_{1/3}Nb_{2/3})O_3$ (PMN) is a well-known relaxor with a diffuse phase transition. The structure is pseudo-cubic with an average space group symmetry Pm3m at room temperature, with no evidence of long range ordering of the dissimilar B site cation sublattices. The disorder in the B site cation is believed to be the cause of relaxor type behavior in these materials. The piezoelectric properties of PMN can be enhanced with the addition of PT. The PMN-PT solid solution system exhibits a morphotropic phase boundary (MPB) between a pseudo-cubic and a tetragonal phase at about 30-35 mole % of PT. [3] The dielectric and piezoelectric constants for materials near the MPB are abnormally high as reported by many researchers such as Lejeune. [4] The properties of high k, high d and high energy

215

density PMN-PTs are very attractive for high-power applications. However, the mechanical quality factor Q_m is quite low. Although PMN-PT system has been actively studied under a small AC electric-field condition, the characterization under high power applications has seldom been performed. Furthermore, there are almost no reports about varying Q_m value in PMN-PT by composition modification. In this study, we investigated doping effects on PMN-PT based ceramics for the goal of improving the materials for high-power applications.

Sample preparation and experimental procedure

In order to eliminate the formation of a parasitic pyrochlore phase ($Pb_3Nb_4O_{13}$), the columbite precursor method proposed by Swartz and Shrout [3] was used to prepare PMN-PT on the MPB. Both A-site and B-site dopants, including the higher valence and lower valence elements were used to study the effect of doping in PMN-PT. These include La, Li, Na, K, Mn, In, Fe. Excess Mg and Nb were also studied for comparison. In the first stage, MgO and Nb_2O_5 were mixed in a stoichiometric ratio, and a precursor columbite phase $MgNb_2O_6$ was formed after calcination at 1200°C for 4hrs. X-ray diffraction patterns were then taken to check phase formation. In the second stage, the precursor was mixed in stoichiometric ratios with PbO and TiO_2 and doping elements. To insure proper mixing, both steric hinderenace and electrostatic repulsion (pH adjustment by ammonia), dispersion mechanisms were required to prepare a 30 vol. % slurry with deionized water. The slurry was vibratory milled, then dried and calcined at 700°C for 4 hr. Calcined powders were examined by x-ray diffraction to insure phase purity. To control PbO volatility, sintering was performed in a lead rich atmosphere by placing a small amount of mixed powder of PbO and ZrO_2 in a closed crucible. After sintering, the samples were polished, and gold-sputtering was used for the electrodes on both surfaces.

The dielectric properties were measured with a computer controlled automated-measurement system from room temperature to 250°C (HP4284A for electric measurement and FLUKE8840 with an oven for temperature controlling). The electromechanical properties were determined by measurement of the admittance spectrum under low level constant voltage using an HP4194, and by measurement of the impedance spectrum vs. different vibration velocity under constant-current driving conditions [1]. The latter method is different from the conventional impedance analyzer measurements, where the vibration velocity is significantly increased near the resonance frequency, leading to jumping and hysteresis problems in the impedance vs. frequency curve due to the nonlinearity become significant under high level driving.

Results and discussions

a. Basic properties

Table I summaries the dielectric and electromechanical properties for different dopings. Data taken from previous studies of various doping elements in PZT or PMN-PT, and the radii of Pb(2+) and Ti(4+), have also been included for reference. Effects of Na and K substituents can be seen to be almost the same. Both are from the same group (s-oribitals with 1+ valance) and substitute Pb onto the A sites which have 12-coordination. Both of these substitutents increase the quality factor Q_m a little and reduce the piezoelectric constant. Li is also from the same chemical group (s-oribital with 1+ valence), yet its ionic radii is smaller (0.76Å) relative to Na (1.39Å) and K(1.64Å). The tolerance factor $t = \dfrac{(r_{A(12-CN)} + r_{O(6-CN)})}{\sqrt{2}(r_{B(6-CN)} + r_{O(6-CN)})}$ is too small for Li to go onto the A-sites. Consequently, the effect of Li modification is different from Na and K doping.

216

Fe-modification does not change the properties of PMN-PT significantly, however for the PZT system, Fe increases Qm to more than 1000. In PZT, both B-site cation sublattice are occupied by 4+ species, while in PMN-PT occupancy is composed of multiple valent species, i.e., 2+ (Mg), 5+ (Nb), and 4+ (Ti). If Fe prefers to substitute for Mg, then, it is either a 3+ (or 2+) species on a 2+ site. In this case, it will not induce acceptor-type (or "harder") behaviors in PMN-PT, as it does in PZT. Similar effects were found in In-modified compositions, as can be seen in Table I. Excess Mg and Nb did not result in any significant effects on the properties. Possibly because concentrations of one at.% excess are too small.

Of all the substitutents investigated in this study, Mn was the only one which was found to behave uniquely. Upon Mn modification, the piezoelectric constant was decreased, however the quality factor Qm was increasesed significantly. The coupling coefficient k_{31} was not significantly affected by Mn modification and had a constant value of ~0.3. These changes in the properties make the materials more suitable for high power transducer applications. Thus, high-power measurements of Mn-modified samples will shown in the next section.

Table I: The properties of .65PMN-.35PT with 1 at.% doping

element	La[*]	K	Na	Li[**]	Mn[***]	Fe[****]	In[*****]	Nb[******]	Mg[*******]
Substitute site	A-site	A-site	A-site		B-site	B-site	B-site	B-site	B-site
Valency	+3	+1	+1	+1	+2, +3, +4, +7	+2, +3	+3	+5	+2
Behavior in PZT	Donor-like	Acceptor-like	Acceptor-like	?	Acceptor-like	Acceptor-like	Acceptor-like	Donor-like	Acceptor-like
Ionic radii(A)	1.36	1.64	1.39	.76	(+7).46 (+4).53 (+3).62 (+2).72	(+3).60 (+2).70	.8	.69	.72
Curie T	50	181.23	178	178.3	175	178	187.62	185.9	189
Dieletric constant	2300	3990	4140	3260	2100	3100	3140	4050	3500
Kmax	23000	34800	34800	25600	21000	33000	33400	33600	38100
Dieletric loss	.025	.012	.0114	.0305	.009	.0116	.0118	.024	.02
d_{33}	280	373	360	546	350	500	564	583	540
Q_m	76	143	150	68	300	80	88	75	78

Pb (+2) 1.49A, Ti (+4) .605A
A-site cation : 12-coordinated, B-site cation : 6-coordinated
*Used to adjust Tc[3]
**Used to improve the electrical resistance, reduce the sintering temperature and reduce the temperature coefficient of capacitance
***1.Used as similar reason of Li. 2.Studied for the age effect.[6]
****Can form PFN[5]
***** Can form PIN[5]
******Can form pyrochlore[3]
******* Sintering aid, can reduce pyrochlore but induce grain growth.[3]

Figure 1 shows the temperature and frequency dependence of the dielectric constant as well as dielectric loss (tanδ) for 0.65PMN-0.35PT with different substituents. Mn and Li substituents both depressed and broadened the peak dielectric constant values, shown in Fig 1(a) and (b), even though Mn had a stronger effect. One possible reason is that they both can form a liquid phase during sintering resulting in secondary phase formation in the grain boundaries, which

generally reduces the dielectric constant. However, they have very different behavior of dielectric loss (Tan Delta). While Mn substituents reduce the dielectric loss to less than 1% near room temperature, specimens with Li retain a value of 3% (Fig1 (d) and (e)). The temperature and frequency dependence of dielectric constant of Na and K-doped samples are shown in Fig1 (b). They both exhibited similar results, however Li-modification resulted in significant differences.

b. Piezoelectric properties under a high-power driving

Heat generation is one of the big problems for materials under high-level driving. The temperature rise, ΔT, with a specific sample due to the heat generation is proportional to the loss as follows

$$\Delta T = \frac{\omega_0 W t'}{Mc} \tag{1}$$

where $\omega_0 W$ is dissipated vibration energy per second, M mass of the sample, t' thickness, and c the specific heat capacitance.

The dissipated-vibration-energy per second, $\omega_0 W$ can be calculated as follows

$$\omega_0 W = \frac{1}{2} M v^2 \omega_0 Q^{-1}$$

and (2)

$$Q^{-1} = Q_M^{-1} + Q_E^{-1}$$

where v, and ω_0 are vibration velocity and resonance angular respectively.

From Eqn(1) and (2), we can get

$$\Delta T = \frac{\frac{1}{2} v^2 \omega_0 Q^{-1} t'}{c} \tag{3}$$

For longitudinal d_{31} mode with both ends of the sample are mechanically free, the relationship of vibration velocity v and the driving field E_{d0} can be written as

$$v = \frac{4}{\pi} \sqrt{\frac{\varepsilon_{33}^T}{\rho}} k_{31} Q E_{d0} \tag{4}$$

It can be calculated from the resonance frequency and the maximum displacement ξ_m of the ends by the following equation

$$v = \frac{1}{\sqrt{2}} \omega_r \xi_m \tag{5}$$

The result of the saturation temperature rise and the total loss increase with an increase of the vibration velocity for Mn-doped samples are shown on Fig.2(a). From Eqn. (3), the temperature
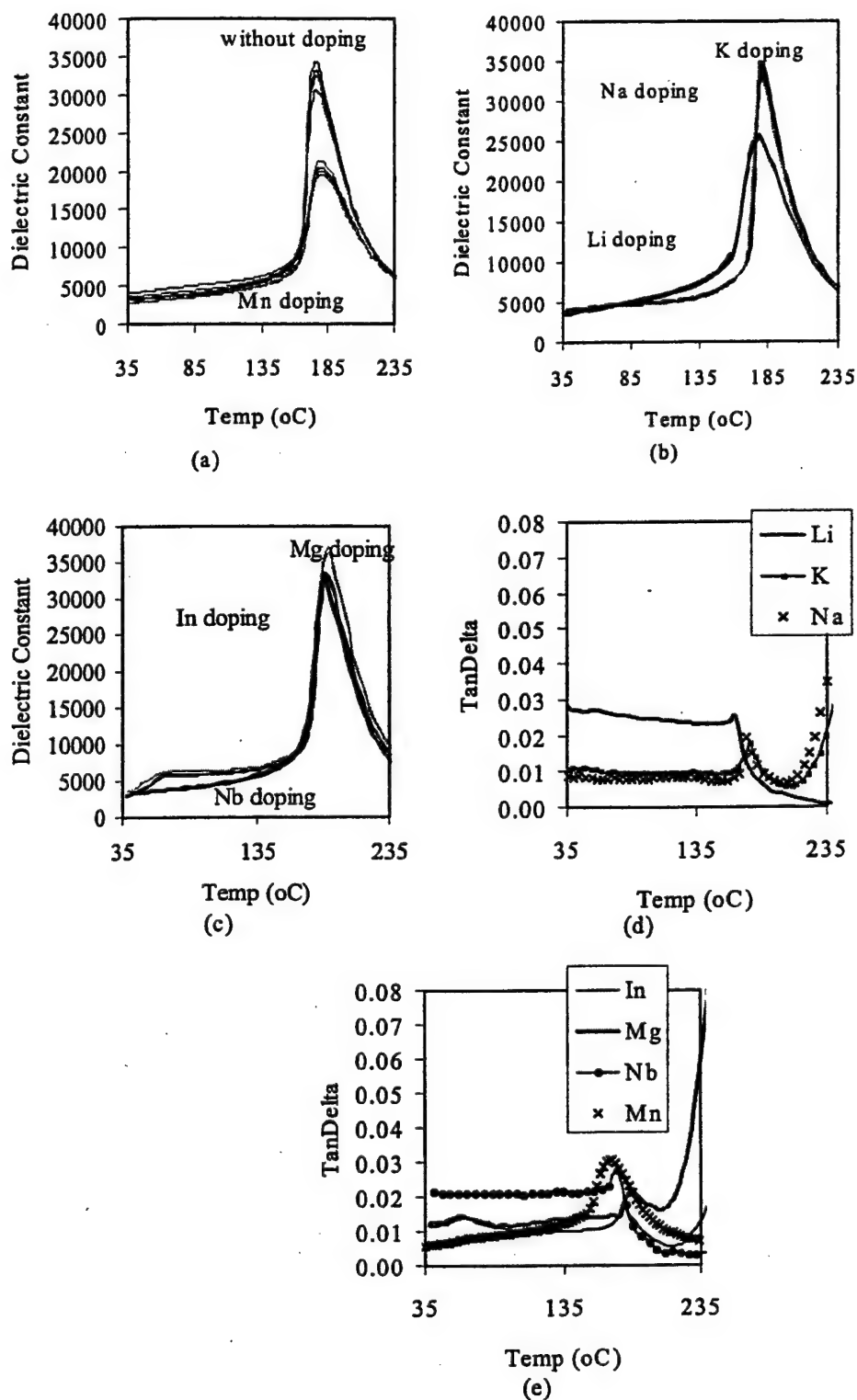
Figure 1: Dielectric constant with different frequencies (100Hz, 1kHz, and 10kHz from the highest to the lowest curve in one group) vs. temperature of .65PMN-.35PT + 1 at.% dopants: (a) pure and Mn, (b) K, Na, Li, (c) In, excess Mg, and excess Nb; Tan Delta vs. Temperature of .65PMN+.35Pt + 1 at.% dopants: (d) Li, Na, K, (e) Mn, In, excess Mg and excess Nb.

rise is proportional to the square of vibrational velocity, and the total loss. The saturation temperature was decided when the sample temperature become stable due to the balance of heat generation and radiation after a period of time when the sample driving under some vibrational velocity. Because the quality factor Q dropped significantly when the vibrational velocity > .2 m/sec (referred to Fig 2(b)), the saturation temperature rise also increased much faster. The larger Q the sample has, the smaller the saturation temperature rise is.
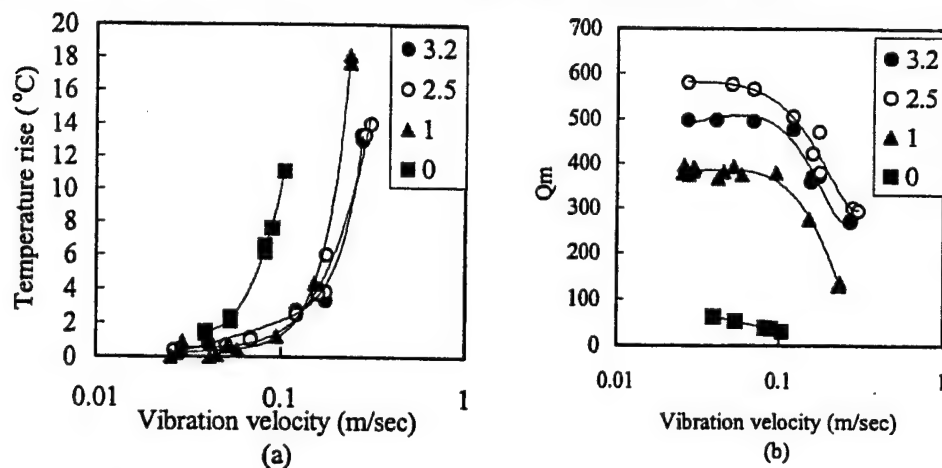
Figure 2: The vibration velocity dependence of temperature rise (a) and quality factor Qm (b) of .65PMN-.35PT + x at.% Mn doping

Summary

In this paper, MPB compositions of PMN-PT with various substituents were studied for high-power applications. Mn-doping was found to improve the properties of PMN-PT significantly for high-power application by reducing the total loss (including mechanical loss as well as the dielectric loss), yet keeping the coupling factor constant. It appears that Mn substituents behave as acceptors in PMN-PT ceramics, resulting in "harder" characteristics. The special effects of Mn may be related to its multiple valance states, however this needs further investigations

Acknowledgement

REFERENCE:

1. S. Takahashi, S. Hirose, K. Uchino, *J. Am. Ceram. Soc.*, Vol. 77, 1994, p2429

2. S. Tashiro, M. Ikehiro and H. Igarashi, *Jpn. J. Appl. Phys.* Vol. 36, 1997, p3004.

3. W. Huebner, S. J. Jany, T. R. Shrout N. Kim, *Ferroelectrics*, Vol.93, 1989, p341.

4. M. Lejeune and J. P. Boilot, *Mater. Res. Bull*, Vol. 20, 1985, p493.

5. Y. Yamashita, *Jpn. J. Appl. Phys.* Vol. 33, 1994, pp3325-3331.

6. W. Y. Pan, Q. Y. Jiang, and L. E. Cross, *Ferroelectrics*, Vol. 82, 1988, pp.111-117.

APPENDIX 52

Mn-Modified Pb(Mg$_{1/3}$Nb$_{2/3}$)O$_3$–PbTiO$_3$ Ceramics:
Improved Mechanical Quality Factors for High-Power Transducer Applications

Yun-Han CHEN^1, Seiji HIROSE^1, Dwight VIEHLAND^2, Sadayuki TAKAHASHI^3 and Kenji UCHINO

International Center for Actuators and Transducers, Material Research Laboratory The Pennsylvania State University, University Park, PA 16802, USA
^{1}*Yamagata University, Yonezawa, Yamagata 992, Japan*
^{2}*Code 2132; Naval Undersea Warfare Center, Newport, RI 02835, USA*
^{3}*NEC Corporation, 4-1-1 Miyazaki, Kawasaki 216, Japan*

Piezoelectric ceramics are potential high-power electroacoustic sources, and have been studied for many years. However, when these devices are driven under high-level vibration, the electromechanical characteristics depart significantly from the conventional linear piezoelectric relationships due to the loss and nonlinear behavior in terms of elastic and dielectric properties. In this paper, we present results concerning the development of modified Pb(Mg$_{1/3}$Nb$_{2/3}$)O$_3$–PbTiO$_3$ (PMN–PT) ceramics with improved mechanical quality factors for high-power application. We have focused efforts on base PMN–PT compositions close to the morphotropic phase boundary. Evidence will be presented which indicates that the improved mechanical quality factor results from the introduction of "hard" characteristics into PMN–PT by the substituents. Investigations of the nonlinearity of the electromechanical properties on the vibrational amplitude were performed using a constant displacement method. The degradation of the mechanical quality factor with increasing drive amplitude also presents thermal stability problems for the usage of these materials in high-power transducer applications.

KEYWORDS: PMN–PT, MPB, high-power piezoelectric, mechanical quality factor, nonlinearity

1. Introduction

Piezoelectric ceramics have been studied for many years, but only recently has interest arisen in using them as high-power electroacoustic projectors/sources such as ultrasonic motors and transformers. However, when these materials are electrically driven to high mechanical vibration levels near resonance, the electromechanical property characteristics depart significantly from the conventional linear piezoelectric relationships.[1–4] The deviations are due to the presence of nonlinear contributions in both the real and imaginary components of the apparent dielectric, electromechanical, and elastic responses. Experimentally, with respect to standard piezoelectric resonance methods, several effects are known to occur under high-level vibration excitations. These include: (i) a shift in the resonance frequency,[1,2] (ii) a decrease in the mechanical quality factor Q_m,[4] (iii) an appearance of a jump and/or a hysteresis in the admittance spectrum during a frequency sweep,[1,2] and (iv) heat generation (due to the lower Q_m) that not only degrades the electromechanical properties[5] but also may result in thermal stability problems for transducer engineers.

The current lack of a deterministic understanding of these nonlinearities presents a serious problem for their usage in high-power applications. Available piezoelectric data on lead zirconate titanate (PZT) and lead magnesium niobate lead titanate (PMN–PT) ceramics have generally been obtained only under small fields. A few researchers have investigated the behavior of piezoelectric materials under high-power driving conditions. Beige and Schmidt[1] have demonstrated the presence of strong nonlinearities in the dielectric, piezoelectric, and elastic responses. These studies were performed using a resonance method and demonstrated the presence of strong asymmetries in resonance curves. Phenomenological analysis demonstrated that the source of all three types of nonlinearities was the acentric nature of the polarization. Also, Takahashi et al.[4] have reported high-power measurements on piezoelectric materials, obtained using the constant vibration velocity method. In this method, the vibration velocity of the specimen is held constant by varying the applied voltage as the frequency is swept through the natural resonance mode of the specimen. With this constant vibrational velocity method, asymmetries or hysteresis jumps in the admittance spectrum can be avoided. This method has been applied to materials such as PZT modified with Nb and Fe, lead manganese antimonate-lead magnesium niobate-lead titanate (PMS–PMN–PT), and lead manganese antimonate-lead zirconate titanate (PMS–PZ–PT). In general, it has been found that with increasing the vibration level, the mechanical quality factor, Q_m, decreases dramatically. Tashiro et al.[5] have also reported a temperature rise, under high-level drive conditions in PZT-based materials using this method.

Undoubtedly, domain wall motions/vibrations contribute significantly to the electromechanical and mechanical nonlinearities. In addition, they will significantly impact the imaginary components of the responses. It is well known that the dielectric loss factor depends strongly on the amplitude of the AC electrical field. The large loss factors under moderate drives result in the conversion of a significant amount of the stored electrical energy into heat. Domain wall motion/vibrations will also contribute significantly to the apparent piezoelectric and mechanical loss factors.[6,7] In general, these loss factors have been shown to be directly related to the dielectric loss factor. Also, previous internal friction investigations of martensitic phases under AC mechanical excitation have revealed the presence of strong nonlinearities in the mechanical quality factor with increasing drive levels.[8,9] These nonlinearities result from a stress dependence of the unrelaxed moduli. With increasing AC drive, the unrelaxed moduli are driven towards the relaxed condition, resulting in ferroelastic domain boundary motion and a significant decrease in the mechanical quality factor. Clearly, in systems containing ferroelectric or ferroelastic (proper or improper) domain boundaries, phase angles are dominantly controlled by the dynamics of the domains. In ferroelectric systems, both the dielectric and mechanical quality factors will be dominated by

the dynamics of the ferroelectric domains.

In high-power applications, heat generation limits the application of many potential materials. "Soft" piezoelectric materials are known to have significantly higher performance coefficients, relative to hard materials.[9] However, the enhanced performance of soft materials cannot be taken advantage of in high-power applications, due to thermal stability conditions in transducer designs. Rather, the only materials which can be used in these applications are "hard" piezoelectrics. These materials have significantly degraded piezoelectric coefficients and electromechanical coupling coefficients, relative to soft materials. The near linear nature of the polarization under drive conditions in hard materials results in greatly reduced hysteretic losses upon the cycling of a field. The reduced losses of hard materials result from a domain wall pinning by defect dipoles. In general, it has been observed that higher valent substituents induce soft behavior, whereas lower valent ones induce hard behavior.[9]

Ideally, for high-power transducer applications, the combination of high electromechanical performance of soft piezoelectrics with the low hysteretic losses of hard ones is desirable. Another alternative is the electrostrictive relaxor ferroelectrics, which develop piezoelectric properties under DC bias.[10] These materials have slim quadratic hysteresis loops, but as of yet, their application in high-power transducers has also been limited in part by thermal stability considerations. One of the purposes of this work was to attempt to develop PMN–PT ceramics which are modified by substituents which might induce hard characteristics to some degree. High-power, high-Q PMN–PT–based ceramics would have important applications in actuators and transducers.

This paper focuses on the high-power piezoelectric characteristics of $Pb(Mg_{1/3}Nb_{2/3})O_3$–$PbTiO_3$ (PMN–PT)-based ceramics which have been modified with Fe or Mn. The perovskite lead magnesium niobate $Pb(Mg_{1/3}Nb_{2/3})O_3$ (PMN) is a well-known relaxant with a diffuse phase transition.[11,12] The piezoelectric properties of PMN can be enhanced by the addition of PT.[13] The PMN–PT solid solution system exhibits a morphotropic phase boundary (MPB) between the pseudocubic and tetragonal phases at about 30–35 mole% of PT.[14] The dielectric and piezoelectric constants for materials near the MPB are abnormally high, as reported by many researchers such as Lejeune.[15] Although the PMN–PT system has been actively studied for a small electric-field response, such characterization for high-power applications has seldom been made.

2. Sample Preparation and Experimental Procedure

PMN–PT powders were formed using the columbite precursor method developed by Swartz and Shrout.[16] In this method, the formation of a parasitic pyrochlore phase $(Pb_3Nb_4O_{13})$ is eliminated. Specimens were prepared for compositions close to the morphotropic phase boundary (MPB) with a PT-content of 33 at.% (i.e., 0.67PMN–0.33PT). This composition will be referred to as PMN–PT throughout the remainder of this paper. Modified PMN–PT ceramics were prepared using Fe or Mn substituents. These particular substituents were chosen in PZT because they are conventionally used for rendering the properties harder.

In the first stage of powder preparation (columbite precursor step), MgO and Nb_2O_5 powders were mixed in a stoichiometric ratio. After calcination at 1200°C for 4 h, a precursor columbite phase, $MgNb_2O_6$, was formed. Single-phase columbite formation was confirmed by X-ray diffraction. In the second stage, the columbite precursor was mixed in stoichiometric ratios with PbO and TiO_2. In order to ensure proper mixing of a 30 vol% slurry with deionized water, careful dispersion was achieved with pH adjustments using am-
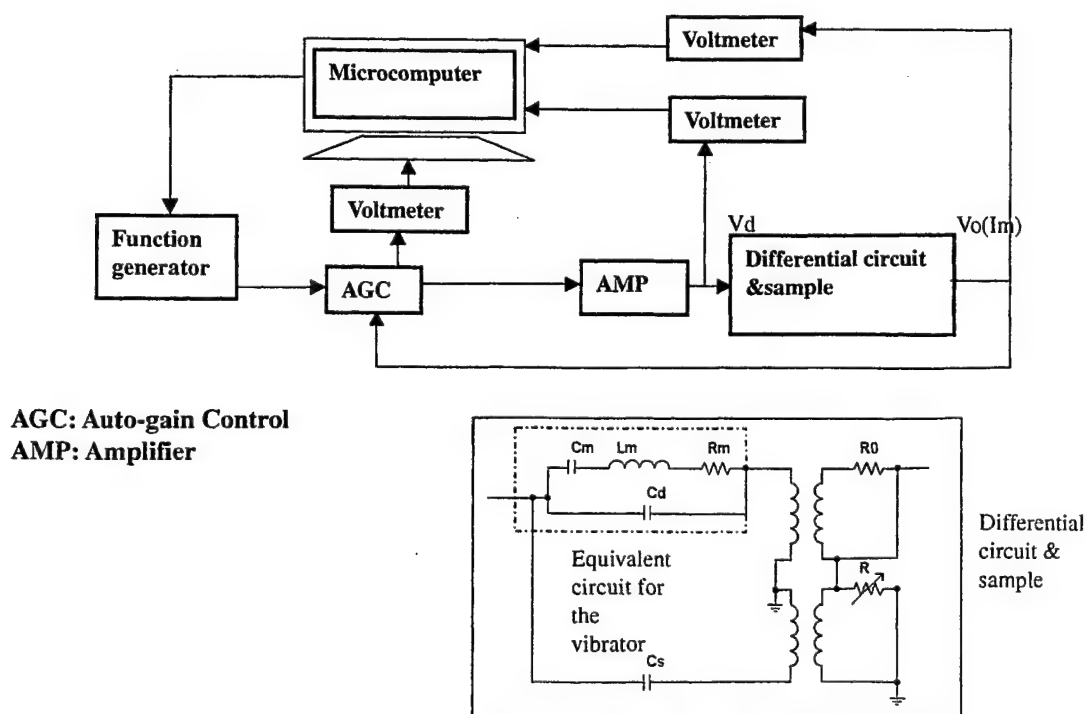

AGC: Auto-gain Control
AMP: Amplifier

Fig. 1.   High-power measurement system with constant-current driving.

monia, thus reducing both steric hindrance and electrostatic repulsion (pH adjustment by ammonia). The slurry was vibratorily milled, dried and then calcined at 700°C for 4 h. The calcined powders were examined by X-ray diffraction to ensure phase purity. The powders were then formed into green bodies by cold isostatic pressing (CIP), in order to increase the green body densities and reduce the deformation due to the inhomogeneous pressure. Sintering was then performed in a Pb-rich atmosphere by placing a small amount of the mixed powders of PbO and ZrO_2 in a sealed crucible to reduce PbO volatility. Different sintering temperatures and times were tested, in order to determine the best sintering profiles for the different samples. After sintering, the samples were cut and polished to 40 mm × 5 mm × 1 mm rectangular plates. Gold sputtering was then used to deposit electrodes on both surfaces. Finally, the specimens were poled by being immersed in silicon oil at 100°C and an applied field of ~2.5 kV/mm for 20 min.

Scanning electron microscopy (SEM) with energy-dispersive X-ray spectroscopy (EDS) (Model HITACHI S-3500N made by Philips) was used to evaluate the grain sizes and the composition homogeneity of the specimens. The dielectric properties were measured using a computer-controlled HP 4284A LCR meter. Temperature-dependent measurements were performed using a FLUKE 8840 multimeter in conjunction with a Delta Design environmental chamber in the temperature range between 25 and 250°C. Dielectric measurements were performed both before and after poling. The polarization and strain were then simultaneously measured as a function of an applied AC electrical field. The $P-E$ behavior was measured using a computer-controlled modified Sawyer-Tower circuit. Low-frequency hysteresis data were obtained using bipolar triangle waves at room temperature. The system measured the $\varepsilon-E$ behavior using an inductance (LVDT) method. The electromechanical properties were determined by measurement of impedance spectra under low-level constant voltage drive using a HP4194, and by measurements of impedance spectra at different vibration velocities under constant-current driving conditions. In the constant-current method, the voltage applied to the specimen is varied as the frequency is varied through the natural resonance in a manner which results in a constant vibration velocity. This method avoids asymmetric resonance curves, which are known to cause problems in impedance measurements under high drive power conditions.[1,2] Figure 1 shows a block diagram of the constant-current method. Further information concerning this method has been published previously.[4]

3. Results and discussion

3.1 Crystallographic structures and microstructures

X-ray diffraction patterns are shown in Fig. 2(a) for specimens with 0, 1, 1.7, 2.5, and 3.2 at.% Mn. The pyrochlore/perovskite phase ratios by volume were much less than 0.1% for all these compositions. Clearly, the Mn-modified specimens used in this investigation were nearly phase pure. However, for a Mn content of 3.2 at.%, a small additional peak was observed close to the perovskite 200 peak, indicating small concentrations of a secondary phase associated with either pyrochlore formation or Mn exsolution. The lattice constants were determined from this data. A plot of the lattice constant as a function of Mn concentration is shown in
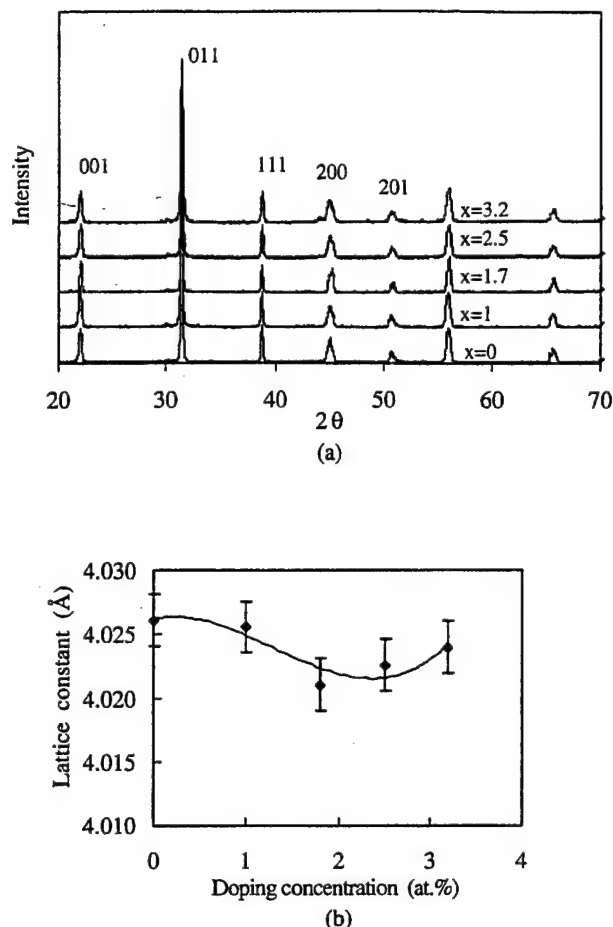

Fig. 2. (a) X-ray diffraction patterns and (b) Lattice constant *a* of $0.67Pb(Mg_{1/3}Nb_{2/3})O_3-0.33PbTiO_3$ with x at.% Mn doping.

Fig. 2(b). From the data in this figure, it can be seen that the pseudocubic structure does not change significantly with varying the Mn doping concentration, over the range investigated. Similarly, phase-pure perovskite materials were found by X-ray diffraction for Fe-modified PMN–PT.

Grain sizes were determined for Fe- and Mn-modified specimens with various substituent concentrations by SEM, as shown in Fig. 3(a). The grain size of the unmodified base PMN–PT composition was found to be about 5 μm. Upon modification with Fe, the average grain size was found to decrease to about 3 μm for $x = 1$ at.% and remained unchanged with further increase in Fe concentration. For the Mn-modified materials, the average grain size was found to be about 5 μm, which is equal to that of the unmodified base composition. These data clearly demonstrate minor microstructural changes with compositional modification and with increasing substituent concentrations. Consequently, changes in properties with increasing substituent concentrations cannot be attributed to changes in microstructural characteristics associated with the polycrystalline nature of the material. Rather, such changes will need to be explained on the basis of changes in structural-chemical-property relationships.

The possibility of secondary-phase formation was further investigated using the EDS attachment of the SEM. Small quantities of secondary phases were observed near the grain boundaries for the Mn-modified materials. EDS analysis re-
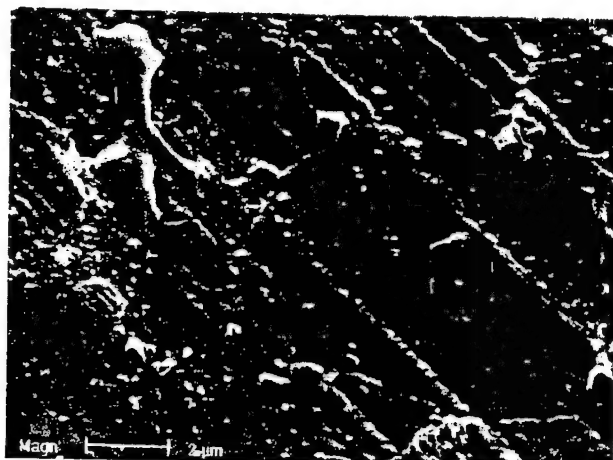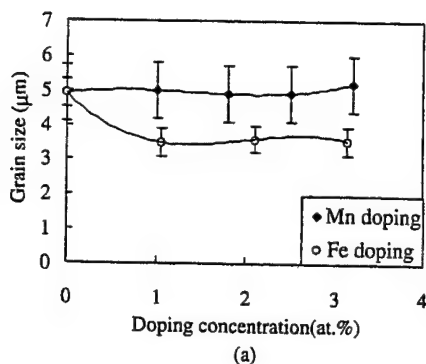
(a)

Fig. 4. Mechanical quality factor Q_m and piezoelectric constant d_{33} of $0.67Pb(Mg_{1/3}Nb_{2/3})O_3-0.33PbTiO_3$ with x at.% Fe.

(b)

Fig. 3. (a) Grain size vs. doping concentration of $0.67Pb(Mg_{1/3}Nb_{2/3})O_3-0.33PbTiO_3+x$ at.% Mn or Fe. (b) SEM image of $0.67Pb(Mg_{1/3}Nb_{2/3})O_3-0.33PbTiO_3 + 3.2$ at.% Mn.

vealed that the local compositions of these regions are rich in Mn and Mg. This result indicates that Mn does have a limited solubility in the PMN–PT perovskite phase, tending to exsolve at concentrations in excess of about 3 at.%. Similarly, Fe substituents are known to have limited solubility in PZT, limiting their concentrations in the fabrication of hard piezoelectric ceramics. Thus, in our investigations, substituent concentrations in excess of 3.2 at.% were not investigated.

3.2 Weak field properties

3.2.1 Fe-modified PMN–PT

Figure 4 shows the mechanical quality factor (Q_m) and d_{33} value for Fe-modified PMN–PT as a function of Fe-concentration. The mechanical quality factor was found to be approximately 75 and nearly independent of Fe concentration over the compositional range investigated. These values are close to those found for conventional soft piezoelectrics, such as La-modified PZT (PLZT) or Nb-modified PZT.[4,5,17] In these cases, the relatively large mechanical losses are believed to be directly due to the large dielectric losses that are incurred under small electrical drives. In soft materials, large losses occur due to domain boundary vibrations or excitations that are readily stimulated under weak AC drive conditions.

The results shown in Fig. 4 are contradictory to those observed for Fe-modified PZT.[4,5,9] In both cases, Fe is substituted onto the B-cation sites, but in PZT-based materials,
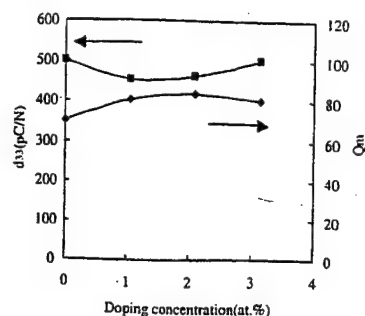
Fe modification results in the development of hard piezoelectric behavior and consequently an enhanced mechanical quality factor. In PMN–PT-based materials, Fe modification results in the preservation of soft piezoelectric behavior and no change in the mechanical quality factor. Clearly, something different is occurring. A possible explanation resides in the consideration of the multiple B-cation sites that are available for substituent occupancy in PMN–PT. In PZT-based materials, Fe substitution on the B-site must result in the displacement of a +4 cation (Zr or Ti) for a +3 one (Fe). However, in PMN–PT-based materials, Fe substitution on the B-site can result in the displacement of either a +2 (Mg), a +4 (Ti) or a +5 (Nb) cation. The B-site cation sublattice that the Fe (+3) preferentially occupies will have a significant impact upon the charge compensation mechanism, and consequently upon the nature of the defects that are introduced into the structure that subsequently interact with domains. The lack of changes in the mechanical quality factor of PMN–PT with increasing Fe concentration indicates that the Fe substituents may prefer to occupy the lower valent sites.

3.2.2 Mn-modified PMN–PT

To induce hard characteristics in PMN–PT, it will be necessary to modify the base composition with a lower valent substituent on a higher valent site, similar to that for PZT.[9] In mixed B-site cation materials, identification of a lower valent substituent is not straightforward, as discussed above. In the course of this work, various other modified PMN–PT compositions were fabricated. Interesting results were found for Mn-modified PMN–PT. Data are shown in Figs. 5(a)–5(d) for these materials.

Figure 5(a) shows the mechanical quality factor as a function of Mn concentration. The unmodified base composition had a Q_m of approximately 75, as reported above. Upon modification with one at.% Mn, the mechanical quality factor increased to about 400. Upon further increase of the Mn concentration, Q_m peaked at about 600 for $x = 2.2$ at.%. At higher concentrations, the value of Q_m decreased slightly. Clearly, the mechanical quality factor is increased significantly by Mn modification. The increment in the mechanical quality factor indicates that the PMN–PT properties may become increasingly hard with moderate Mn concentrations. The hardening of piezoelectric behavior is believed to occur due to a pinning of domains by dipolar defects at domain boundaries.[9] Thus, the domain boundaries cannot dissipate mechanical/electrical energies under weak drives. Before dielectric or mechanical absorption can occur, the domain de-
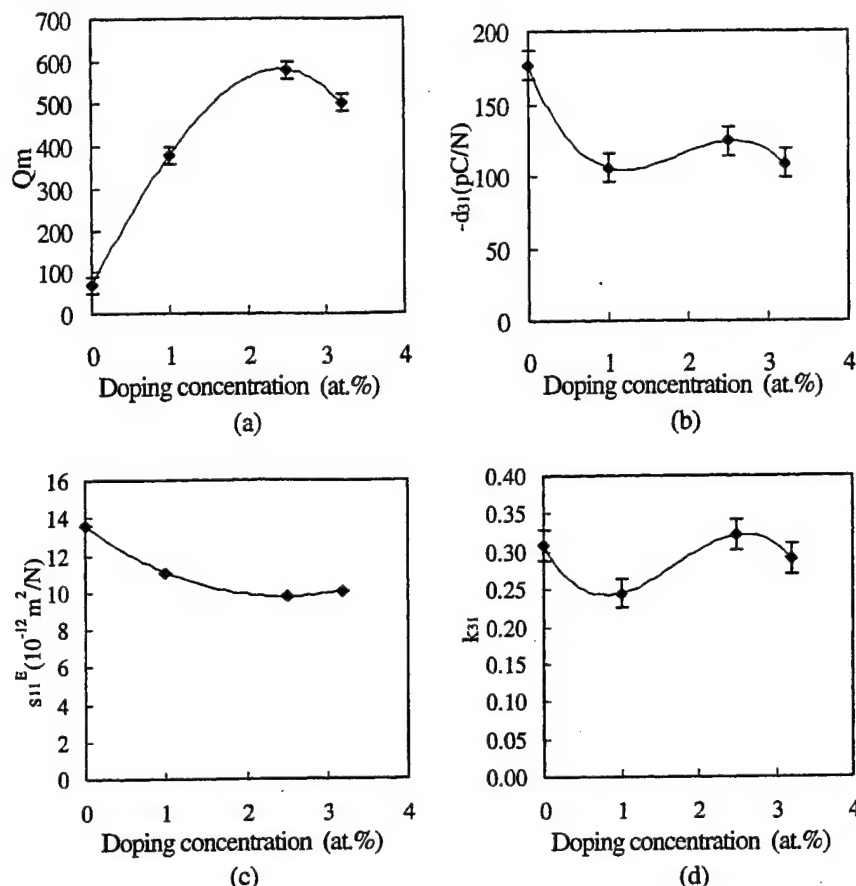
Fig. 5. (a) Mechanical quality factor Q_m, (b) piezoelectric constant d_{31}, (c) elastic constant s_{11}^E, and (d) coupling factor k_{31} of $0.67Pb(Mg_{1/3}Nb_{2/3})O_3-0.33PbTiO_3$ with x at.% Mn.

pinning must be stimulated.

Further evidence of the hardening of the PMN–PT electromechanical behavior can be seen in Figs. 5(b)–5(d). In Fig. 5(b), the piezoelectric coefficient (d_{31}) is shown as a function of Mn concentration. With increasing Mn concentration, the value of d_{31} can be seen to decrease significantly. Upon the increment of the Mn content between 0 and 1 at.%, the value of d_{31} decreased by approximately 50%. In Pb-based perovskites, the piezoelectric constant at room temperature is believed to be mainly due to domain wall contributions.[18] In fact, in PZT, Landau-Devonshire analysis has revealed that the intrinsic (single-crystal single domain) response can account for only about 20–25% of the experimentally observed values. The remaining portions of the piezoelectric response have been attributed to domain wall contributions. Consequently, modification of PMN–PT or PZT-based compositions with impurities and/or defects which tend to pin domain boundaries will result in dramatic decreases in the piezoelectric response. In fact, hard PZT materials are known to have significantly lower electromechanical performance coefficients for this particular reason. The data shown in Fig. 5(b) is consistent with the conjecture that Mn modification results in a partial hardening of the piezoelectric behavior of PMN–PT. Also, the elastic compliance (s_{11}^E) is shown in Fig. 5(c) as a function of Mn concentration. With increasing Mn concentration, the elastic compliance was found to decrease by about 40%, i.e., the elastic constant stiffened. Domain boundary motion is a dissipative phenomenon

which results in a softening of the elastic constant, as is well known in ferroelastic and martensitic materials.[8, 19] Thus, the pinning of domain boundaries would result in a stiffening of the linear elastic constant. In general, as an unrelaxed elastic modulus (i.e., the mechanical quality factor) is decreased, more elastic energy can be stored within the specimen during a cycle of a field.[8] Consequently, the relaxed modulus (i.e., the elastic stiffness) is increased.

The electromechanical coupling coefficient as a function of Mn concentration is shown in Fig. 5(d). The value of the coupling coefficient can be seen to vary between 0 and 3.2 at.%, but the value remains in the vicinity of 0.30. The coupling factor does not decrease with increasing Mn concentration as the value of d_{33} is decreased. This is because the elastic constant is stiffened as the piezoelectric constant is decreased. Less displacement occurs under electrical drive in the Mn-modified materials; however, the displacement has greater force due to the enhanced elastic stiffness. Thus, the electromechanical coupling coefficient between stored electrical and mechanical energy forms is not significantly altered.

The dielectric responses of the Mn-modified PMN–PT specimens are shown in Fig. 6. Figure 6(a) shows the 10^2 Hz room temperature dielectric constant and loss as a function of Mn concentration. The dielectric constant and dielectric loss factor were both decreased by about 50% with increasing Mn concentration between 0 and 3.2 at.%. The temperature-dependent characteristics of the dielectric con-
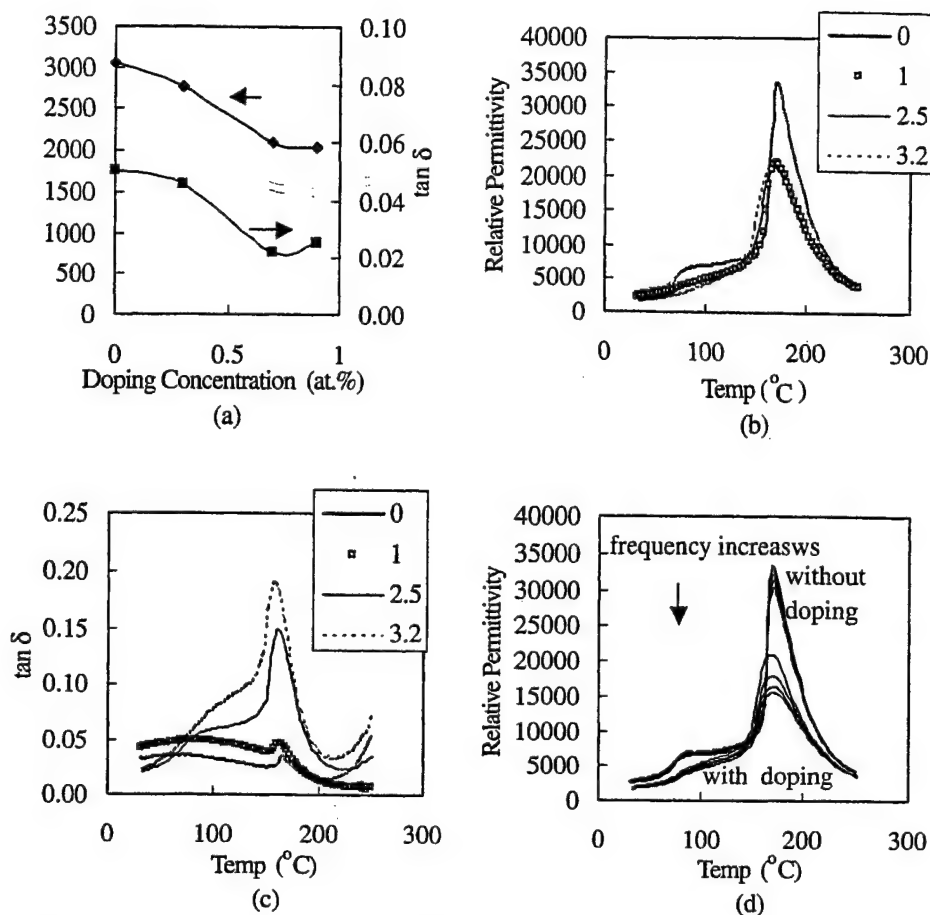
Fig. 6. (a) Relative permittivity and dielectric loss of $0.67Pb(Mg_{1/3}Nb_{2/3})O_3$–$0.33PbTiO_3$ + x at.% Mn doping at 100 Hz at room temperature. (b) Relative permittivity and (c) dielectric loss vs. temperature of 0.67PMN–0.33PT with x at.% Mn doping at 100 Hz. (d) Relative permittivity of PMN–PT (67/33) with 2.5 at.% Mn doping (lower curves) and without doping (upper curves) after poling, at frequencies of 100, 1 k, 10 k, and 100 kHz.

stant for these specimens are shown in Fig. 6(b). The temperature of the dielectric constant maximum, which is the effective phase-transition temperature, was nearly independent of the Mn concentration. However, the magnitude of the dielectric constant was significantly altered over a wide temperature range. In the temperature range below about 150°C, the dielectric constant was continuously decreased with increasing Mn concentration, as illustrated in Fig. 6(b). In the temperature range between about 150°C and T_{max}, the dielectric constant was increased by Mn modification. However, at temperatures above T_{max}, the dielectric constant was decreased by Mn modification. Furthermore, in this temperature range, the dielectric constant was strongly dependent upon small Mn concentrations (<1 at.%), but was nearly independent of further increments in concentration.

The changes in the Mn dependence of the dielectric constant with temperature might be explained by considering the influence of pinning upon the domain dynamics. In the lower temperature range (25–150°C), domains may be pinned by defects induced by Mn modification. Increasing Mn concentration then results in enhanced pinning effects, and thus a reduction in the magnitude of the dielectric constant. However, with increasing temperature, the thermal energy may be sufficient to cause a depinning of domains. Over a narrow temperature range near T_{max}, the enhancement of the dielectric

constant by Mn modification may occur due to the dynamics of domain depinning under thermal fluctuations. Stronger dielectric losses were also observed in this temperature range, as shown in Fig. 6(c). Enhanced dielectric absorption with increasing Mn concentration can be understood on the basis of the domain depinning effects.

The suppression of the dielectric constant near and above T_{max} by Mn modification, which was nearly independent of concentration for $x > 1$ at.%, may reflect the influence of defects/impurities on the residual nature of the diffuse phase transition in PMN–PT. Further evidence in support of this possibility can be seen in Fig. 6(d), which shows the temperature dependent dielectric data taken at various frequencies (100, 1 k, 10 k, 100 kHz) for undoped and Mn-modified specimens ($x = 2.5$ at.%). In the unmodified material, a slight frequency dependence was observed over only a narrow temperature range around T_{max}. However, upon Mn modification, much stronger frequency dispersion was induced. In PMN–PT materials, over a wide range of PT contents, a local polarization is known to persist until about 320°C.[20] The data in Fig. 6(d) indicate that Mn modification results in changes in the local polarization formation and the subsequent dynamics of the polarization fluctuations. However, Mn does not induce relaxant behavior in the lower temperature states. Rather, defect-domain interactions seem to occur which result

in domain pinning. Further evidence of domain pinning can be found in the strong field properties.

3.3   Strong field properties of Mn-modified PMN–PT
3.3.1   Polarization and strain behavior

The P–E behaviors are shown in Figs. 7(a)–7(d) for $x = 0$, 1, 2.5, and 3.2 at.% Mn, respectively. Correspondingly, the S–E behaviors are shown in Figs. 7(e)–7(h). With increasing Mn concentration, the saturation polarization and remanent polarizations are decreased, whereas the coercive field is increased. These results are consistent with the conjecture that Mn induces a degree of hardness into PMN–PT. In hard PZTs, domain pinning by dipolar defects internally biases the polarization. Poling, then, results in the development of a net dipolar field and an asymmetric hysteresis loop.[9,21] However, in the quenched state, random dipolar fields are believed to reduce the switchable polarization, as can also be observed in Fig. 7. Defect pinning enhances the squareness of the P–E curves, and at the same time also reduces the switchable polarization. Under low to moderate drive levels, reduced energy losses will be incurred under the cycling of an AC electrical field. However, if a threshold field is exceeded and domain depinning occurs, the amount of energy lost per cycle will increase dramatically.

The hardening of the P–E behavior with increasing Mn concentration also results in reduced electrically induced strains, as shown in Figs. 7(e)–7(h). In these figures,

it can be seen that the saturation strain decreases from ~0.3% to 0.2% with increasing Mn concentration between 0 and 3.2 at.%. In addition, the degree of hysteresis in the butterfly-like loops is also significantly increased, and similarly the value of the piezoelectric coefficient was reduced [see Figs. 7(a)–7(d)]. These results demonstrate that increasing "hardness" in PMN–PT ceramics results in decreased electromechanical performance. Higher mechanical quality factors and lower energy dissipations may be achieved under low to moderate drives with increasing Mn concentration; however, electromechanical performance is also degraded. Similar trade-offs exist in modified PZT ceramics between hard and soft varieties.

3.3.2   Amplitude-dependent electromechanical properties

For a longitudinal d_{31} mode in which both ends of the sample are mechanically free, the relationship between vibration velocity v and the driving field E_{d0} can be written as given in the following equation:

$$- At E_{d0} + Zv = 0 \tag{1}$$

and

$$v = \frac{At E_{d0}}{Z} = \frac{4}{\pi}\sqrt{\frac{\varepsilon_{33}^{T}}{\rho}} k_{31} Q E_{d0}, \tag{2}$$

where A is the force factor, t is the thickness, Z is the mechanical impedance at the end of the sample, ρ is the density, ε_{33}^{T} is the relative permittivity at constant stress, and k_{31} is the coupling factor. From the resonance frequency and the maximum displacement ξ_m at the ends of the specimen, the vibration velocity (v) can be estimated by the following equation:

$$v = \frac{1}{\sqrt{2}}\omega_{r}\xi_{m}. \tag{3}$$

Figure 8 shows the room-temperature impedance spectra for PMN–PT modified with 3.2 at.% Mn. Data are shown for various vibration velocities. This data was obtained using the constant current/displacement method, which is illustrated in Fig. 1.

The impedance spectra in Fig. 8 clearly demonstrate significant changes with increasing vibration velocity. The vibration velocity is linearly proportional to the AC electrical drive field. With increasing vibration velocity, the minimum in the impedance is shifted in frequency. The frequency of
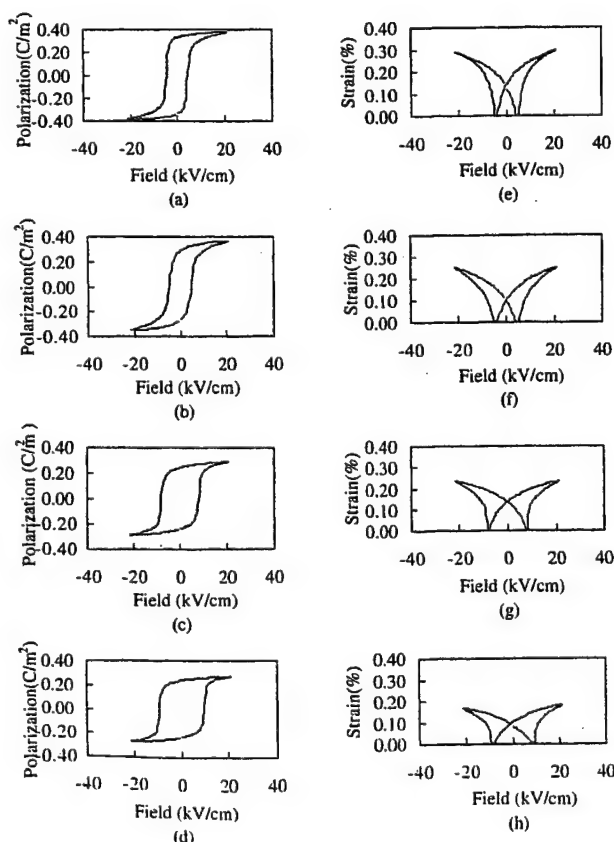

Fig. 7.   P–E hysteresis loop of 0.67Pb($Mg_{1/3}Nb_{2/3}$)O_3–0.33PbTiO$_3$ with (a) 0 at.% Mn (b) 1 at.% Mn (c) 2.5 at.% Mn (d) 3.2 at.% Mn and the strain vs. electrical field for (e) 0 at.% Mn (f) 1 at.% Mn (g) 2.5 at.% Mn (h) 3.2 at.% Mn.
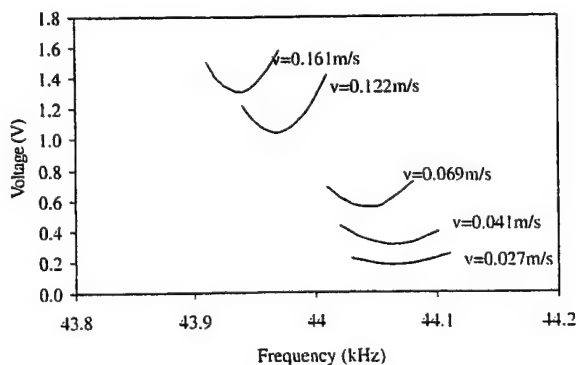

Fig. 8.   Impedance spectrum of 0.67Pb($Mg_{1/3}Nb_{2/3}$)O_3–0.33PbTiO$_3$+3.2 at. Mn with different vibration velocities x m/s at room temperature.

minimum impedance represents a characteristic frequency at which the amplitude displacement is most susceptible to small electrical drives. At low vibration velocities, the resonance frequency did not shift significantly with increasing velocity in the range of 0.027 to 0.041 m/s, although significant changes in impedance were observed. However, with increasing vibration velocity between 0.041 and 0.122 m/s, significant changes in both the frequency and impedance were observed. With further increments in the drive velocity, significant changes in frequency were observed, although the magnitude of the impedance was not changed significantly. Also, changes in the curvatures of the impedance spectra can be seen with increasing vibration velocity.

These results clearly indicate the presence of nonlinearities in the complex elastic response, which are stimulated under electrical drive. The shift in the characteristic frequency indicates the presence of higher order elastic constants. The shifting to lower frequencies is due to a softening of the elastic stiffness under excitation. The changes in the impedance magnitude reflect changes in the drive amplitude required to achieve a constant displacement. The decrease in the changes in impedance at higher drive levels indicates the occurrence of a positive third-order nonlinear damping. However, to be more accurate, it is necessary to calculate the dependence of the elastic constant and mechanical quality factor on the vibration velocity. To achieve this, we used eq. (4) to calculate the observed mechanical quality factor Q_m near the resonance frequency, where V_d is the driving voltage at a frequency f_1 and $f_2 = f_r^2/f_1$, V_{do} is the driving voltage at the resonance

frequency f_r, and k_p is then equal to $(V_d - V_{do})/V_{do}$:

$$Q_m = \frac{f_r}{f_2 - f_1}\sqrt{k_p(k_p + 2)}. \qquad (4)$$

Figure 9(b) shows the dependence of the resonance frequency on the vibration velocity. This data could have also been shown as a function of AC electrical drive, because the driving voltage is linearly proportional to the vibration velocity for low field and becomes nonlinear when the field becomes large, as shown in Fig. 9(a). From the data in Fig. 9(b), the corresponding data for the dependence of the elastic compliance was calculated, as shown in Fig. 9(c). In both figures, data are shown for specimens with various Mn concentrations. In these figures, the elastic stiffness (and the resonance frequency) can be seen to increase with increasing Mn concentration. Similar results were shown earlier, in §3.2. The data also reveals that the elastic stiffness decreases with increasing vibration velocity for all specimens investigated. However, the degree of elastic nonlinearity was decreased significantly with increasing Mn concentration.

Figure 9(d) shows the dependence of the mechanical quality factor on the vibration velocity for specimens with various Mn concentrations. For the base composition, the value of Q_m was low and decreased from ~75 to 35 with increasing vibration velocity between 0.04 and 0.1 m/s. In the vibration velocity range investigated, no threshold was found below which nonlinearity in Q_m did not occur. However, these trends were significantly altered by Mn modification. For Mn concentrations greater than or equal to 1 at.%, the value of Q_m was dramatically increased and a pronounced threshold
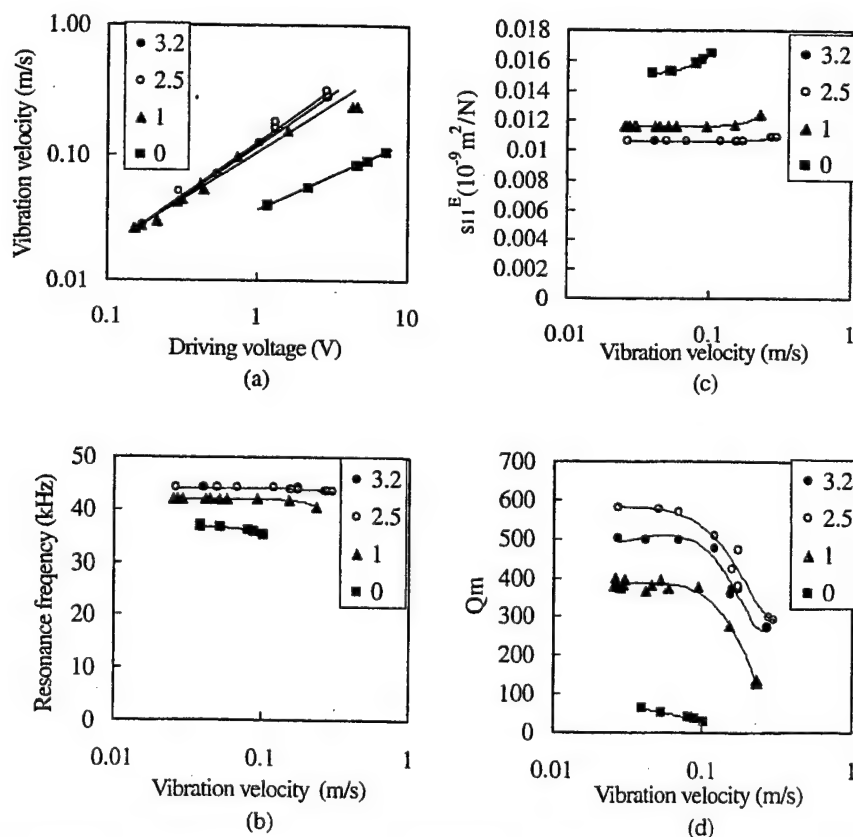

· Fig. 9.   (a) Vibration velocity vs. driving voltage; (b) resonance frequency, (c) compliance elastic constant, and (d) mechanical quality factor Q_m vs. vibration velocity of 0.67Pb(Mg$_{1/3}$Nb$_{2/3}$)O$_3$–0.33PbTiO$_3$ + x at.% Mn.

Jpn. J. Appl. Phys. Vol. 39 (2000) Pt. 1, No. 8

Y.-H. CHEN *et al.*   4851

in the vibration velocity was observed below which nonlinearity in Q_m was not found. This threshold velocity was equal to ~ 0.1 m/s, and was not observed to be dependent upon the Mn concentration for $1 < x < 3.2$ at.%. With increasing the vibration velocity above that of the threshold, the value of Q_m decreased rapidly, beginning to approach that of the base composition for higher drive levels. Also, the value of Q_m was different for the various Mn-modified compositions at a constant drive level, however the degree of change in Q_m with increasing the drive level was relatively constant.

We believe that the nonlinearities in Q_m and in the elastic stiffness can be best explained by considering the domain dynamics and domain pinning effects. As discussed in §3.2, mechanical damping is incurred due to domain wall vibrations. Nonlinearity in Q_m occurs when the domain wall dynamics are driven by external excitation. Consequently, the relaxed modulus (i.e., the elastic stiffness) is decreased, as less elastic energy can be stored within the specimen during the cycle of a field. In the base composition, domain pinning effects may not occur. Consequently, no threshold vibration velocity is observed. However, in Mn-modified materials, before domain dynamics can be excited, domain breakaway (depinning domains from defects) must be driven by the external field. Consequently, the mechanical quality factor would be high at low and moderate drive levels, but would decrease significantly as a critical field level is surpassed.

The data in Fig. 9 provide important information concerning the role of Mn in PMN–PT ceramics. The nonlinear complex elastic data provide the strongest support presented in this paper concerning the occurrence of domain pinning effects. This data also clearly underscores the limitations of these materials in applications requiring high-power density, high-Q materials. Our materials do have an improved combination of properties, i.e., a high Q_m and good electromechanical properties. However, the operational range over which these optimized properties can be realized is limited, as the hard characteristics induced in the PMN–PT are degraded with increasing drive amplitude. The degradation of Q_m with increasing drive amplitude will also result in heat generation and thermal stability problems, which will also limit the usage of the materials as high-power sources.

3.3.3 Heat generation and thermal stability considerations

Heat generation is one of the serious problems for materials under high-level drive conditions. The temperature rise, ΔT, resulting from heat generation and dissipation effects can be expressed as follows:

$$\Delta T = \frac{\omega_r W}{k(T)A}(1 - e^{-\frac{t}{\tau}}). \tag{5}$$

where W is the loss of energy of the sample per driving cycle, ω_r is the resonant angular frequency, A is the surface of the sample, $k(T)$ is defined as the overall heat-transfer coefficient, and the time constant τ is expressed as:

$$\tau = \frac{Mc}{k(T)A}, \tag{6}$$

where M is the mass of the sample, and c is the specific heat. As $t \to \infty$, the maximum temperature rise in the sample becomes

$$\Delta T = \frac{W\omega_r}{k(T)A} = \frac{W\omega_r}{Mc}\tau. \tag{7}$$

The dissipated-vibration-energy per second, $\omega_r W$, can then be calculated as follows:

$$\omega_r W = U\omega_r Q_m^{-1} = \frac{1}{2}Mv^2\omega_r Q_m^{-1} \tag{8}$$

$$U = \frac{1}{2}\kappa Y_0^E S_m^2 V \tag{9}$$

$$S_m = \frac{\pi\xi_m}{l} \tag{10}$$

$$Y_0^E = \frac{l^2}{\pi^2}\rho\omega_r^2, \tag{11}$$

where U, v, S_m, l, V, ρ, and κ are the stored mechanical energy, the vibration velocity, the maximum strain, the vibrator length, the volume, the density and the shape factor, respectively. The shape factor depends on the vibrator shape and the vibration mode.

Figure 10 shows the the saturation temperature rise induced by the mechanical damping as a function of the vibration velocity. The saturation temperature was determined by balancing the heat generated by the mechanical dissipation process and that heat radiated after a period of time while the sample was being driven under particular vibrational velocities. From eqs. (7) and (8), it can be seen that the temperature rise is proportional to the square of the vibrational velocity and inversely proportional to the mechanical quality factor. Because the mechanical quality factor Q_m dropped significantly for vibrational velocities greater than 0.2 m/s, the temperature rise increased rapidly, as shown in Fig. 10. For a vibrational velocity of 0.2 m/s, the temperature rise was equal to approximately 20°C for all Mn-modified specimens. This is large, but is a significant improvement over that for the base PMN–PT composition, which will induce similar temperature rises at significantly lower vibrational velocities.

Considering that the dielectric loss factor increases with increasing temperature [see Fig. 5(c)], the temperature rise induced by higher vibrational velocities shown in Fig. 10 presents a serious problem for thermal stability conditions. For example, assuming a vibrational velocity of 0.2 m/s, a temperature rise of 20°C is encumbered. This temperature rise results in an increase in the dielectric loss factor, and consequently the mechanical quality factor. In turn, this will increase the temperature rise, according to eq. (8), resulting in yet higher loss factors and lower quality factors. For applications such as high-power transducers, this presents a serious heat flux/dissipation problem.

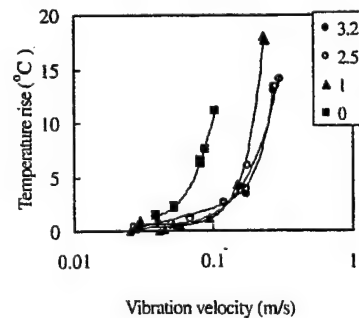Our results are important in that they show significantly

Fig. 10.   Temperature rise vs. vibration velocity of $0.67\text{Pb}(\text{Mg}_{1/3}\text{Nb}_{2/3})\text{O}_3$–$0.33\text{PbTiO}_3 + x$ at.% Mn.

improved mechanical quality factors in PMN–PT ceramics which are induced by Mn modification. Under high excitation levels, the mechanical quality factor is seriously degraded. Mn-modified PMN–PT ceramics have promise for improved performance under moderate drive conditions as high-performance transducers and actuators. However, the mechanical quality factor and the nonlinearities induced by increasing the vibrational velocity are still inferior to those found in commercially available hard PZT materials, but the modified PMN–PT compositions developed in this investigation have superior electromechanical properties.

4. Summary

In this paper, investigations of the influence of Mn and Fe substituents on the electromechanical properties of PMN–PT were performed. These substituents have conventionally been used to make PZT electrically harder. The purpose of the work was to develop high-performance PMN–PT ceramics with significantly improved mechanical quality factors for higher power transducer applications. Our results show that Fe substituents do not significantly affect the properties of PMN–PT, as commonly occurs in PZT. However, Mn substituents significantly improve the mechanical quality factor, although its piezoelectric constant is partially compromised in relation to the base composition. Investigations of the vibrational amplitude dependence of the mechanical factor revealed a serious decrease with increasing the displacement magnitude. Mn-modified PMN–PT has significant promise for high-power applications. However, it will be necessary not to exceed a critical operational power level in order to reduce the total losses and subsequent heat generation.

Acknowledgements

1) H. Beige and G. Schmidt: Ferroelectrics **41** (1982) 39.
2) G. Sorge, H. Beige and C. Scheiding: Ferroelectrics **41** (1982) 51.
3) V. Mueller and Q. M. Zhang: J. Appl. Phys. **83** (1998) 3754.
4) S. Takahashi, S. Hirose and K. Uchino: J. Am. Ceram. Soc. **77** (1994) 2429.
5) S. Tashiro, M. Ikehiro and H. Igarashi: Jpn. J. Appl. Phys. **36** (1997) 3004.
6) A. Nowick and B. Berry: *Anelastic Relaxations in Crystalline Solids* (Academic Press, New York, 1972).
7) D. Damjanovic, Ph. D. Dissertation, The Pennsylvania State University, University Park, PA, USA (1987).
8) A. Aning, T. Suzuki and M. Wuttig: J. Phys. Chem. Solids **45** (1984) 481.
9) Tan Qi, Ph. D. Dissertation, University of Illinois, Urbana, IL, USA (1998).
10) W. Pan, W. Gu, D. Taylor and L. E. Cross: Jpn. J. Appl. Phys. **28** (1989) 653.
11) L. E. Cross: Ferroelectrics **76** (1987) 241.
12) G. Schmidt: Phase Transitions **20** (1990) 127.
13) N. C. Kim, Ph. D. Dissertation, The Pennsylvania State University, University Park, PA, USA (1992).
14) W. Huebner, S. Jany, T. R. Shrout and N. Kim: Ferroelectrics **93** (1989) 341.
15) M. Lejeune and J. P. Boilot: Mater. Res. Bull. **20** (1985) 493.
16) S. Swartz and T. Shrout: Mater. Res. Bull. **17** (1982) 1245.
17) D. Viehland, M. Wuttig and L. E. Cross: J. Appl. Phys. **69** (1991) 6595.
18) M. J. Haun, Ph. D. Dissertation, The Pennsylvania State University, University Park, PA, USA (1987).
19) M. Wuttig and C. Lin: Acta Metall. **31** (1983) 1117.
20) G. Burns and F. Dacol: Sol. State Commun. **58** (1980) 567.
21) A. P. Levanyuk and A. S. Sigov: *Defects and Structural Phase Transitions* (Gordon and Breach, New York, 1988) p. 24.

APPENDIX 53

Eu and Yb Substituent Effects on the Properties of $Pb(Zr_{0.52}Ti_{0.48})O_3$–$Pb(Mn_{1/3}Sb_{2/3})O_3$ Ceramics: Development of a New High-Power Piezoelectric with Enhanced Vibrational Velocity

Yongkang GAO, Yun-Han CHEN, Jungho RYU, Kenji UCHINO and Dwight VIEHLAND[1]

International Center for Actuators and Transducers, Materials Research Laboratory, The Pennsylvania State University, University Park, PA 16802, USA
[1]*Naval Seasystems Command, Newport, RI 02841, USA*

Improved piezoelectric materials with higher vibrational velocities are needed to meet the demands of advanced high power electromechanical applications. In this paper, the effects of Eu and Yb substituents on the vibrational velocity and the piezoelectric properties of $Pb(Zr, Ti)O_3$–$Pb(Mn, Sb)O_3$ ceramics will be reported. Both of these substituents resulted in a significant increase in the mechanical quality factor Q_m, a decrease in the dielectric constant, and improvements in the electromechanical properties. Root mean square value (rms value) of vibration velocity as high as 1.0 m/s under an electric field of 10 kV/m (rms value) has been found for Yb-substituted specimens, which is 1.7 times higher than that of $Pb(Zr, Ti)O_3$–$Pb(Mn, Sb)O_3$ ceramics and 3 times higher than that of the commercialized hard $Pb(Zr, Ti)O_3$ ceramics.

KEYWORDS: high power, piezoelectric, maximum vibration velocity, doping, $Pb(Zr, Ti)O_3$–$Pb(Mn, Sb)O_3$, rare earth metals.

1. Introduction

The high-power characteristics of piezoelectric materials have recently been investigated for device applications in ultrasonic motors, piezoelectric actuators and piezoelectric transformers.[1,2] To achieve the requirements of these high-power applications, higher vibrational levels and velocities (v_0) at lower AC electric fields are required. Currently, the practical upper-limit of vibrational velocity is restricted by heat generation, as above a certain vibrational level increasing hysteretic effects result in thermal instability. Consequently, approaches to enhance the maximum vibration velocity are an important issue, which to date has proven difficult to achieve. However, it is known that the dissipation of vibrational energy is due to internal friction effects associated with domain dynamics and/or nucleation. Accordingly, heat generation under drive can be represented as a function of vibration velocity and other material constants.

The vibrational velocity v_0 is proportional to the product of the mechanical quality factor Q_m and the electromechanical coupling factor k, for example, $v_0 \propto Q_m k_{31}$ for a rectangular plate working under d_{31} mode.[3-5] Consequently, for high-power applications, a piezoelectric material is needed which has simultaneously both high Q_m and k_{31} values. Previous investigations of $Pb(Zr, Ti)O_3$ (PZT) have reported that v_0 is increased by lower valent substituents (for example, Fe on the B-site), whereas it is decreased by higher valent ones (for example, Nb on the B-site).[6] However, practically, the development of a material with significantly higher values of v_0 has been in vain, as previous investigations have shown that either Q_m or k_{31} can be enhanced only at the expense of the other. Generally, substituents can be categorized into three classifications:[7-9] lower valent (effective acceptors), higher valent (effective donors), and isovalent. substituents with lower valence introduce "hard" piezoelectric characteristics, while higher valent substituent induce "soft" ones. "Hard" piezoelectrics have higher Q_m values, but lower k_{31} values. On the other hand, "soft" piezoelectrics have lower Q_m values, but higher k_{31} values.

Interestingly, Cr^{+3} and U^{+3} substituents have previously been reported to induce some attributes of "hard" and "soft" piezoelectric characteristics.[10] However, further investigations have not been reported. Investigations of rare-earth (RE) substituents on piezoelectric properties have in general not been reported. Although, Hagimura *et al.* have reported that RE elements smaller than 0.938 Å increase the coercive field (E_c) and field-induced strain (ε) of PZT ceramics.[11] No reports have been published concerning the effects of rare earth species on the piezoelectric vibration velocity.

Pseudo-ternary crystalline solutions of $Pb(Zr, Ti)O_3$–$Pb(Mn, Sb)O_3$ have been reported to have significantly higher electromechanical coupling factors, higher mechanical quality factors and higher maximum vibration velocities than PZT.[12,13] In this system, a maximum vibration velocity (defined by an rms value which raises the temperature to 20°C above room temperature) of 0.6 m/s has been found.

The work presented in this paper focuses on optimizing the vibration velocity of $Pb(Zr, Ti)O_3$–$Pb(Mn, Sb)O_3$. The RE^{+3} species Eu^{+3} and Yb^{+3} were chosen for as substituents. The ionic radii of Eu^{3+} and Yb^{3+} are smaller than that of Pb^{2+}, but bigger than any of the various B-site species. Thus, no preferred site-occupancy for Eu^{3+} and Yb^{3+} would seemingly exist, rather substitution on both site might be expected. The results demonstrate a new promising material for high power application with a maximum vibration velocity of 1.0 m/s.

2. Experimental

We have chosen a base composition of $0.90Pb(Zr_{0.52}Ti_{0.48})O_3$–$0.10Pb(Mn_{1/3}Sb_{2/3})O_3$, following a previous publication.[13] The following RE^{3+} modified compositions were synthesized by conventional mixed oxide processing: (i) $0.90Pb(Zr_{0.52}Ti_{0.48})O_3$–$0.10Pb(Mn_{1/3}Sb_{2/3})O_3$–$x$ at.% Eu ($x = 0, 2, 4, 6$), and (ii) $0.90Pb(Zr_{0.52}Ti_{0.48})O_3$–$0.10Pb(Mn_{1/3}Sb_{2/3})O_3$–$y$ at.% Yb ($y = 0, 2, 4, 6$). The sintered samples were cut into rectangular plates of dimensions 42 mm × 7 mm × 1 mm. Gold sputtering was used to deposit electrodes on both surfaces. Then, the specimens were poled under 2.5 kV/mm for 15 min at 130°C in silicon oil. All electrical measurements were
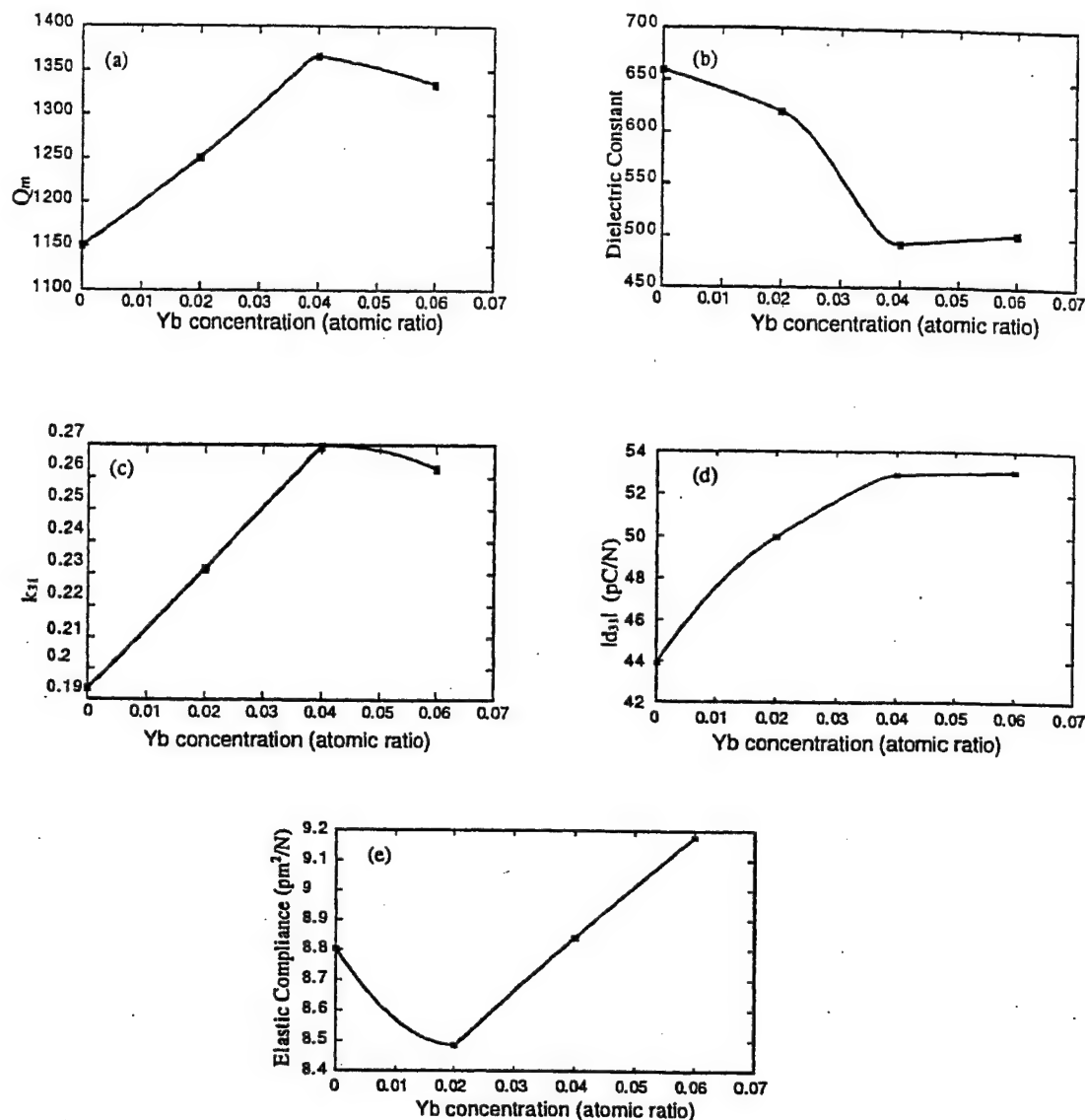
Fig. 4. (a) Mechanical quality factor Q_m (b) Dielectric constant K (c) Coupling factor k_{31} (d) Piezoelectric constant d_{31} (e) Elastic compliance of 0.90PZT–0.10PMS with 0, 2, 4, 6 at.% Yb.

concentration. It was found that T_c dropped a little with Eu or Yb doping, and T_c value decreased from 290°C to about 260°C and 250°C, respectively. This insignificant Curie temperature drop implies that the increase in k_{31} could be mainly contributed by Eu or Yb doping.

Another intriguing behavior of Eu and Yb doping is shown in Figs. 3(e) and 4(e). With 2 at.% Eu and Yb doping, the elastic compliance of the $Pb(Zr, Ti)O_3–Pb(Mn, Sb)O_3$ ceramics has been decreased first, i.e., the elastic constant stiffened, then, it went up to $8.8 \times 10^{-12} \, m^2/N$ and $9.2 \times 10^{-12} \, m^2/N$, respectively, with further increasing doping concentration.

In general, substituents that increase the piezoelectric constant and electromechanical coupling coefficient are said to induce "soft" piezoelectric characteristics.[7-9] Accordingly, the increase of d_{31} and k_{31} upon Eu and Yb substitution indicate that these species induce some degree of "soft" piezoelectric characteristics. Comparisons of the results in Figs. 3 and 4 indicate an unique effect of RE^{3+} substituents in PZT–PMS, as both Eu^{+3} and Yb^{+3} introduce combinatory "hard" and "soft" piezoelectric characteristics.
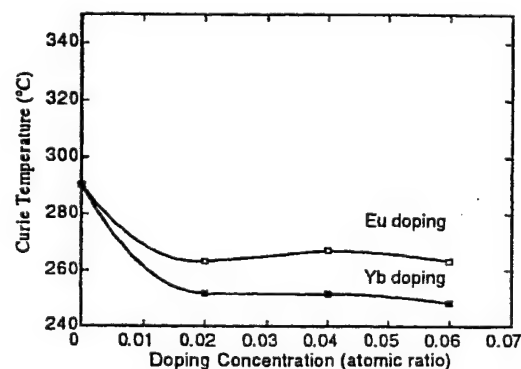

Fig. 5. Curie Temperature of $0.90Pb(Zr_{0.52}Ti_{0.48})O_3–0.10Pb(Mn_{1/3}Sb_{2/3})O_3$ with x at.% Eu ($x = 0, 2, 4, 6$), y at.% Yb ($y = 0, 2, 4, 6$).

Combinatory attributes of "hard" and "soft" piezoelectric characteristics have previously been reported in Cr^{+3} and U^{+3} substituted PZT.[10] Furthermore, recent investigations of $PZT–Pb(Mg_{1/3}Nb_{2/3})O_3$ have shown that Cr^{+3} also intro-

duces combinatory characteristics "hard" and "soft" piezo-electric characteristics.[16]

Here, one possible explanation to understand these particular characteristics is proposed as following. "Hard" piezoelectric characteristics are believed to be due to pinning of domains by dipolar fields of defect complexes.[15,17,18] Fine "wavy" domains have previously been reported in these types of materials.[17] Accordingly, polarization pinning is found in polarization–electric Field (P–E) curves. Defect complexes form because of enhanced transport due to charge compensation by oxygen vacancies.[15,17,18] Oxygen sites are relatively large and interconnected. Thus, defect species can remain relatively mobile until temperatures below the ferroelectric phase transformation T_c. Accordingly, it is believed that point defects diffuse to domain boundaries and form extended defect structures that have dipolar fields that pin the polarization. "Soft" piezoelectric characteristics are believed to be due to defects of the random-field type,[15,17,18] as originally proposed by Imry and Ma.[19] These defects are quenched-in as randomly-distributed point defects from temperatures significantly above T_c. Accordingly, the long-range polar interactions are disturbed, and the defect-free regions are relatively small. Recent investigations have shown that under electric field polarization irregularities are excited inside of the domain in the vicinity of quenched random-fields,[20] producing the "soft" characteristics.[21]

The results in this section demonstrate that RE^{3+} species play a unique role inducing combinatory "hard" and "soft" piezoelectric properties. Combinatory "hard" and "soft" characteristics would require that defects are non-randomly distributed as extended structures (i.e., "hard") and at the same time exist as randomly quenched-in point defects (i.e., "soft"). These are contradictory situations, which at least in simple systems can not be simultaneously satisfied.

Only in the presence of a multi-substitution (Eu^{3+} or Yb^{3+}) with Mn and Sb was combinatory "hard" and "soft" characteristics found. We believe that multi-substitution is necessary in order to induce combinatory characteristics. Also, we believe that the RE^{3+} species must be of the correct intermediate ionic size to occupy both A- and B-site positions, without preference. In this case, more complicated extended defect structures would be possible, due to the number of species that can be involved and the positions they can occupy. Then, small concentrations of Eu^{3+} or Yb^{3+} residing on the B-sites could significantly enhance the defect dipole moments, resulting in a more highly pinned polarization and reduced domain boundary losses. At the same time, small concentrations of the RE species could reside on the A-sites, resulting in quenched random fields in the vicinity of point defects that subsequently create polarization irregularities within the domain regions between regions of defect complexes, resulting in enhanced d_{31} and k_{31} values.

Accordingly, Q_m at moderate drive levels for $E < E_c$ would be higher due to lower domain boundary contributions, whereas d_{31} and k_{31} would also be higher because of the excitations of structural irregularities in the vicinity of quenched random fields. Recent investigations of oriented single crystals of PMN–PT have revealed a previously unrealized type of polarization mechanism where large changes in strain can occur with low hysteretic losses.[22,23] Investigations by Viehland[24] and by Egami et al.[25] have indicated an inho-

mogenous polarization process in the presence of quenched random-fields where polarization "rotation" occurs by mesoscale structures with hierarchial symmetries. To achieve optimum performance in a polycrystalline material (i.e., higher d_{31} and Q_m), domain boundaries must be strongly pinned to prevent boundary mobility under moderate drives ($E < E_c$). In addition, a relatively high concentration of quenched random fields is needed in order to enhance structural irregularities within the domains allowing for ease of polarization "rotation".

The results of this section demonstrate the importance of defect engineering of domain stability. However, to more precisely identify the structure of the defect complexes responsible for property optimizations, local structural and chemical probes are necessary.

3.3 High field properties

For a longitudinal sample, driven under the d_{31} mode, with both ends mechanically free, the relationship between the vibrational velocity v_0 and the effective driving field (i.e., the rms value) E_{d0} can be written as given in eq. (2):

$$-At E_{d0} + Z v_0 = 0 \tag{2}$$

where A is the force factor, t is the thickness, and Z is the mechanical impedance. Thus, v_0 can be represented as a function of E_{d0} as given in eq. (3):

$$v_0 = \frac{At}{Z} E_{d0} = \frac{4}{\pi} \sqrt{\frac{\varepsilon_{33}^T}{\rho}} \frac{k_{31}}{Q_m^{-1}} E_{d0} \tag{3}$$

where ρ is the density, and ε_{33}^T is the permittivity.

From eq. (3), it can be seen that v_0 is proportional to the product $E_{d0} k_{31} Q_m$. Accordingly, to have the highest vibration velocity possible, it is essential to have a combination of both high Q_m and high k_{31}. However, to achieve simultaneous high values of Q_m and k_{31} is against conventional concepts of "hard" and "soft" piezoelectric characteristics. But, the results in the previous section demonstrate the existence of such combinatory characteristics in RE^{3+} modified PZT–PMS. Consequently, the high field properties of these materials were investigated.

Figures 6 and 7 show v_0 as a function of the electric field (E_{ac}, rms value) of $Pb(Zr, Ti)O_3$–$Pb(Mn, Sb)O_3$ for various Eu and Yb concentrations, respectively. Data are shown in both figures for $x = 0, 2, 4$, and 6 at.%. Under relatively low driving fields ($<10^4$ V/m), v_0 was nearly proportional to E_{ac}. With increasing E_{ac}, saturation in the value of v_0 started to become evident. This saturation was due to a decrease in Q_m with increasing E_{ac} above a critical vibrational level, as well as heat generation. At $E = 1.0 \times 10^4$ V/m (rms value), v_0 was found to be as high as 1.0 m/s (rms value) for a specimen with 2 at.% Yb. This was the highest value observed during this investigation. At higher Yb concentrations, v_0 decreased slightly but remained significantly higher than that of the base PZT–PMS ceramic which had a value of 0.62 m/s (rms value) at the same drive level. Strong enhancements in v_0 were also observed upon Eu substituion. In this case, a maximum v_0 of 0.92 m/s was found at $x = 4$ at.% and $E = 1.0 \times 10^4$ V/m (rms value). Again, at higher substituent concentration, v_0 decreased.

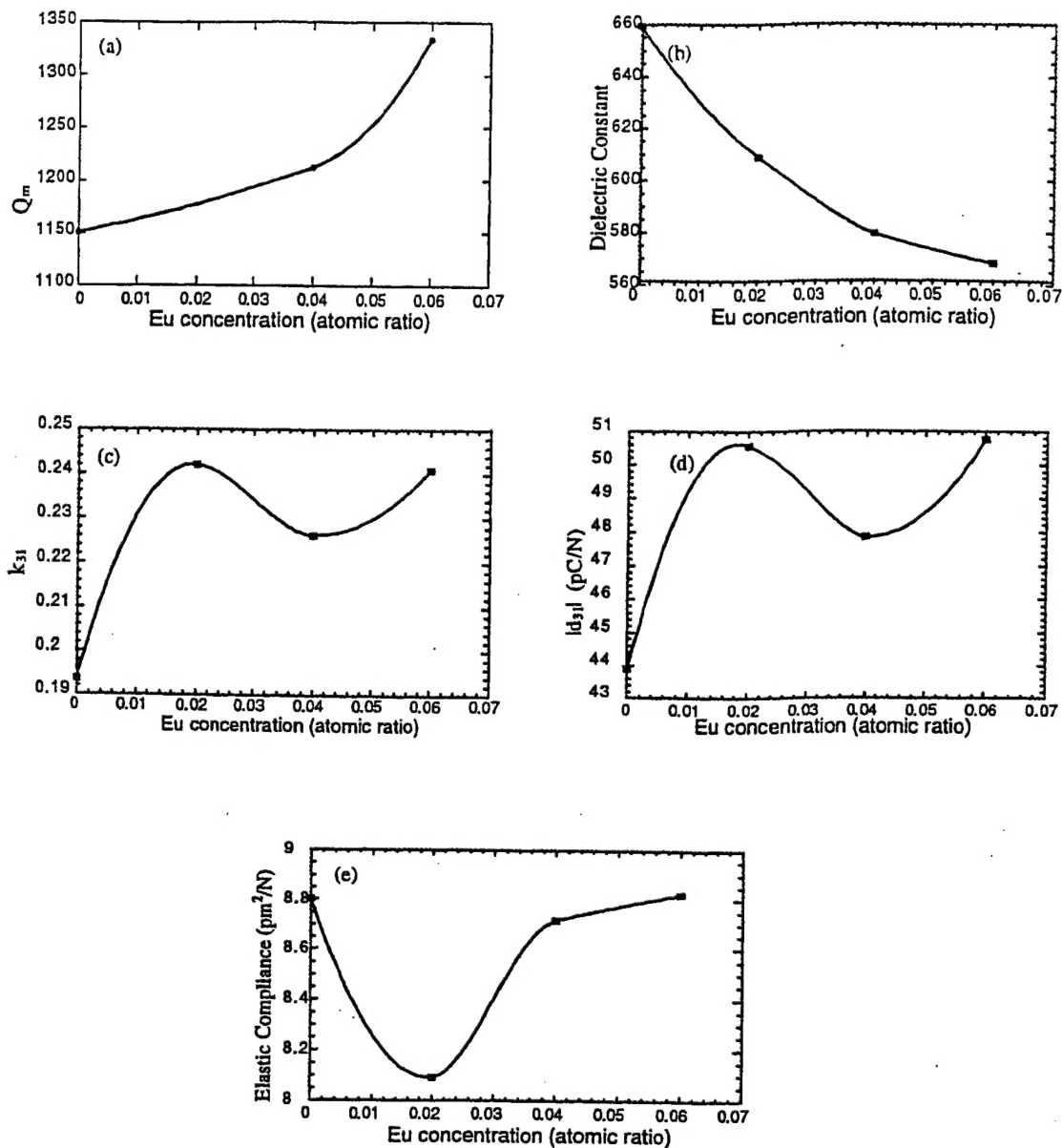Above a certain vibrational level, the increase in tempera-

Fig. 3. (a) Mechanical quality factor Q_m (b) Dielectric constant K (c) Coupling factor k_{31} (d) Piezoelectric constant d_{31} (e) Elastic compliance of 0.90PZT–0.10PMS with 0, 2, 4, 6 at.% Eu.

to influences on ferroelectric and piezoelectric responses.

3.2 Low field behavior

Figures 3(a) and 4(a) show Q_m as a function of x (atomic ratio) for Eu and Yb substituents, respectively. Both Eu and Yb substituents increased Q_m significantly, from ~1150 to ~1350 with increasing x. However, with increasing Yb concentration, Q_m exhibited a maximum near $x = 0.04$ and then decreased slightly upon further increment of x, whereas with increasing Eu concentration Q_m increased continuously over the range investigated. Figures 3(b) and 4(b) show the dielectric constant as a function of x (atomic ratio) for Eu and Yb subsituents in PZT–PMS, respectively. A significant decrease in the dielectric constant K was observed with either increasing Eu or Yb concentrations.

Previous investigations have demonstrated that PZT–PMS has "hard" piezoelectric characteristics.[12,13] The data presented in Figs. 3(a), 3(b) and Figs. 4(a), 4(b) demonstrates that Eu or Yb substituents increase the degree of "hard" characteristics, as mechanical quality factor was increased and dielectric constant was decreased. "Hardening" of piezoelectric behavior is believed due to the interaction between domain wall and acceptor impurity-oxygen vacancy dipoles.[15] Accordingly, an internal bias field would pin ferroelectric domains, decreasing their contribution to the total permittivity and loss factors.

Figures 3(c) and 4(c) show k_{31} as a function of Eu and Yb concentrations, respectively. Upon increment of the Eu (or Yb) concentration between 0 and 4 at.%, k_{31} increased by 17% (or 39%), respectively. Correspondingly, Figs. 3(d) and 4(d) show that the absolute value of d_{31} increased with Eu or Yb concentrations, respectively. The absolute value of d_{31} increased from 44 pC/N to 51 pC/N upon Eu substitution and from 44 to 53 pC/N upon Yb substitution. This result implies that Eu and Yb doping has "softening" side. Figure 5 shows the Curie temperature (T_c) as a function of Eu or Yb doping

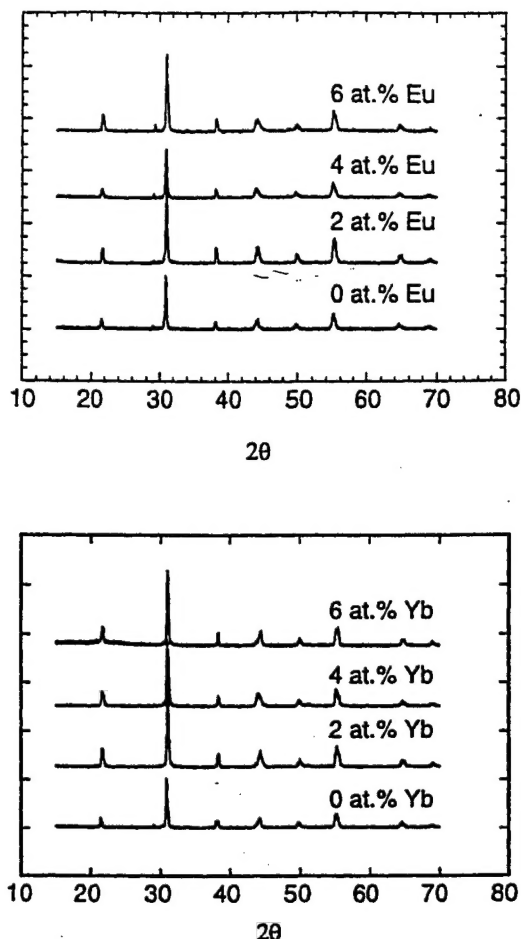Fig. 1. X-ray diffraction patterns of $0.90Pb(Zr_{0.52}Ti_{0.48})O_3$–$0.10Pb(Mn_{1/3}Sb_{2/3})O_3$ with x at.% Eu ($x = 0, 2, 4, 6$), y at.% Yb ($y = 0, 2, 4, 6$).

Table I. The ionic radii of the constituent elements in $Pb(Zr, Ti)O_3$–$Pb(Mn, Sb)O_3$–Eu/Yb systems.

Constituent ion	Ionic size/Å
Eu^{3+}	0.947
Yb^{3+}	0.858
Pb^{2+}	1.19
Zr^{4+}	0.72
Ti^{4+}	0.605
Sb^{5+}	0.76
Mn^{2+}	0.46
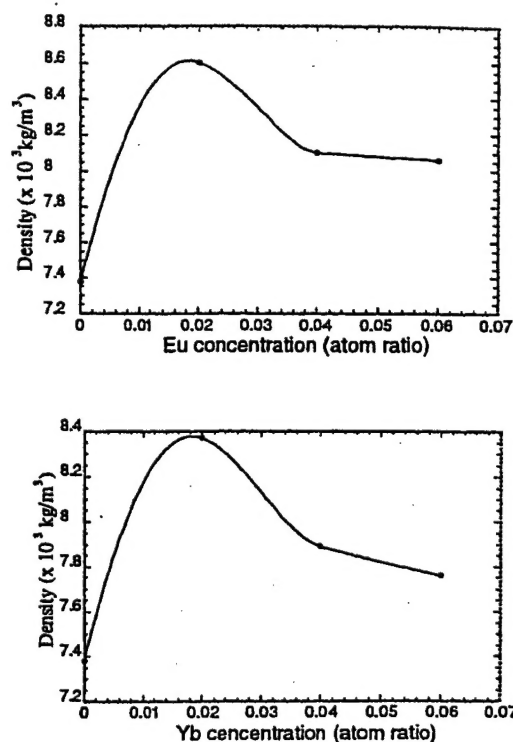
Fig. 2. Densities of $0.90Pb(Zr_{0.52}Ti_{0.48})O_3$–$0.10Pb(Mn_{1/3}Sb_{2/3})O_3$ with x at.% Eu ($x = 0, 2, 4, 6$), y at.% Yb ($y = 0, 2, 4, 6$).

carried out about 36 h after poling.

The electromechanical properties were determined by two methods: (i) by impedance spectra under a low-level constant-voltage drive using a HP4194 impedance analyzer, and (ii) by impedance spectra under various vibration velocities using a constant current drive method.[4] The vibration velocity v_0 was measured using laser doppler vibrometer (LDV) models OFV-3001 and OFV-511 (Polytec PI). The vibration level was the rms value of vibration velocity v_0, which is independent of the sample size. The value of v_0 can be calculated by the relationship given in eq. (1):

$$v_0 = \frac{1}{\sqrt{2}}\omega_0 \xi_m, \tag{1}$$

where ξ_m and ω_0 are the maximum vibration amplitude and angular resonance frequency, respectively. Temperature rise was determined by a thermocouple, which was put at the center of the vibrating sample (i.e., the nodal point).

3. Results and Discussion

3.1 Crystallographic and microstructure studies

Pb(Mn, Sb)O_3 does not exist as a stable single phase. However, Pb(Zr, Ti)O_3–Pb(Mn, Sb)O_3 (PZT–PMS) ceramics have a single phase structure. Figures 1(a) and 1(b) show X-ray diffraction patterns for specimens with 0, 2, 4, 6 at.% Eu, and 0, 2, 4, 6 at.% Yb, respectively. Within experimental limits

of determination, all samples studied were single phase perovskite. Table I[14] gives the ionic radii of the various constituents in the modified PZT–PMS compositions. In this table, Eu^{3+} and Yb^{3+} can be seen to be intermediate in size between Pb (A-site) and the various B-site cations.

Grain sizes were determined for Eu or Yb modified specimens by scanning electron microscopy (SEM). The grain size of the pure Pb(Zr, Ti)O_3–Pb(Mn, Sb)O_3 was ~3 μm. Upon Eu modification, the grain size increased only slightly. Upon Yb modification, the grain size decreased slightly to 2.3 μm. From the SEM micrographs, it was also clear that the degree of sintering was significantly improved upon Eu or Yb modification. Figures 2(a) and 2(b) show the density of PZT–PMS as a function of Eu or Yb concentrations, respectively. The density of samples increased with doping of Eu and Yb up to 2 at.% but decreased with further doping.

These results eliminate perovskite phase stability and grain sizes as sources of potential difference in property values between specimens. Rather, property variations with either increasing Eu and Yb doping concentrations must be attributed
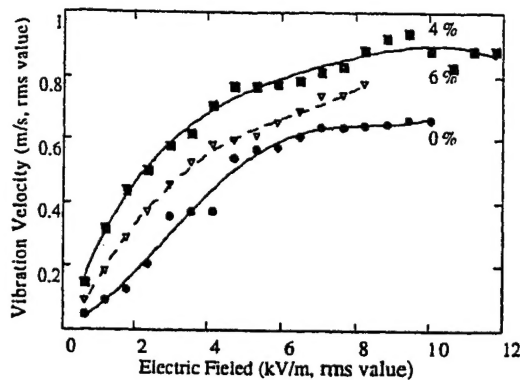
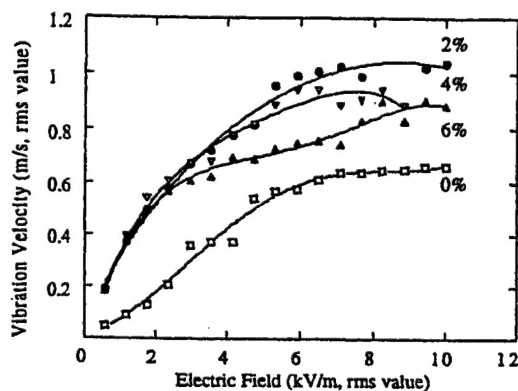Fig. 6. Vibration velocity (rms value) vs electric field (rms value) for PZT–PMS–Eu.

Fig. 8. Temperature rise vs vibration velocity (rms value) for PZT–PMS–Eu.

Fig. 7. Vibration velocity (rms value) vs electric field (rms value) for PZT–PMS–Yb.

Fig. 9. Temperature rise vs vibration velocity (rms value) for PZT–PMS–Yb.

Fig. 10. The maximum vibration velocity of PZT–PMS–Yb and PZT–PMS–Eu vs doping concentration.

ture (ΔT) under electrical drive is significant, as a partial depoling begins to occur under reverse bias with increasing E_{ac}. This restricts the practical upper limit for v_0. The desired performance characteristics for a high-power device application is a high v_0 and a low heat generation (ΔT). This is because the operational conditions to reach higher v_0 values must be restricted in order to maintain thermal stability. This is a difficult task, as ΔT is known to be proportional to v_0^2. From a practical perspective, the maximum vibrational velocity can be defined as the v_0 which produces a $\Delta T = 20°C$.

Figures 8 and 9 show the temperature rise as a function of v_0 for Eu and Yb substitued PZT–PMS, respectively. Data are shown in each figure for $x = 0$, 2, 4, and 6 at.%. The maximum vibrational velocity, v_0 ($\Delta T = 20°C$), for PZT–PMS was found to be ~0.6 m/s, which is close to that reported by Takahashi.[13] Upon Eu-substitution, values of v_0 ($\Delta T = 20°C$) as high as 0.9 m/s were found at $x = 4$ at.%. Yb substitution was found to result in even higher values of v_0 ($\Delta T = 20°C$). In this case, for $x = 2$ at.%, v_0 ($\Delta T = 20°C$) was found to be as high as 1.0 m/s, which is by far the highest value of v_0 ever reported for PZT based ceramics.

Figure 10 summarizes the results of v_0 ($\Delta T = 20°C$) for all Yb, Eu modified PZT–PMS as a function of x. From this figure, significant enhancements in v_0 ($\Delta T = 20°C$) can be seen upon substitution with either element. With 2 at.% Yb doping, the rms vibration velocity has been increased from 0.60 m/s ($x = 0$ at.%) to 1.0 m/s. It is also clear that Yb produces the highest values and at significantly lower concentrations. At higher concentrations, v_0 ($\Delta T = 20°C$) decreased

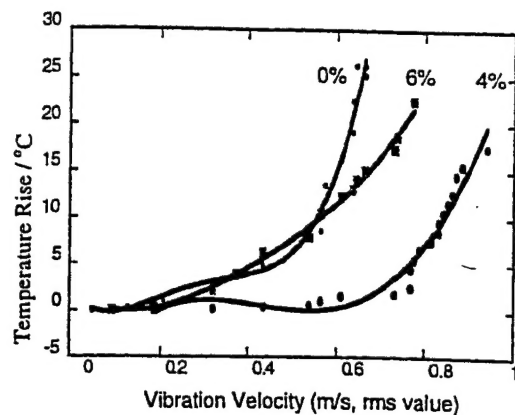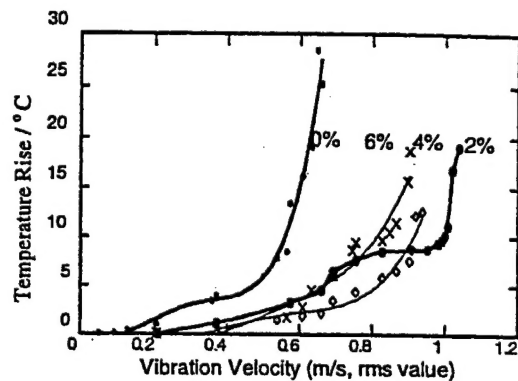for both Yb, and Eu substituted materials. With 6 at.% Eu or Yb doping, the vibration velocity at $\Delta T = 20°C$ has been dropped to 0.77 m/s and 0.88 m/s, respectively.

4. Summary

The effects of Eu and Yb substitutents on the piezoelectric properties of $Pb(Zr, Ti)O_3$–$Pb(Mn, Sb)O_3$ ceramics have been investigated. The following findings can be stated.
1) Combinatory "hard" and "soft" characteristics are found upon Eu and Yb substitution in PZT–PMS. Eu or Yb result in significant increases in Q_m, d_{31}, and k_{31}.

2) Under high drive level conditions, v_0 has been significantly increased by Eu or Yb substitution, relative to that of the base PZT–PMS ceramic.

3) PZT–PMS modified with 2 at.% Yb has been identified as a new high-power material. It has a v_0 ($\Delta T = 20°C$) as high as 1.0 m/s (rms value) under an electric field of 10 kV/m (rms value). This new material can provide one order of magnitude higher power than conventional PZT ceramics driven under high power conditions where v_0 ($\Delta T = 20°C$) is equal to 0.3 m/s.

Acknowledgement

1) K. Uchino: *Piezoelectric Actuators and Ultrasonic Motors* (Kluwer Academic Publishers, Norwell, 1996).
2) K. Uchino: *Ferroelectric Devices* (Marcel Dekker, New York, 2000).
3) K. Uchino, H. Negishi and T. Hirose: Proc. Int. Conf. FMA-7, Jpn. J. Appl. Phys. 28 (1989) Suppl. 28-2, p. 47.
4) K. Uchino, J. Zheng, A. Joshi, Y. H. Chen, S. Yoshikawa, S. Hirose, S. Takahashi and J. W. C. DE Vries: J. Electroceram. 2 (1998) 33.
5) Y. H. Chen, S. Hirose and K. Uchino: Jpn. J. Appl. Phys. 39 (2000) 4843.
6) S. Takahashi and S. Hirose: Jpn. J. Appl. Phys. 31 (1992) 2422.
7) D. Berlincourt and H. Krueger: J. Underwater Acoust. 15 (1965) 266.
8) D. Berlincourt and H. Jaffee: *Physical Acoustics*, ed. W. Cady (Academic Press, New York, 1964) vol. 1.
9) B. Jaffe, W. Cook and H. Jaffe: *Piezoelectric Ceramics* (Academic Press, London and New York, 1971).
10) L. Wu, C. C. Lee, T. S. Wu and C. C. Wei: Ferroelectrics 41 (1982) 157.
11) A. Hagimura, M. Nakajima, K. Miyata and K. Uchino: Proc. Int. Symp. Applied Ferroelectrics 90 (1991) p. 185.
12) T. Ohno, N. Tsubouchi, M. Takahashi, Y. Matsuo and M. Akashi: Tech. Rep. IEICE Jpn. (1972) US71-37.
13) S. Takahashi, Y. Sasaki, S. Hirose and K. Uchino: Mater. Res. Soc. Symp. Proc. 360 (1995) 305.
14) Darrell D. Ebbing: *General Chemistry* (Houghton Mifflin Co., Boston, 1993) 4th ed.
15) Q. Tan, Z. Xu and D. Viehland: J. Mater. Res. 14 (1999) 465.
16) L. X. He, M. Gao, C. E. Li, W. M. Zhu and H. X. Yan: private communication.
17) Q. Tan, J. F. Li and D. Viehland: Philos. Mag. B 76 (1997) 59.
18) Q. Tan: PhD Dissertation, University of Illinois, Urbana, IL, USA, 1998.
19) Y. Imry and S. Ma: Phys. Rev. Lett. 35 (1975) 1399.
20) Q. Tan and D. Viehland: Phys. Rev. B 53 (1996) 14103.
21) D. Viehland and Y. H. Chen: to be published in J. Appl. Phys.
22) J. Kuwata, K. Uchino and S. Nomura: Ferroelectrics 37 (1981) 579.
23) S. Park and T. Shrout: J. Appl. Phys. 82 (1997) 1804.
24) D. Viehland: to be published in J. Appl. Phys.
25) T. Egami: to be published in Proc. 12th Int. Symp. Applications of Ferroelectrics, IEEE.